学位論文（要約）

Observation of Higgs Boson with Di-photon Events in Proton-Proton Collisions

（陽子・陽子衝突を用いたヒッグス粒子の二光子事象の観測）

平成 25 年 12 月博士（理学）申請

東京大学大学院理学系研究科

物理学専攻

山口 洋平

Observation of Higgs Boson with Di-photon Events in Proton-Proton Collisions

Yohei Yamaguchi

Contents

Abstract

A search for the Standard Model Higgs boson with a di-photon final state in proton-proton collisions with the ATLAS detector at the Large Hadron Collider is presented. The data sample used corresponds to integrated luminosities of 4.8 fb^{-1} at center-of-mass energy $\sqrt{s} = 7$ TeV in 2011 and 20.3 fb^{-1}at $\sqrt{s} = 8$ TeV in 2012. There is clear evidence for the production of a Higgs boson in a two photon resonance with a measured mass of 126.8 ± 0.2(stat.) $\pm$ 0.7(syst.) GeV on background expectations with the significance of 7.4 standard deviations. The Higgs mass, which is an input parameter of the Standard Model, is measured with 0.6 % accuracy. The measurements of coupling property and natural width of the Higgs boson are carried out. The measured signal strength (μ), which is a cross section times branching fraction normalized to the Standard Model prediction, is $\mu = 1.65 \pm 0.24\,(\text{stat.})\ ^{+0.25}_{-0.18}$ (sysy.). The upper limit on natural width of the Higgs boson is set to be 1.8 GeV (95%CL). They are consistent with expectations of the Standard Model Higgs boson.

Chapter 1

Introduction

The Standard Model of particle physics is a theory to describe elementary particles and their interactions. Developed in the early 1970s, the Standard Model has successfully described precisely experimental results below an energy scale of the order of 100 GeV. All the known matter is made up of elementary fermions called quarks and leptons. These fermions exchange elementary particles called gauge bosons, which mediate one of fundamental interactions. The Standard Model consists of six flavors of quarks and six flavors of leptons with their corresponding antiparticles, as well as four gauge bosons and one Higgs boson which is the visible manifestation of a Higgs field.

Before the Robert Brout, François Englert and Peter Higgs's work, a theory including massive bosons which carry interactions was not able to be constructed. However several experiments verified the weak force is carried by massive boson. In 1964, they proposed a new theory which is called the Brout-Englert-Higgs (BEH) mechanism or simply Higgs mechanism [1, 2, 3, 4, 5, 6]. According to their theory, Z and W bosons gain their mass through electroweak symmetry breaking. The Higgs field is introduced in order to break the symmetry spontaneously. In addition, the mass of fermions can also be generated by the interactions with the Higgs field. Thus the Higgs field is considered as the origin of mass for all massive elementary particles.

The observation of the Higgs boson confirms the existence of the Higgs field, hence it is crucial for the completion of the Standard Model. In addition, the precise measurement of Higgs boson properties represents critical tests of the Standard Model. However the boson was the last unobserved particle predicted by the Standard Model. In the last 50 years, many experiments, particularly at the LEP and Tevatron colliders, have searched for the Higgs boson; no significant signal was observed. A lower bound of 114.4 GeV has been established at 95 % CL on the mass of the Higgs boson from searches at the LEP [7]. The results from experiments at the Tevatron have excluded the Higgs mass between 100 and 103, as well as between 147 and 180 GeV [8].

The Large Hadron Collider (LHC) at CERN enables us to search for new physics at the TeV energy scale. The center-of-mass energy ($\sqrt{s}$) of the LHC was 7 TeV during 2011, and 8 TeV during 2012 run. The instantaneous luminosity reached 7×10^{33} cm^{-2}s^{-1} in 2012. Four main experiments are equipped with complex detectors which have been installed to collect and analyze the corresponding collision data. The Higgs boson is studied at two of them, ATLAS and CMS, which are general-purpose experiments.

In July 2012, CERN announced the discovery of a new boson at the LHC based on

combination results in di-photon ($H \to \gamma\gamma$), ZZ, W^+W^-, $\tau^+\tau^-$ and $b\bar{b}$ channels [9, 10]. The significance was 5.9 standard deviations for the ATLAS experiment, while 5.8 for the CMS experiment using data samples corresponding to integrated luminosity up to 5.1 fb^{-1} at $\sqrt{s} = 7$ TeV and 5.8 fb^{-1} at $\sqrt{s} = 8$ TeV. The nature of the new particle (couplings, mass and spin) has been studied, and the results show that the new boson has a mass of about 125 GeV and is compatible with the Higgs boson predicted by the Standard Model. The observation of the Higgs boson was confirmed by the Tevatron experiments with a local significance of 3.0 standard deviations [8].

More precise measurements of the properties of this new boson are crucial to elucidate the mass generation mechanism. The $H \to \gamma\gamma$ channel has great advantages of the property measurement. In this thesis, a measurement on the boson in the di-photon mode alone is presented with the full 2011 and 2012 data set. The coupling properties and mass measurements are updated, a first direct measurement of the natural width is presented as well.

1.1 Higgs mechanism

The Standard Model describes three interactions, electromagnetic, weak and strong interactions, which are based on the gauge theory [11, 12, 13, 14]. The electromagnetic and weak interactions are sort of unified in a gauge theory based on the group $SU(2) \times U(1)$. The Higgs field is introduced to break the symmetry and generate masses of the weak gauge bosons. The mechanism of mass generation through the spontaneous breaking of the gauge symmetry is called the Brout-Englert-Higgs mechanism (Higgs mechanism). The Higgs boson is the visible manifestation of the Higgs field.

In the Standard Model, the Higgs boson has neither spin, charge nor color charge. Because there is no other elementary particle which does not have spin, the Higgs boson is unique. The fermions, which are grouped into three generations, have spin of $1/2$. Each generation contains two quakes and two leptons. Thus there are six quarks (up, down, charm, strange, top and bottom) and six leptons (electron, electron neutrino, muon, muon neutrino, tau and tau neutrino). The Standard Model has spin-1 particles which carry the forces between these elementary particles. Photons mediate the electromagnetic force; the massive W^+, W^- and Z bosons carry the weak force; and eight gluons carry the strong force.

Quantum electrodynamics Quantum electrodynamics (QED) describes the dynamics of charged fermions and their electromagnetic interactions. The QED is an abelian gauge theory with the symmetry group $U(1)_{EM}$. The law of motion of a free fermion is given by the Dirac equation for a spinor ψ:

$$(i\gamma^\mu \partial_\mu - m)\,\psi|_{\text{free}} = 0 \tag{1.1.1}$$

where γ^μ ($\mu = 0$, 1, 2 and 3) is the four Dirac gamma 4×4 matrices. The local gauge transformation of ψ under $U(1)_{EM}$ writes:

$$\psi \to \psi' = e^{-\chi(x)}\psi \tag{1.1.2}$$

where χ is an arbitrary function of space-time coordinates. The requirement of local gauge invariance has led us to introduce a photon field A_μ, which is transformed as:

$$A_\mu \to A'_\mu = A_\mu + \frac{1}{e}\partial_\mu \chi \tag{1.1.3}$$

where e is elementary charge. The Lagrangian of QED is defined as:

$$\mathcal{L}_{\text{QED}} = \bar{\psi}\left(i\gamma^\mu D_\mu - m\right)\psi - \frac{1}{4}A_{\mu\nu}A^{\mu\nu} \tag{1.1.4}$$

where $\bar{\psi} = \psi^\dagger\gamma^0$, $A_{\mu\nu} = \partial_\mu A_\nu - \partial_\nu A_\mu$ and D_μ is a covariant derivative $D_\mu \equiv \partial_\mu - ieA_\mu$. The Lagrangian is invariant under the $U(1)_{EM}$ local gauge transformations of fields. The A_μ field is the photon. Hence the Lagrangian has no mass term of A_μ.

Weak interaction The weak interaction only acts on left-handed fermions ψ_L. Thus three W^i bosons (i =1, 2, 3) of weak isospin triplet of $SU(2)_L$, where the i-th W boson couples to Pauli matrix τ_i, are introduced. Left-handed fermions have weak isospin 1/2 (doublet) and the right-handed fermions have weak isospin 0 (singlet). For the first generation, this writes:

$$\text{leptons}: \begin{pmatrix} \nu_L \\ e_L \end{pmatrix}, (e_R), \qquad \text{quarks}: \begin{pmatrix} u_L \\ d_L \end{pmatrix}, (u_R), (d_R)$$

$\begin{pmatrix} \nu_L \\ e_L \end{pmatrix}$ or $\begin{pmatrix} u_L \\ d_L \end{pmatrix}$ is written as ψ_L. The W^+ and W^- bosons are formed as

$$W^\pm_\mu = \frac{1}{\sqrt{2}}\left(W^1_\mu \mp iW^2_\mu\right) \tag{1.1.5}$$

The local gauge transformation of ψ_L and W^i_μ under $SU(2)_L$ writes:

$$\begin{aligned} \psi_L \to \psi'_L = &\quad \exp\left(\frac{i}{2}\tau^i\chi_i(x)\right)\psi_L \\ W^i_\mu \to W'^i_\mu = &\quad W^i_\mu - \frac{1}{g}\partial_\mu\chi^i + \epsilon^i_{jk}\chi^j W^k_\mu \end{aligned} \tag{1.1.6}$$

where ϵ^i_{jk}, antisymmetric symbol, is the $SU(2)_L$ structure constant, and g is the weak coupling constant. The g is expressed in Fermi's constant G_{F}: $G_{\text{F}} = \frac{\sqrt{2}g^2}{8m_W^2}$. In contrast, right-handed singlets do not rotate under $SU(2)_L$ because they have isospin 0. The following covariant derivative is introduced:

$$D_\mu = \partial_\mu - ig\frac{\tau^i}{2}W^i_\mu \tag{1.1.7}$$

The Lagrangian for weak interaction writes:

$$\mathcal{L}_{\text{W}} = \bar{\psi}_L\left(i\gamma^\mu D_\mu - m\right)\psi_L - \frac{1}{4}W^i_{\mu\nu}W^{\mu\nu}_i \tag{1.1.8}$$

where $W^i_{\mu\nu} = \partial_\mu W^i_\nu - \partial_\nu W^i_\mu + ig\epsilon^i_{jk}W^j_\mu W^k_\nu$. The Lagrangian could include the mass terms of fermions ($m\bar{\psi}\psi = m\left(\bar{\psi}_L\psi_R + \bar{\psi}_R\psi_L\right)$) and W bosons ($m^2_W W_\mu W^\mu$). However they are not invariant under local gauge transformation. Therefore $SU(2)_L$ forbids the fermion and boson mass terms, which are incompatible with experiment results. This is attributed to the symmetry breaking of $SU(2)$.

1.1.1 Electroweak unification

In the Standard Model, the electromagnetic interaction and the weak interaction are unified under an $SU(2)_L \times U(1)_Y$ gauge group and referred to the electroweak interaction. The corresponding gauge bosons are the three W^i bosons which are introduced in the previous subsection, and the B boson with weak hypercharge of $U(1)_Y$. The corresponding gauge coupling constants for $SU(1)_Y$ and $U(1)_Y$ are given by g and g', respectively. These bosons and fermions are massless before symmetry breaking. The Z boson and photon field A are formed by mixing the W^3 and B bosons.

Similarly to QED, B boson couples both to left- and right-handed components of the fermion fields, respectively noted as ψ_L and ψ_R. The local gauge invariance under $SU(2)_L \times U(1)_Y$ is obtained by introducing two covariant derivatives:

$$\begin{aligned} D_{L\,\mu} =& \partial_\mu + \frac{i}{2} g \tau_i W_\mu^i + \frac{i}{2} g' Y B_\mu \\ D_{R\,\mu} =& \partial_\mu + \frac{i}{2} g' Y B_\mu \end{aligned} \tag{1.1.9}$$

which are respectively applied to left-handed and right-handed fermions in the part of Lagrangian describing the electroweak interaction. Y is a hypercharge operator. The Lagrangian writes:

$$\mathcal{L}_{EW} = i\bar{\psi}_L \gamma^\mu D_{L\,\mu} \psi_L + i\bar{\psi}_R \gamma^\mu D_{R\,\mu} \psi_R - \frac{1}{4} W_{\mu\nu}^i W_i^{\mu\nu} - \frac{1}{4} B_{\mu\nu} B^{\mu\nu} \tag{1.1.10}$$

where $B_{\mu\nu} = \partial_\mu B_\nu - \partial_\nu B_\mu$. The Lagrangian could include mass terms of bosons such as $m_W^2 W_\mu W^\mu$. They are not invariant under the $U(1)$ local transformations of fields. Since charge is conserved, $U(1)$ symmetry is not broken unlike $SU(2)$. Therefore a solution to the mystery of the mass generation is needed. Hence the Higgs mechanism was proposed.

1.1.2 Electroweak symmetry breaking

A complex scalar field ϕ of group $SU(2)_L$, representing the Higgs field, is introduced with four real fields:

$$\phi = \begin{pmatrix} \phi^+ \\ \phi^0 \end{pmatrix} = \frac{1}{\sqrt{2}} \begin{pmatrix} \phi_1 + i\phi_2 \\ \phi_3 + i\phi_4 \end{pmatrix} \tag{1.1.11}$$

Then they are added into the Lagrangian of the theory:

$$\mathcal{L} = \left(D_{L\,\mu}\phi\right)^\dagger \left(D_L^\mu \phi\right) - \frac{1}{4} W_{\mu\nu}^i W_i^{\mu\nu} - \frac{1}{4} B_{\mu\nu} B^{\mu\nu} - V(\phi) \tag{1.1.12}$$

where $V(\phi)$ is the potential of ϕ:

$$V(\phi) = \mu_\phi^2 \phi^\dagger \phi + \lambda \left(\phi^\dagger \phi\right)^2 \tag{1.1.13}$$

The parameters of Eq.(1.1.13) are constrained by $\lambda > 0$ so that the field is stable. The Lagrangian is invariant under a local gauge transformation under $SU(2)_L$:

$$\phi \to \phi' = \exp\left(\frac{i}{2} \tau_i \chi^i(x)\right) \phi \tag{1.1.14}$$

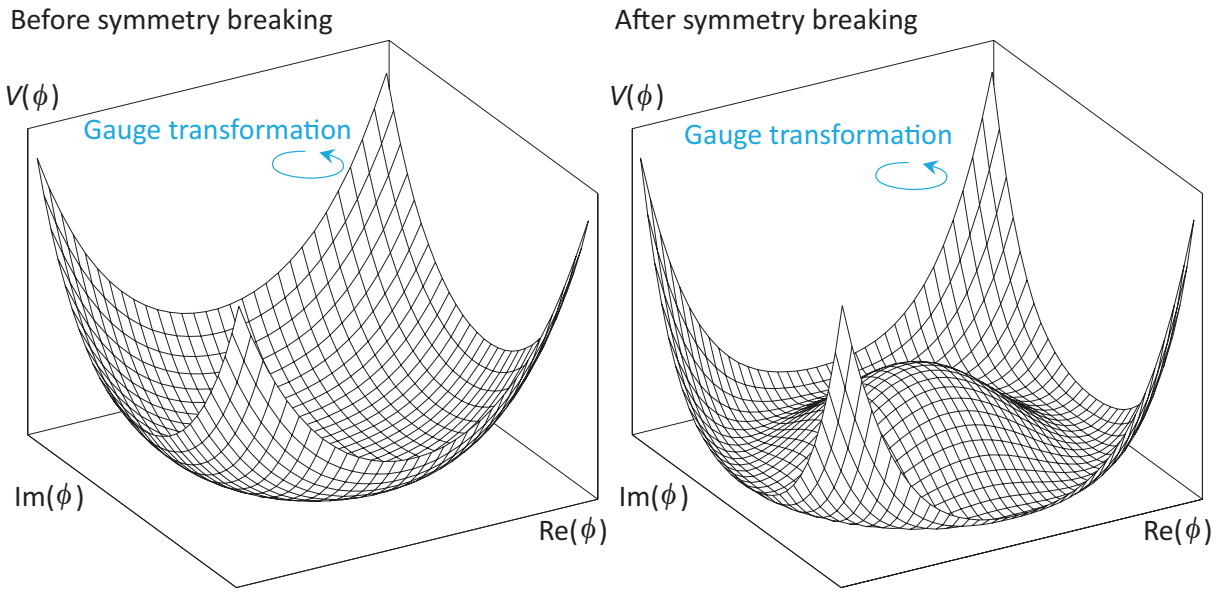

Figure 1.1.1: Illustration of the potential before and after the symmetry breaking of $SU(2)$.

The value of the ϕ at the vacuum is obtained when by minimizing $V(\phi)$ $(\partial V/\partial\phi = 0)$. In case $-\mu_\phi^2 > 0$, the $V(\phi)$ has its minimum value at $\phi^0 = v/\sqrt{2} = \sqrt{-\mu_\phi^2/2\lambda}$, while in case $-\mu_\phi^2 < 0$, $\phi^0 = 0$ gives the minimum of $V(\phi)$. The v is called vacuum expectation value. In the former case, the $SU(2)$ symmetry is broken. It is appropriate to expand ϕ near its minimum:

$$\phi = \frac{1}{\sqrt{2}} \exp\left(\frac{i}{2}\tau_i \chi'^i(x)\right) \begin{pmatrix} 0 \\ v + h(x) \end{pmatrix} \tag{1.1.15}$$

where $h(x)$ represents the Higgs boson which is associated with the Higgs field. There are three freedoms for the rotation by χ^i. A local gauge transition chooses a specific rotation angle as:

$$\phi = \frac{1}{\sqrt{2}} \begin{pmatrix} 0 \\ v + h(x) \end{pmatrix} \tag{1.1.16}$$

then $\phi_1 = \phi_2 = \phi_4 = 0$ and $\phi_3 = v + h(x)$. The symmetry vanishes by the choice of the specific gauge, that is the symmetry breaking of $SU(2)$. Figure 1.1.1 illustrates the potential before and after the symmetry breaking. Eq.(1.1.16) is substituted into the Lagrangian:

$$\begin{aligned} \mathcal{L} = & \left| \partial_\mu h + i\frac{1}{2\sqrt{2}}(v+h) \begin{pmatrix} gW_\mu^1 - igW_\mu^2 \\ -gW_\mu^3 + g'B_\mu \end{pmatrix} \right|^2 \\ & -\frac{1}{4}W_{\mu\nu}^i W_i^{\mu\nu} - \frac{1}{4}B_{\mu\nu}B^{\mu\nu} - \frac{\mu^2}{2}(v+h)^2 - \frac{\lambda}{4}(v+h)^4 \end{aligned} \tag{1.1.17}$$

where $|\quad|^2$ corresponds to $(\quad)^\dagger(\quad)$. The Lagrangian has terms $(g^2v^2/8)\left(\left(W_\mu^1\right)^2 + \left(W_\mu^2\right)^2\right)$ and $(v^2/8)\left(gW_\mu^3 - g'B_\mu\right)^2$, which represent mass terms of W and Z bosons. Z boson and

photon field A are formed by mixing W^3 and B

$$\begin{aligned} A = &\quad B\cos\theta_W + W^3\sin\theta_W \\ Z = &-B\sin\theta_W + W^3\cos\theta_W \end{aligned} \tag{1.1.18}$$

where $\theta_W = \arctan(g'/g)$ is the electroweak mixing angle, so called Weinberg angle. The relations between e and g, g' are obtained.

$$e = g\sin\theta_W = g'\cos\theta_W \tag{1.1.19}$$

From Eq.(1.1.5) and (1.1.18), the masses of $W^\pm$ and Z are extracted.

$$\begin{aligned} m_\gamma =& m_A = 0 \\ m_Z =& \frac{v}{2}\sqrt{g^2+g'^2} \\ m_W =& \frac{v}{2}g \end{aligned} \tag{1.1.20}$$

Therefore the mass terms for the physical $W^\pm$ and Z bosons naturally appear through the symmetry breaking of $SU(2)_L$. The A_μ field does not acquire mass, as no corresponding mass term is found in the Lagrangian. The relation between the Weinberg angle and boson masses is also obtained: $\cos\theta_W = \frac{m_W}{m_Z}$. There is also a term $-\mu_\phi^2 h^2 = \lambda v^2 h^2$, hence the Higgs boson gains mass itself. The corresponding mass m_H is:

$$m_H = \sqrt{-2\mu_\phi^2} = \sqrt{2\lambda}v \tag{1.1.21}$$

Since λ is a free parameter of the theory, the Higgs mass cannot be predicted within the Standard Model. After the symmetry breaking, $U(1)_{EM}$ symmetry remain unbroken, hence photon is massless. From the relation between v, m_W and Fermi's constant G_F, the vacuum expectation value is calculated to be [15]:

$$v = \frac{2m_W}{g} = \frac{1}{\sqrt{\sqrt{2}G_F}} \simeq 246.22\,\mathrm{GeV} \tag{1.1.22}$$

Yukawa coupling As described above, fermion mass terms $m\bar{\psi}\psi$ are not invariant under $SU(2)_L$ local gauge transformation. Thus fermion also should be massless before the symmetry breaking of $SU(2)_L$, and has to have a mass after the breaking. In the Standard Model, the fermion mass is also generated with the Higgs mechanism. It is possible to use the Higgs field to define Yukawa couplings g_f, where f represents a fermion, into the Lagrangian. For down type fermions, the same ϕ is used. On the other hand for up type fermions, the charge conjugate of the Higgs doublet ϕ^c is used:

$$\phi^c = i\tau_2\phi^* = \begin{pmatrix} \phi^{0*} \\ -\phi^{+*} \end{pmatrix} \tag{1.1.23}$$

ϕ^c is equivalent to ϕ because they can be connected by a unitary transformation in case of $SU(2)_L$. Therefore for example for quarks, the following terms are added into the Lagrangian:

$$\mathcal{L}_q = \left[-g_d\left(\bar{\psi}_L^d\phi\psi_R^d\right) + \mathrm{h.c.}\right] + \left[-g_u\left(\bar{\psi}_L^u\phi^c\psi_R^u\right) + \mathrm{h.c.}\right] \tag{1.1.24}$$

these terms are gauge invariant before the symmetry breaking. After the breaking of $SU(2)_L$:

$$\phi^c \to \frac{1}{\sqrt{2}} \begin{pmatrix} v+h \\ 0 \end{pmatrix}$$

and then

$$\mathcal{L}_q = -\frac{1}{\sqrt{2}} g_d v \bar{d}_L d_R \left(1 + \frac{h}{v}\right) - \frac{1}{\sqrt{2}} g_u v \bar{u}_L u_R \left(1 + \frac{h}{v}\right) \tag{1.1.25}$$

In case of leptons, the following terms are added into the Lagrangian before the symmetry breaking, since neutrinos are massless:

$$\mathcal{L}_e = \left[-g_e \left(\bar{\psi}^e_L \phi \psi^e_R\right) + \text{h.c.}\right] \tag{1.1.26}$$

and then after the breaking of $SU(2)_L$:

$$\mathcal{L}_e = -\frac{1}{\sqrt{2}} g_e v \bar{e}_L e_R \left(1 + \frac{h}{v}\right) \tag{1.1.27}$$

The mass of fermion is obtained:

$$m_f = \frac{1}{\sqrt{2}} g_f v \tag{1.1.28}$$

1.1.3 Properties of the Standard Model Higgs boson

From the Lagrangian of the Standard Model, the vertex factors are obtained:

$$\begin{aligned} Hf\bar{f} &: -i\frac{m_f}{v} \\ HWW &: 2i\frac{m_W^2}{v} g_{\mu\nu} \qquad HHWW : 2i\frac{m_W^2}{v^2} g_{\mu\nu} \\ HZZ &: 2i\frac{m_Z^2}{v} g_{\mu\nu} \qquad HHZZ : 2i\frac{m_Z^2}{v^2} g_{\mu\nu} \\ HHH &: -3i\frac{m_H^2}{v} \qquad HHHH : -3i\frac{m_H^2}{v^2} \end{aligned} \tag{1.1.29}$$

The Higgs couplings are therefore proportional to m_f, m_W^2 and m_Z^2. The Higgs boson also couples to itself. From the vertex factors, decay widths are calculated of order one [16].

$$\Gamma\left(H \to \bar{f}f\right) = \frac{N_c m_H m_f^2}{8\pi v^2} \left(1 - 4\frac{m_f^2}{m_H^2}\right)^{\frac{3}{2}} \tag{1.1.30}$$

$$\Gamma\left(H \to W^+W^-\right) = \frac{m_H^3}{16\pi v^2} \sqrt{1 - 4\frac{m_W^2}{m_H^2}} \left(1 - 4\frac{m_W^2}{m_H^2} + 12\left(\frac{m_W^2}{m_H^2}\right)^2\right) \tag{1.1.31}$$

$$\Gamma\left(H \to ZZ\right) = \frac{m_H^3}{32\pi v^2} \sqrt{1 - 4\frac{m_Z^2}{m_H^2}} \left(1 - 4\frac{m_Z^2}{m_H^2} + 12\left(\frac{m_Z^2}{m_H^2}\right)^2\right) \tag{1.1.32}$$

$$\Gamma\left(H \to \gamma\gamma\right) = \frac{\alpha^2}{256\pi^3}\frac{m_H^3}{v^2}\left|\sum_i N_{ci} e_i^2 F_i\right|^2 \tag{1.1.33}$$

where the terms $N_{ci}e_i^2F_i$ are summed for all charged particles, N_c is 1 for leptons and bosons as well as 3 for quarks, α is the fine structure constant and e_i is the electric charge in units of e. The function expression of F depends on the spin of the particle:

$$\begin{aligned} F_1 = &\quad 2 + 3\tau + 3\tau\left(2-\tau\right) f\left(\tau\right) \\ F_{1/2} = &\quad -2\tau\left(1 + \left(1-\tau\right) f\left(\tau\right)\right) \\ F_0 = &\quad \tau\left(1 - \tau f\left(\tau\right)\right) \end{aligned} \tag{1.1.34}$$

where 1, 1/2, 0 corresponds to the spin, $\tau = 4\frac{m_i^2}{m_H^2}$ and

$$f\left(\tau\right) = \begin{cases} \left(\sin^{-1}\left(\tau^{-\frac{1}{2}}\right)\right)^2 & \text{if } \tau > 1 \\ -\frac{1}{4}\left(\ln\left(\frac{1+\sqrt{1-\tau}}{1-\sqrt{1-\tau}}\right) - i\pi\right)^2 & \text{if } \tau < 1 \end{cases} \tag{1.1.35}$$

If the Higgs mass at 125 GeV is considered, the contributions of t/W loops are calculated as:

$$\begin{aligned} N_{cW}e_W^2F_W\big|_{m_H=125\,\text{GeV}} =& 8.32 \\ N_{ct}e_t^2F_t\big|_{m_H=125\,\text{GeV}} =& -1.84 \end{aligned} \tag{1.1.36}$$

1.2 Higgs boson physics at the LHC

1.2.1 Production and decay of Higgs boson

The dominant Higgs boson production processes in proton-proton collisions are gluon-gluon fusion (ggF), vector boson fusion (VBF), associated production with a W or Z boson (VH), or associated production with a pair of top quarks ($t\bar{t}H$ or simply, ttH). The leading-order Feynman diagrams for these four processes are represented in Figure 1.2.1. Since the vertex factors to the Higgs boson have m_H dependence, the expected cross sections for these four processes depend on the Higgs boson mass, as represented in Figure 1.2.2 and 1.2.3, at a center-of-mass energy of $\sqrt{s} = 7$ and 8 TeV, respectively. They are provided by the LHC Higgs Cross Section Working Group [17, 18, 19].

The gluon-gluon fusion has the largest production cross section at the LHC. The Higgs boson is produced by the annihilation of two gluons through a heavy quark loop. The loop is dominated by the top quark due to the large Yukawa coupling to the Higgs boson. The cross section of ggF production process is computed at next-to-next leading order (NNLO) in QCD with electroweak corrections. At $m_H = 125$ GeV, the ggF cross section is $\sigma_{\text{ggF}} = 15.13$ (19.27) pb at $\sqrt{s} = 7$ (8) TeV, which corresponds to 87 % of the Higgs production. Although the cross section is the largest, thee ggF events tend to have low signal to background ratio because they do not have high p_{T} particles in the final states except decay products of the Higgs boson. The vector boson fusion (VBF) has the second largest cross section at the LHC. The VBF process is written with two steps: $q_1q_2 \to VV^{(*)}q_1'q_2' \to Hq_1'q_2'$. The quarks radiate electroweak bosons, which fuse

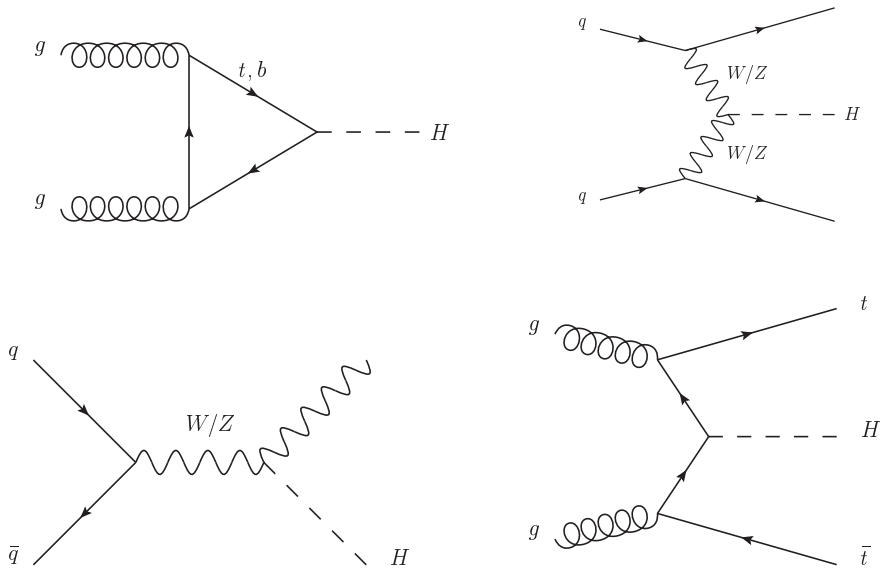

Figure 1.2.1: Leading order Feynman diagrams of the four main SM Higgs boson production processes: gluon gluon fusion (ggF, top left), Vector Boson Fusion (VBF, top right), associated production (VH, bottom left) and associated production with a pair of top quarks (ttH, bottom right).

インターネット公表に関する同意が
得られなかったため非公表

Figure 1.2.2: Standard Model Higgs boson production cross sections at $\sqrt{s} = 7$ GeV [19]. The cross sections provided by the LHC Higgs Cross Section Working Group [17, 18, 19] are used, following the ATLAS recommendations.

インターネット公表に関する同意が
得られなかったため非公表

Figure 1.2.3: Standard Model Higgs boson production cross sections at $\sqrt{s} = 8$ GeV [19]. The cross sections provided by the LHC Higgs Cross Section Working Group [17, 18, 19] are used, following the ATLAS recommendations.

together and produce the Higgs boson. At the leading order, it is a pure electroweak interaction. With respect to q_1 and q_2, the corresponding outgoing quarks q_1', q_2' gain a typical transverse momentum around $m_V/2$, where V denotes one of the weak bosons. Then, these two quarks fragment and hadronize into high energy jets in the forward and backward direction, respectively. The jets are characterized by a large separation in rapidity and a large di-jet mass. The VBF cross section is computed at NLO in QCD including electroweak and approximate NNLO QCD corrections. At $m_H = 125$ GeV, the VBF cross section is $\sigma_{\mathrm{VBF}} = 1.22$ (1.58) pb at $\sqrt{s} = 7$ (8) TeV. The VBF process is responsible for about 7 % of the Higgs production. The VH processes are generically called Higgs-strahlung, as the Higgs boson is radiated from an off-shell $W^{\pm}$ or Z boson from quark-antiquark annihilation. In the final state, the presence of a weak boson is a distinguishing signature. The VH cross section is computed at NNLO in QCD and NLO in electroweak corrections. At $m_H = 125$ GeV, the WH and ZH cross sections are $\sigma_{WH} = 0.58$ (0.70) pb and $\sigma_{ZH} = 0.34$ (0.42) pb at $\sqrt{s} = 7$ (8) TeV, respectively. The VH processes are responsible for about 5 % of the Higgs production. The ttH process is similar to the gluon-gluon fusion process. The Higgs boson is produced by the annihilation of a pair of top quarks as shown in Figure 1.2.1. The same order diagrams can be obtained from the Higgs radiation off a top quarks. The top decays lead to high jet multiplicity in the final state including two b-jets, or leptons and transverse missing energy. The ttH cross section is computed at NLO in QCD. At $m_H = 125$ GeV, the ttH cross section is $\sigma_{ttH} = 0.09$ (0.13) pb at $\sqrt{s} = 7$ (8) TeV. The ttH process is responsible for only 0.6 % of the Higgs production.

The Higgs boson can decay into di-photon via a loop. The dominant contributions are top and W boson loops as shown in Eq.(1.1.33) and (1.1.36). The Feynman diagrams of the three processes involved in the $H \to \gamma\gamma$ decay is shown in Figure 1.2.4. The branching fractions, as a function of the Higgs boson mass, are represented in Figure 1.2.5. They also are provided by the LHC Higgs Cross Section Working Group [17, 18, 19]. For $H \to \gamma\gamma$ branching fraction, all partial widths are calculated as accurately as possible. Then the branching fraction is derived from the total width and the di-photon partial width. For the diphoton partial width, NLO QCD correction and NLO electroweak correction are used. The $H \to \gamma\gamma$ branching fraction is between 1.36×10^{-3} and 2.28×10^{-3} in the range of $m_H \in [110, 150]$ GeV. The peak is at around $m_H = 125$ GeV.

Figure 1.2.6 shows the total width of the Higgs boson as a function of the Higgs mass. If m_H is smaller than m_W, the total decay width is smaller than 1 GeV. At $m_H = 125$ GeV, the width is expected to be 4 MeV. Table 1.2.1 summarizes the cross section, branching fraction, expected number of signal events and total width for several Higgs mass.

1.2.2 Feature of $H \to \gamma\gamma$ events

The signal di-photon decay mode has a clean signature, two high E_{T} photons, therefore the events can be surely triggered. Hence the efficiency of event reconstruction is large (~ 0.4), and the number of reconstructed events is expected to be significantly larger than other channels even though the branching fraction of di-photon final state is smaller than many other decay modes. Because a trigger to the signal events does not need anything else but decay products of the Higgs boson, the ggF signal is a main channel in the $H \to \gamma\gamma$ analysis.

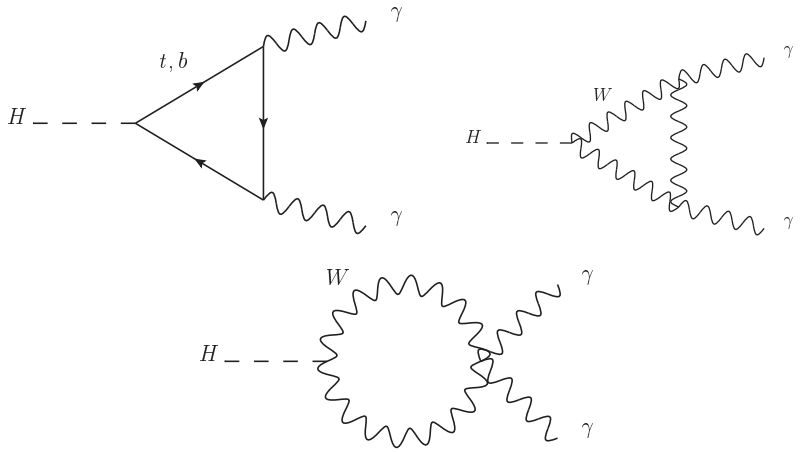

Figure 1.2.4: Leading-order Feynman diagrams of the three processes involved in the $H \to \gamma\gamma$ decay.

インターネット公表に関する同意が
得られなかったため非公表

(a)

インターネット公表に関する同意が
得られなかったため非公表

(b)

Figure 1.2.5: Standard Model Higgs boson decay branching ratios with m_H between 80 and 200 GeV (a) and with a wider range (b) [19].

インターネット公表に関する同意が
得られなかったため非公表

Figure 1.2.6: Total decay width of the Standard Model Higgs boson as a function of the Higgs mass [19].

		m_H		
		120 GeV	125 GeV	130 GeV
Cross section at $\sqrt{s} = 7$ TeV [pb]	ggF	16.43	15.13	13.98
	VBF	1.279	1.222	1.168
	WH	0.6617	0.5785	0.5059
	ZH	0.3808	0.3351	0.2957
	ttH	0.09758	0.08632	0.07660
Cross section at $\sqrt{s} = 8$ TeV [pb]	ggF	20.86	19.27	17.85
	VBF	1.649	1.578	1.511
	WH	0.8052	0.7046	0.6169
	ZH	0.4710	0.4153	0.3671
	ttH	0.1459	0.1293	0.1149
Branching fraction		0.00223	0.00228	0.00224
Expected number of signal events at $\sqrt{s} = 7$ TeV		203	191	173
Expected number of signal events at $\sqrt{s} = 8$ TeV		1082	1022	929
Total width [MeV]		3.51	4.07	4.91

Table 1.2.1: Cross section of the Higgs boson production, branching fraction to diphoton, the expected number of signal events and total width for $m_H = 120$, 125 and 130 GeV.

Because there is no missing particles in the Higgs decay particles, the Higgs mass can be reconstructed by the invariant mass of the di-photon ($m_{\gamma\gamma}$). The signal events make a sharp peak at the Higgs mass on the smoothly falling background in the $m_{\gamma\gamma}$ distribution. The di-photon mass is calculated as:

$$m_{\gamma\gamma} = \sqrt{2E^{\gamma 1}E^{\gamma 2}\left(1 - \cos\Delta\theta\right)} \tag{1.2.1}$$

where $E^{\gamma 1(2)}$ is energy of a photon and $\Delta\theta$ is opening angle of two photons. The background events are γ-γ, γ-jet and jet-jet events. In the γ-jet and jet-jet events, jets fake photons. Because the LHC is the hadron collider, these events have large cross section. Accordingly, the following three are crucial to discover the Higgs boson by the $H \to \gamma\gamma$ analysis:

1. Good mass resolution
2. High photon reconstruction efficiency
3. Strong photon-jet separation

At the ATLAS experiment, the energy of photons is measured with the electomagnetic (EM) calorimeter. The direction of photons is measured from the position of a primary vertex where a Higgs boson is produced to the position of energy deposit in the EM calorimeter. The primary vertex is determined by the inner tracker as well as the EM calorimeter. The EM calorimeter is used for reconstruction and identification of photons. Thus the excellent performance of the EM calorimeter is essential for the $H \to \gamma\gamma$ analysis.

Thanks to the great performance of the detector, many kinds of property of the Higgs boson can be measured by the $H \to \gamma\gamma$ analysis. The observed particle should be a boson and its spin should not be 1 according to the Landau-Yang theorem [20]. The mass of the

インターネット公表に関する同意が
得られなかったため非公表

Figure 1.2.7: The Standard Model renormalization group evolution (RGE) of λ varying the top mass Mt, the Higgs mass M_h and the strong coupling α_s [22].

new particle can be measured accurately in the $H \to \gamma\gamma$ analysis because of the narrow mass peak. In addition, the efficiencies of event reconstruction are high for all production processes, the data accumulated in 2011 and 2012 allows to measure the signal yields for each production process (ggF, VBF and VH) except for ttH process which has small cross section. Top-Higgs Yukawa coupling has large contributions to both production process and decay process. Consequently, the observation of the particle with di-photon channel provides a supporting evidence of the top-Higgs Yukawa coupling.

The Higgs mass is an input parameter of the Standard Model, hence it has to be determined by experiments to complete the Standard Model. For example, the production cross section and decay branching ratio of the Higgs boson depend on the Higgs mass. On the other hand, it is predicted in many beyond the Standard Model (BSM) theories. Therefore the measurement of the Higgs mass constrains these theories. The Supersymmetry (SUSY) is one of the most popular extension of the Standard Model. In SUSY models, Higgs mass is related to scalar top (stop) mass. For example, the simplest SUSY extension of the Standard Model, the MSSM, predicts that the tree-level mass of Higgs is smaller than the Z boson one [21]. The radiative corrections, however, make the mass larger, and the largest contribution of the correction comes from stop which is a supersymmetric partner of top quark. In order to correct the Higgs mass up to about 126 GeV, either a contribution of stop mass or large mixing between left and right handed stop is required. The observation of the Higgs boson at$\sim$ 126 GeV favors a heavy stop.

In the Standard Model, the Higgs potential is determined by the Higgs mass as shon in Eq.(1.1.21). The Higgs potential reveals the stability of vacuum and the dynamics of the symmetry breaking. They are significant hints to BSM. The vacuum stability is studied with a renormalization group equation (RGE) [22]. When the running of the quartic Higgs coupling λ is calculated as a function of RGE scale, λ may drop to negative before the Planck scale depending on the Higgs mass as shown in Figure 1.2.7. In case $\lambda < 0$, the Higgs potential can go to negative infinity as shown in Figure 1.2.8. In this case, the vacuum is not stable. If the vacuum is instable, the existence of new physics before the Planck scale is proved because the Standard Model is not established at the energy scale. However even if $\lambda < 0$, going to negative infinity need a tunnel effect. If the probability of the quantum tunneling is quite low, the vacuum does not go to the false vacuum. This status is called metastable. According to NNLO analysis of the Standard Model Higgs potential, the absolute vacuum stability requires the Higgs mass to be larger than 129.4 ± 1.8 GeV [22]. Therefore a precise measurement of mass of the Higgs boson can verify the vacuum stability. Figure 1.2.9 shows regions of absolute stability, metastability and instability of the vacuum.

The Higgs coupling measurement is a test of the Standard Model. In general, if a new physics exists, the effect of a new particle is significant in a loop process. Thus couplings to

インターネット公表に関する同意が
得られなかったため非公表

Figure 1.2.8: Illustration of the potential when $\lambda < 0$.

インターネット公表に関する同意が
得られなかったため非公表

Figure 1.2.9: Regions of absolute stability, metastability and instability of the Standard Model vacuum in the top mass and the Higgs mass plane [22].

massless particles, such as gluons and photons, are good probes to study BSM because one loop processes are leading order. In the $H \to \gamma\gamma$ signal, loop contributions are significant in both production and decay processes. The process of 2 gluons to Higgs, which has the largest contribution to the production process as ggF, is sensitive to colored particles. Furthermore, the decay of the Higgs boson into diphoton process allows to study a new particle which has no color charge but electric charge. Thus the di-photon mode has the great advantages to BSM studies.

The $H \to \gamma\gamma$ mode is one of the most important discovery channels, and has various physics motivations.

1.3 Thesis objective

In this thesis, a search for the Higgs boson in the di-photon decay channel alone at the ATLAS experiment is presented. The data used from proton-proton collisions is more than doubled from the observation paper [9], corresponding integrated luminosities of 4.8 fb^{-1} at $\sqrt{s} = 7$ and 20.3 fb^{-1} at $\sqrt{s} = 8$ TeV. In July 2013, the ATLAS collaboration published results indicating that the observed particle has no spin. Therefore the observed particle is assumed to be a Higgs boson in this thesis.

This thesis is organized as follows. In the Chapter 2, outlines of the LHC and the ATLAS detector are described. Because of the importance of the EM calorimeter for the $H \to \gamma\gamma$ analysis, this subdetector is focused in the chapter. The data set and Monte Carlo simulation used in this analysis are given in the Chapter 3. The Chapter 4 describes reconstruction of photons, as well as the primary vertex selection for di-photon events with the ATLAS detector. In the Chapter 5, the performance of the ATLAS detector for identifying and measuring photons is described. In the Chapter 6, the event selection and categorization of the $H \to \gamma\gamma$ analysis in both 2011 and 2012 data sets are given. Several event categories are introduced for study of VH process after the observation paper. In the Chapter 7, the signal and background modeling is discussed including their systematic uncertainties. The systematic uncertainties are estimated for the signal and background models. The Chapter 8 presents statistical procedures and results of the search for the Higgs boson in di-photon events. The significance of observed excess of the Higgs boson

signal is amount to 7.4 standard deviations, which is accomplished by the di-photon mode alone. Then measurements of the couplings, mass and width of the observed Higgs boson are described. Finally in the Chapter 9, conclusion of this thesis is given.

As described in Section 1.2.2, high mass resolution, high photon reconstruction efficiency and great photon-jet separation are required. In order to satisfy these demands, I have developed a photon-jet separation technique. This technique provides a strong separation even in the extreme environment of high instantaneous luminosity. In addition, I have developed a data-driven technique to estimate the performance of the photon reconstruction with the EM calorimeter. In the LHC, this is the only technique enabling to obtain very high purity samples of genuine photons. I made a significant contribution on the estimation of the systematic uncertainties. For example, the uncertainty of the photon identification is reduced by considering the correlation between two photons.

Chapter 2

LHC and ATLAS detector

2.1 LHC

The Large Hadron Collider (LHC) is a two-ring largest energy proton-proton collider with superconducting magnets at CERN (European Organization for Nuclear Search). It is installed in the tunnel of 26.7 km of circumference located underground of about 100 m.

2.1.1 Injection chain

The LHC injecting system is a chain of accelerators that protons are accelerated to increasingly higher energies as shown in Figure 2.1.1. Each machine boosts the energy of a beam, before injecting the beam into the next machine in the chain. The LHC is the last element of the chain.

The proton source is a bottle of hydrogen gas. An electric field breaks down the hydrogen into its constituent protons and electrons. The protons are accelerated and focused by a radio frequency quadrupole, and then are sent to the linear accelerator (Linac2). The Linac2 accelerates the protons to the energy of 50 MeV with radio frequency cavities. The beam is then injected into the Proton Synchrotron Booster (PSB), which is constructed of synchrotron rings. The PSB contains four superimposed rings with a radius of 25 meters, and pushes the protons to 1.4 GeV, followed by the Proton Synchrotron (PS). The PS is a synchrotron with a circumference of 628 m, which accelerates the beam to 25 GeV. Protons are then sent to the Super Proton Synchrotron (SPS) where they are

インターネット公表に関する同意が得られなかったため非公表

Figure 2.1.1: The CERN accelerator complex [23].

	Design	2011	2012
Maximum proton energy [TeV]	7	3.5	4
Number of bunches	2808	1380	1380
Bunch length (r.m.s) [cm]	7.55	5.5	4.5
Circumference of ring [m]	26658.88	-	-
Frequency of bunch crossing [ns]	25	50	50
Number of interaction point	4	-	-
Injection energy [GeV]	450	-	-
Number of particles per bunch	1.15×10^{11}	1.1 - 1.4 $\times 10^{11}$	1.5×10^{11}
Crossing angle [μrad]	300	-	-
β function at interaction point [m]	0.55	1.0 - 1.5	0.6
Normalized emittance [μm]	3.75	2.4	2.4
Peak luminosity [$\mathrm{cm}^{-2}\mathrm{s}^{-1}$]	10^{34}	$< 3.65 \times 10^{33}$	$< 7.73 \times 10^{33}$

Table 2.1.1: LHC design and operation parameters [24, 25, 26, 27].

accelerated to 450 GeV. The SPS, with a circumference of 7 km, is the second largest machine in the accelerator complex at CERN. The protons are finally injected to the two beam pipes of the LHC.

2.1.2 LHC ring design

The LHC ring is designed to collide protons at the nominal energy of 7 TeV per beam, giving a total center-of-mass energy of $\sqrt{s} = 14$ TeV. The design luminosity is 10^{34} $\mathrm{cm}^{-2}\mathrm{s}^{-1}$, providing a beam bunch crossing rate of 40 MHz. The beam in one pipe circulates clockwise while the beam in the other pipe circulates anticlockwise. It takes 260 seconds to fill each LHC ring, and tens minutes for the protons to reach their maximum energy. Beams circulate for many hours inside the LHC beam pipes under normal operating conditions. The design parameters of the LHC ring are summarized in Table 2.1.1.

The LHC ring includes 1232 super-conducting dipole magnets to bend the proton trajectory to the curvature radius of the LHC ring. Those dipoles produce the magnet field of 8.33 T. A proton loses energy due to synchrotron radiation when in turns by the magnetic field. The energy loss per turn is 6.7 keV and is recovered by radio frequency cavities located at one of the straight lines of the ring. Another main role of the radio frequency cavities is to keep 2808 proton bunches tightly bunched to ensure high luminosity at the interaction points (IPs). The LHC ring has 4 IPs in which experimental detectors are installed; ATLAS, CMS, ALICE and LHCb. On upstream of each experiment, beams are focused by using three superconducting quadrupole magnets. Proton beams are designed to be focused into transverse radius of 16.7 μm at ATLAS and CMS.

2.1.3 LHC operation

The LHC operation started on September 2008 with 450 GeV proton beams. In 2010, the beam energy is increased to 3.5 TeV and delivered $\mathcal{L} = 48$ pb^{-1} proton-proton collision data. In 2011, the LHC performed $\sqrt{s} = 7$ TeV collisions. The peak luminosity was up to $\mathcal{L} = 3.65 \times 10^{33}$ $\mathrm{cm}^{-2}\mathrm{s}^{-1}$. Compared with the design parameters, the bunch spacing

was reduced to 50 ns, the number of bunches was up to 1380, as well as the β function at IP (β^*) was 1.5 or 1.0 m. The resulting transverse beam spot size is about 20 μm, and longitudinal size is about 55 mm. The integrated luminosity delivered by the LHC in 2011 is 5.46 fb^{-1} [28]. In 2012, the center-of-mass energy was increased to $\sqrt{s} = 8$ TeV. With respect to 2011, the peak luminosity was up to $\mathcal{L} = 7.73 \times 10^{33}$ cm^{-2}s^{-1} with helped by decreasing β^* to 0.6 m and increasing protons per bunch higher than the design value. The transverse beam spot size is about 15 μm, and longitudinal size is about 45 mm. The total integrated luminosity delivered in 2012 is 22.8 fb^{-1}. The LHC operation parameters are summarized in Table 2.1.1. The data recorded in 2011 and 2012 is used for analysis in this thesis.

2.2 ATLAS detector

2.2.1 Concept of ATLAS detector

The ATLAS (A Toroidal LHC ApparatuS) is a multi-purpose detector constructed at the LHC. The main target physics of the ATLAS experiment is discovery for the Higgs boson and new physics beyond the Standard Model, precise measurement for the electroweak and top quark physics, as well as stringent test of QCD. The ATLAS is designed to adapt to the extreme LHC running conditions of high instantaneous luminosity and deposited energy. It covers nearly 4π around the IP and has a small dead time. Thus geometrical and timing acceptance of the ATLAS is very high. The ATLAS has a cylindrical geometry, which surrounds the beam pipe. The center of the detector is at one of the IPs of the LHC. The size of the ATLAS is 25 m $\times$ 44 m as diameter times length. The huge size enables precise measurement of muon tracks.

The ATLAS detector consists of four major components: magnet system, inner detector, calorimeter and muon spectrometer. A schematic representation of the detector and its subsystems is shown in Figure 2.2.1. The complete ATLAS detector is split into a barrel part, where detector layers are in cylindrical layers around the beam axis, and two end-cap parts, where detector layers are located in transverse planes. Table 2.2.1 summarizes the dimensions of the detector. The magnet system for the ATLAS detector is required to provide optimized magnetic field configuration for particle bending around the sub-detectors. It consists of three subsystems:one central solenoid, one barrel toroid and two endcap toroids. It is designed to minimize multiple-scattering effects. The inner detector identifies charged particles, and enables precise measurement of their momenta as well as the reconstruction of their tracks, and of primary and secondary vertices. The calorimeter is divided into electromagnetic (EM) calorimeter and hadronic calorimeter. They allow the identification of electromagnetic (photon, electron) and hadronic particles by a reconstruction of their shower shapes and measurement of their energies. The missing transverse energy is also measured by the calorimeters. The muon spectrometer is located at the outermost of the detector. The identification of muons and precise measurement of their momenta are performed by the muon spectrometer.

The trigger system is crucial components of the detector. It allows reducing the rate of selected events.

インターネット公表に関する同意が得られなかったため非公表

Figure 2.2.1: Overview of ATLAS detector [23].

Component	outer radius [m]	length [m]	η coverage
Barrel + endcap inner detector	1.15	6.8	$\|\eta\| < 2.4$
Central solenoid magnet	1.32	5.3	-
Barrel EM calorimeter	2.25	6.42	$\|\eta\| < 1.4$
Barrel hadronic calorimeter	4.25	12.2	$\|\eta\| < 1.0$
Barrel toroid magnet	10.05	25.3	-
Barrel muon spectrometer	11	26	$\|\eta\| < 1.4$
Endcap EM calorimeter	2.25	0.63	$1.4 < \|\eta\| < 3.2$
Endcap hadronic calorimeter	2.25	2.25	$1.5 < \|\eta\| < 3.2$
Endcap toroid magnet	5.35	5	-
Endcap muon spectrometer	11	2.8	$1.1 < \|\eta\| < 2.8$
Forward/backward calorimeter	integrated in endcap		$3.1 < \|\eta\| < 4.9$

Table 2.2.1: Dimensions of the ATLAS subsystem.

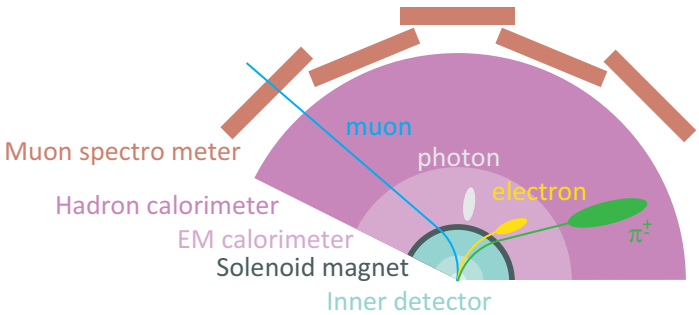

Figure 2.2.2: Illustration of barrel of ATLAS subdetectors.

2.2.2 ATLAS coordinate system

The origin of the coordinate system is defined to be the nominal proton-proton interaction point. The z-axis is set to be the beam direction. The positive direction of z-axis is anticlockwise around the LHC ring. The x-y plane is transverse to the beam direction. The x-axis is horizontal, while the y-axis is vertical. The positive x values point towards the center of the ring, and the positive y values point upwards. The azimuthal angle ϕ is defined around z-axis, the polar angle θ is the angle from the z-axis and $R \equiv \sqrt{x^2 + y^2}$ defines the polar radius. (E, p_x, p_y, p_z) is the four momentum of a particle. The rapidity y is defined as follows:

$$\mathrm{y} \equiv \frac{1}{2} \ln \frac{E + p_z}{E - p_z} \tag{2.2.1}$$

$p_{\mathrm{T}} \equiv \sqrt{p_x^2 + p_y^2}$ defines the transverse momentum, and $E_{\mathrm{T}} \equiv \sqrt{m^2 + p_{\mathrm{T}}^2}$ is the transverse energy. The pseudo-rapidity η is defined as:

$$\eta \equiv -\ln \left(\tan \frac{\theta}{2} \right) \tag{2.2.2}$$

$\eta \to \infty\,(-\infty)$ when $\theta \to 0\,(\pi)$ and $\eta = 0$ when $\theta = \frac{\pi}{2}$. The Eq.(2.2.2) is rewritten as follows:

$$\eta = \frac{1}{2} \ln \frac{|\vec{p}| + p_z}{|\vec{p}| - p_z} \tag{2.2.3}$$

for massless particles, $\mathrm{y} = \eta$.

2.2.3 Magnet system

The ATLAS detector has the superconductive magnet system. The central solenoid provides an axial magnetic field of 2 T for the inner detector. It is located inside the EM calorimeter [31]. One of the advantages of the small solenoid in the EM calorimeter is a compact design. Another is reduction of the transverse spread of showers. The number of radiation length of the solenoid is ~ 0.66 radiation length (X_0).

The barrel toroid consists of 8 flat superconducting race-track coils. Two endcap toroidal magnets, located inside the barrel toroid at both ends of the central solenoid. Each coil of the barrel toroid has an axial length of 25.3 m and extends radially from 4.7 m to 10.05 m. The endcap toroids have a length of 5 m, an outer diameter of 10.7 m and an inner diameter of 1.65. The toroidal magnet fields enable to measure the momentum for low-p_{T} muon by bending for θ-direction. Magnetic field made by the toroidal magnetic system is not uniform in ϕ. The toroidal magnetic field has not only ϕ component but also z component. The peak of the magnetic field provided by the toroids is 3.9 T by the barrel toroid and 4.1 T by the endcap toroids. Figure 2.2.3 shows the three-dimensional view of the magnet system.

2.2.4 Inner detector

The ATLAS Inner Detector (ID) [29, 30] is the innermost sub-detector. It is a tracking detector providing excellent charge determination and particle momentum resolution capabilities. Primary and secondary vertices which include photon conversion vertices are

インターネット公表に関する同意が
得られなかったため非公表

Figure 2.2.3: Three-dimensional view of the ATLAS magnet system: the central solenoid, the 8 coils of the barrel toroid and the 2×8 coils of the end-cap toroids [31].

インターネット公表に関する同意が
得られなかったため非公表

Figure 2.2.4: Cut-away view of the ATLAS Inner Detector [32].

also reconstructed by the tracking. The ID also has particle identification capabilities, for example electron and photon separation as described its detail later. Immersed in the solenoid magnetic field, the ID consists of three sub-detectors: Pixel detector, Semiconductor Tracker (SCT) and Transition Radiation Tracker (TRT). Each of them have a barrel and two endcaps, one located on each side of the barrel as shown in Figure 2.2.4. The total size of the ID is 2.1 m $\times$6.2 m as diameter times length. It covers $|\eta| < 2.5$ and full azimuthal coverage. Figure 2.2.5 shows an over view of barrel ID. Material distribution as a function of $|\eta|$ is shown in Figure 2.2.6.

2.2.4.1 Pixel detector

The Pixel detector is the nearest detector to the beam-pipe with very high granularity followed by the SCT [30]. It consists of three barrel layers and three endcap disks, completing the $|\eta| < 2.5$ coverage. Table 2.2.2 summarizes the parameters of the Pixel detector. The pixel size is 50×400 μm. The thickness of the Pixel detector is about 0.025 X_0 per layer. The innermost layer is especially important for the separation between electrons and photons. Charge sharing between adjacent pixels improves spatial resolution better than the pixel intrinsic resolution (pitch/$\sqrt{12}$). The typical position resolution of the pixel detector is 10 μm in $r - \phi$ direction and 115 μm in z direction.

2.2.4.2 Semiconductor tracker

The Semiconductor Tracker (SCT) is the middle component of the ID, covering $|\eta| < 2.5$ [30]. It consists in four layers in the barrel and nine disks in endcaps. An SCT module consists of two pairs of single-sided silicon microstrip sensors glued back-to-back with a 40 mrad stereo rotation angle around the geometrical center of the module. Table 2.2.3 and 2.2.4 summarize the parameters of the SCT. Each of the barrel strip is 126 mm long and the readout units are in 80 μm pitch. In the endcaps, the strips have an active

インターネット公表に関する同意が
得られなかったため非公表

Figure 2.2.5: Drawing showing the sensors and structural elements traversed by a charged track of 10 GeV p_{T} in the barrel inner detector ($\eta = 0.3$). The track traverses successively the beryllium beam pipe, the three cylindrical silicon-pixel layers with individual sensor elements of 50×400 $\mu\mathrm{m}^2$, the four cylindrical double layers (one axial and one with a stereo angle of 40 mrad) of barrel silicon-microstrip sensors (SCT) of pitch 80 μm, and approximately 36 axial straws of 4 mm diameter contained in the barrel transition-radiation tracker modules within their support structure [32].

インターネット公表に関する同意が
得られなかったため非公表

Figure 2.2.6: Material distribution (X_0) at the exit of the ID envelope, including the services and thermal enclosures. The distribution is shown as a function of $|\eta|$ and averaged over ϕ. The breakdown indicates the contributions of external services and of individual sub-detectors, including services in their active volume [32].

	Radius [mm]	Number of pixels
Barrel layer 1	50.5	13.2×10^6
Barrel layer 2	88.5	22.8×10^6
Barrel layer 3	122.5	31.2×10^6
	$\lvert z \rvert$ [mm]	Number of pixels
Endcap disk 1	495	2.2×10^6
Endcap disk 2	580	2.2×10^6
Endcap disk 3	650	2.2×10^6

Table 2.2.2: Parameters of the Pixel detector.

	Radius [mm]	Length [mm]	Rotation [deg]
Layer 1	299	1498	11.00
Layer 2	371	1498	11.00
Layer 3	443	1498	11.25
Layer 4	514	1498	11.25

Table 2.2.3: Parameters of the SCT in barrel.

	$\|z\|$ [mm]	Inner R [mm]
Disk 1	853.8	337
Disk 2	934.0	270
Disk 3	1091.5	270
Disk 4	1299.9	270
Disk 5	1399.7	270
Disk 6	1771.4	270
Disk 7	2115.2	337
Disk 8	2505.0	408
Disk 9	2720.2	439

Table 2.2.4: Parameters of the SCT in endcaps.

length between 55 and 120 mm, and the readout pitch has a width between 57 and 90 μm depending on the modules. The average design thickness of the barrel SCT is 0.08 X_0, while that of the endcap SCT is 0.3 X_0.

2.2.4.3 Transition Radiation Tracker

The Transition Radiation Tracker (TRT) is the outermost sub-detector of the ID [30]. It is based on the use of straw detectors with diameter of 4 mm, which can operate at the expected high rates due to their small diameter and the isolation of the sense wires within individual gas volumes. Each straw is equipped with a 30 μm diameter gold-plated tungsten wire. The straw tube volume is filled with the gas mixture of Xe : CO_2 : O_2 = 70 : 27 : 3. A gas gain is 2.5×10^4 with the high voltage of 1530 V. The length of the straw is 144 cm in barrel or 39 cm in endcaps. The TRT tubes cover the radius $563 < R < 1066$ mm, as well as $|z| < 712$ mm in the barrel region where the tubes lie along z-direction. On the other hand, in the endcap region where the straws point toward the R-direction, straw planes are placed $644 < R < 1004$ mm, as well as $848 < |z| < 2710$ mm. Thus the TRT covers $|\eta| < 2$. The thickness of the TRT is $\sim 0.3\ X_0$ in barrel and $\sim 0.2\ X_0$ in endcap.

The TRT provides continuous tracking with many measurements in individual straw tubes. Typically 36 tracking points are provided by the TRT. It uses not only ionization but also transition radiation. The X-ray emission depends on the Lorentz boost of the particle, and therefore on its mass. The output of the X-ray due to the transition radiation is expected to be larger than ionization for high energy electrons, and hence electrons can be identified from heavier particles with the number of high-threshold hits in the TRT. The expected charged pion rejection factor for electron identification with using TRT alone is about 10 for $20 < p_{\mathrm{T}} < 40$ GeV.

インターネット公表に関する同意が
得られなかったため非公表

Figure 2.2.7: Cut-away view of the ATLAS calorimeter system [32].

η region	Lead thickness [mm]
$0 < \|\eta\| < 0.8$	1.5
$0.8 < \|\eta\| < 1.4$	1.1
$1.4 < \|\eta\| < 2.5$	1.7
$2.5 < \|\eta\| < 3.2$	2.2

Table 2.2.5: Lead thickness of the EM calorimeter.

2.2.5 Calorimeter

The calorimeter in ATLAS is composed of electromagnetic (EM) calorimeter and hadronic calorimeter [33]. The EM calorimeter is designed for the reconstruction and identification of photons and electrons, while the hadronic calorimeter is aimed at the identification and reconstruction of hadrons (protons, neutrons, pions, etc.). Both calorimeters cover full azimuthal angle. The missing and total transverse energies (E_{T}^{miss} and $\sum E_{\mathrm{T}}$) are measured with the calorimeters. They are sampling calorimeters. Therefore they consist of succession of dense material layers (absorber) and active material layers. The former develops particle shower, while the latter produces an output signal proportional to the deposit energy. Figure 2.2.7 shows the layout of the ATLAS calorimeter sub-detectors. The EM calorimeter is constituted of a barrel part ($|\eta| < 1.475$) and two endcaps parts ($1.375 < |\eta| < 3.2$) of each side. It is located outside of the solenoid. The hadronic calorimeter is placed outside of the EM calorimeter and is divided into a barrel ($|\eta| < 1.$), 2 extended barrels ($0.8 < |\eta| < 1.7$), 2 endcaps ($1.5 < |\eta| < 3.2$) and 2 forward calorimeters ($3.1 < |\eta| < 4.9$) which cover the region closest to the beam.

2.2.5.1 Electromagnetic calorimeter

The EM calorimeter uses liquid argon (LAr) as the active material, kept at a temperature of about 89 K by a cryostat [34]. LAr has natural response linearity, homogeneity, radiation tolerance and slow aging. The LAr fills the gaps between the sampling layers of absorbers made of lead. The gap between the absorbers are ~ 4 mm. In the middle of a gap, three planar layers of copper, which is 275 μm thick, are separated by insulator layers of kapton. The two outer layers distribute the high voltage of about 2000 V, while the inner is the electrode that collects the signal. The absorbers are at ground voltage. The lead thickness in the absorber plates has been optimized as a function of η in terms of the EM calorimeter performance of energy resolution. The thickness is summarized in Table 2.2.5.

インターネット公表に関する同意が
得られなかったため非公表

Figure 2.2.8: Signal shape as produced in the detector (triangle), and after shaping (curve with dots). The sampling points, every 25 ns, are shown in dots [34].

インターネット公表に関する同意が
得られなかったため非公表

Figure 2.2.9: Sketch of a barrel module where the different layers are clearly visible with the ganging of electrodes in ϕ. The granularity in η and ϕ of the cells of each of the three layers and of the trigger towers is also shown [32].

In the EM calorimeters, LAr is ionized by secondary particles of the particle showers, resulting in electron-ion pairs drifting under the influence of an electric field. The ionization signal is collected from the electrodes by capacitive effect. Since LAr has high ionization density, great many electron-ion pairs are produced. Another merit of LAr is the high mobility of the electrons in the LAr. Then the LAr has the small drift time and hence the great detector time response. The total integration of the charge is typically $\sim$ 500 ns. The shape of a current pulse collected at the electrodes as a function of time is triangular and it is shaped with a bipolar CR$\cdot$(RC)^2 filter as shown in Figure 2.2.8.

The EM calorimeter has an accordion geometry as shown in Figure 2.2.9. This geometry enables to achieve full coverage in ϕ because of absence of any cracks or dead materials. In addition, signal can be extracted fast at the rear or the front of electrodes. In the barrel, the accordion waves are axial and run in ϕ, the folding angles of the waves vary with radius in order to keep the gap constant (Figure 2.2.10). On the other hand in the endcaps, the accordion waves are parallel to R-direction and run axially as shown in Figure 2.2.11. Since the LAr gap increases with radius in the endcaps, the wave amplitude and the folding angle of the absorbers and electrodes vary with radius. All these features of the accordion geometry lead to a very uniform performance in terms of linearity and resolution as a function of ϕ.

The LAr calorimeter is composed of three layers plus a presampler (Figure 2.2.9). The 1st layer has high granularity along η to identify electrons and photons, and to determine the direction of photons. The 2nd layer is long in R-direction ($\sim$ 16 X_0) and measures the

インターネット公表に関する同意が
得られなかったため非公表

Figure 2.2.10: Perspective view of one half of the barrel cryostat [34].

インターネット公表に関する同意が
得られなかったため非公表

Figure 2.2.11: Perspective view of one endcap cryostat [34].

インターネット公表に関する同意が
得られなかったため非公表

(a)

インターネット公表に関する同意が
得られなかったため非公表

(b)

Figure 2.2.12: Cumulative amounts of material, in units of radiation length X_0 and as a function of $|\eta|$, in front of and in the electromagnetic calorimeters. The two plots show, in contrast, separately for the barrel (a) and endcap (b), the thicknesses of each accordion layer as well as the amount of material in front of the accordion [32].

most of energy deposit of electrons and photons. Because photons and electrons deposit almost all of their energies before reaching to the 3rd layer, the 3rd layer is used for identification of electrons, photons and hadrons with using the ratio of energy deposits between 2nd and 3rd layers. The presampler, which covers $|\eta| < 1.8$, is used to correct for the energies of electrons and photons lost upstream of the calorimeter. It consists of a LAr layer of thickness 1.1 cm (0.5 cm) in the barrel (end-cap) region. Thus it does not have the accordion structure. The 1st and 2nd layer covers $|\eta| < 3.2$, the 3rd layer covers $|\eta| < 2.5$ and the coverage of the presampler is $|\eta| < 1.8$. Table 2.2.6 summarizes the granularity of each layer. Figure 2.2.12 shows the material distribution of each layer as a function of $|\eta|$. The total thickness of the EM calorimeter is more than 22 X_0 in the barrel regions and more than 24 X_0 in the endcap region. The layout of the layers with η is shown in Figure 2.2.13.

The raw output of the calorimeter is longer than the bunch crossing. For making

インターネット公表に関する同意が
得られなかったため非公表

Figure 2.2.13: Layout of the signal layer for the four different types of electrodes before folding. The two top electrodes are for the barrel and the two bottom electrodes are for the endcap inner (left) and outer (right) wheels. Dimensions are in millimeters. The drawings are all at the same scale [32].

Layer	η region	Granularity ($\eta \times \phi$)
Presampler	$\lvert\eta\rvert < 1.52$	$0.025 \times \pi/32$
Sampling 1	$\lvert\eta\rvert < 1.4$	$0.025/8 \times \pi/32$
	$1.4 < \lvert\eta\rvert < 1.475$	$0.025 \times \pi/128$
Sampling 2	$\lvert\eta\rvert < 1.4$	$0.025 \times \pi/128$
	$1.4 < \lvert\eta\rvert < 1.475$	$0.075 \times \pi/128$
Sampling 3	$\lvert\eta\rvert < 1.35$	$0.05 \times \pi/128$

(a)

Layer	$\lvert\eta\rvert$ region	Granularity ($\eta \times \phi$)
Presampler	$1.5 < \lvert\eta\rvert < 1.8$	$0.025 \times \pi/32$
Sampling 1	$1.375 < \lvert\eta\rvert < 1.425$	$0.050 \times \pi/32$
	$1.425 < \lvert\eta\rvert < 1.5$	$0.025 \times \pi/32$
	$1.5 < \lvert\eta\rvert < 1.8$	$0.025/8 \times \pi/32$
	$1.8 < \lvert\eta\rvert < 2.0$	$0.025/6 \times \pi/32$
	$2.0 < \lvert\eta\rvert < 2.4$	$0.025/4 \times \pi/32$
	$2.4 < \lvert\eta\rvert < 2.5$	$0.025 \times \pi/32$
	$2.5 < \lvert\eta\rvert < 3.2$	$0.1 \times \pi/32$
Sampling 2	$1.375 < \lvert\eta\rvert < 1.425$	$0.050 \times \pi/128$
	$1.425 < \lvert\eta\rvert < 2.5$	$0.025 \times \pi/128$
	$2.5 < \lvert\eta\rvert < 3.2$	$0.1 \times \pi/32$
Sampling 3	$1.5 < \lvert\eta\rvert < 2.5$	$0.05 \times \pi/128$

(b)

Table 2.2.6: Granularity of the EM calorimeter ($\eta \times \phi$) in barrel (a) and in endcap (b).

インターネット公表に関する同意が
得られなかったため非公表

Figure 2.2.14: Block diagram of the Front-end board architecture, depicting the data flow for four of the 128 channels [32].

rise time of the ionization signal fast and minimizing the impact of out-of-time pileup, which refers to events from successive bunch crossings, the bipolar shaping is applied to the output pulse. In addition, the output is amplified in order to suppress thermal noise effect. As Figure 2.2.10 and 2.2.11 show, the sensitive analog electronics are located on the detector. Inside the cryostat, the calorimeter electrodes are grouped to form readout cells and small coaxial cables bring the cell signals to the cold-to-warm cables. Front-end boards (FEB) are mounted near the cold-to-warm cables. The FEB receives the raw calorimeter signals and perform the analog processing, digitization and transmission off-detector of the calorimeter signals. Each FEB processes up to 128 calorimeter channels. Figure 2.2.14 shows a block diagram indicating the main features of the FEB architecture. Four channel preamplifier matches accurately the cable impedance. The preamplifier outputs are coupled into a four channel shaper, which splits each signal into three overlapping, linear gain scales in the ratio 1/10/100, and applies bipolar filter. The shape of output is shown in Figure 2.2.8.

The shaped signal are then sampled at the design LHC bunch crossing frequency of 40 MHz by four channel switched capacitor array (SCA). The SCA stores the analogue signals during the L1 trigger latency in pipelines of 144 cells. For events accepted by the L1 trigger, only five sample points per channel and only one of the three gain scales are read out from the SCA. A gain selector chip (GSEL) is used to select the optimal readout gain individually for each calorimeter channel. Two dual op-amp chips couple the SCA outputs to 12-bit ADC which is used for digitization.

The electronics is calibrated cell-to-cell basis. Then an energy scale factor is applied to all the cells. The linearity of the LAr calibrated response with energy has been demonstrated in the electron test beam [35]. For electrons with $E > 20$ GeV, the dispersion from $E_{\mathrm{rec}}/E_{\mathrm{beam}} = 1$ is within ± 0.1 %, where E_{rec} is reconstructed energy and E_{beam} is the energy of test beam. Details on the energy calibration for photons as well as electrons can be found in Section 4.5.

Since the intrinsic relative resolution of energy deposit in a layer E is proportional to the number of drift charges N crossing the LAr gaps, it follows a Poisson fluctuation law:

$$\left.\frac{\Delta E}{E}\right|_{\mathrm{intrinsic}} = \frac{\sqrt{N}}{N} \propto \frac{1}{\sqrt{E}} \tag{2.2.4}$$

There are other effects, which affect the resolution. The thermal noise from electronics or out-of-time pileup events can be parametrized by a relative resolution term proportional to $1/E$ because the noise is independent of energy deposit. In addition, impurities in LAr,

インターネット公表に関する同意が
得られなかったため非公表

Figure 2.2.15: Schematic drawing the tile calorimeter [32].

imperfection of detector geometry, temperature gradients, radiation damage, nonlinearities of response, or other sources, have an impact on the relative resolution. Finally, the relative resolution on the shower energy can be parametrized as:

$$\frac{\Delta E}{E} = \frac{a}{\sqrt{E}} \oplus \frac{b}{E} \oplus c \tag{2.2.5}$$

where the symbol $\oplus$ indicates that the two terms are added in quadrature, b is the noise term and c is called constant term. The resolution is estimated by test beam: $a = 10.1 \pm 0.1$ $\% \cdot \sqrt{\mathrm{GeV}}$ and $c = 0.17 \pm 0.04$ % [35]. The parameter b is not estimated in the beam test because this term does not have an impact under the condition of beam test. However, the resolution can be worse due to the many sources such as pileup.

2.2.5.2 Hadronic calorimeter

The barrel and extended barrels of the hadronic calorimeter use tile scintillators which are built from a succession of steel absorbers and doped plastic scintillators, while 2 endcaps and 2 forward calorimeters use the LAr.

The scintillation light of the tile calorimeter is collected to the PMT through the wavelength shifting fibers. Figure 2.2.15 shows the schematic drawing the tile calorimeter. The central barrel is 5.8 m in length, 8.5 m in diameter. Each extended barrel is 2.6 m in length, with inner (outer) radii of 2.28 m (4.5 m). The tile calorimeters are segmented into three layers in the radial direction, and the cells granularity is between $\eta \times \phi = 0.1 \times 0.1$ (first two layers) and $\eta \times \phi = 0.1 \times 0.2$ (third layer). They cover $|\eta| < 1.7$. The expected jet energy resolution with the tile calorimeter (E in GeV) is:

$$\left.\frac{\Delta E}{E}\right|_{\text{expected}}^{\text{Tile}} = \frac{50\,\%}{\sqrt{E}} \oplus 3\,\% \tag{2.2.6}$$

The hadronic endcap calorimeter is a copper and LAr sampling calorimeter. It covers $1.5 < |\eta| < 3.2$, located behind the endcap EM calorimeters. It consists of two wheels in each endcap: a front wheel and a rear wheel. The wheels are cylindrical with an outer radius of 2030 mm. The modules of the front wheels are made of copper plates of 25 mm thick, while the rear wheels use copper plates of 50 mm thick. The gap between the plates is 8.5 mm thick. The size of the readout cells is $\eta \times \phi = 0.1 \times 0.1$ for $1.5 < |\eta| < 2.5$ and $\eta \times \phi = 0.2 \times 0.2$ for $2.5 < |\eta| < 3.2$. The expected jet energy resolution with the hadronic endcap calorimeter (E in GeV) is:

$$\left.\frac{\Delta E}{E}\right|_{\text{expected}}^{\text{HCal Endcap}} = \frac{50\,\%}{\sqrt{E}} \oplus 3\,\% \tag{2.2.7}$$

Layer	η region	Granularity ($\eta \times \phi$)
1st layer	$3.15 < \|\eta\| < 4.30$	0.1×0.1
	$3.10 < \|\eta\| < 3.15$	4 times finer
	$4.30 < \|\eta\| < 4.83$	4 times finer
2nd layer	$3.24 < \|\eta\| < 4.50$	3.3×4.2
	$3.20 < \|\eta\| < 3.24$	4 times finer
	$4.50 < \|\eta\| < 4.81$	4 times finer
3rd layer	$3.32 < \|\eta\| < 4.60$	5.4×4.7
	$3.29 < \|\eta\| < 3.32$	4 times finer
	$4.60 < \|\eta\| < 4.75$	4 times finer

Table 2.2.7: Granularity of the forward calorimeter ($\eta \times \phi$).

インターネット公表に関する同意が
得られなかったため非公表

Figure 2.2.16: Cumulative amount of material, in units of interaction length, as a function of $|\eta|$, in front of the electromagnetic calorimeters, in the electromagnetic calorimeters themselves, in each hadronic compartment, and the total amount at the end of the active calorimetry. Also shown for completeness is the total amount of material in front of the first active layer of the muon spectrometer ($|\eta| < 3.0$) [32].

The forward calorimeter covers over $3.1 < |\eta| < 4.9$. It consists of three modules. The 1st layer consists of copper plates stacked one behind the other. The 2nd and 3rd layers use tungsten as a absorber. The granularity of the forward calorimeter is shown in the Table 2.2.7. The expectation for the jet energy resolution with the forward calorimeter (E in GeV) is:

$$\left.\frac{\Delta E}{E}\right|^{\text{HCal Forward}}_{\text{expected}} = \frac{100\,\%}{\sqrt{E}} \oplus 10\,\% \tag{2.2.8}$$

The passage of hadrons in material is characterized by the interaction length λ_I, which can be approximated roughly to:

$$\lambda_I \sim 35 \cdot A^{\frac{1}{3}}\ \mathrm{g} \cdot \mathrm{cm}^{-2} \tag{2.2.9}$$

The material distribution of the ATLAS calorimeter as a function of λ_I is shown in Figure 2.2.16. Because the integral interaction length in front of the hadronic calorimeter is about 2 λ_I, the most of energy deposit of hadrons is measured with the hadronic calorimeter which has a total thickness of about 11 λ_I.

2.2.6 Muon spectrometer

Muon spectrometer is the outermost part of the ATLAS detector. It is designed to detect the charged particle which penetrates the calorimeter of the ATLAS, especially muons. It consists of four detectors, Monitored Drift Tube (MDT), Cathode Strip Chamber (CSC),

インターネット公表に関する同意が
得られなかったため非公表

Figure 2.2.17: Cut-away view of the ATLAS muon system [32].

Thin Gap Chamber (TGC) and Resistive Plate Chamber (RPC). Purpose of MDT and CSC are precise tracking, meanwhile that of TGC and RPC are firing triggers and providing the bunch-crossing identification. Conceptual layout of the muon spectrometer is shown in Figure 2.2.17. The muon spectrometer covers $|\eta| < 2.7$.

2.2.6.1 Monitored drift tube

The Monitored drift tube (MDT) consists of many layers of drift tubes. The MDT covers $|\eta| < 2.7$ [32]. A diameter of the drift tube, which is made from aluminum, is 29.970 mm. The tube encloses a Tungsten-Rhenium central conducting wire of 50 μm in radius. The MDT volume is filled with a gas mixture of Ar : CO_2 : H_2O = 93 :7: $<$ 1000 pm. The gas pressure is 3 bar and the gas gain is 2×10^4. The wire is operated at a 3080 V electric potential. When a muon traverses the tube, the gas is ionized and the potential gradient amplifies the ionization signal in the avalanche mode. The spatial resolution per tube of 80 μm, is obtained through the relation between the drift time and drift length of the ionization electrons.

2.2.6.2 Cathode strip chamber

The safe operation of the MDT is limited about 150 Hz/cm^2. Then the Cathode strip chamber (CSC) which is a multi-proportional chamber with radially-oriented wires is installed in the region which has the highest counting rate instead of the MDT [32]. The safe operation limit of CSC is up to 1000 Hz/cm^2. The distance from interaction point to CSC is about 7 m. Inner radius is 881 mm and outer radius is 2081 mm. Therefore the CSC covers $2 < |\eta| < 2.7$. Figure 2.2.18 shows the average expected single-plane counting rates at 10^{34} cm^{-2}s^{-1}.

Anode wires are along radial direction applied high voltage of 1900 V. The diameter of the wires is 30 μm, while the wire pitch is 2.5 mm. Two cathodes are segmented to strips. One cathode strips is orthogonal to the wires and the other is parallel. The anode-cathode spacing is 2.5 mm. The chambers are filled with gas mixture of Ar : CO_2 = 80 : 20, and the gas gain is 6×10^4. The position of a track is determined by interpolating the induced charge of neighboring strips. The charge distribution in the anode allows the measurement of the position in the bending plane with a 40 μm resolution, while the charge distribution in the strips yields a 5 mm resolution on the position in the transverse direction.

インターネット公表に関する同意が
得られなかったため非公表

Figure 2.2.18: Average expected single-plane counting rates in Hz/cm^2 at 10^{34} cm^{-2}s^{-1} and for various regions in the muon spectrometer [32].

2.2.6.3 Thin gap chamber

The Thin gap chambers (TGC) is one of the trigger chambers located in endcaps[32]. It is a multi-wire proportional chamber with distance of 1.4 mm between wire and cathode which is smaller than the distance of 1.8 mm between wire to wire. The gas mixture is CO2 : n-C_5H_{12} = 55 : 45. High voltage around the wires and small distance between wires leads to good time resolution. The TGC is robust against noise due to neutron and photon background. The spatial resolution of the TGC is between 2 and 6 mm in R-direction, as well as between 3 and 7 mm in ϕ-direction. The timing resolution is 4 ns.

2.2.6.4 Resistive plate chamber

The Resistive plate chamber (RPC) is located in the barrel and used for trigger system[32]. The RPC is not a wire chamber but a gaseous parallel electrode-plate detector. Is has two resistive plates which are kept 2 mm apart with insulating spacer. The electric field of 4.9 kV/mm is applied between the plates. The electric field causes avalanche along the track of particle towards anode. The RPC volume is filled with the gas mixture of $C_2H_2F_4$: Iso - C_4H_{10} : SF_6 = 94.7 : 5 : 0.3. The position resolution of the RPC is 10 mm in the z- and ϕ-direction. while the timing resolution is 1.5 ns.

2.2.7 Trigger system

Trigger system is a key component of the ATLAS detector. The trigger is aimed at the online rejection of the huge background and the efficient selection of processes of interest. The ATLAS trigger system is performed in three stages, Level 1 (L1), Level 2 (L2) and Event Filter (EF) [36]. Together, the L2 and EF are usually called the High Level Trigger (HLT) [37]. Starting from L1, each level makes a decision if the event should be passed or not to the next level, and eventually be saved for offline analysis. L1 trigger is implemented in the detector and works with the hardware. HLT is using computer and network hardware. L1 is required to make a decision in less than 2.5 μs and to lessen the trigger rate to about 75 kHz. Then, L2 uses the L1 seed, which is defined as Region of Interest (RoI). L2 is required to reduce the trigger rate to 5 kHz. Finally, the information is passed to EF. EF uses the whole detector information and is required to reduce the rate up to 400 Hz. The trigger characteristics are summarized in Table 2.2.8.

The L1 trigger looks for high transverse momentum (p_{T}) muons, photons, electrons, jets, taus decaying into hadrons, large missing transverse energy (E_{T}^{miss}) and large total

Characteristics	Value
Bunch crossing rate	20-40 MHz
Interaction rate	1 GHz
ATLAS event size	1.5 MB
L1 output rate (decision time)	75 kHz ($<$2.5 μs)
L2 output rate (decision time)	5 kHz (40 ms)
EF output rate (decision time)	400 Hz (1 s)
Data output	450 MB/s

Table 2.2.8: Typical ATLAS trigger characteristics.

インターネット公表に関する同意が
得られなかったため非公表

Figure 2.2.19: Block diagram of the L1 trigger. The overall L1 accept decision is made by the central trigger processor, taking input from calorimeter and muon trigger results. The paths to the detector front-ends, L2 trigger, and data acquisition system are shown from left to right in red, blue and black, respectively [32].

transverse energy ($\sum E_{\mathrm{T}}$). The diagram of L1 trigger scheme is shown in the Figure 2.2.19. Muon candidates are identified using trigger chambers in the RPC and TGC. Electrons, photons, τ leptons, jets are identified by the calorimeters with reduced granularity. L1 trigger is made a decision at Central Trigger Processor (CTP). When an event is passed in L1 trigger, the information for the positions of trigger objects are sent to L2 trigger as RoI. Another important role of L1 is to identify a bunch crossing of interest.

The RoI builder receives the RoI information from the different sources within the L1 trigger and merges them into the single data structure. L2 selection is seeded with RoIs. Contrary to L1, L2 uses full granularity of the sub-detectors in the RoIs. It reconstructs the objects quickly with using a cascade of algorithms of increasing complexity and hardened requirements, and rejects the event as soon as no objects are found to pass the criteria in one of these algorithms. L2 is designed to perform to execute event selection with an average throughout per farm node of about 300 Hz.

Seeded by L2, at the last stage of the trigger event selection, EF reconstructs the full event. The EF reconstruction is almost the same as the one at offline analysis. With a decision time between 1 and 4 s, EF is designed to reduce the trigger rate from about 3 kHz to a 300 Hz output, which is limited by data processing and storage capabilities.

2.2.8 Luminosity detector

The Beam Condition Monitor (BCM) detector consists of diamond sensors, which is divided in 4 small components $\sim$ 1 cm^2 and arranged around the beam pipe [38]. The two BCMs are at $|z| = 184$ cm on each side of the interaction point. The BCM detects very forward signals of inelastic proton-proton interactions around $|\eta| = 4.2$. The measured signals are used for the luminosity determination (Appendix A) and the average number

of inelastic interactions per bunch crossing μ_{av}.

Chapter 3

Data set and Monte Carlo samples

3.1 Data set

The cumulative luminosity as a function of date is shown in Figure 3.1.1. In 2011 at $\sqrt{s} = 7$ TeV, the integrated luminosity delivered is 5.48 fb^{-1}, while 22.8 fb^{-1} at $\sqrt{s} = 8$ TeV in 2012 [28]. The delivered luminosity accounts for the luminosity delivered from the start of stable beams until the LHC requests ATLAS to put the detector in a safe standby mode to allow a beam dump or beam studies. The 93 % of the delivered luminosity was recorded with the ATLAS detector. The recorded luminosity reflects the DAQ inefficiency, as well as the inefficiency of the so-called "warm start": when a stable beam flag is raised, the tracking detectors undergo a ramp of the high-voltage and, for the pixel system, turning on the preamplifiers. Data collected during stable beam periods in which sub-detectors were fully operational are used in the $H \to \gamma\gamma$ analysis. The total integrated luminosity is 4.8 (20.3) fb^{-1} for $\sqrt{s} = 7$ (8) TeV analysis. The difference between the value for $\sqrt{s} = 7$ TeV analysis and that (4.57 fb^{-1}) shown in the Figure 3.1.1 is due to the requirement of sub-detectors in data quality criteria. Since muons are not used in $\sqrt{s} = 7$ TeV analysis, data quality of the muon spectrometer is not required for $\sqrt{s} = 7$ TeV data.

インターネット公表に関する同意が得られなかったため非公表

インターネット公表に関する同意が得られなかったため非公表

(a) (b)

Figure 3.1.1: Cumulative luminosity versus time delivered to (green), recorded by ATLAS (yellow), and certified to be good quality data (blue) during stable beams and for proton-proton collisions at $\sqrt{s} = 7$ TeV in 2011 (a) and 8 TeV in 2012 (b) [28].

Process	Generator
ggF, VBF	POWHEG [41, 42] + PYTHIA
WH, *ZH*, *ttH*	PYTHIA
$q\bar{q}/gg \to \gamma\gamma$	SHERPA [43], DIPHOX [44], MADGRAPH [45]
γ-jet	SHERPA
jet-jet	PYTHIA

Table 3.2.1: Event generators used to model the signal and the main background processes. "PYTHIA" indicates that PYTHIA6 [46] and PYTHIA8 [47] are used for the simulations of 7 TeV and 8 TeV data, respectively.

3.2 Monte Carlo simulation

3.2.1 Samples

Monte Carlo (MC) simulation samples are produced using the several event generators and a GEANT4 [39] based detector simulation [40]. The energy deposited by particles in the active detector material is converted into detector signals in the same format as the detector read-out. The MC events are processed through the GEANT4-based detector simulation and a trigger simulation and then are reconstructed with the same software as for the real data. Samples of MC events are employed to model Higgs boson production and compute signal selection efficiencies. Table 3.2.1 lists the event generators. Cross section normalizations and other corrections (e.g. Higgs boson p_{T} spectrum) are obtained from calculations in Refs. [9, 17, 18, 19], [48]-[76]. Backgrounds are determined from data-driven estimates and MC simulations.

PYTHIA6 (for $\sqrt{s} = 7$ TeV samples) or PYTHIA8 (for $\sqrt{s} = 8$ TeV samples) are used to generate parton showers and their hadronization, and to simulate underlying events. Alternatively, HERWIG [77] and JIMMY [78] are used. When PYTHIA6 or HERWIG are used, PHOTOS [79, 80] is used to provide additional photon radiations from charged leptons. The following parton distribution function (PDF) sets are used: CT10 [81] for the POWHEG samples; CTEQ6L1 [82] for the PYTHIA8, MADGRAPH, HERWIG and SHERPA samples; and MRSTMCal [83] for the PYTHIA6 samples. Pileup events, which are additional soft events overlaid hard interaction, are simulated in MC events by adding additional inelastic proton-proton collisions. Events from successive bunch crossings are called out-of-time pileup, while events occur during the same bunch crossing as the hard scattering are called in-time pileup.

3.2.2 Corrections

Corrections obtained from measurements in the data are applied to the simulation to account for small differences between data and simulation. The following corrections are applied:

- The MC events are reweighted to match pileup condition in data as shown in Figure 3.2.1 The measurement of the average number of interactions μ_{av} is described in Appendix A.

インターネット公表に関する同意が
得られなかったため非公表

Figure 3.2.1: Distribution of the mean number of interactions per crossing for the 2011 and 2012 data [28].

- Beam spread is measured with vertices which are reconstructed with the inner detector. The MC events are reweighted such that the MC events have the same spread as data. The beam spread before reweighting is 65 mm and after reweighting is 55 (45) mm in simulation samples for $\sqrt{s} = 7$ (8) TeV analysis.

- The shower shape variables of photons in the EM calorimeter in MC is rescaled with *Fudge factors* obtained from the comparison between data and simulation to correct for the differences [84]. The distributions of shower shape variables are checked in Section 4.4. The values of Fudge factors are about 1 ± 0.01 depending on variables.

- The photon energies are smeared to account for differences in resolution between data and simulation. The smearing has been derived from comparison of the $Z \to ee$ peak in data and the MC events as described in Section 4.5.2. Energy or momentum smearing is also applied to leptons and jets.

The following corrections are additionally applied to the MC events obtained from computing effects which are not taken into account in the simulation.

- The signal $gg \to H \to \gamma\gamma$ process is interfered with $gg \to \gamma\gamma$ background because they have same final state [85]. Then the ggF MC events are reweighted based on the calculation of the interference. The reweighting factor, depending on the Higgs mass and η of photons, is between 3.8 and 4.5 %.

- In case of ggF, the MC events for $\sqrt{s} = 7$ TeV analysis are reweighted in order that the distribution of the Higgs boson p_{T} matches the one obtained from Hqt2.0 package [86], which is a program to compute the p_{T} spectrum of the Standard Model Higgs boson in hadron collisions. In $\sqrt{s} = 8$ TeV MC, the p_{T} distribution is corrected with the Hqt2.0 at the stage the MC generation.

Chapter 4

Photon reconstruction

The photon reconstruction and identification algorithms used in the ATLAS are designed to achieve both a high efficiency for photons with transverse energies above 20 GeV and a high background rejection [87]. The background rejection is quite challenging because of the overwhelming majority of photons from neutral hadron decays (main contribution is $\pi^0 \to \gamma\gamma$) or from radiative decays of other particles. Photons from a Higgs boson are different from fake photons due to the neutral hadrons because of the shape of the associated EM showers and isolation from other particles. In addition, tracks associated to the showers are used for separation of photons and electrons in order to reject $Z \to ee$ background where electrons fake photons.

4.1 Primary vertex selection for di-photon events

The precise identification of the primary vertex from a hard scattering process is crucial for the $H \to \gamma\gamma$ analysis because the position of the primary vertex is used to calculate the photon direction,as well as to form jets. However, many inelastic proton-proton interactions occur in a bunch crossing along the beam spot. A hard collision process of interest occurs at most once per beam crossing. The other vertices, called pileup vertex, obscure the primary vertex. Accordingly, primary vertex candidates are reconstructed by using at least two charged tracks, and one vertex is selected as the primary vertex as described later.

The beam spot size depends on beam condition such as the β function and the emittance at the interaction point. In 7 TeV runs, the transverse beam spot size $\sigma_x \sim \sigma_y \sim 20$ μm and the longitudinal beam spot size $\sigma_z \sim 55$ mm on average. They are $\sigma_x \sim \sigma_y \sim 15$ μm and $\sigma_z \sim 45$ mm on average in 8 TeV runs. The maximum number of such interactions per bunch crossing is 20 (40) in $\sqrt{s} = 7$ (8) TeV data taking. Figure 4.1.1 shows an event display under high pileup environment in 8 TeV run where a Z boson candidate decays into two muons with 25 reconstructed vertices.

4.1.1 Reconstruction of primary vertex candidates

Primary vertex candidates are reconstructed with using tracks in the inner detector. The tracks are required to be originated from a beam spot. An iterative vertex finding algorithm is used [89, 90]:

インターネット公表に関する同意が
得られなかったため非公表

Figure 4.1.1: An event candidate of a di-muon decay of a Z boson with 25 reconstructed vertices in 8 TeV run. This event was recorded on April 15th 2012 [88].

- A vertex seed is obtained from the global maximum in the distribution of the z-positions at the beam line of the reconstructed tracks.
- χ^2 is evaluated for each track with the distance between a track and the seed, as well as the uncertainty of the distance.
- The vertex position is determined using the seed and the tracks around it which have $\chi^2 < 7\sigma$.
- Tracks incompatible with the vertex by more than 7σ are used to seed a new vertex.
- This procedure is repeated until no unassociated tracks are left in the ever or no additional vertex can be found.

The loose requirement $\chi^2 < 7\sigma$ is intended to reduce the number of single vertices which split into two due to the presence of outlying track measurements.

4.1.2 Primary vertex selection

After the reconstruction of vertices, one primary vertex is selected. If charged particles with high p_{T} are created in the primary vertex such as in $Z \to ll$ events, the primary vertex can be selected with the sum of squared momentum of track associated to the vertex $\sum p_{\mathrm{T}}^2$. In these events, the primary vertex has the largest $\sum p_{\mathrm{T}}^2$ in almost all cases. However in di-photon events, a primary vertex may not have charged particle with high p_{T} unless additional objects are generated like jets in VBF events. For efficient primary vertex selection, direction of energy clusters of photons in the EM calorimeter are used as well as track information.

4.1.2.1 Calo pointing

Shower developments of photons in the EM calorimeter are reconstructed not only with $\eta - \phi$ plane but also R or z direction because the calorimeter has three layers and the presampler in R direction in barrel and z direction in endcap. The direction of a photon can be determined with the 3-dimensional shower shape. This is the basic idea of *calo pointing*. The material amount of the presampler is so small (0.08 to 0.15 X_0) that shower developments tend to start at the 1st layer. Then the presampler is not used for the calo pointing. Also 3rd layer is not used since shower developments tend to end in the 2nd layer and the uncertainty of shower shape in the 3rd layer deteriorates the resolution of the direction. Hence the pseudo-rapidity of photon $\eta^{\gamma}_{\mathrm{calo}}$ and the primary vertex position z_{calo} are extracted from the 1st and 2nd layers. Figure 4.1.2a illustrates *calo pointing*. When the centroids of the energy deposit in the 1st and 2nd layers are reconstructed at (z_{1st}, R_{1st}) and (z_{2nd}, R_{2nd}) in z-R plane , $\eta^{\gamma}_{\mathrm{calo}}$ and z_{calo} are calculated as:

$$\begin{aligned} \eta^{\gamma}_{\mathrm{calo}} =& \sinh^{-1}\left(\frac{z_{\mathrm{2nd}} - z_{\mathrm{1st}}}{R_{\mathrm{2nd}} - R_{\mathrm{1st}}}\right) \\ z_{\mathrm{calo}} =& \frac{z_{\mathrm{1st}} R_{\mathrm{2nd}} - z_{\mathrm{2nd}} R_{\mathrm{1st}}}{R_{\mathrm{2nd}} - R_{\mathrm{1st}}} \end{aligned} \tag{4.1.1}$$

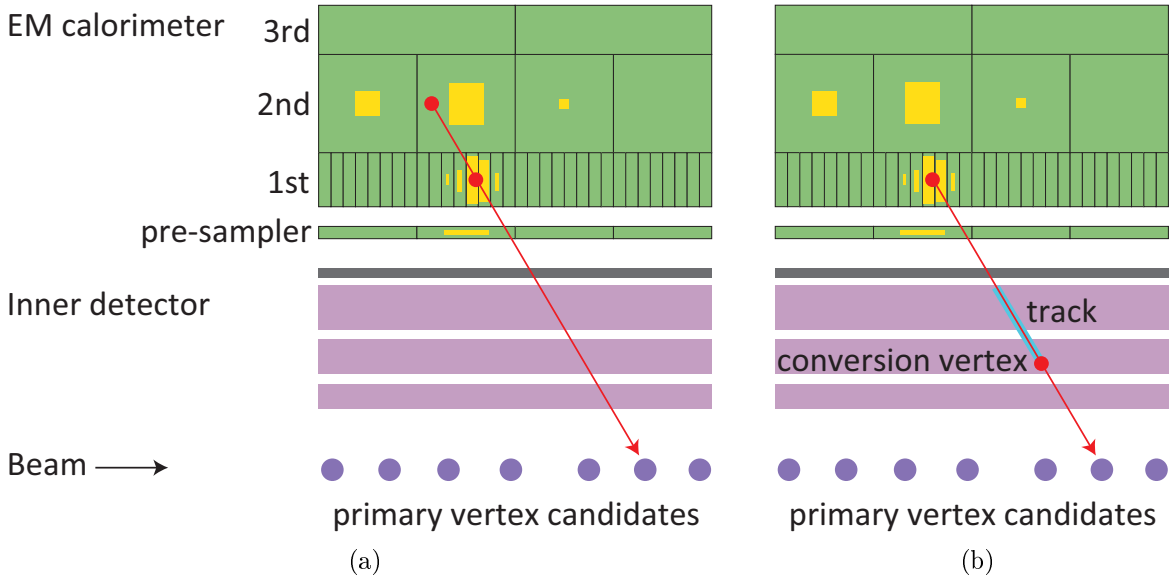

Figure 4.1.2: Illustration of calo pointing (a) and z_{HPV}(b).

The resolution of z_{calo} is shown in Figure 4.1.3a. The distribution has a sharp peak around 0 and a broad tail. A double Crystal-Ball which has a Gaussian core and power-law functions both in high tail and low tail describe the resolution distribution well and is used for fit. The double Crystal-Ball is defined as:

$$f_{\mathrm{CB}}(x) \equiv N \times \begin{cases} \left(\frac{n_{\mathrm{R}}}{|\alpha_{\mathrm{R}}|}\right)^{n_{\mathrm{R}}} \exp\left(-\frac{|\alpha_{\mathrm{R}}|^2}{2}\right) \left(\frac{n_{\mathrm{R}}}{|\alpha_{\mathrm{R}}|} - |\alpha_{\mathrm{R}}| + \frac{x-\bar{x}}{\sigma_{\mathrm{CB}}}\right)^{-n_{\mathrm{R}}} & \text{for } \alpha_{\mathrm{R}} \leq \frac{x-\bar{x}}{\sigma_{\mathrm{CB}}} \\ \exp\left(-\frac{(x-\bar{x})^2}{2\sigma_{\mathrm{CB}}^2}\right) & \text{for } -\alpha_{\mathrm{L}} < \frac{x-\bar{x}}{\sigma_{\mathrm{CB}}} \leq \alpha_{\mathrm{R}} \\ \left(\frac{n_{\mathrm{L}}}{|\alpha_{\mathrm{L}}|}\right)^{n_{\mathrm{L}}} \exp\left(-\frac{|\alpha_{\mathrm{L}}|^2}{2}\right) \left(\frac{n_{\mathrm{L}}}{|\alpha_{\mathrm{L}}|} - |\alpha_{\mathrm{L}}| - \frac{x-\bar{x}}{\sigma_{\mathrm{CB}}}\right)^{-n_{\mathrm{L}}} & \text{for } \frac{x-\bar{x}}{\sigma_{\mathrm{CB}}} \leq -\alpha_{\mathrm{L}} \end{cases} \tag{4.1.2}$$

where σ_{CB} is the width of a Gaussian core and represents the resolution. In Figure 4.1.3a, $\sigma_{\mathrm{CB}} = 15$ mm is estimated for $\sqrt{s} = 8$ TeV analysis.

4.1.2.2 Conversion vertex

When a photon is converted to an electron-positron pair in the inner detector, a conversion vertex where the electron pair is generated is reconstructed. The conversion vertex is used for the primary vertex selection. When a conversion vertex is reconstructed at (z_{conv}, R_{conv}) in z-R plane, the pseudo-rapidity of photon $\eta^{\gamma}_{\mathrm{HPV}}$ and the primary vertex position z_{HPV} are calculated from the straight line between the conversion vertex and the centroids of the energy deposit in the 1st layer of the EM calorimeter as illustrated in Figure 4.1.2b. Therefore $\eta^{\gamma}_{\mathrm{HPV}}$ and z_{HPV} are obtained with exchanging (z_{2nd}, R_{2nd}) to (z_{conv}, R_{conv}) in Eq.(4.1.1) as:

$$\begin{aligned} \eta^{\gamma}_{\mathrm{HPV}} &= \sinh^{-1}\left(\frac{z_{\mathrm{conv}} - z_{\mathrm{1st}}}{R_{\mathrm{conv}} - R_{\mathrm{1st}}}\right) \\ z_{\mathrm{HPV}} &= \frac{z_{\mathrm{1st}} R_{\mathrm{conv}} - z_{\mathrm{conv}} R_{\mathrm{1st}}}{R_{\mathrm{conv}} - R_{\mathrm{1st}}} \end{aligned} \tag{4.1.3}$$

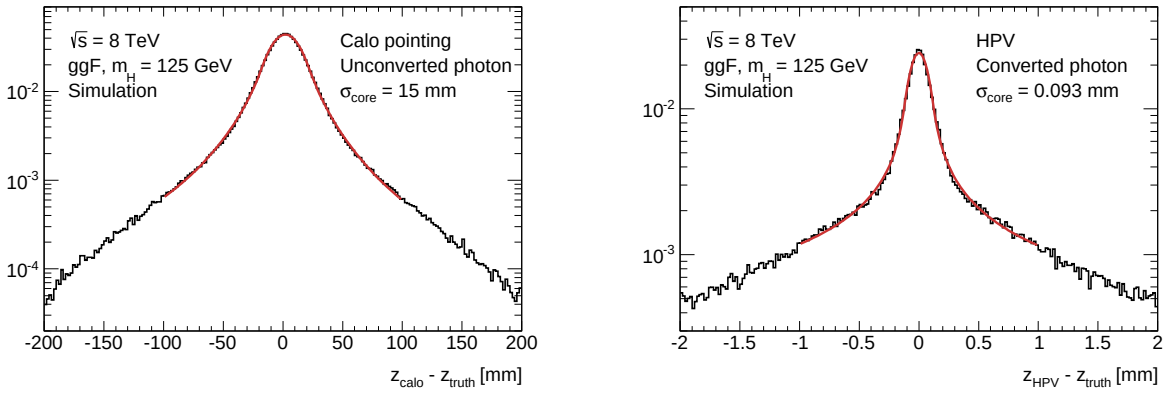

(a) (b)

Figure 4.1.3: Comparison between the reconstructed primary vertex of the photon by using the calo pointing (a) or the calo pointing + conversion vertex (b) and the truth vertex. z_{truth} is true z position of the primary vertex

Figure 4.1.3b shows the resolution of z_{HPV}. Compared with using only calo pointing, the hybrid method which uses both calo pointing and conversion vertex implements 1/100 better resolution. This is because the position resolution of the tracker is better than that of energy cluster, as well as $R_{\mathrm{conv}} - R_{\mathrm{1st}} \gg R_{\mathrm{2nd}} - R_{\mathrm{1st}}$. Hence the hybrid method is used for converted photons.

4.1.2.3 Final primary vertex selection

In addition to calo pointing and conversion vertex, variables of tracks which associate to each primary vertex candidates, as well as the beam spot position are also used for the primary vertex selection for $\sqrt{s} = 8$ TeV analysis. The primary vertex is finally identified by combining those variables with a neural network based algorithm [91]. Four variables are input parameters to the algorithm:

- The barycenter of the beam spot and z_{calo} or z_{HPV} of the two photons. z_{calo} is used for unconverted photons, while z_{HPV} is used for converted photons.
- The sum of the squared momentum $\sum p_{\mathrm{T}}^2$ of tracks associated with each reconstructed vertex
- The scalar sum of the momentum $\sum p_{\mathrm{T}}$ of tracks associated with each reconstructed vertex
- The difference in azimuthal angle $\Delta\phi$ between the direction defined by the vector sum of the tracks momenta and the di-photon system.

The neural network algorithm gives scores for each primary vertex candidate and the vertex with the highest score is selected as the primary vertex.

For $\sqrt{s} = 7$ TeV analysis, a likelihood with $\sum p_{\mathrm{T}}^2$ of each primary vertex candidates is used. The likelihood has signal and background templates of the $\sum p_{\mathrm{T}}^2$. The primary vertex is selected with combining the output of the likelihood and z_{calo} or z_{HPV}.

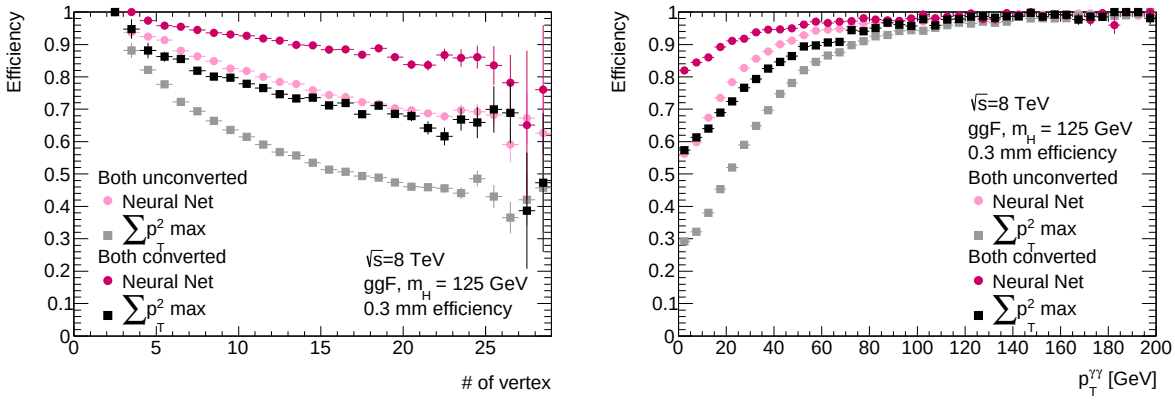

Figure 4.1.4: The efficiency of the primary vertex reconstruction as a function of the di-photon system transverse momentum $p_{\mathrm{T}}^{\gamma\gamma}$ (left), the number of primary vertices (right).

4.1.3 Efficiency of primary vertex selection for di-photon events

Although no threshold is applied to the primary vertex selection for the $H \to \gamma\gamma$ analysis, the efficiency of finding the primary vertex within 0.3 mm of the true one is used for a performance estimation. Figure 4.1.4 shows the efficiency in the $H \to \gamma\gamma$ signal samples for $\sqrt{s} = 8$ TeV analysis. The overall efficiency is 83 %. Converted photons have 10 % larger efficiency than unconverted ones because of using conversion vertex. The neural network based algorithm makes the primary vertex selection more robust against pileup and then increases the efficiency 20 % compared to selecting a vertex which has the highest $\sum p_{\mathrm{T}}^2$ under the $\sqrt{s} = 8$ TeV beam condition. The efficiency increases as the di-photon system transverse momentum increases. This is because when the di-photon system is boosted, some jets are present in the opposite side then the tracks of the jets increase $\sum p_{\mathrm{T}}^2$, $\sum p_{\mathrm{T}}$ and $\Delta\phi$.

The vertex selection is studied in $Z \to ee$ decays to compare data and MC by removing the electron tracks from the events. These events emulate two unconverted photon events. The highest $\sum p_{\mathrm{T}}^2$ vertex before electron track removing is used as a reference point instead of the true vertex. Before removing the electron tracks, the primary vertex tends to have the highest $\sum p_{\mathrm{T}}^2$ due to the electrons from Z boson. In case selecting these vertices, the efficiency of finding the primary vertex within 0.3 mm of true one is about 97 %. We demonstrate in Figure 4.1.5 that the shapes of efficiency curves are very similar as that of $H \to \gamma\gamma$ samples when both photons are not converted in front of the EM calorimeter (Figure 4.1.4). Although the efficiency is slightly low compared with $H \to \gamma\gamma$ samples because of the difference of reference points, different distributions of $\sum p_{\mathrm{T}}^2$, $\sum p_{\mathrm{T}}$ and $\Delta\phi$ between $H \to \gamma\gamma$ and $Z \to ee$ events, Figure 4.1.5 demonstrates the data/MC agreement very well.

4.2 Photon trigger

As described in Section 2.2.7, the ATLAS trigger system is subdivided in three levels: L1, L2 and EF. For di-photon events in the $H \to \gamma\gamma$ analysis, di-photon trigger chains are used.

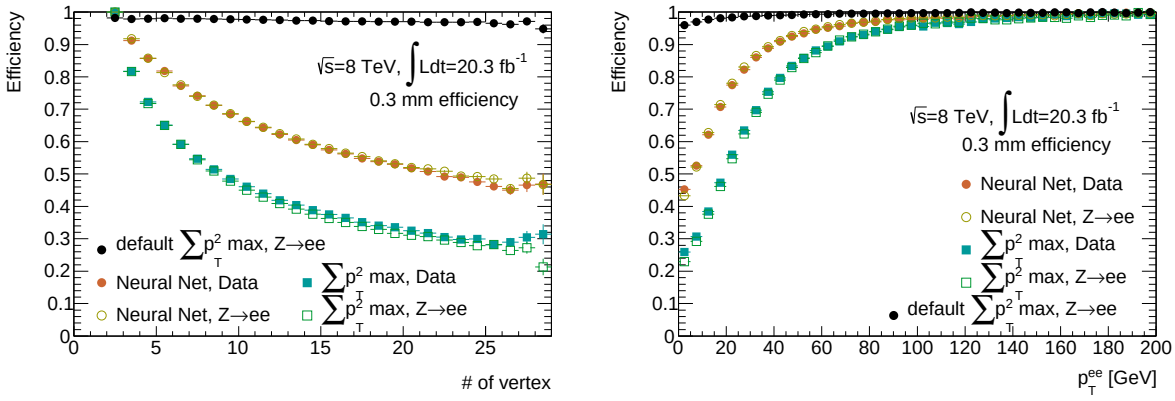

Figure 4.1.5: The efficiency of the primary vertex reconstruction as a function of the di-electron system transverse momentum $p_{\mathrm{T}}^{\gamma\gamma}$ (left), the number of primary vertices (right). The reference point is the highest $\sum p_{\mathrm{T}}^2$ vertex before electron track removing. The black graph shows the efficiency of finding the primary vertex within 0.3 mm of true one when the highest $\sum p_{\mathrm{T}}^2$ vertex before the electron removing is selected.

The photon selection at L1 is based on energy deposit in the EM calorimeter. At L1, granularity of the calorimeter is reduced to 0.1×0.1 in $\eta \times \phi$ to manage high frequency. In order to find energy clusters, programmable thresholds are applied to the cells. 4×4 sliding window is used towards measuring a local energy maximum. If at least one cell in the 2×2 core of the window has larger energy deposit than the threshold, the information of the window is stored[1]. For $\sqrt{s} = 8$ TeV analysis, at least two clusters are required to pass 12 GeV threshold and additionally one of them is required to pass higher threshold depends on η.

From L2, full granularity data 0.025×0.025 in $\eta \times \phi$ is used. L2 is seeded by the L1 cluster position and builds 3×7 rectangular clusters of cells in the EM calorimeter The shower shape variables are computed using the 1st and 2nd layer and the 1st layer of the hadron calorimeter. Then L2 imposes the following criteria:

- a lower cut on the transverse energy of the cluster.
- an upper cut on the energy leakage in the 1st layer of hadronic calorimeter.
- a lower cut on the fraction of energy deposit in the 1st layer.
- a lower cut on the lateral leakage (the ratio of the energy in the 2nd layer in the 3×7 cluster to the energy in a 7×7 cluster).
- a lower cut on the ratio of the difference between the energies of the two most energetic cells to the sum of these two energies.

EF trigger system uses the same tools as the offline selection, but is only seeded by L2 triggered clusters. Besides, any tracker information is not used for photon EF. The energies and shower shapes of photons are computed in the same as offline analysis which

[1]The outer cells can be used for evaluation of isolation. The cells in the hadron calorimeter behind the sliding window can be used for hadronic leakage measurement. But they are not used so far.

is described in the following section. For $\sqrt{s} = 7$ TeV analysis, two photon candidates with $E_{\mathrm{T}} > 20$ GeV are required. On the other hand, $E_{\mathrm{T}} > 35$ GeV and 25 GeV thresholds are required to leading and sub-leading photons for $\sqrt{s} = 8$ TeV analysis. The variables of shower shape are as follow:

- the energy leakage in the 1st layer of hadronic calorimeter (R_{had1}) (used in $|\eta| < 0.8$ and $1.37 < |\eta|$).
- the energy leakage in the all hadronic calorimeter (R_{had}) (used in $0.8 < |\eta| < 1.37$).
- the ratio of the energy in the 2nd layer in the 3×7 cluster to the energy in a 7×7 cluster (R_{η}).
- the lateral width of the shower (w_2) : $\sqrt{\frac{\sum_i E_i \eta_i^2}{\sum_i E_i} - \left(\frac{\sum_i E_i \eta_i}{\sum_i E_i}\right)^2}$, where E_i is the energy and η_i is the pseudo-rapidity of cell i and the sum is calculated within a window of 3×5 cells.

The efficiency of the di-photon trigger for events fulfilling the final event selection is extracted from Bootstrap method, where the efficiency is determined with using samples which is selected by lower threshold trigger [92]. For the di-photon trigger used for $\sqrt{s} = 7$ TeV analysis, a sample passing the 14 GeV E_{T} L1 threshold is used. In the $H \to \gamma\gamma$ analysis, the photon candidates are required to pass the identification criteria which is described in the following section. Therefore in order to reject fake photon contamination, the efficiency is measured with respect to the identified photons. The estimated efficiency is 98.9 ± 0.2 % for $\sqrt{s} = 7$ TeV data and 99.6 ± 0.1 % for $\sqrt{s} = 8$ TeV data [93].

4.3 Photon reconstruction procedure

In the EM calorimeter, photons deposit energy in cells of the EM calorimeter. These cells are clustered and used as a seed for reconstruction. There are three steps in the photon reconstruction as follows [87].

Clustering The transverse energies in cells are summed in the $\eta \times \phi = 0.075 \times 0.125$ window, which corresponds to 3×5 cells, as a function of the window position (η and ϕ). A window with the local maximum transverse energy deposit with $E_{\mathrm{T}} > 2.5$ GeV is obtained as a seed.

Track matching Track information is used for photon/electron separation and photon conversion reconstruction.

A Track with $p_{\mathrm{T}} > 0.5$ GeV is matched to a clustering window if the track and the cluster are generated from the same charged particle. For the track-to-cluster matching, a track trajectory is extrapolated to the 2nd layer of the EM calorimeter. Thus $\Delta\eta$ and $\Delta\phi$ are calculated with the extrapolated point and the barycenter of a cluster. The track-to-cluster matching requires $\Delta\eta < 0.05$ and $\Delta\phi < 0.05$ on each side and $\Delta\phi < 0.1$ on the side where the bremsstrahlung losses are expected during the track extrapolation. A cluster which has no matched track is reconstructed as an unconverted photon candidate. On the

other hand, a photon which is converted to an electron-positron pair in the inner detector is reconstructed as a converted photon. The converted photons are required to have at least one matched track. However, because the energy deposit of electrons are clustered and the clusters have matched tracks, separation of converted photons and electrons is needed.

For converted photons, conversion vertices, where an electron-positron pair is produced, are reconstructed in the inner detector. Conversion vertices with two tracks are reconstructed by performing a constrained vertex fit with using the track parameters of the two participating electrons under the condition that the photon is a massless particle. If both of tracks are matched to window clusters, these objects are reconstructed as *double-track converted photons*. By contrast, sometimes one of the two produced electron tracks failed to be reconstructed. This occurs when one of them is too soft to be reconstructed, or when the two tracks are too close to be distinguished. In this case, a conversion vertex with one electron track is reconstructed at a point of the first measurement of the participating track. The conversion vertex is required to be out the innermost layer of the Pixel detector. Consequently, in the same way as the double-track converted photons, these objects are reconstructed as *single-track converted photons* if the track is matched to a window cluster. When a cluster is not reconstructed unconverted photons or converted photons, it is reconstructed as electrons. The track matching is illustrated in Figure 4.3.1.

Re-clustering Finally re-clustering is applied to photon candidates. The clustering window is centered on the energy barycenter defined by the previous cluster. In the endcap of the EM calorimeter, the window size is $\Delta\eta \times \Delta\phi = 0.125 \times 0.125$ which corresponds to 5×5 cells. In the barrel of the EM calorimeter, 3×5 window is used for unconverted photon candidates, while 3×7 for converted photon candidates because the magnetic field bents the conversion track trajectories in ϕ direction.

4.4 Photon identification

Reconstructed photon candidates are contaminated with QCD jets. Genuine photons have more localized energy deposit than jets. Therefore the jets are rejected by photon identification based on the shower shape in the calorimeter. The jets include less interactive particles than photons in the EM calorimeter, hence they have larger longitudinal leakage to the hadronic calorimeter. Fake photons due to jets have wider shower shape than photons because π^0 decays produce two photons and because other particles in the jets have energy deposits in the EM calorimeter. Figure XXX illustrates the difference of shower shapes between photons and π^0. The 1st layer of the EM calorimeter has the fine granularity in η (Table 2.2.6), and then the shower width in the 1st layer has strong rejection power to π^0 decays. Based on these differences of shower shape, ten variables are computed with energy cluster of photon candidates as shown in Table 4.4.1. The variables of shower shape in MC are rescaled with Fudge factors to agree with those in data.

The distribution of the ten variables are shown in Figure 4.4.2 and 4.4.3 with using $Z + \gamma$ events. High purity photon sample in $Z \to ll\gamma$ events is labeled as *FSR*, while fake photon enriched sample is labeled as *ISR*. The photon purity in the ISR sample is 8.4 %

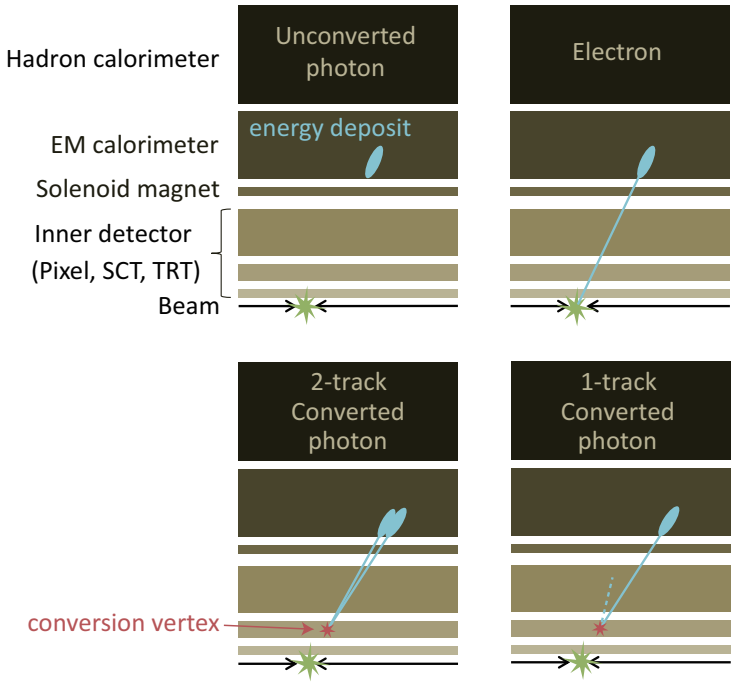

Figure 4.3.1: Illustration of track matching.

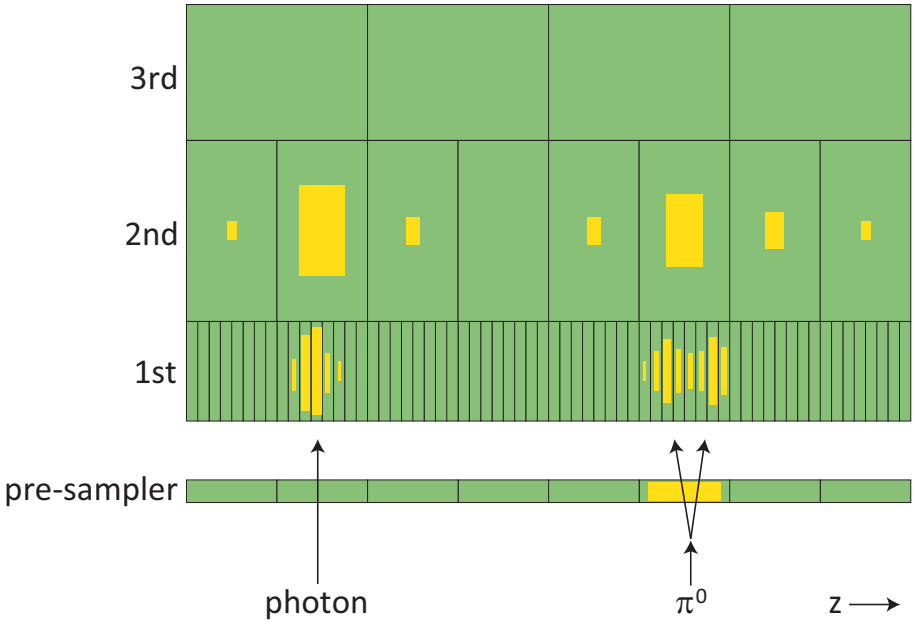

Figure 4.4.1: Illustration of difference of shower shapes between photons and π^0.

Category	Description	Name
Hadronic leakage	Ratio of E_{T} in the first sampling of the hadronic calorimeter to E_{T} of the EM cluster (used in $\lvert\eta\rvert < 0.8$ and $1.37 < \lvert\eta\rvert$)	R_{had1}
	Ratio of E_{T} in all the hadronic calorimeter to E_{T} of the EM cluster (used in $0.8 < \lvert\eta\rvert < 1.37$)	R_{had}
EM 2nd layer	Ratio in η of cell energies in 3×7 versus 7×7 cells	R_{η}
	Lateral width: $\sqrt{\frac{\sum_i E_i \eta_i^2}{\sum_i E_i} - \left(\frac{\sum_i E_i \eta_i}{\sum_i E_i}\right)^2}$	w_2
	Ratio in ϕ of cell energies in 3×3 versus 3×7 cells	R_{ϕ}
EM 1st layer	Shower width for three strips around maximum strip $\sqrt{\frac{\sum_i^3 (i - i_{\max})^2 E_i}{\sum_i^3 E_i}}$ ($i_{\max}$ is the maximum strip index)	w_{s3}
	Total lateral shower width $\sqrt{\frac{\sum_i (i - i_{max})^2 E_i}{\sum_i E_i}}$	$w_{s\mathrm{tot}}$
	Fraction of energy outside core of three central strips but within seven strips	F_{side}
	Difference between the second largest energy of the strip and the the smallest energy of the strip between the two leading strips	ΔE
	Ratio of energy difference between the first and the second maximum to total energy $\frac{E_{1max} - E_{2max}}{E_{1max} + E_{2max}}$	E_{ratio}

Table 4.4.1: Variables for photon identification to reject fake photons due to $\pi^0 \to \gamma\gamma$.

Variable	Unconverted photons	Converted photons
R_{had1}	< 0.02 for $E_{\mathrm{T}} < 80$ GeV	
	< 0.01825 for $E_{\mathrm{T}} > 80$ GeV	
R_{η}	> 0.92	
R_{ϕ}	> 0.93	> 0.57
w_2	< 0.011	
w_{stot}	< 3.0	< 2.8
w_{s3}	< 0.67	< 0.73
F_{side}	< 0.28	< 0.33
ΔE	< 0.18 GeV	< 0.16 GeV
E_{ratio}	> 0.80	> 0.85

Table 4.4.2: Thresholds for shower shape variables used to identify photons in $|\eta| < 0.6$ for $\sqrt{s} = 8$ TeV analysis.

in $\sqrt{s} = 8$ TeV data. The definitions of these samples are described in Section 5.1. The shower variables in MC are rescaled with the Fudge factors obtained from the comparison between data and MC. Before the correction, the shower depth in MC is narrower than that in data. After rescaling with the Fudge factors in MC, the photon shower shapes in data and MC agree well. Compared with fake photons, genuine photons have narrow width and small leakage from the EM calorimeter as expected.

For $\sqrt{s} = 7$ TeV analysis, a neural net based identification is used. The ten variables are used as input parameters to the neural net. The neural net is trained in single photon MC simulation. For $\sqrt{s} = 8$ TeV, because the pileup condition is high, the neural net based identification has large systematic uncertainty. Accordingly, cut based criteria are used for $\sqrt{s} = 8$ TeV. The cut thresholds are optimized in $|\eta|$ bin, while no photon E_{T} dependence is introduced except for the hadronic leakage. Table 4.4.2 shows the thresholds for the shower shape variables for photons in $|\eta| < 0.6$ as an example.

4.5 Calibration of photon

Energies of photons and electrons are measured by the EM calorimeter with the cluster window. However particles deposit their energy not only in the active medium of the EM calorimeter but also out of clusters as well as in dead material. These energy losses are corrected in both data and MC with *Calibration hits method*. The remaining energy difference between data and MC is corrected with comparison of Z line shapes.

4.5.1 Calibration hits method

This method is based on MC based studies of energy deposits in both the uninstrumented and instrumented parts of the detector. It uses the cluster position and shower shape in the EM calorimeter. Through the correction, five corrections are applied: energy loss in front of the calorimeter, sampling fraction, lateral and longitudinal leakage, as well as energy modulation. The energy is reconstructed with the following formula:

$$E = E_{\mathrm{front}} + E_{\mathrm{Acc}} \times F_{\mathrm{sampling}} \times F_{\mathrm{longitudinal}} \times F_{\mathrm{lateral}} \times F_{\mathrm{mod}} \tag{4.5.1}$$

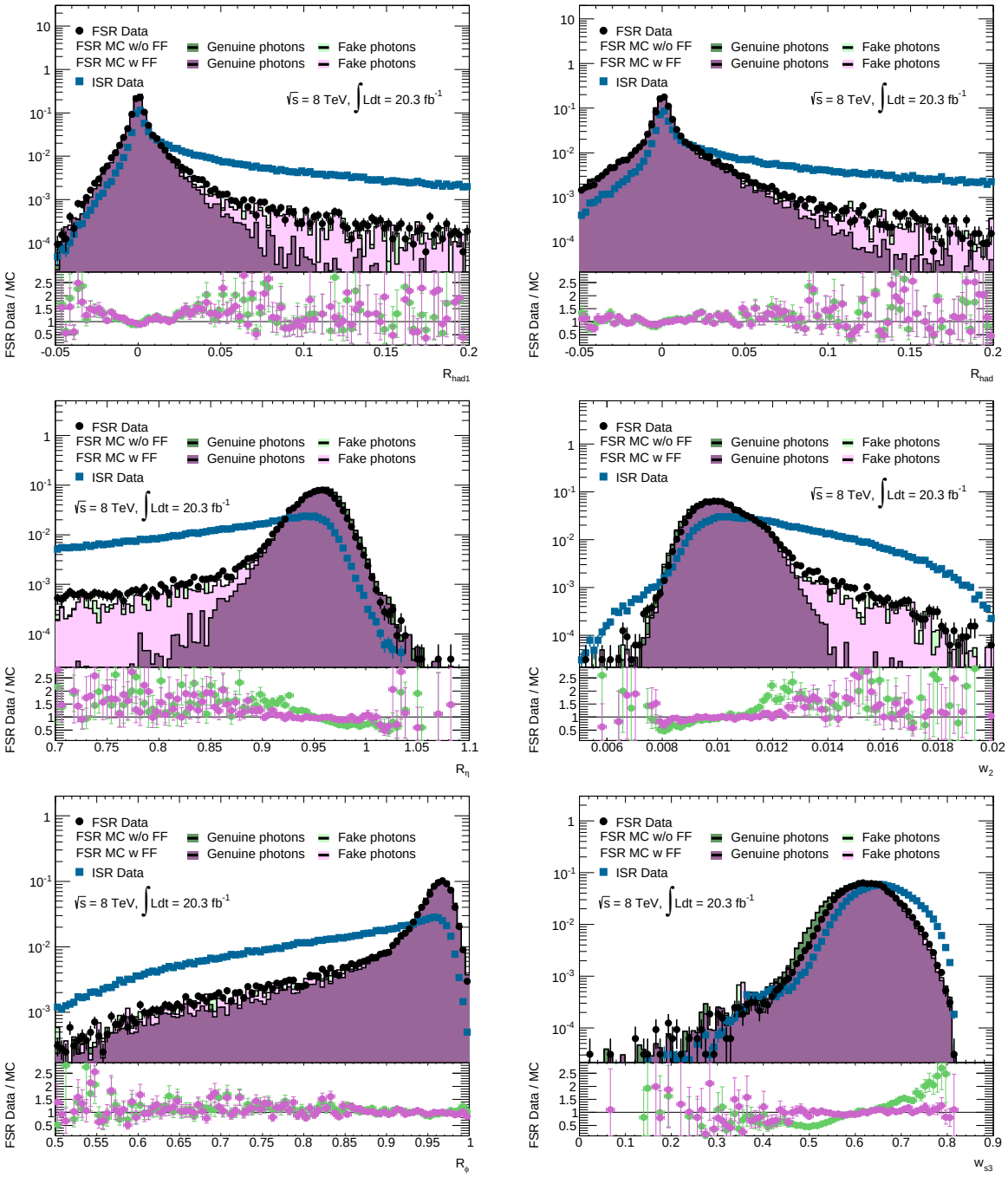

Figure 4.4.2: Shower shape variables for the photon identification in $\sqrt{s} = 8$ TeV data. *FF* means rescaled with Fudge factors. In the ratio plots, FSR events in data and rescaled (pink) or not-rescaled (lightgreen) MC are compared.

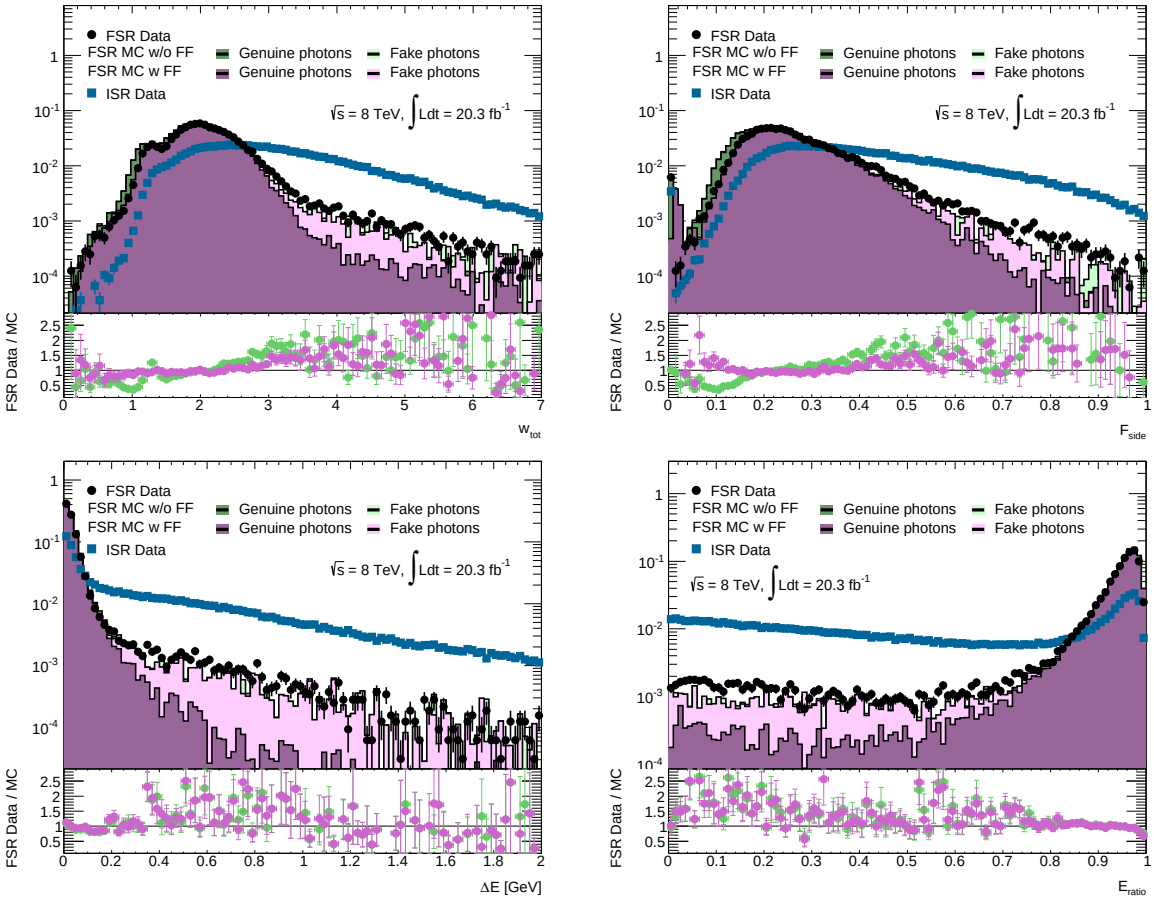

Figure 4.4.3: Shower shape variables for the photon identification. *FF* means rescaled with Fudge factors. In the ratio plots, FSR events in data and rescaled (pink) or not-rescaled (light green) MC are compared.

where E_{front} is the energy deposit in front the of the calorimeter, E_{Acc} is sum of energies in 1st, 2nd and 3rd layers, called Accordion energy because of their geometries, F_{sampling} is correction factor to the Accordion sampling fraction in the cluster, $F_{\text{longitudinal}}$ is correction factor for the longitudinal leakage, F_{lateral} is factor of the lateral leakage correction, and F_{mod} is energy correction depending on the impact point inside a cell.

E_{front} depends on the part of the cluster energy measured in the presampler (E_{ps}), E_{Acc} and η. E_{front} is expressed as follows:

$$E_{\text{front}} = a\left(E_{\text{Acc}}, |\eta|\right) + E_{\text{ps}} \times b\left(E_{\text{Acc}}, |\eta|\right) + E_{\text{ps}}^2 \times c\left(E_{\text{Acc}}, |\eta|\right) \tag{4.5.2}$$

where a, b and c are parameters determined as a function of E_{Acc} and $|\eta|$. For $|\eta| > 1.8$, since this region is not covered with the presampler, E_{front} is parametrized as a function of the shower longitudinal barycenter computed with the information given by the three layers only.

F_{sampling}, $F_{\text{londitudinal}}$ and F_{lateral} are parametrized as a function of X and η, where X is the longitudinal barycenter of the shower (*Shower depth*) defined by:

$$X = \frac{\sum_{i=0}^{3} E_i X_i}{\sum_{i=0}^{3} E_i} \tag{4.5.3}$$

where E_i is the energy deposit measured in the presampler ($i = 0$) and the three layers ($i = 1, 2, 3$), as well as X_i is the depth, expressed in radiation length, of the longitudinal center of each component from the center of the ATLAS detector ($R = 0$). X_i is a function of η.

The amount of the absorber material is modulated in ϕ and η depending on the position inside a cell due to the accordion geometry. Consequently, E_{Acc} is also modulated in ϕ and η. The factor $F_{\text{mod}} = F_{\text{mod}}\left(\phi, \eta\right)$ corrects the modulation.

The energy correction with the Calibration hits method is applied in both data and MC

4.5.2 Energy correction in data

After the MC based correction, the energies of photons and electrons in data are corrected to match those in MC with using the invariant mass distributions of $Z \to ee$ peak. The invariant mass of a reconstructed $Z \to ee$ is computed as:

$$m_{12} = \sqrt{2E_1E_2\left(1 - \cos\Delta\theta_{12}\right)} \tag{4.5.4}$$

where E_1 and E_2 are the electron energies measured with the EM calorimeter, as well as $\Delta\theta_{12}$ is the opening angle of the two electrons measured by the ID. Residual miscalibration in data to be corrected is parametrized by α:

$$E_{\text{rec}} = E_{\text{true}}\left(1 + \alpha\right) \tag{4.5.5}$$

where E_{rec} and E_{true} are the reconstructed and initial energies, respectively. α is estimated in 34 η bins, without any E_{T} bin. Neglecting second-order terms and supposing that the angle between the two electrons is perfectly known, the effect on the di-electron invariant mass is:

$$m_{ij}^{\text{rec}} = m_{ij}^{\text{true}}\left(1 + \frac{\alpha_i + \alpha_j}{2}\right) \tag{4.5.6}$$

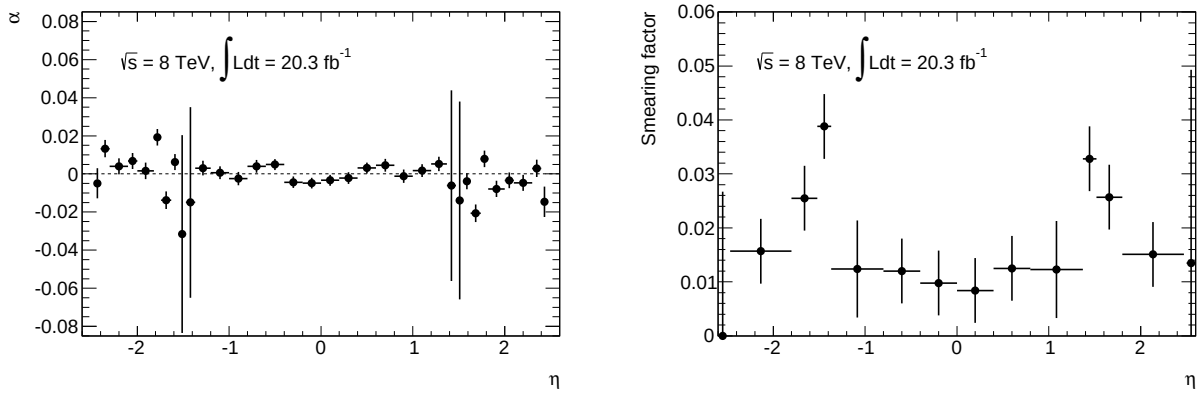

(a) (b)

Figure 4.5.1: Estimated energy correction factor(a) and smearing factor (b) for $\sqrt{s} = 8$ TeV analysis.

where m^{rec} is the measured di-electron mass, m^{true} is the invariant mass computed from true energies and α_i represents the α in a i-th η bin. Because the α values in two different η bins shift the invariant mass, the α_i cannot be estimated individually. The following unbinned likelihood is introduced in order to estimate the value of α :

$$-\ln L_{\mathrm{tot}} = \sum_{k}^{N_{evt}} -\ln L_{ij}\left(m_k\left(1+\frac{\alpha_i+\alpha_j}{2}\right)^{-1}\right) \tag{4.5.7}$$

where N_{evt} is the total number of selected events and $L\,(m)$ is the probability density function (PDF) of the invariant mass m. The PDF is an expected Z boson line shape when electrons fall in i- and j-th η bins respectively. It is obtained from the MC simulation, which takes into account some impacts on the Z line shape: theoretical ones like relativistic Breit-Wigner shape, γ^* contribution, $Z-\gamma^*$ interference, parton density function, and final state radiation, as well as experimental ones like detector resolution, effect of the bremsstrahlung. Thus the α of each η bin are estimated with the maximum likelihood fit. The PDF is computed with di-electron mass within [70, 110] GeV, and the likelihood fit is performed in [80, 100] GeV. Figure 4.5.1a shows the estimated α values for $\sqrt{s} = 8$ TeV analysis.

Thus the scale factor $(1+\alpha)^{-1}$ is applied to energy in data:

$$E \to E' = \frac{E_{\mathrm{rec}}}{1+\alpha} \tag{4.5.8}$$

Note that α is applied not only to electrons but also to photons.

As described in Section 3.2, the energy smearing for MC simulation is also derived from comparison of the $Z \to ee$ peaks in data and MC. The smearing factor (β) is defined as:

$$E \to E' = E_{\mathrm{rec}} \times G(1,\beta) \tag{4.5.9}$$

where $G(\mu,\sigma)$ is a random number followed by a Gaussian function with mean μ and variance σ^2. The values of β are determined by the likelihood fit in the same way as

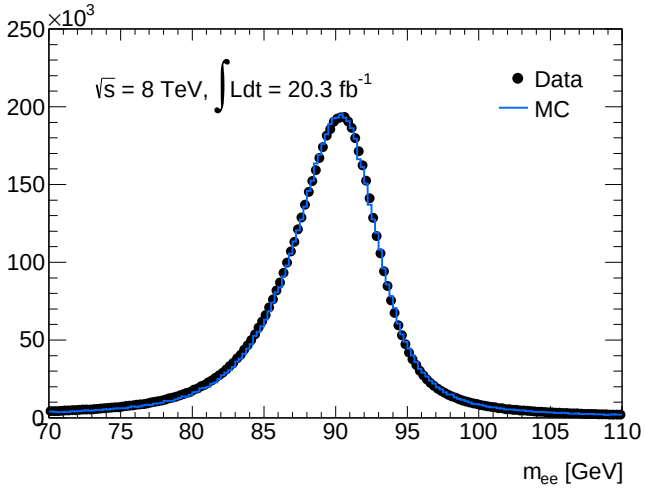

Figure 4.5.2: Invariant mass of di-electron (m_{ee}). The selected electrons with opposite charges are required to have p_{T}>25, 20 GeV and $|\eta| < 2.47$.

energy scale. Figure 4.5.1b shows the estimated β values for $\sqrt{s} = 8$ TeV analysis. Figure 4.5.2 shows the Z line shapes after applying the energy scale α to data as well as energy smearing to MC. The shapes in data and MC agree very well.

4.6 Direction of photon

Photon direction is determined from the straight line between the barycenter of the energy deposit in the 1st layer of the EM calorimeter and the primary vertex as described in Section 4.1.

The direction determination of photons is crucial for the resolution of Higgs mass because the opening angle of the two photons ($\Delta\theta$) is used in the calculation of their invariant mass:

$$m_{\gamma\gamma} = \sqrt{2E^{\gamma 1}E^{\gamma 2}\left(1 - \cos\Delta\theta\right)} \tag{4.6.1}$$

where $E^{\gamma 1(2)}$ is the energy of a photon. The opening angle is calculated from the pseudo-rapidity η and the azimuthal angle ϕ of the photons. Eq.(4.6.1) is rewritten as follows:

$$m_{\gamma\gamma} = \sqrt{\frac{2E^{\gamma 1}E^{\gamma 2}}{\cosh\eta^{\gamma 1}\cosh\eta^{\gamma 2}}\left[\cosh\left(\eta^{\gamma 1} - \eta^{\gamma 2}\right) - \cos\left(\phi^{\gamma 1} - \phi^{\gamma 2}\right)\right]} \tag{4.6.2}$$

where $\eta^{\gamma 1(2)}$ and $\phi^{\gamma 1(2)}$ are the pseudo-rapidity and the azimuthal angle of a photon. η and ϕ are determined using the trajectories of the photons.

The resolution of η is determined by the determination of primary vertex selection. When the barycenter of beam spot is assumed as a primary vertex, the resolution of primary vertex is 45 mm in $\sqrt{s} = 8$ TeV data. In this case, the degradation of the η resolution of photons is 0.03, and then the mass resolution is degraded 1.5 % by the η resolution. The $m_{\gamma\gamma}$ resolution improves 23 % (19 %) when using the neural network based algorithm ($\sum p_{\mathrm{T}}^2$ max) compared with using a barycenter of beam spot as shown in Figure 4.6.1.

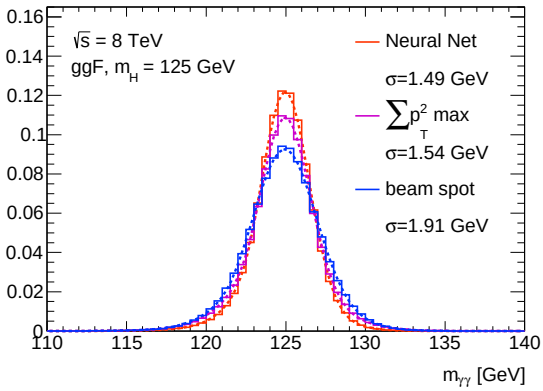

Figure 4.6.1: Distributions of the expected di-photon invariant mass for ggF signal events as a function of the algorithm of the primary vertex selection.

Track momentum	$p_{\mathrm{T}} > 1$ GeV
Transverse impact parameter	$d_0 < 1.5$ mm
Longitudinal impact parameter	$z_0 \sin\theta < 15$ mm
Inner detector hit	Si hits(Pixel + SCT) ≥ 9
B-layer	B-layer hit (if expected)
Self-track exclusion	Exclude conversion tracks of the photon

Table 4.7.1: Track selection for photon track isolation. z_0 and θ are with respect to reconstructed primary vertex in di-photon events.

4.7 Track isolation

Trajectories of photons from a decay of a Higgs boson are well isolated from tracks of charged particles. In contrast, a fake photon in a jet can become distinct due to the existence of charged particle tracks in the jet. This feature separates photons from fake photons in jets. The degree of the isolation is measured with a variable *track isolation*. The presence of pileup jets which are from pileup vertices decreases the separation power of the track isolation. Accordingly, tracks used for calculation of the track isolation are required to have small impact parameters so as to reject the influence of pileup jets. Accurate measurement of the impact parameters needs precise determination of the primary vertex. When any selections for impact parameters are not applied, the track isolation has looser pileup robustness than the energy cluster based isolation in the EM calorimeter. Therefore the primary vertex reconstruction is important for rejection of background events in which jets fake photons. The definition of the track isolation is the scalar sum of p_{T} of tracks that pass the selection on Table 4.7.1 and within a cone around the photon. The selection is optimized on MC to get best signal-background separation and pileup robustness. Because one of the advantages of the track isolation is pileup robustness, the track isolation is only used for $\sqrt{s} = 8$ TeV analysis where pileup is high. The track isolation for photon is called $p_{\mathrm{T}cone X}$ where X is cone size ($\Delta R = \sqrt{\Delta\eta^2 + \Delta\phi^2}$) times 100. For the $H \to \gamma\gamma$ analysis $X = 20$ is selected.

4.8 Calorimeter isolation

The calorimeter isolation uses energy clusters in the calorimeter. Not only charged objects but also neutral objects are taken into account unlike the track isolation. Thus the calorimeter isolation have stronger separation photons from fake photons than the track isolation under low pileup condition.

The calorimeter isolation $E_{\mathrm{T}cone40}$, is defined as the scalar sum of transverse energy of clusters in a cone of $\Delta R = 0.4$ except $\eta \times \phi = 5 \times 7$ rectangular core centered on the object.

Topological clustering Topological clustering is used for calculating the isolation. The basic idea is extending a cluster to neighbor cells when the cells have significant energy deposit. More precisely, a cell that has $E_{\mathrm{cell}} > 4\sigma_{\mathrm{noise}}$ can be a seed of a cluster where E_{cell} is the energy deposit in the cell and σ_{cell} is the noise of the cell. If a cell next to the edge of a cluster satisfies $E_{\mathrm{cell}} > 2\sigma_{\mathrm{noise}}$, the cell is newly included in the cluster. This operation is repeated until the cluster are unable to be extended further.

Leakage correction The lateral leakage to the core from the cone from the outside of the core becomes larger as the energy of the photon candidates increases. This is corrected as a function of η, E_{T} and conversion status of the photon, which is defined from MC samples.

Pileup correction The performance of the calorimeter isolation is improved by subtracting the energies of pileup jets because only activities from a primary vertex contribute to photon-jet separation. The correction factor is computed from estimation of energy density surround the cone.

Chapter 5

Measurements of photon performance with $Z \to \ell\ell\gamma$

5.1 Event selection

The measurements of the photon performance of the ATLAS detector is crucial for the $H \to \gamma\gamma$ analysis. The $Z \to \ell\ell\gamma$ process, where a Z boson decays into a pair of leptons (μ or e) and one of the leptons emit a final state radiation (FSR) photon, provides photon candidates in data with a high purity. In this chapter, the estimation of photon energy scale, photon identification efficiency, isolation efficiency and conversion fraction with the $Z \to \ell\ell\gamma$ are described.

The mass of the Z boson can be reconstructed by not $m_{\ell\ell}$ but $m_{\ell\ell\gamma}$. On the other hand, initial state radiation (ISR) jets can be removed by requirements for $m_{\ell\ell\gamma}$ and $m_{\ell\ell}$. This feature strongly increases the purity of photons.

To select $ee\gamma$ events single lepton triggers are used since they have higher efficiencies than di-lepton triggers. This is because sub-leading leptons tend to have small p_{T} due to emitting hard FSR photons. For the $Z \to ee\gamma$ analysis, single electron triggers are used. For $\sqrt{s} = 7$ TeV analysis, three different single electron triggers are used one after the other as the luminosity increase. The triggered electron is identified by requiring the EM shower shape and track-cluster matching. The matched track is required to have enough hits in the inner detector and have small transverse impact parameter (< 5 mm). The triggered electron p_{T} threshold is 20 GeV for lower luminosity run, while 22 GeV for

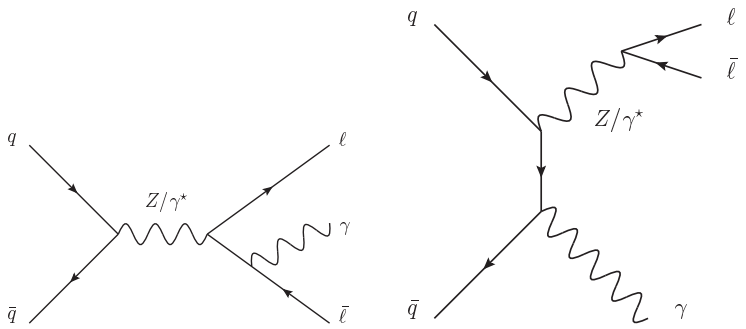

Figure 5.1.1: Diagrams of $Z + \gamma$ events: FSR (left) and ISR (right)

Lepton requirement	At least 2 opposite charged leptons passing the lepton selection
Photon requirement	At least 1 photon passing the photon identification
Photon isolation	$E_{\mathrm{T}cone40} < 4$ GeV
Photon E_{T}	$E_{\mathrm{T}} > 15$ GeV for leading photon
Photon pseudo-rapidity	$\|\eta\| < 1.37$ or $1.56 < \|\eta\| < 2.37$
Lepton p_{T}	$p_{\mathrm{T}} > 25/15$ GeV for leading/sub-leading lepton
ISR rejection	$45 < m_{\ell\ell} < 85$ GeV
Z mass	$80 < m_{\ell\ell\gamma} < 100$ GeV
Overlap removal	Photon and its closest electron (muon) must have $\Delta R > 0.4\,(0.2)$

Table 5.1.1: Event selection for $Z \to \ell\ell\gamma$ analysis.

higher luminosity run. For $\sqrt{s} = 8$ TeV analysis, the p_{T} threshold is increased to 24 GeV. In addition, track isolation is required to the triggered electron. On the other hand, in the $Z \to \mu\mu\gamma$ analysis, single muon triggers are used. The triggered muon is required to have good track quality in the muon spectrometers. The p_{T} threshold of the muon trigger for $\sqrt{s} = 7$ TeV is 18 GeV. For $\sqrt{s} = 8$ TeV analysis, two triggers are used in OR condition. One requires isolation criteria to the muon and uses a p_{T} threshold of 24 GeV. The other does not require any isolation criteria but uses a 36 GeV p_{T} threshold. The off-line event selection is shown in Table 5.1.1. The reconstruction of electrons and muons are described in Appendix B and C. Photons in the transition region between the barrel and the endcap calorimeters ($1.37 < |\eta| < 1.56$) are removed because the transition region has high fake rate of jet→photon. The events that have $m_{ll} \sim m_Z$ are removed in order to reject initial state radiation (ISR) events (Z+ jets or Z+ ISR photons). In the $Z \to ee\gamma$ channel, the wider ΔR is used for overlap removal with leptons than $Z \to \mu\mu\gamma$. This is because electrons very close to photons increase the calorimeter isolation of photons. The number of selected events is 3795 (16544) in $Z \to ee\gamma$ channel and 6452 (20877) in $Z \to \mu\mu\gamma$ channel in $\sqrt{s} = 7$ (8) TeV data.

5.1.1 $Z +$ jet background

The main background of $Z \to \ell\ell\gamma$ events is $Z +$ jet events, where π^0s in ISR jets fake photons. Because the fake photons have different energy scale compared with genuine photons, $Z +$ jet events have an impact on the measurement of photon scale. FSR events are also contaminated by Z+ISR photon events. However since the Z+ISR photon events have genuine photons, they only increase the high mass tail in $m_{\ell\ell\gamma}$ distributions and do not affect the photon scale measurement. Therefore Z + ISR photon events are treated as signal.

The fraction of $Z +$ jet events is estimated with comparing isolation distributions between genuine photons and fake photons in an ISR control region. The control region is defined by the event selection same as FSR selection except the following requirements:

- the isolation cut to photons is removed
- the invariant mass cuts are modified to $80 < m_{\ell\ell} < 100$ GeV and $105 < m_{\ell\ell\gamma}$ GeV

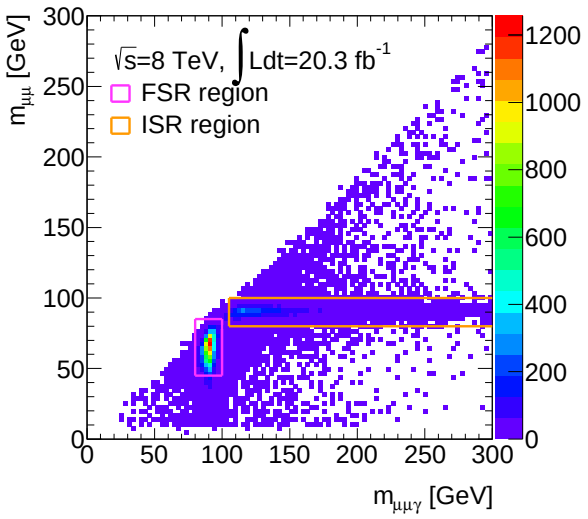

Figure 5.1.2: FSR and ISR regions in $m_{\mu\mu\gamma}$-$m_{\mu\mu}$ plane in $\sqrt{s} = 8$ TeV data. Isolation criteria are required.

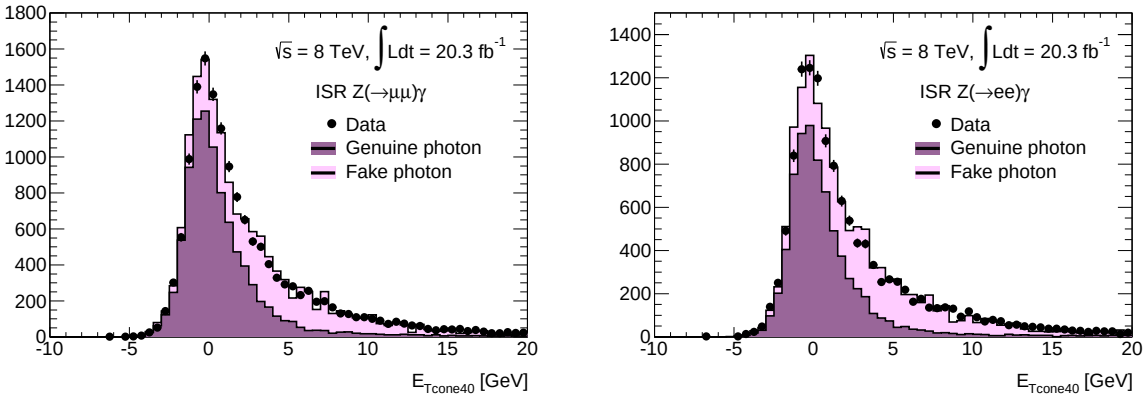

Figure 5.1.3: Isolation distribution in the ISR control region after the template fit in $\sqrt{s} = 8$ TeV data.

Figure 5.1.2 shows FSR and ISR regions in $m_{\mu\mu\gamma}$ vs. $m_{\mu\mu}$ plane. The normalization factors for MC events are obtained from a template fit with the calorimeter isolation distribution in the control region in data as shown in Figure 5.1.3. The templates are obtained from $Z \to \ell\ell\gamma$ and Z+jet MC. From the fit result, the purity of photons in the FSR region is estimated to be 99.6 %. Figure 5.1.4 shows $m_{\ell\ell\gamma}$ distributions. The E_{T} and η distributions of selected photons in $Z \to \ell\ell\gamma$ events are shown in Figure 5.1.5.

5.2 Photon energy scale

The calibration obtained from $Z \to ee$ events is applied not only to electrons but also to photons. The differences between electrons and photons on the energy calibration are taken into account based only on the MC simulation. Then the energy calibration for genuine photons with respect to the calibration for electrons is the remaining uncertainty. A check of the photon energy calibration with pure photon samples is necessary to assure

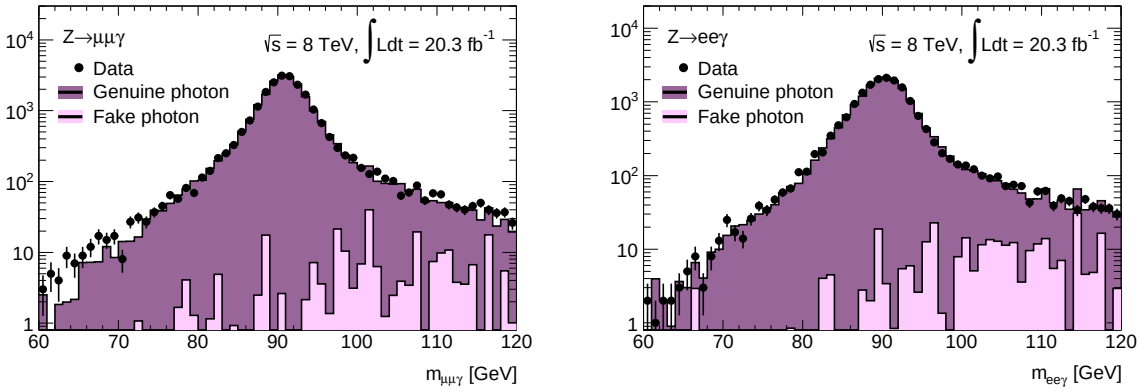

Figure 5.1.4: Three-body invariant mass $m_{\ell\ell\gamma}$ distribution in the FSR region in $\sqrt{s} = 8$ TeV data.

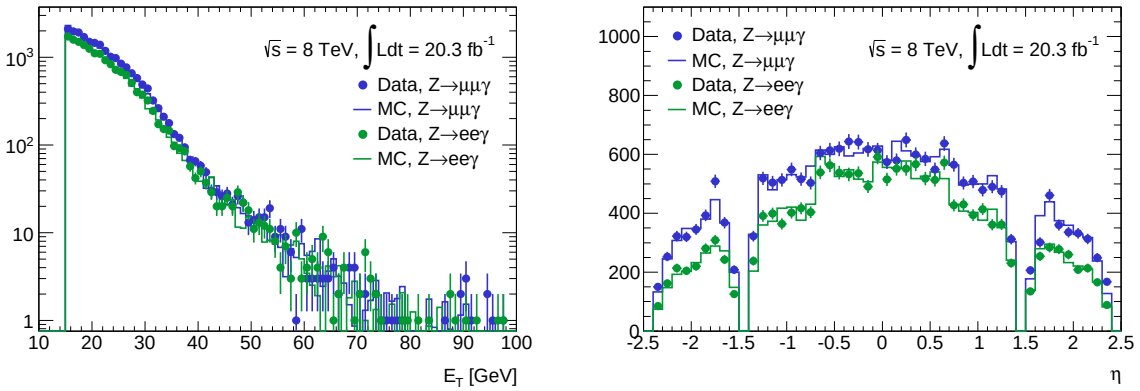

Figure 5.1.5: E_{T} and η distributions of selected photons in $Z \to \ell\ell\gamma$ events in $\sqrt{s} = 8$ TeV data.

the EM calorimeter performance for the $H \to \gamma\gamma$ analysis. This section describes a data-driven measurement of photon energy scale with $Z \to \ell\ell\gamma$ events.

A photon energy scale factor α is applied to photons in $Z \to \ell\ell\gamma$ events in data after applying all energy corrections as a probe to check that photons in data have the same scale as MC.

$$E_{\gamma,\mathrm{Data}} \to E'_{\gamma,\mathrm{Data}}(\alpha) = \frac{E_{\gamma,\mathrm{Data}}}{1+\alpha} \tag{5.2.1}$$

α is binned in η, E_{T} and conversion status of photons. For $\sqrt{s} = 8$ TeV analysis, η, E_{T} and conversion status binning are used.

- 4 bins in η: $|\eta| = \{0, 0.6, 1.37, 1.56, 1.82, 2.37\}$ without the crack region $\{1.37, 1.56\}$.
- 3 bins in E_{T}: $E_{\mathrm{T}} = \{15, 20, 30, 100\}$ GeV.
- 3 bins in conversion status: unconverted, 1-track converted and 2-track converted photon

For $\sqrt{s} = 7$ TeV analysis, only 2 conversion bins are used because of small statistics.

- 2 bins in conversion status: unconverted and converted photon

After applying α in data, the three-body invariant mass is recalculated ($m_{\ell\ell\gamma}(\alpha)$) written as the following equation shows:

$$m_{\ell\ell\gamma} \to m_{\ell\ell\gamma}(\alpha) \simeq m_{\ell\ell\gamma}\left[1 - \frac{\alpha}{2}\left(1 - \left(\frac{m_{\ell\ell}}{m_{\ell\ell\gamma}}\right)^2\right)\right] \tag{5.2.2}$$

where $m_{\ell\ell}$ is the invariant mass of di-lepton in the FSR events. The distributions of $m_{\ell\ell\gamma}(\alpha)$ is compared to MC by changing theα value and the best value of α is estimated such that data and MC agree well. If the best agreement of the distributions in data and MC is given by $\alpha = 0$, the energy scale of photons is well calibrated by the electron energy calibration. We have the following three methods for estimation of the best value of α.

Ratio method In this method, the peak positions of $m_{\ell\ell\gamma}$ in data and MC are measured with Gaussian fits. For different value of α, the recomputed distribution is fitted in data. The fit range is $\pm 1.5\sigma$ around the peak, where σ denotes the deviation of the Gaussian. In addition to $m_{\ell\ell\gamma}$, the $m_{\ell\ell}$ peak in non-radiative Z decay events ($m_{\ell\ell}^{\mathrm{non-rad}}$) are also fitted with a Gaussian in order to suppress an influence of lepton scale uncertainty.

After the Gaussian fits to $m_{\ell\ell\gamma}$ and $m_{\ell\ell}$, the ratio $\langle m_{\ell\ell\gamma}(\alpha)\rangle / \langle m_{\ell\ell}^{\mathrm{non-rad}}\rangle$ are compared between data and MC, where $\langle X\rangle$ is the peak position of X. When a value of α is applied to data as Eq.(5.2.1) shows, the ratio is shifted as:

$$\frac{m_{\ell\ell\gamma}}{\langle m_{\ell\ell}^{\mathrm{non-rad}}\rangle} \to \frac{m_{\ell\ell\gamma}(\alpha)}{\langle m_{\ell\ell}^{\mathrm{non-rad}}\rangle} \simeq \frac{m_{\ell\ell\gamma}}{\langle m_{\ell\ell}^{\mathrm{non-rad}}\rangle}\left[1 - \frac{\alpha}{2}\left(1 - \left(\frac{m_{\ell\ell}}{m_{\ell\ell\gamma}}\right)^2\right)\right] \tag{5.2.3}$$

The best value of α is estimated such that the double-ratio $R = 1$ which is defined as:

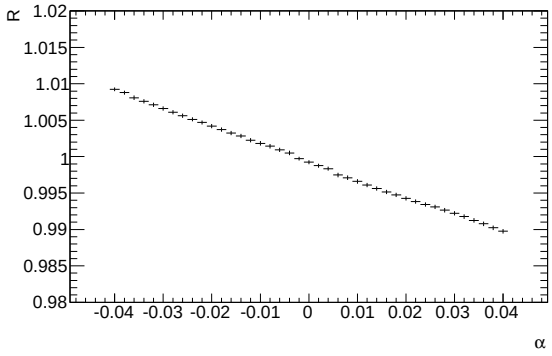

Figure 5.2.1: Distribution of R. The best fit value of α is estimated from the point at $R = 1$.

$$R \equiv \frac{\langle m_{\ell\ell\gamma}(\alpha)\rangle_{\rm Data} \,/\, \left\langle m_{\ell\ell}^{\rm non-rad}\right\rangle_{\rm Data}}{\langle m_{\ell\ell\gamma}\rangle_{\rm MC} \,/\, \left\langle m_{\ell\ell}^{\rm non-rad}\right\rangle_{\rm MC}} \tag{5.2.4}$$

Statistics error of α is calculated by propagating the errors of $\langle m_{\ell\ell\gamma}\rangle$ and $\left\langle m_{\ell\ell}^{\rm non-rad}\right\rangle$ to R. Figure 5.2.1 shows the distribution of R. The distribution R is obtained to be a linear function of α, and the slope is ~ 0.25. The slope is determined by $(m_{\ell\ell}/m_{\ell\ell\gamma})$ in Eq.(5.2.3).

χ^2 method In this method, the best value of α is estimated by minimizing χ^2 which represents the degree of agreement of $m_{\ell\ell\gamma}$ shapes between data and MC. One of the merits of the χ^2 method is that the best α can be estimated without assuming any function to the invariant mass distribution. χ^2 is calculated for each α by comparing the histograms of $m_{\ell\ell\gamma}$.

$$\chi^2(\alpha) \equiv \sum_i^{n_{bin}} \frac{\left(N_{{\rm Data},i}(\alpha) - N_{{\rm MC},i}\right)^2}{\sigma^2_{{\rm Data},i}(\alpha) + \sigma^2_{{\rm MC},i}} \tag{5.2.5}$$

where i is the bin label of the histogram, N_i is the number of events and σ_i is the error in each bin. $\chi^2(\alpha)$ is minimized by the best agreement of the distributions. When the shape of the histograms are described by Gaussian, $\chi^2(\alpha)$ follows parabola distribution. But because the actual shapes are asymmetrical distributions due to some kinematic cuts, asymmetric parabola well describes $\chi^2(\alpha)$.

$$\chi^2(\alpha) = \begin{cases} \frac{(\alpha-\alpha_{\rm best})^2}{\sigma_R^2} + \chi^2_{\rm min} & \alpha > \alpha_{\rm min} \\ \frac{(\alpha-\alpha_{\rm best})^2}{\sigma_L^2} + \chi^2_{\rm min} & \alpha \le \alpha_{\rm min} \end{cases} \tag{5.2.6}$$

where $\sigma_{R(L)}$ corresponds to the statistical upper(lower) error of α and $\alpha_{\rm best}$ is the best fit value of α. The distribution of $\chi^2(\alpha)$ is fitted with the asymmetric parabola. All parameters in Eq.(5.2.6) are floating in the fit. Figure 5.2.2 is an illustration of χ^2 distribution.

E/p method for double-track converted photon When a photon is reconstructed as a double-track converted photon, the sum of momentum of the two conversion tracks

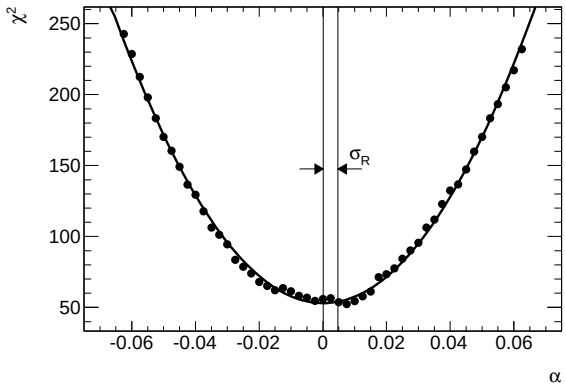

Figure 5.2.2: Illustration of χ^2. The best fit value of α is measured form the minimum point ($\chi^2(\alpha_{\rm best}) = \chi^2_{\rm min}$). The upper error of α (σ_α) is estimated the point where $\chi^2(\alpha_{\rm best} + \sigma_\alpha) = \chi^2_{\rm min} + 1$.

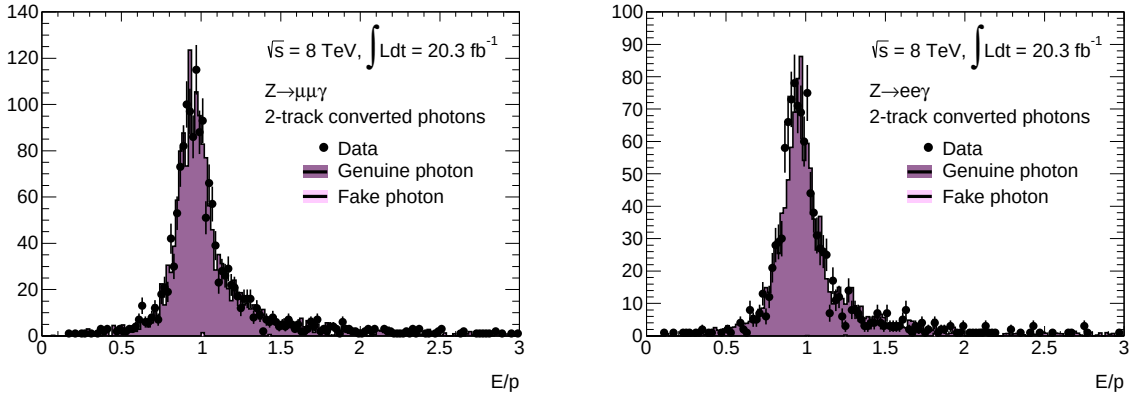

Figure 5.2.3: Distribution of E/p of double-track converted photons in $\sqrt{s} = 8$ TeV data.

$p_\gamma \equiv |\vec{p}_{\rm conv1} + \vec{p}_{\rm conv2}|$ is equal to the energy of the converted photon E_γ. The p_γ is a good reference to the E_γ because the performance of the inner tracker is well studied [94]. A distribution of E_γ/p_γ has sharp Gaussian peak around 1, hence the energy scale of double-track converted photons can be estimated with Gaussian fitting to the E_γ/p_γ distribution. The photon scale α in Eq.(5.2.1) is determined such that $\langle E_\gamma(\alpha)/p_\gamma\rangle_{\rm Data} = \langle E_\gamma/p_\gamma\rangle_{\rm MC}$, where $\langle E_\gamma/p_\gamma\rangle$ represents the mean of the Gaussian. The fit range is -1.5σ to $+1\sigma$ around the peak, where σ is the deviation of the Gaussian. The distribution of E/p is shown in Figure 5.2.3.

5.2.1 Correlation of energy scales between photons and electrons

Both electron and photon energies are measured with the EM calorimeter. Consequently, the miscalibration should be correlated between electrons and photons. However, it is difficult to estimate the correlation coefficient exactly. Accordingly, in $Z \to ee\gamma$ mode, photons are assumed to be uncorrelated with electrons.

In case electrons and photons are fully correlated and have a common bias Δ for their energies, the energies of electrons and photons are sifted as $E_e \to E_e(\Delta) = E_e(1+\Delta)$

and $E_\gamma \to E_\gamma(\Delta) = E_\gamma(1+\Delta)$. Hence the peak position of $m_{ee\gamma}$ is shifted as:

$$m_{ee\gamma} \to m^{corr}_{ee\gamma}(\Delta) = m_{ee\gamma}(1+\Delta) \tag{5.2.7}$$

In this case, energy scale α is applied not only to photons but also to electrons:

$$m_{ee\gamma} \to m^{corr}_{ee\gamma}(\alpha) = \frac{m_{ee\gamma}}{1+\alpha} \tag{5.2.8}$$

From a requirement that α cancels the shift of $m_{ee\gamma}$ by Δ, $\alpha = \Delta$ is obtained. On the other hand when they are uncorrelated and electrons have a bias Δ, $m_{ee\gamma}$ is shifted as:

$$m_{ee\gamma} \to m^{uncorr}_{ee\gamma}(\Delta) \simeq m_{ee\gamma}\left[1+\frac{\Delta}{2}\left(1+\left(\frac{m_{ee}}{m_{ee\gamma}}\right)^2\right)\right] \sim m_{ee\gamma}(1+0.75\Delta) \tag{5.2.9}$$

In the last term, an approximation $m_{ee}/m_{ee\gamma} \sim 0.7$ is used. Since energy scale α is applied only to photons in this case, $m_{ee\gamma}$ is shifted as Eq.(5.2.2). From a comparison with Eq.(5.2.9), $\alpha \sim 3\Delta$ is obtained. Thus the best fit value of α in uncorrelated model is about three times larger than full correlated model. Therefore the uncorrelated model is conservative.

5.2.2 Systematic uncertainty

5.2.2.1 Lepton energy scale

The peak position of $m_{\ell\ell\gamma}$ is sensitive to the uncertainty of lepton energy scale. If lepton energy scale is shifted by Δ, as $E_\ell \to E_\ell(\Delta) = E_\ell(1+\Delta)$, $m_{\ell\ell\gamma}$ and the ratio $m_{\ell\ell\gamma}/\left\langle m^{\mathrm{non-rad}}_{\ell\ell}\right\rangle$ are shifted as:

$$\begin{aligned} m_{\ell\ell l\gamma} \to m_{\ell\ell\gamma}(\Delta) \simeq & \quad m_{\ell\ell\gamma}\left[1+\frac{\Delta}{2}\left(1+\left(\frac{m_{\ell\ell}}{m_{\ell\ell\gamma}}\right)^2\right)\right] \\ \frac{m_{\ell\ell\gamma}}{\left\langle m^{\mathrm{non-rad}}_{\ell\ell}\right\rangle} \to \frac{m_{\ell\ell\gamma}(\Delta)}{\left\langle m^{\mathrm{non-rad}}_{\ell\ell}(\Delta)\right\rangle} \simeq & \quad \frac{m_{\ell\ell\gamma}}{\left\langle m^{\mathrm{non-rad}}_{\ell\ell}\right\rangle}\left[1-\frac{\Delta}{2}\left(1-\left(\frac{m_{\ell\ell}}{m_{\ell\ell\gamma}}\right)^2\right)\right] \end{aligned} \tag{5.2.10}$$

Because $m_{\ell\ell}/m_{\ell\ell\gamma} \sim 0.7$ in the selected FSR events, Eq.(5.2.10) can be written approximately as:

$$\begin{aligned} m_{\ell\ell\gamma}(\Delta) \sim & m_{\ell\ell\gamma}(1+0.75\Delta) \\ \frac{m_{\ell\ell\gamma}(\Delta)}{\left\langle m^{\mathrm{non-rad}}_{\ell\ell}(\Delta)\right\rangle} \sim & \frac{m_{\ell\ell\gamma}}{\left\langle m^{\mathrm{non-rad}}_{\ell\ell}\right\rangle}(1-0.25\Delta) \end{aligned} \tag{5.2.11}$$

This is why the ratio can suppress the lepton scale uncertainty.

The systematic uncertainty on α due to the lepton scale uncertainty is evaluated with shifting lepton energies by their uncertainties. The error of muon scale is provided by comparing the peak positions of Z resonance between data and MC. The electron scale errors are the uncertainty of energy correction using Z line shapes, the uncertainty of the material mapping in the inner detector and the presampler energy scale. The photon energy scale uncertainties due to lepton scale are 0.1% for muons and 0.4% for electrons.

Conversion	Method	α		
Unconverted	Ratio	0.001	$\pm$0.003 (stat.)	$\pm$0.002 (syst.)
	χ^2	0.001	$\pm$0.002 (stat.)	$\pm$0.003 (syst.)
Converted	Ratio	-0.005	$\pm$0.005 (stat.)	$\pm$0.002 (syst.)
	χ^2	0.003	$\pm$0.005 (stat.)	$\pm$0.005 (syst.)

Table 5.2.1: Photon energy scale for $\sqrt{s} = 7$ TeV data.

5.2.2.2 Z + jet contamination

The fraction of Z+jet background is determined by the signal and background samples which is normalized with a template fit as described in Section 5.1.1. The signal normalization factor can also be determined from very high purity mass region in the FSR events ($80 < m_{\ell\ell\gamma} < 90$ GeV) as in Figure 5.1.4. The difference of above two normalization factors, assumed as the uncertainty of the factor, is 11%. This is so small that it does not influence on photon scale measurement. However, the uncertainty of energy scale of fake photon have to be taken into account. The systematic error due to Z+jet contamination is estimated to be $< 4 \times 10^{-4}$ by comparing photon energy scales between only using genuine photons and adding fake photons in MC.

5.2.2.3 Electron $\leftrightarrow$ photon confusion

Mismatching tracks to energy clusters in the EM calorimeter can cause electron $\leftrightarrow$ photon confusion. When one of the electrons from Z boson is confused with a FSR photon, $m_{\ell\ell\gamma}$ is slightly shifted due to the difference of calibration between electrons and photons. The impact of electron $\leftrightarrow$ photon confusion is estimated with exchanging energy scales between the electron that emit the photon and the emitted photon to be less than 10^{-4}. The radiative electron is chosen by requiring smaller ΔR from the photon than the other among leading two electrons.

5.2.3 Results

The photon energy scale α is estimated by the Ratio method, χ^2 method and the E/p method. The estimated photon scale α for $\sqrt{s} = 7$ data set is shown in Table 5.2.1, while α for $\sqrt{s} = 8$ data set is shown in Figure 5.2.4 and 5.2.5. α is consistent with 0 in all bins. Therefore photons are well calibrated. Table 5.2.2 and 5.2.3 summarize the systematic uncertainties of α. The largest contribution comes from lepton scale uncertainties. The total uncertainties are about 1 %. They are slightly larger than the uncertainties in the MC based calibration. Therefore the estimated photon energy scales are not used for final results. Nevertheless this is very important cross check with the data-driven method.

5.3 Photon identification efficiency

The shape of shower development of photons in the EM calorimeter is used for the photon identification in order to separate photons from jets as described in Section 4.4. The

Systematic uncertainty source		$\Delta\alpha_{\text{Ratio}}$	$\Delta\alpha_{\chi^2}$
Electron scale	Energy correction using Z line shape	2.9×10^{-3}	1.8×10^{-2}
	Material mapping	3.0×10^{-3}	3.2×10^{-3}
	Presampler energy scale	7.4×10^{-4}	9.7×10^{-4}
	Linearity	3.8×10^{-4}	6.1×10^{-4}
Electron smearing		2.5×10^{-3}	6.6×10^{-4}
Z+jet		1.0×10^{-4}	3.5×10^{-4}
Electron $\leftrightarrow$ photon confusion		$< 10^{-4}$	$< 10^{-4}$

Table 5.2.2: Systematic uncertainties of α in inclusive category of $Z \to ee\gamma$ channel. $\Delta\alpha_{\text{Ratio}}$ denotes systematic uncertainty in Ration method, and $\Delta\alpha_{\chi^2}$ is systematic uncertainty in χ^2 method.

Systematic uncertainty source	$\Delta\alpha_{\text{Ratio}}$	$\Delta\alpha_{\chi^2}$
Muon scale	1.3×10^{-3}	6.2×10^{-3}
Muon smearing	1.4×10^{-4}	1.1×10^{-4}
Z+jet	3.8×10^{-4}	1.8×10^{-4}

Table 5.2.3: Systematic uncertainties of α in inclusive category of $Z \to \mu\mu\gamma$ channel. $\Delta\alpha_{\text{Ratio}}$ denotes systematic uncertainty in Ration method, and $\Delta\alpha_{\chi^2}$ is systematic uncertainty in χ^2 method.

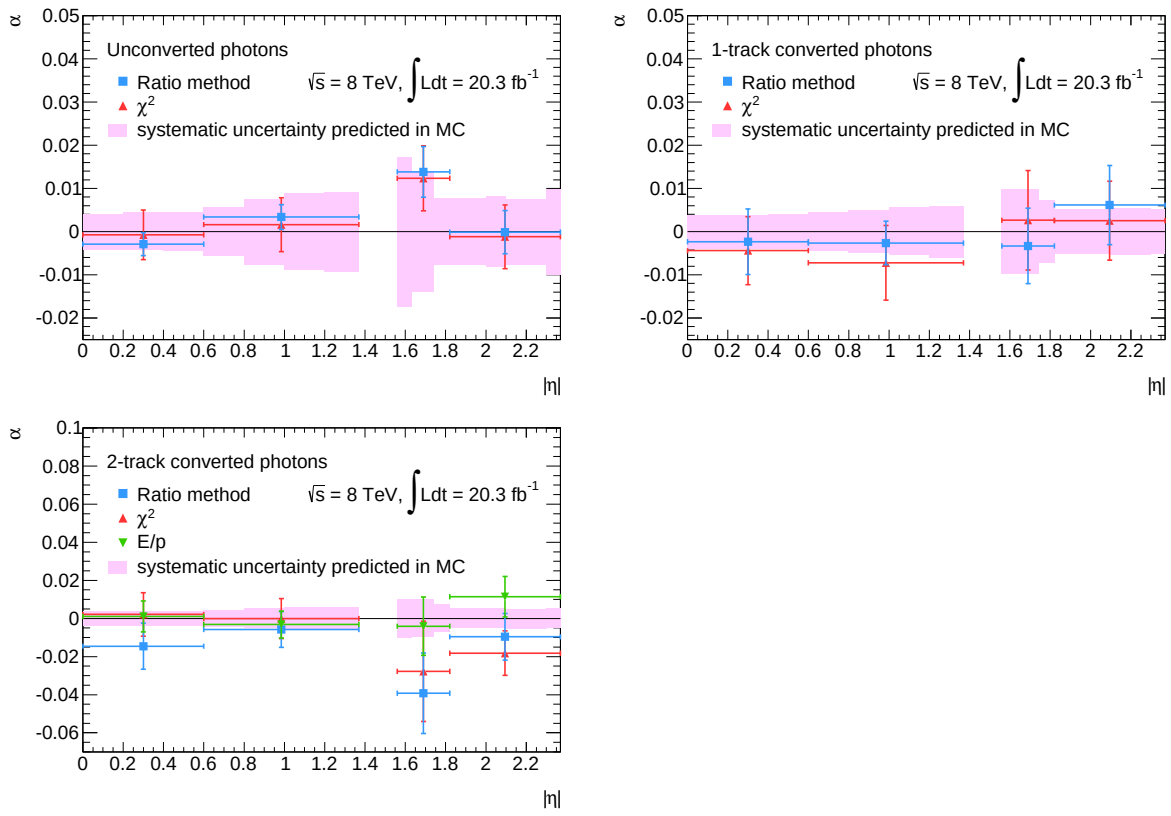

Figure 5.2.4: Photon scale extracted from $Z \to \ell\ell\gamma$ events with $|\eta|$ in $\sqrt{s} = 8$ TeV data.

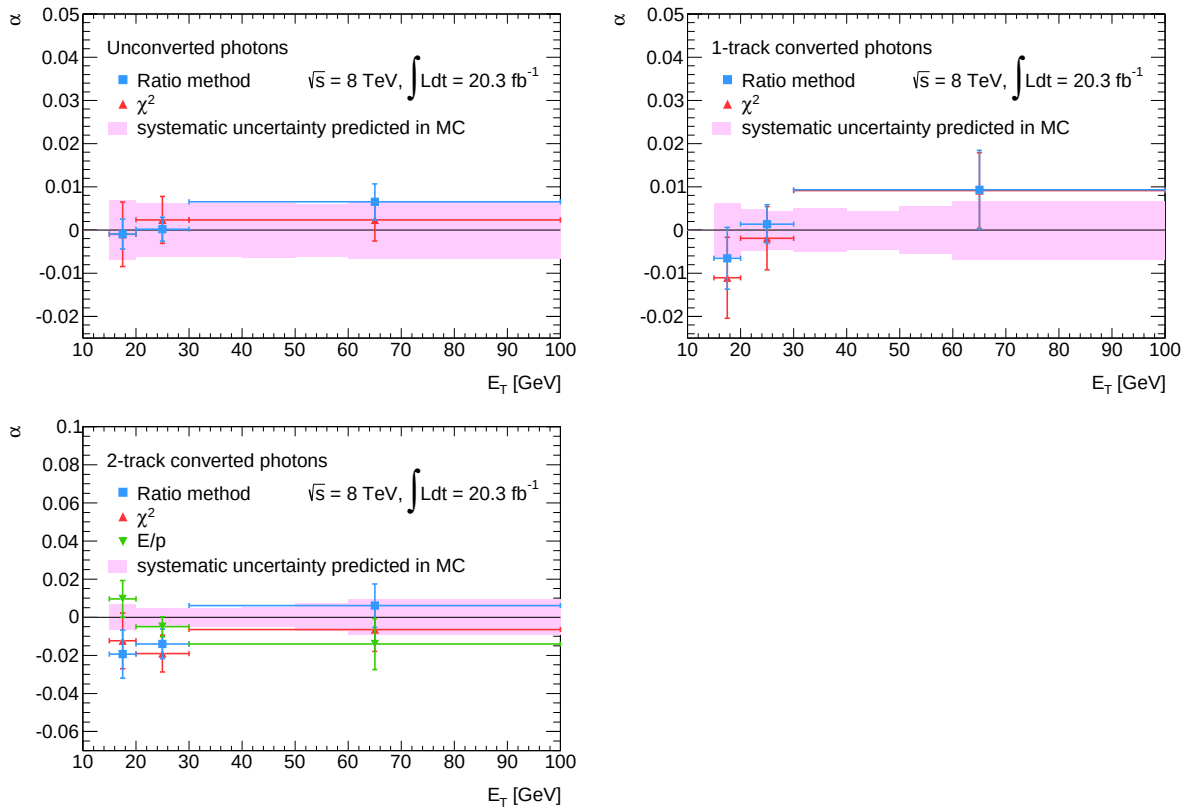

Figure 5.2.5: Photon scale extracted from $Z \to \ell\ell\gamma$ events with E_{T} in $\sqrt{s} = 8$ TeV data.

ten variables of photon shower shape used in the photon identification are checked with $Z \to \ell\ell\gamma$ events as shown in Figure 4.4.2 and 4.4.3.

The efficiency of the photon identification is measured in data-driven methods [84]. One of them is relied on the use of photon sample selected from $Z \to \ell\ell\gamma$ events. The efficiency is defined as the efficiency for reconstructed prompt photons to pass the identification criteria in a given E_{T}, η region.

$$\epsilon_{\mathrm{ID}}\left(E_{\mathrm{T}}, \eta\right) \equiv \frac{N^{\gamma}_{\mathrm{ID}}\left(E_{\mathrm{T}}, \eta\right)}{N^{\gamma}_{\mathrm{rec}}\left(E_{\mathrm{T}}, \eta\right)} \tag{5.3.1}$$

where N^{γ}_{ID} represents the number of identified photons and $N^{\gamma}_{\mathrm{rec}}$ is the number of reconstructed photons.

$Z \to \ell\ell\gamma$ events are selected with the procedure described in Section 5.1 except the photon identification and isolation criteria for counting the denominator. Then the identification criteria are applied and the numerator is counted. The photon purities are evaluated in both before and after the identification requirement (ρ_{rec} and ρ_{ID}) with the template fit described in 5.1.1. Eq. 5.3.1 is rewritten as:

$$\epsilon_{\mathrm{ID}}\left(E_{\mathrm{T}}, \eta\right) = \frac{\rho_{\mathrm{ID}}\left(E_{\mathrm{T}}, \eta\right) N^{Z\to\ell\ell\gamma}_{\mathrm{ID}}\left(E_{\mathrm{T}}, \eta\right)}{\rho_{\mathrm{rec}}\left(E_{\mathrm{T}}, \eta\right) N^{Z\to\ell\ell\gamma}_{\mathrm{rec}}\left(E_{\mathrm{T}}, \eta\right)} \tag{5.3.2}$$

where $N^{Z\to\ell\ell\gamma}_{\mathrm{ID}}$ is the number of selected events in the FSR region after applying the identification criteria and $N^{Z\to\ell\ell\gamma}_{\mathrm{rec}}$ is the number before applying the identification criteria.

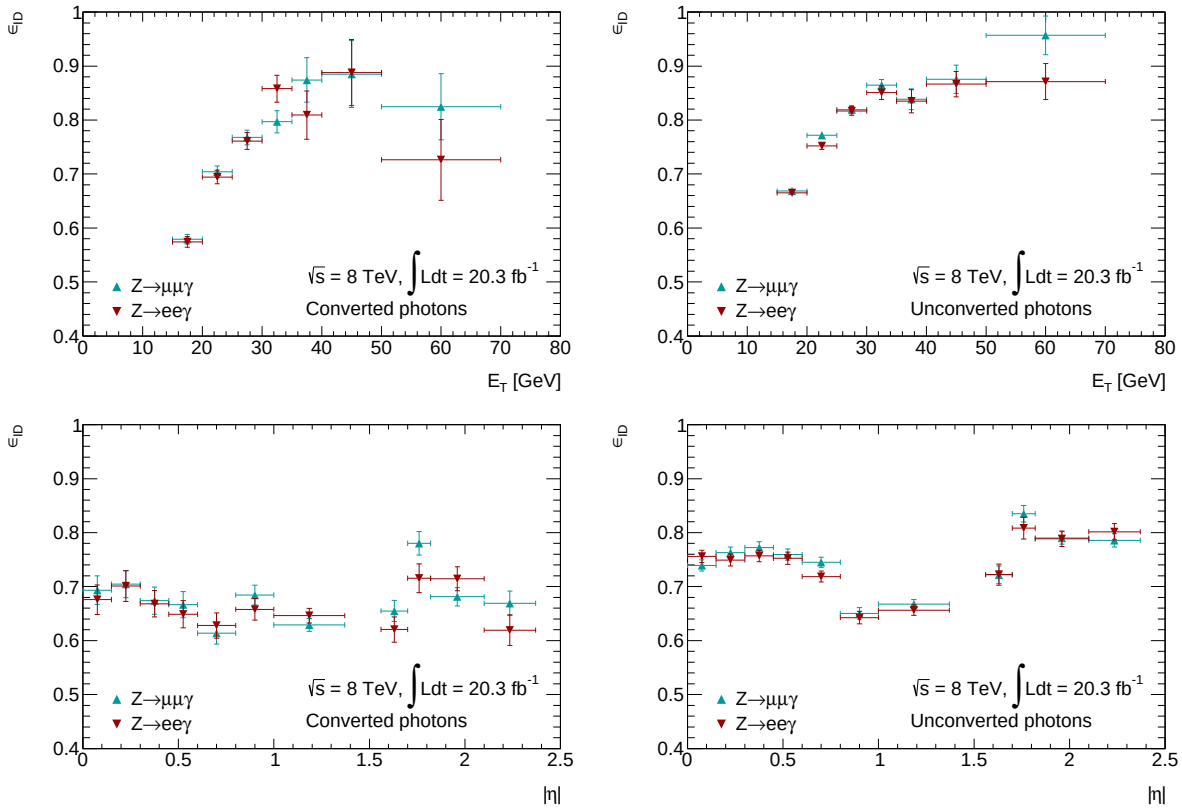

Figure 5.3.1: Efficiencies of photon identification in $\sqrt{s} = 8$ TeV data.

Figure 5.3.1 shows the efficiencies of photon identification. Both results in $Z \to ee\gamma$ and $\mu\mu\gamma$ modes agree very well. The shower shape variables of high E_{T} photons have narrower distributions than those of low E_{T} photons because of better energy resolution for high energy photons. Therefore higher E_{T} photons have higher identification efficiency. If a photon is converted in front of the EM calorimeter, the photon has wider shower. Hence the dependence of the efficiency on η comes from material traversed. However because the thresholds for each shower variable are changed in $|\eta|$, the efficiency is not so strongly correlated with the material traversed.

5.3.1 Other data-driven estimation measurements and combination

The efficiency of photon identification is also estimated in Electron extrapolation and Matrix method. The difference of shower shapes between electrons and photons are studied in MC. From the results, electrons in data, obtained from $Z \to ee$ events are extrapolated to photons in the Electron extrapolation method. Therefore the photon identification efficiencies are estimated with using the extrapolated electrons. This method provides a larger E_{T} sample than the $Z \to \ell\ell\gamma$ analysis. The main systematic uncertainty in the Electron extrapolation method is the material uncertainty which have an impact on the transform functions for the extrapolation. On the other hand, in the Matrix method photon candidates in data are selected using single photon triggers. In the collected sample, the observed numbers of photon candidates are expressed in $N^S_{\mathrm{pass}} + N^S_{\mathrm{fail}} + N^B_{\mathrm{pass}} +$

Figure 5.3.2: Comparison of combined data-driven measurements of converted ϵ_{ID} to MC predictions in $\sqrt{s} = 7$ data [84].

Figure 5.3.3: Comparison of combined data-driven measurements of unconverted ϵ_{ID} to MC predictions in $\sqrt{s} = 7$ data [84].

N^B_{fail}, where the superscripts S and B represent genuine photons and fake photons and the subscripts pass and fail mean passing and failing the identification criteria. Next, the identification criteria are applied to the photon candidates, and the number of events which pass or fail the identification criteria (N^T_{pass} or N^T_{fail}) are counted. They can be expressed as:

$$\begin{aligned} N^T_{\mathrm{pass}} =& N^S_{\mathrm{pass}} + N^B_{\mathrm{pass}} \\ N^T_{\mathrm{fail}} =& N^S_{\mathrm{fail}} + N^B_{\mathrm{fail}} \end{aligned} \tag{5.3.3}$$

In addition, the number of events which pass or fail not only the identification but also isolation criteria (N^{TI}_{pass} or N^{TI}_{fail}) are counted. They can be expressed as:

$$\begin{aligned} N^{TI}_{\mathrm{pass}} =& \epsilon^S_p N^S_{\mathrm{pass}} + \epsilon^B_p N^B_{\mathrm{pass}} \\ N^{TI}_{\mathrm{fail}} =& \epsilon^S_f N^S_{\mathrm{fail}} + \epsilon^B_f N^B_{\mathrm{fail}} \end{aligned} \tag{5.3.4}$$

where ϵ^S_p, ϵ^S_f, ϵ^B_p and ϵ^B_f are the isolation efficiencies for signal and background candidates passing or failing the identification criteria. ϵ^B_p and ϵ^B_f are estimated from a data sample enriched in fake photons. Besides, ϵ^S_p and ϵ^S_f are estimated from MC simulation. Then N^S_{pass}, N^S_{fail}, N^B_{pass} and N^B_{fail} are calculated using the counted numbers and the efficiencies. Therefore the efficiency of photon identification is calculated as $\epsilon_{\mathrm{ID}}=\frac{N^S_{\mathrm{pass}}}{N^S_{\mathrm{pass}}+N^S_{\mathrm{fail}}}$. The main systematic uncertainty is signal leakage into fake photon enriched sample.

Finally the efficiencies from the three measurements are combined and compared to MC simulation as shown in Figure 5.3.2 and 5.3.3.

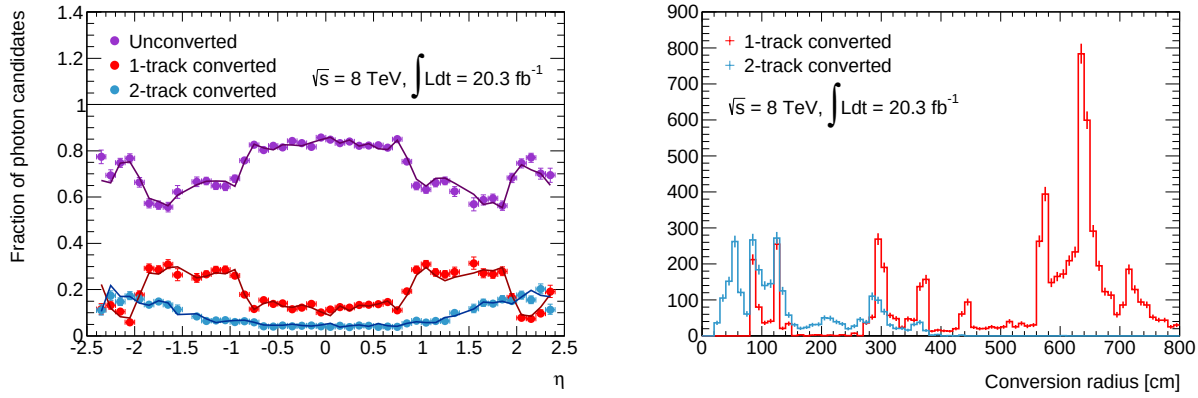

(a) (b)

Figure 5.4.1: Fraction of photon conversion status with η (a). The fraction in data is shown with markers, while that in MC is shown with line. Radius of conversion vertex (b) in $\sqrt{s} = 8$ TeV data.

5.4 Photon conversion fraction

The conversion reconstruction is crucial for primary vertex selection since the selection efficiency is increased by conversion tracks. In addition, it has an impact on photon energy calibration because energy clustering in the EM calorimeter uses two different window sizes according to conversion status of photons.

Figure 5.4.1a shows the fractions of each photon conversion status with η. The fraction of converted photons increases in high η region where the material traversed is large. The fraction of single-track converted photons is not proportional to that of double-track converted photons. When a photon is converted at the more interior than the SCT, the efficiency of double-track conversion reconstruction is higher than that of single-track reconstruction because of a good separation of two conversion tracks (Figure 5.4.1b). Therefore the fractions of double- and single-converted photons depend on material distribution along the radial direction.

The photon conversion fractions also depend on the photon E_{T} as shown in Figure 5.4.2a. This is because a low E_{T} converted photon has low p_{T} conversion tracks, and the efficiency of conversion track reconstruction decrease as the p_{T} of the track decreases. Figure 5.4.2b shows the pileup dependence on the conversion fractions. Even under the high pileup condition, the fractions keep flat. The reconstruction of conversion vertex is robust against pileup. The fractions in data and MC agree well in all the plots, .

5.5 Isolation efficiency estimation

The isolation efficiency for di-photon events is estimated in $H \to \gamma\gamma$ MC samples. The systematic uncertainty of the efficiency is studied with comparing the efficiencies between data and MC in $Z \to ee$ decays where an electron emulates a photon. The performance of track isolation depends on the primary vertex selection efficiency. Hence several algorithms are used for the primary vertex selection in order to estimate the impact of

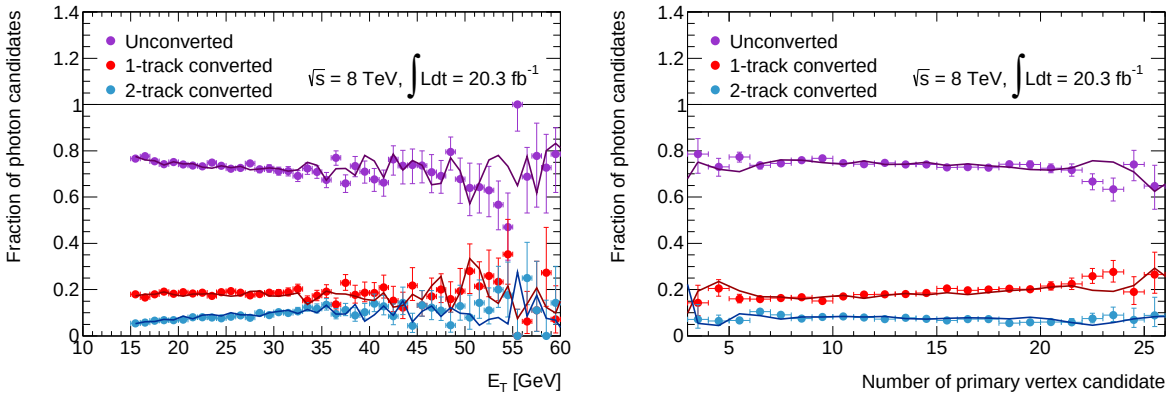

(a) (b)

Figure 5.4.2: The fraction of photon conversion status with photon E_{T} (a) and pileup (b) in $\sqrt{s} = 8$ TeV data. The fraction in data is shown with markers, while that in MC is shown with line.

the efficiency of the primary vertex selection. Figure 5.5.1 shows the efficiency and the uncertainty predicted in $H \to \gamma\gamma$ events. The error bars include systematic uncertainty estimated with $Z \to ee$ events.

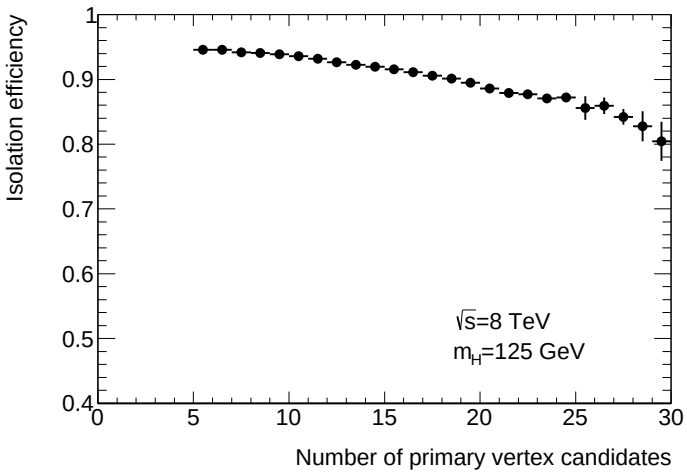

Figure 5.5.1: Isolation efficiency for di-photon in $H \to \gamma\gamma$ MC samples. The error bars include systematic uncertainty.

Chapter 6

Event selection and categorization

6.1 Event selection

Events recorded with di-photon triggers as described in Section 4.2 are used in the analysis. For $\sqrt{s} = 7$ TeV data analysis, the transverse energy (E_{T}) threshold is 20 GeV for leading (the highest E_{T}) and sub-leading (the second highest E_{T}) photons. The thresholds for $\sqrt{s} = 8$ TeV are 35 GeV and 25 GeV for leading photons and sub-leading photons, respectively. The efficiencies of the triggers are about 99 % for events passing the following final event selection.

The offline event selection is summarized in Table 6.1.1. Events are required to have at least 2 photon candidates. The two leading photons are required to pass the neural net identification for $\sqrt{s} = 7$ TeV or cut-based criteria for $\sqrt{s} = 8$ TeV. The E_{T} thresholds are 40 GeV and 30 GeV for the leading and sub-leading photons. Both two photons need to be within the fiducial calorimeter region $|\eta| < 2.37$ with excluding the transition region between the barrel and the endcap calorimeters $1.37 < |\eta| < 1.56$, where the reconstructed efficiency is low, the energy resolution is worse and the fake rate of jet→photon is high. After selecting the two leading photon candidates, the primary vertex is selected with using the photons as described in Section 4.1. The track isolation is calculated with respect to the primary vertex. The η of the photons are corrected with respect to the primary vertex as well. The two photons are required to pass the track and calorimeter isolation criteria in order to reject events having fake photons. The calorimeter isolation $E_{\mathrm{T}cone40}$ is required to be smaller than 4 GeV for $\sqrt{s} = 7$ TeV data. For $\sqrt{s} = 8$ TeV, the requirement of < 2.6 GeV on the track isolation $p_{\mathrm{T}cone20}$ as well as < 6 GeV on the calorimeter isolation are applied. Finally the events in a mass window $100 < m_{\gamma\gamma} < 160$ GeV are selected. The distributions of E_{T}, η, $E_{\mathrm{T}cone40}$ and $p_{\mathrm{T}cone20}$ of the photon candidates are shown in Figure 6.1.1, 6.1.2, 6.1.3 and 6.1.4. The E_{T} distributions in the signal MC have peaks at about $m_H/2$ as well as sharp cut-offs at trigger thresholds. The η distributions in the signal MC are centered compared to the observed data because the Higgs boson is tend to be produced at rest due to the high mass. The observed data has larger transverse energy deposit near the photon than signal MC because of the fake photon contamination.

The number of selected events is 23788 in $\sqrt{s} = 7$ data, 118893 in $\sqrt{s} = 8$ TeV data. The cut flow for $H \to \gamma\gamma$ selection is summarized in Table 6.1.2. Figure 6.1.5 and 6.1.6 show the observed $m_{\gamma\gamma}$ distributions, as well as the expected signal distributions after the event selection. Figure 6.1.7 shows an event display of a di-photon signal candidate. The

	$\sqrt{s} = 7$ TeV analysis	$\sqrt{s} = 8$ TeV analysis
2 photons	At least 2 reconstructed photons	
Pseudo-rapidity	$\|\eta\| < 1.37$ or $1.56 < \|\eta\| < 2.37$	
Transverse energy	$E_{\mathrm{T}} > 40(30)$ GeV for the leading (sub-leading) photons	
Identification	Neural net based	Cut based
Calorimeter isolation	$E_{\mathrm{T}cone40} < 4$ GeV	$E_{\mathrm{T}cone40} < 6$ GeV
Track isolation	-	$p_{\mathrm{T}cone20} < 2.6$ GeV
Mass window (only in data)	$100 < m_{\gamma\gamma} < 160$ GeV	

Table 6.1.1: Event selection for $H \to \gamma\gamma$ analysis.

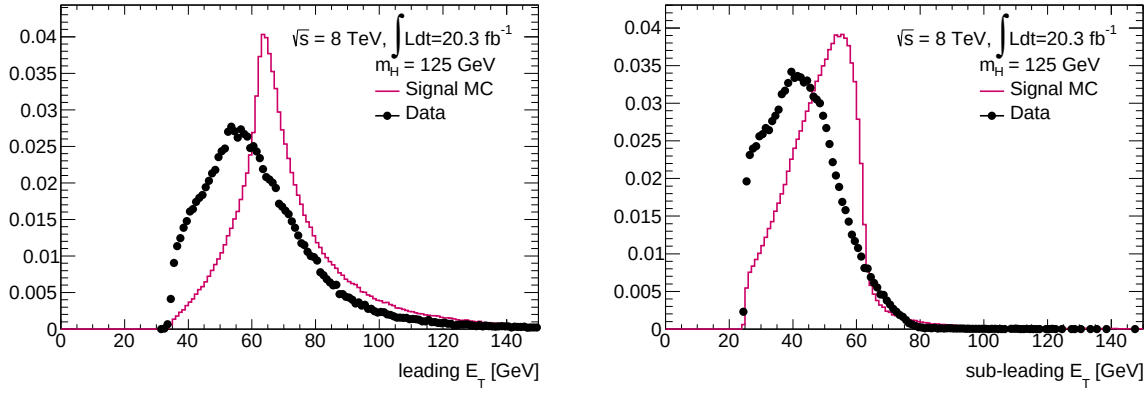

Figure 6.1.1: Distributions of E_{T} of the selected photons in $\sqrt{s} = 8$ TeV data. The sum of histograms are normalized to 1.

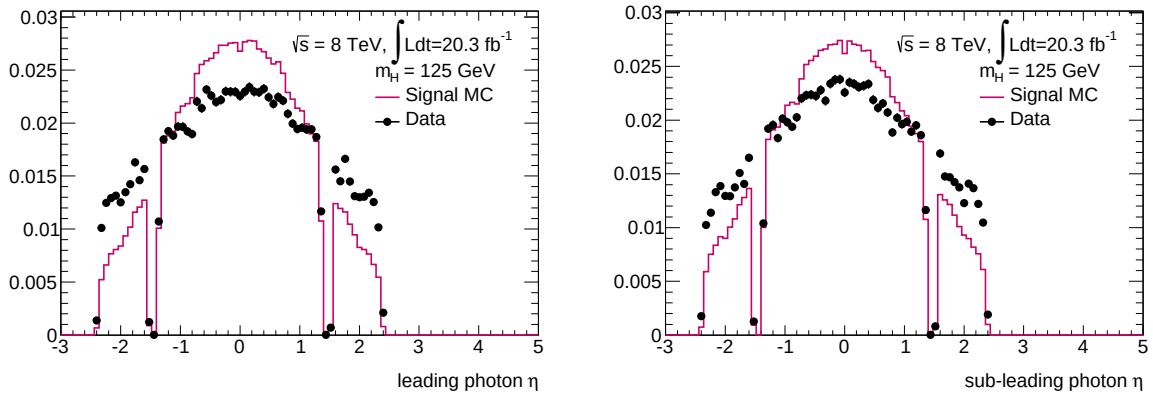

Figure 6.1.2: Distributions of η of the selected photons in $\sqrt{s} = 8$ TeV data. The sum of histograms are normalized to 1.

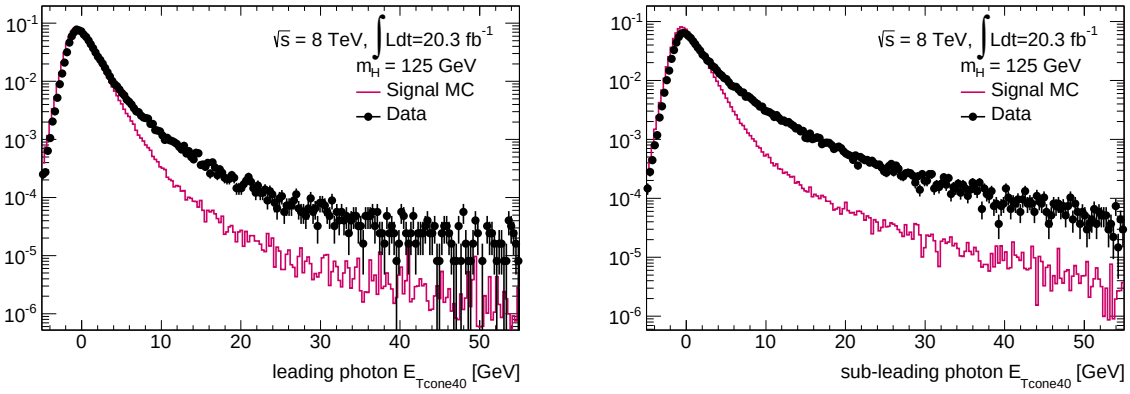

Figure 6.1.3: Distributions of $E_{\mathrm{T}cone40}$ of the selected photons in $\sqrt{s} = 8$ TeV data. The sum of histograms are normalized to 1.

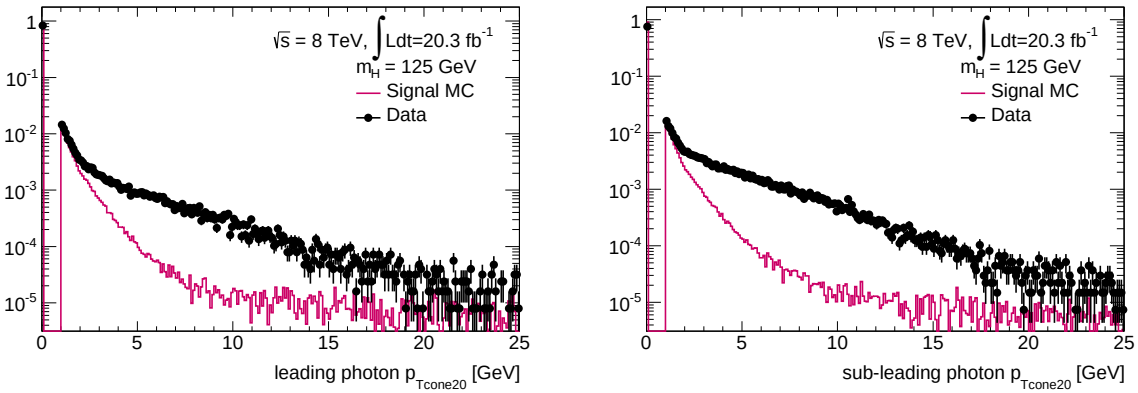

Figure 6.1.4: Distributions of $p_{\mathrm{T}cone20}$ of the selected photons in $\sqrt{s} = 8$ TeV data. The sum of histograms are normalized to 1.

	$\sqrt{s} = 7$ TeV		$\sqrt{s} = 8$ TeV	
	Data	MC	Data	MC
		100 %		100 %
Di-photon Trigger	6459127	69 %	25501602	67 %
Photon reconstruction	1207197	54 %	11907820	51 %
E_{T}	437396	49 %	6550457	48 %
Identification	111699	45 %	675075	42 %
Isolation	66058	41 %	311723	38 %
$m_{\gamma\gamma}$	23788	41 %	118893	38 %

Table 6.1.2: Cut flow for $H \to \gamma\gamma$ selection. The MC simulation for $\sqrt{s} = 7$ TeV is ggF at $m_H = 120$ GeV sample. The MC simulation for $\sqrt{s} = 8$ TeV is ggF at $m_H = 125$ GeV sample. The statistical error of the MC simulation is < 0.1 %.

invariant mass of di-photon in this event is 126.9 GeV. This event contains not only two photons but also two forward jets. The jet selection is described in Section 6.2.1. The information of the event is matched to the feature of VBF process.

6.2 Event categorization

Events are separated into categories, which have different signal-to-background ratios, for the improvement of the sensitivity to the Higgs signal. The selected di-photon events are divided into 10 categories for $\sqrt{s} = 7$ TeV analysis and 14 categories for $\sqrt{s} = 8$ TeV analysis. There are two strategies in the event categorization;

1. The events are divided into categories which have good and bad mass resolutions resulting in high and low signal-to-background ratios.

2. Some categories are designed to have high sensitivity to VBF and VH Higgs production processes.

Based on the first strategy, η and conversion status are used for categorization. Unconverted photons have better energy resolution than converted photons since unconverted photons do not loose the energy in the inner detector. When both photons are unconverted, the mass resolution is 1.8 GeV (r.m.s.), while 2.6 GeV (r.m.s) when both are converted. Similarly photons in low η region have better energy resolution because the amount of material in this region is smaller than high η region. The mass resolution is 1.7 GeV (r.m.s) when both photons are in $|\eta| < 0.6$, and 2.7 GeV (r.m.s) when both are in $1.56 < |\eta| < 2.37$. In addition, the signal to background ratio in the low η region is higher than the high η region. Higgs $p_{\mathrm{T}t}$ is the other parameter for categorization according to the first strategy, which is defined as

$$p_{\mathrm{T}t} \equiv \left| \vec{p}_{\mathrm{T}}^{\,\gamma\gamma} \times \frac{\vec{p}_{\mathrm{T}}^{\,\gamma 1} - \vec{p}_{\mathrm{T}}^{\,\gamma 2}}{\left| \vec{p}_{\mathrm{T}}^{\,\gamma 1} - \vec{p}_{\mathrm{T}}^{\,\gamma 2} \right|} \right| \tag{6.2.1}$$

where $\vec{p}_{\mathrm{T}}^{\,\gamma\gamma}$ is the transverse momentum of di-photon, $\vec{p}_{\mathrm{T}}^{\,\gamma 1}$ and $\vec{p}_{\mathrm{T}}^{\,\gamma 2}$ are the transverse momenta of the two photons, and $\left(\vec{p}_{\mathrm{T}}^{\,\gamma 1} - \vec{p}_{\mathrm{T}}^{\,\gamma 2}\right) / \left|\vec{p}_{\mathrm{T}}^{\,\gamma 1} - \vec{p}_{\mathrm{T}}^{\,\gamma 2}\right|$ denotes the transverse thrust axis.

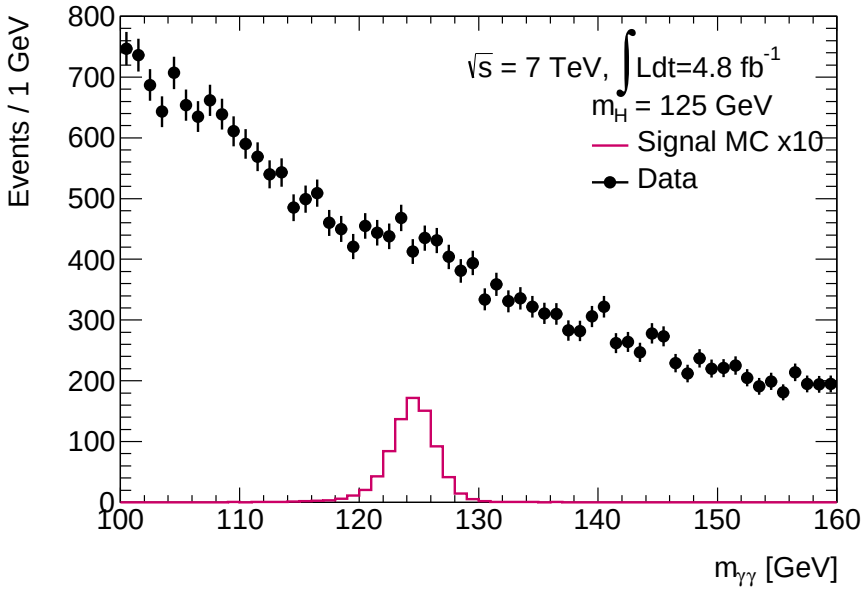

Figure 6.1.5: $m_{\gamma\gamma}$ distributions in $\sqrt{s} = 7$ TeV data. The expected signal distributions ($m_H = 125$ GeV) are shown in the pink histogram.

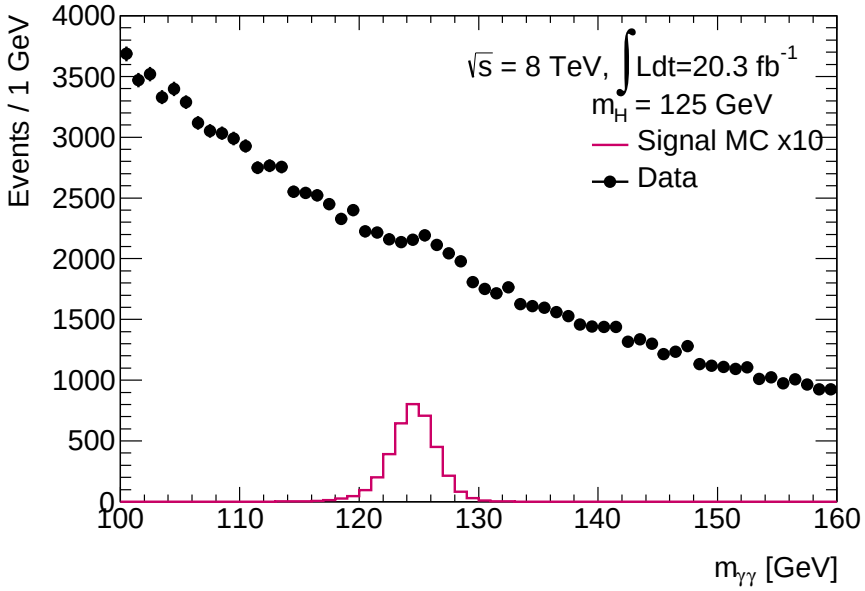

Figure 6.1.6: $m_{\gamma\gamma}$ distributions in $\sqrt{s} = 8$ TeV data. The expected signal distributions ($m_H = 125$ GeV) are shown in the pink histogram.

インターネット公表に関する同意が
得られなかったため非公表

Figure 6.1.7: Event display of a VBF $H \to \gamma\gamma$ candidate, containing two converted photons and two high-mass jets. The event was recorded at $\sqrt{s} = 8$ TeV. The leading photon has $E_{\mathrm{T}} = 80.1$ GeV and $\eta = 1.01$. The sub-leading photon has $E_{\mathrm{T}} = 36.2$ GeV and $\eta = -0.17$. The measured di-photon mass is 126.9 GeV. The p_{T} and $p_{\mathrm{T}t}$ of the di-photon system are 44.3 GeV and 6.2 GeV, respectively. The leading jet has $E_{\mathrm{T}} = 121.6$ GeV and $\eta = -2.90$. The subleasing jet has $E_{\mathrm{T}} = 82.8$ GeV and $\eta = 2.72$. The measured di-jet mass is 1.67 TeV. The $\Delta\phi$ between the di-photon system and the system of the di-jet is 2.90 [91].

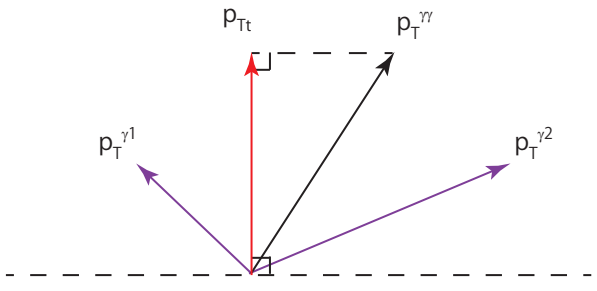

Figure 6.2.1: sketch of $p_{\mathrm{T}t}$

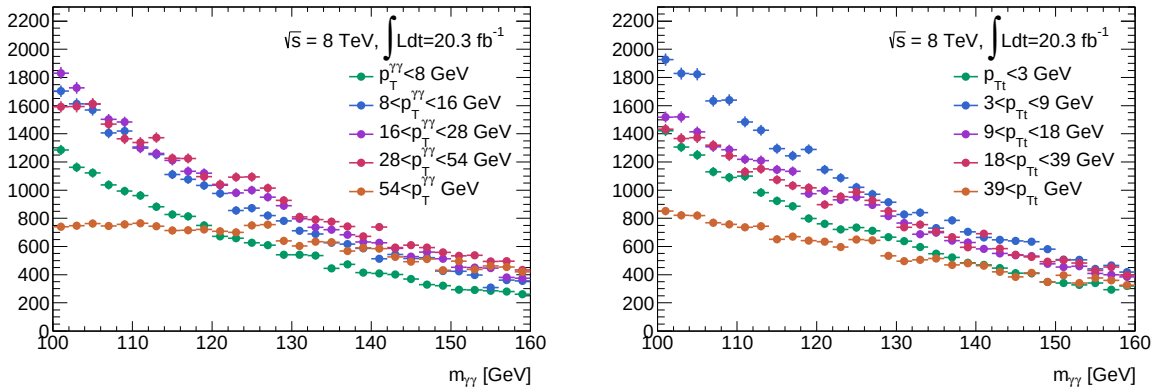

Figure 6.2.2: $m_{\gamma\gamma}$ distributions in different $p_{\mathrm{T}t}$ and $p_{\mathrm{T}}^{\gamma\gamma}$ regions in data

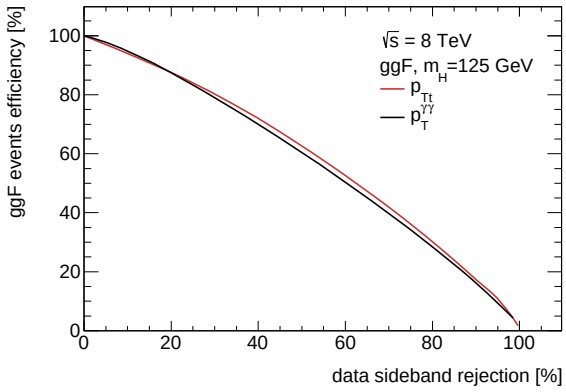

Figure 6.2.3: Separation of ggF signal events and backgrounds. The backgrounds are emulated by data sideband (excluding $m_{\gamma\gamma} \in [120, 130]$ GeV).

Figure 6.2.1 illustrates the $p_{\mathrm{T}t}$. In case $\left(\vec{p}_{\mathrm{T}}^{\,\gamma 1} + \vec{p}_{\mathrm{T}}^{\,\gamma 2}\right) \perp \left(\vec{p}_{\mathrm{T}}^{\,\gamma 1} - \vec{p}_{\mathrm{T}}^{\,\gamma 2}\right)$, $p_{\mathrm{T}t} = p_{\mathrm{T}}^{\gamma\gamma}$. The mean value of $p_{\mathrm{T}}^{\gamma\gamma}$ in the signal MC is 45 GeV, while that in data contaminated by very intense background is 31 GeV. The signal events have higher $p_{\mathrm{T}}^{\gamma\gamma}$ than the background events, hence the $p_{\mathrm{T}}^{\gamma\gamma}$ is also a candidate of parameters for the categorization. With the categorization based on $p_{\mathrm{T}}^{\gamma\gamma}$, $m_{\gamma\gamma}$ distributions are distorted as shown in Figure 6.2.2. On the other hand, the $p_{\mathrm{T}t}$-based categorization does not distort $m_{\gamma\gamma}$, that is a good feature to model the background from data as mentioned in Section 7.2.

Compared with $p_{\mathrm{T}}^{\gamma\gamma}$, $p_{\mathrm{T}t}$ has the same discriminative power as the $p_{\mathrm{T}}^{\gamma\gamma}$ as shown in Figure 7.2. The mean value of $p_{\mathrm{T}t}$ in the signal MC is 30 GeV, while that in data is 19 GeV.

The second strategy requires additional objects associated to some kinds of Higgs production processes. The signature of VBF process is the presence of forwards two jets. Hence two jets are required. In VH ($= WH$ and ZH) process, objects from the vector boson are tagged; leptons, jets and $E_{\mathrm{T}}^{\mathrm{miss}}$. The distinct topologies provide better discrimination against the background events. Taking the second strategy the sensitivity to discovery can be increased. Moreover, the Higgs couplings can be measured for each process due to the enhancement a particular production process.

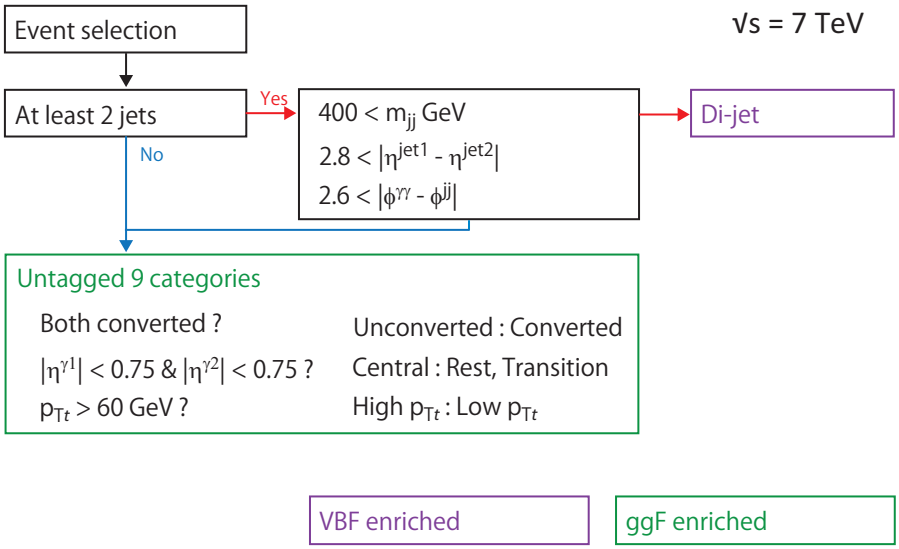

Figure 6.2.4: Flowchart of the event categorization for $\sqrt{s} = 7$ TeV analysis. Selected events are separated into 10 categories.

The ordering of the categorization shown in Figure 6.2.4 and 6.2.5 is applied, since the categories are not completely orthogonal. For $\sqrt{s} = 7$ TeV, the di-jet category is selected for VBF process and remaining events are divided into 9 categories for ggF. For $\sqrt{s} = 8$ TeV analysis, VH enriched categories are selected before the ggF and VBF enriched categories. The object selection which is needed to define the categories is described in the following section.

6.2.1 Object selection

6.2.1.1 Isolated electrons

Electrons are reconstructed by matching tracks in the inner detector to energy clusters in the EM calorimeter as described in Appendix B. The energies of electrons are measured with the EM calorimeter. They are corrected against energy losses in material in front of the EM calorimeter, as well as lateral and longitudinal leakages. For MC, the electron energy is smeared to match the observed m_{ee} resolution of the Z peak. The energy scale of electrons in data is corrected based on the peak position of the Z peak. The directions of electrons are measured with the inner detector. The curvature of electron tracks may be changed by radiative energy losses due to bremsstrahlung. Accordingly, the parameters of tracks (ϕ, d_0) are corrected with Gaussian Sum Fitter (GSF) [94] by which the bremsstrahlung effect is taken into account in the calculation of track parameters. After all corrections, $E_{\mathrm{T}} > 15$ GeV and $|\eta| < 2.47$ are required. Electron identification is performed based on the shower shapes of the EM calorimeter and track quality. Electron candidates are requires to be isolated from other tracks and from other clusters in the calorimeter. The isolation parameters $E_{\mathrm{T}cone40}$ and $p_{\mathrm{T}cone20}$ are calculated in the same way as photons. $E_{\mathrm{T}cone40}/E_{\mathrm{T}} < 0.2$ and $p_{\mathrm{T}cone20} < 0.15$ are required. Electron separation from the leading two photons is required to be $\Delta R > 0.4$.

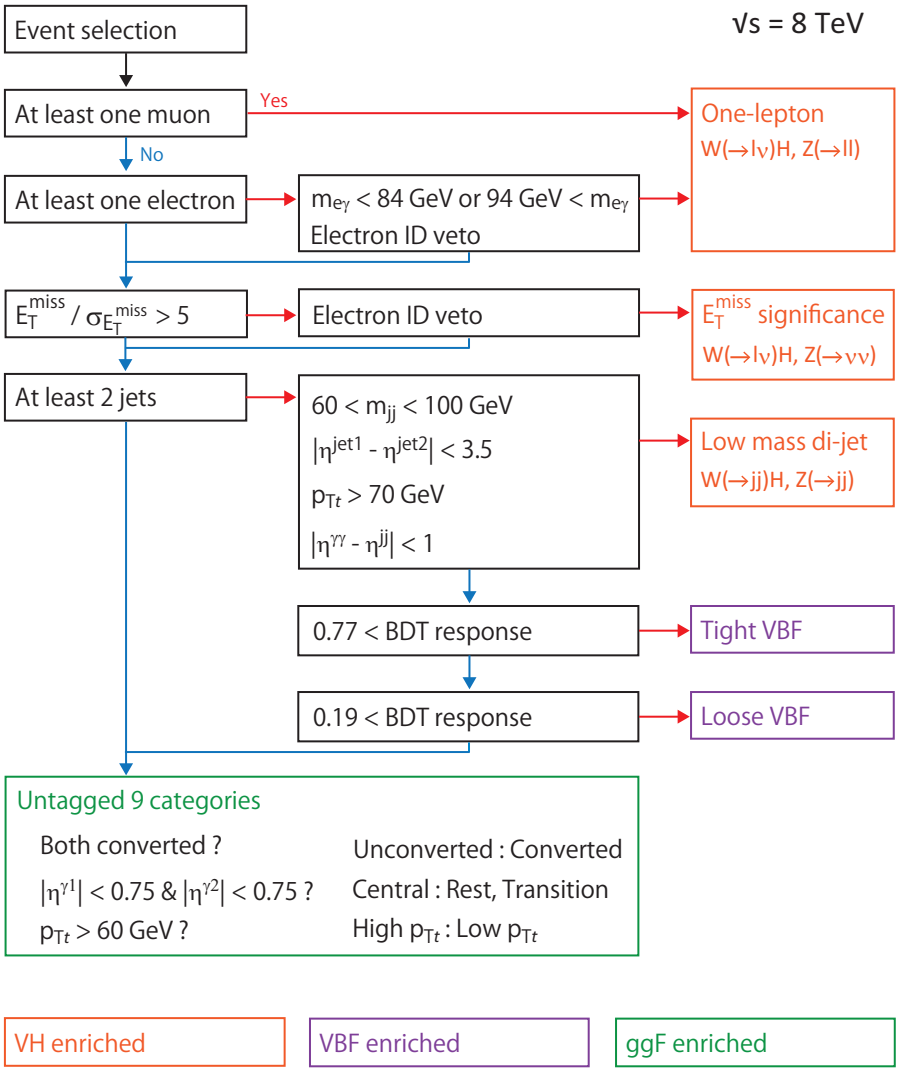

Figure 6.2.5: Flowchart of the event categorization for $\sqrt{s} = 8$ TeV analysis. Selected events are separated into 14 categories.

6.2.1.2 Isolated muons

Tracks reconstructed in the muon spectrometer are muon candidates, which are required to be $|\eta| < 2.7$. In the region covered by the inner detector ($|\eta| < 2.5$), muon candidates are required to be reconstructed from tracks in the inner detector and the muon spectrometer. In the forward region ($2.5 < |\eta| < 2.7$), they are reconstructed from the muon spectrometer alone as described in Appendix C. The momentum scale and resolution corrections are derived from the $Z \to \mu\mu$ candidates in data. A transverse momentum $p_{\mathrm{T}} > 10$ GeV is required. Identification criteria are based on track quality. The impact parameters with respect to the primary vertex d_0 and z_0 are required to be $|d_0| < 1$ mm and $|z_0| < 10$ mm. The isolation cuts $p_{\mathrm{T}cone20}/p_{\mathrm{T}} < 0.15$ and $E_{\mathrm{T}cone40}/p_{\mathrm{T}} < 0.2$ are applied. Muon candidates must be separated from the photons and reconstructed jets by $\Delta R > 0.4$.

6.2.1.3 Jets

Jets are reconstructed with energy clusters in the hadronic and EM and calorimeters using anti-k_{T} algorithm [95] with a cone size $R = 0.4$ as described in Appendix D. Then $p_{\mathrm{T}} > 25$ GeV and $|\eta| < 4.5$ are required. The jet candidates are contaminated by low p_{T} pileup jets especially in high η region. Accordingly, $p_{\mathrm{T}} > 30$ GeV is required in $2.4 < |\eta| < 4.5$ for $\sqrt{s} = 8$ TeV analysis. In addition, Jet Vertex Fraction (JVF) cut is applied to reduce pileup jets (Appendix D). JVF > 0.5 (0.25) is required for $\sqrt{s} = 7$ (8) TeV analysis.

6.2.1.4 Missing transverse energy ($E_{\mathrm{T}}^{\mathrm{miss}}$)

Missing transverse energy $E_{\mathrm{T}}^{\mathrm{miss}}$ is reconstructed by object-based algorithm. All photon, electron and muon candidates and all jets after overlap removal, and all calorimeter clusters not associated to such objects are used for calculation of $E_{\mathrm{T}}^{\mathrm{miss}}$. The last object is called *CellOut*. The other objects (photons, electrons, muons and jets) used are exactly the same as objects defined before. The $E_{\mathrm{T}}^{\mathrm{miss}}$ is defined as:

$$E_{\mathrm{T}}^{\mathrm{miss}} \equiv -\left| \sum_{\mathrm{photon}} \vec{p}_{\mathrm{T}}^{\,\mathrm{photon}} + \sum_{\mathrm{electron}} \vec{p}_{\mathrm{T}}^{\,\mathrm{electron}} + \sum_{\mathrm{muon}} \vec{p}_{\mathrm{T}}^{\,\mathrm{muon}} + \sum_{\mathrm{jet}} \vec{p}_{\mathrm{T}}^{\,\mathrm{jet}} + \sum_{\mathrm{CellOut}} \vec{p}_{\mathrm{T}}^{\,\mathrm{CellOut}} \right| \quad (6.2.2)$$

The $E_{\mathrm{T}}^{\mathrm{miss}}$ significance is defined as the ratio between $E_{\mathrm{T}}^{\mathrm{miss}}$ and the resolution of $E_{\mathrm{T}}^{\mathrm{miss}}$ ($E_{\mathrm{T}}^{\mathrm{miss}}/\sigma_{E_{\mathrm{T}}^{\mathrm{miss}}}$) where $\sigma_{E_{\mathrm{T}}^{\mathrm{miss}}}$ is the resolution. $\sigma_{E_{\mathrm{T}}^{\mathrm{miss}}}$ can be parametrized as $\sigma_{E_{\mathrm{T}}^{\mathrm{miss}}} = k\sqrt{\sum E_{\mathrm{T}}}$, where $\sum E_{\mathrm{T}}$ is a scalar sum of p_{T} of all objects except muons. The factor k is obtained from $Z \to \mu\mu$ events, where no genuine $E_{\mathrm{T}}^{\mathrm{miss}}$ is expected. The resulting value is $k = 0.67$ [GeV$^{1/2}$] [96]. Due to the jet energy resolution, $E_{\mathrm{T}}^{\mathrm{miss}}$ can be overestimated in multi-jet events. The $E_{\mathrm{T}}^{\mathrm{miss}}$ significance allows higher rejection of the fake $E_{\mathrm{T}}^{\mathrm{miss}}$ events than $E_{\mathrm{T}}^{\mathrm{miss}}$. Therefore the $E_{\mathrm{T}}^{\mathrm{miss}}$ significance is used for categorization instead of $E_{\mathrm{T}}^{\mathrm{miss}}$.

6.2.2 *VH* enriched categories ($\sqrt{s} = 8$ TeV)

VH candidates are selected first in the categorization for $\sqrt{s} = 8$ TeV data as shown in Figure 6.2.5.

	$W(\to e\nu)H$	$W(\to \mu\nu)H$	$W(\to \tau\nu)H$
At least one lepton	72.3 %	80.7 %	15.3 %
$m_{e\gamma} < 84$ and $94 < m_{e\gamma}$	70.1 %	80.7 %	14.9 %
Electron ID veto	58.6 %	80.7 %	13.5 %

Table 6.2.1: Efficiency in the one-lepton category for $W(\to \ell\nu)H$ events at $m_H = 125$ GeV.

	$Z(\to ee)H$	$Z(\to \mu\mu)H$	$Z(\to \tau\tau)H$	data (sideband)
At least one lepton	92.7 %	94.1 %	23.6 %	0.21 %
$m_{e\gamma} < 84$ and $94 < m_{e\gamma}$	85.1 %	94.1 %	22.8 %	0.17 %
Electron ID veto	70.3 %	94.1 %	22.1 %	0.12 %

Table 6.2.2: Efficiency of the one-lepton category for$Z(\to \ell\ell)H$ events at $m_H = 125$ GeV and data sideband (excluding $m_{\gamma\gamma} \in [120, 130]$ GeV) which emulate backgrounds.

6.2.2.1 One-lepton category

At least one electron or muon is required for lepton(s) from the leptonic decay of Z or W boson. One of the considerable background in electron channel is $Z \to ee\gamma$ events where one of the electrons fakes a photon. In case of the FSR ($Z(\to ee\gamma)$) events, $m_{ee\gamma} = m_Z \neq m_H$, thus the FSR events are rejected by mass window cut ($100 < m_{\gamma\gamma} < 160$ GeV). On the other hand, the ISR events ($Z(\to ee)\gamma$) can be background because of $m_{ee} = m_Z$ and $m_{ee\gamma} > m_Z$. If an electron fakes a photon in an ISR $Z(\to ee)\gamma$ event, $m_{e\gamma} = m_Z$, where γ is one of the selected photons. In order to reject the ISR $Z(\to ee)\gamma$ background, $m_{e\gamma} < 84$ or $94 < m_{e\gamma}$ GeV are required. The ISR $Z(\to ee)\gamma$ background is also removed from the category by vetoing events if one of the selected two photons passes the electron identification (*Electron ID veto*). For muon channel, the rate that a muons fakes photon is so small that no additional cut is needed. The dominant backgrounds after the categorization are $Z\,(\to ee)\,\gamma$ and $\gamma\gamma$+fake lepton events.

The category selection efficiencies are summarized in Table 6.2.1 and 6.2.2. The efficiency is a fraction whose numerator is the number of events passing the event selection. The p_{T}, $m_{e\gamma}$ and $m_{\mu\gamma}$ distributions when at least one lepton is required are shown in Figure 6.2.6. The data sideband, which is defined by $100 < m_{\gamma\gamma} < 120$ GeV or $130 < m_{\gamma\gamma} < 160$ GeV, is used to check background contributions. In $m_{e\gamma}$ distributions, Z peak from ISR $Z\gamma$ background is seen. This background is removed by $m_{e\gamma}$ selection. Z peak is not seen in $m_{\mu\gamma}$ distributions because the $\mu \to \gamma$ fake rate is quite lower than the $e \to \gamma$ fake rate.

6.2.2.2 $E_{\mathrm{T}}^{\mathrm{miss}}$ significance category

In order to select $W(\to \ell\nu)H$ and $Z(\to \nu\nu)H$ events, the $E_{\mathrm{T}}^{\mathrm{miss}}$ significance is used for the event categorization: $E_{\mathrm{T}}^{\mathrm{miss}}/\sigma_{E_T^{\mathrm{miss}}} > 5$ is required. The electron ID veto is applied to reject electroweak backgrounds particularly $W(\to e\nu)\gamma$ background events where the electron fakes a photon. $E_{\mathrm{T}}^{\mathrm{miss}}/\sigma_{E_{\mathrm{T}}^{\mathrm{miss}}}$ distribution in $Z(\to \nu\nu)H$ and $W(\to \ell\nu)H$ are shown in Figure 6.2.7. The distributions of ggF and data sideband look similar in low $E_{\mathrm{T}}^{\mathrm{miss}}$ region because no genuine $E_{\mathrm{T}}^{\mathrm{miss}}$ is expected in these events. After the event categorization, the electroweak background dominates [91]. Table 6.2.3 shows the categorization efficiencies in the VH events.

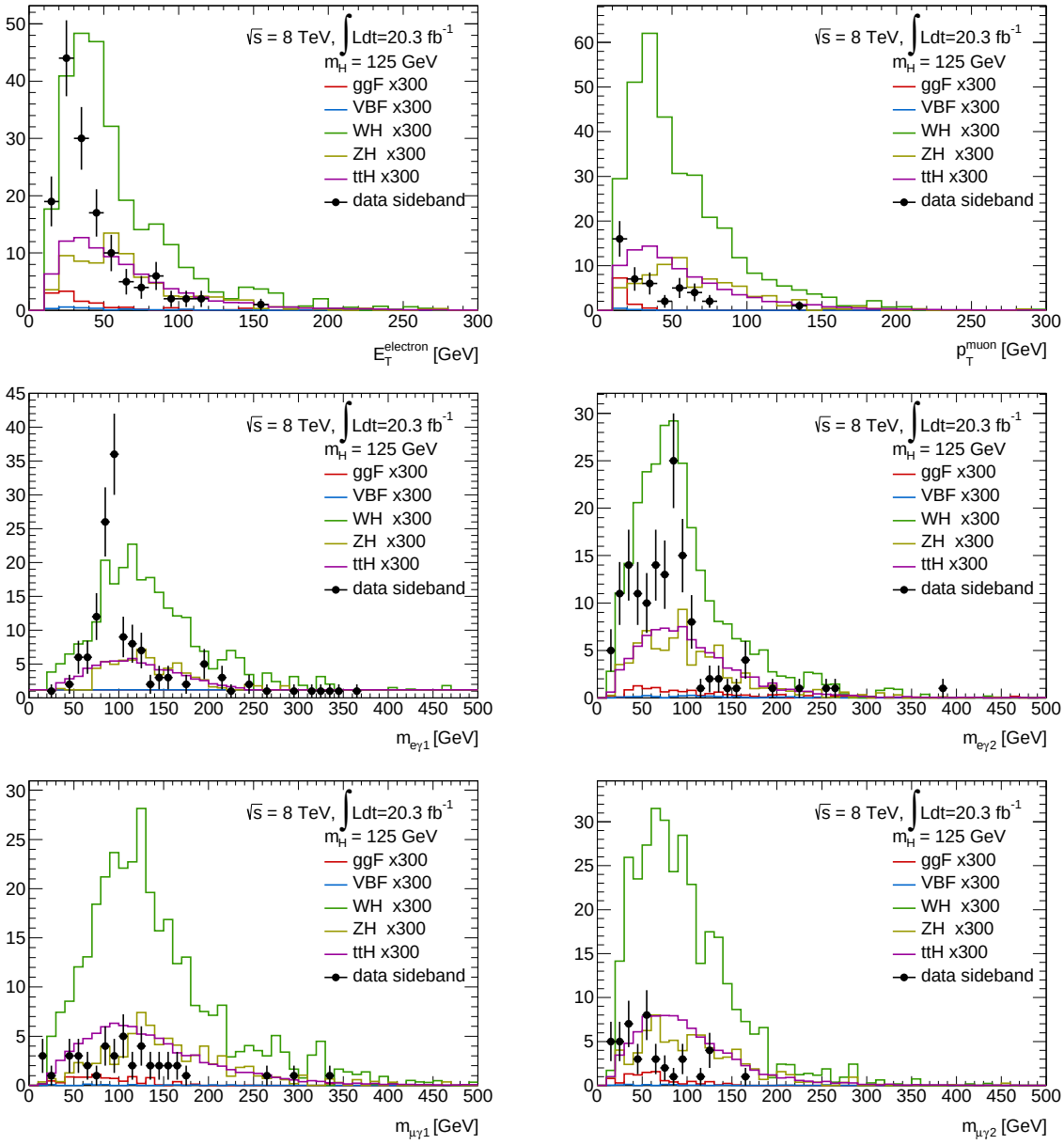

Figure 6.2.6: Distributions of lepton variables when at least one lepton is required after event selection. The signal distributions are separately for different production process. The backgrounds are emulated by data sideband (excluding $m_{\gamma\gamma} \in [120, 130]$ GeV).

	$W(\to e\nu)H$	$W(\to \mu\nu)H$	$W(\to \tau\nu)H$	$Z(\to \nu\nu)H$	data (sideband)
Category ordering	41.4 %	19.3 %	86.5 %	100 %	99.9 %
$E_{\mathrm{T}}^{\mathrm{miss}}/\sigma_{E_{\mathrm{T}}^{\mathrm{miss}}} > 5$	8.2 %	4.7 %	26.9 %	46.0 %	0.07 %
Electron ID veto	7.2 %	4.7 %	25.9 %	43.8 %	0.06 %

Table 6.2.3: Efficiency of the $E_{\mathrm{T}}^{\mathrm{miss}}$significance category for $W(\to \ell\nu)H$ and $Z(\to \nu\nu)H$ events at $m_H = 125$ GeV and data sideband (excluding $m_{\gamma\gamma} \in [120, 130]$ GeV) which emulate backgrounds. Before the $E_{\mathrm{T}}^{\mathrm{miss}}$significance categorization, the one-lepton categorization is performed. The efficiency from event selection to the one-lepton categorization is shown in *Category ordering*.

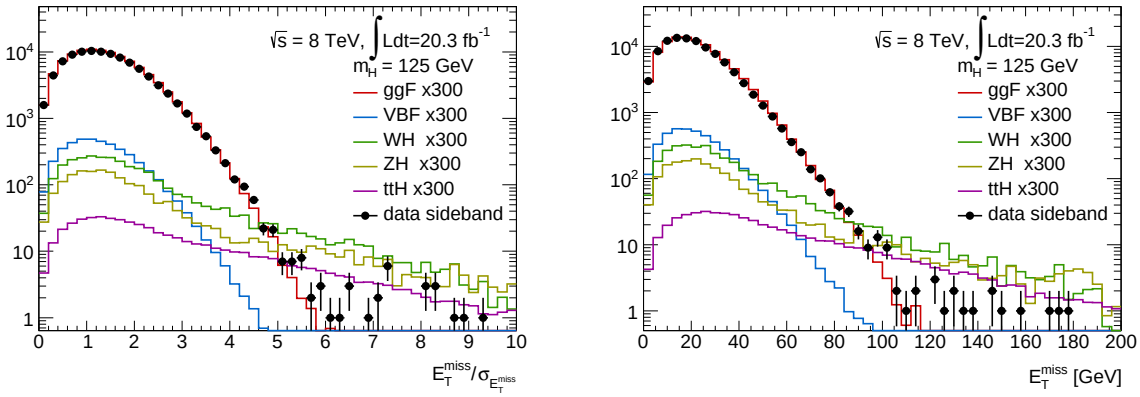

Figure 6.2.7: Distributions of MET variables after event selection. The signal distributions are separately for different production process. The backgrounds are emulated by data sideband (excluding $m_{\gamma\gamma} \in [120, 130]$ GeV).

	$W(\to \text{hadrons})H$	$Z(\to \text{hadrons})H$	data (sideband)
Category ordering	100 %	99.7 %	99.8 %
At least 2 jets	68.2 %	70.4 %	16.7 %
$60 < m_{jj} < 100$ GeV	39.4 %	35.1 %	3.6 %
$\left\|\eta^{\text{jet1}} - \eta^{\text{jet2}}\right\| < 3.5$	39.4 %	35.1 %	3.6 %
$p_{\text{T}t} > 70$ GeV	17.0 %	13.2 %	0.55 %
$\left\|\eta^{\gamma\gamma} - \eta^{\text{jj}}\right\| < 1$	13.0 %	10.5 %	0.23 %

Table 6.2.4: Efficiency of the low mass di-jet category for $W(\to \text{hadrons})H$ and $Z(\to \text{hadrons})H$ events at $m_H = 125$ GeV and data sideband (excluding $m_{\gamma\gamma} \in [120, 130]$ GeV) which emulate backgrounds.

6.2.2.3 Low mass di-jet category

Events with hadronic decaying vector bosons are selected by requiring the presence of two reconstructed jets. The main background in this category is QCD events ($\gamma\gamma$+di-jet). In order to separate the VH events from the QCD background, some additional cuts are applied. The di-jet mass is required to reconstruct Z or W mass; $60 < m_{jj} < 100$ GeV. In the $\gamma\gamma$+di-jet backgrounds, t-channel which have large pseudo-rapidity gap largely contributes. In contrast with the VH events, the di-jet is produced in decay of a vector boson with momentum of ~ 250 GeV in average. Hence the difference of η between the jets from Z or W tend to be smaller than non-resonance $\gamma\gamma$+di-jet backgrounds. Thus $\left|\eta^{\text{jet1}} - \eta^{\text{jet2}}\right| < 3.5$ is required. When produced with a vector boson, the Higgs boson can be boosted. This leads to a higher di-photon $p_{\text{T}t}$. Therefore $p_{\text{T}t} > 70$ GeV is required. The difference between η of the di-photon system and the di-jet system ($\left|\eta^{\gamma\gamma} - \eta^{\text{jj}}\right|$) is small in the VH events as shown in Figure 6.2.8. The threshold is optimized as $\left|\eta^{\gamma\gamma} - \eta^{\text{jj}}\right| < 1$. The categorization efficiencies are summarized in Table 6.2.4. Figure 6.2.8 shows the distributions of variables for the low mass di-jet category when the di-jet is selected. The m_{jj} histograms in WH and ZH have W and Z peak as expected. The distributions of m_{jj} and $p_{\text{T}t}$ have peaks around 80 GeV. Their peak positions are determined by kinematic selection criteria. The $\gamma\gamma$+di-jet is the dominant background after the event categorization.

6.2.3 VBF enriched categories ($\sqrt{s} = 7$ and 8 TeV)

One category is defined for VBF events for $\sqrt{s} = 7$ TeV and two categories for $\sqrt{s} = 8$ TeV. VBF process leads to forward two jets with large pseudo-rapidity gap ($\left|\eta^{\text{jet1}} - \eta^{\text{jet2}}\right|$). The invariant mass of di-jet m_{jj} is larger as the gap bigger as shown in Figure 6.2.9. $|\phi^{\gamma\gamma} - \phi^{jj}|$ is used for the categorization because Higgs boson and the di-jet are back-to-back in transverse plane. The main background is QCD events such as $\gamma\gamma$+di-jet.

6.2.3.1 VBF category for $\sqrt{s} = 7$ TeV analysis

As shown in Figure 6.2.4, events for the VBF category is selected first in $\sqrt{s} = 7$ TeV analysis. After two jets are selected, $m_{jj} > 400$ GeV, $\left|\eta^{\text{jet1}} - \eta^{\text{jet2}}\right| > 2.8$ and $|\phi^{\gamma\gamma} - \phi^{jj}| > 2.6$ are required. Table 6.2.5 shows the selection efficiency for VBF events for $\sqrt{s} = 7$ TeV

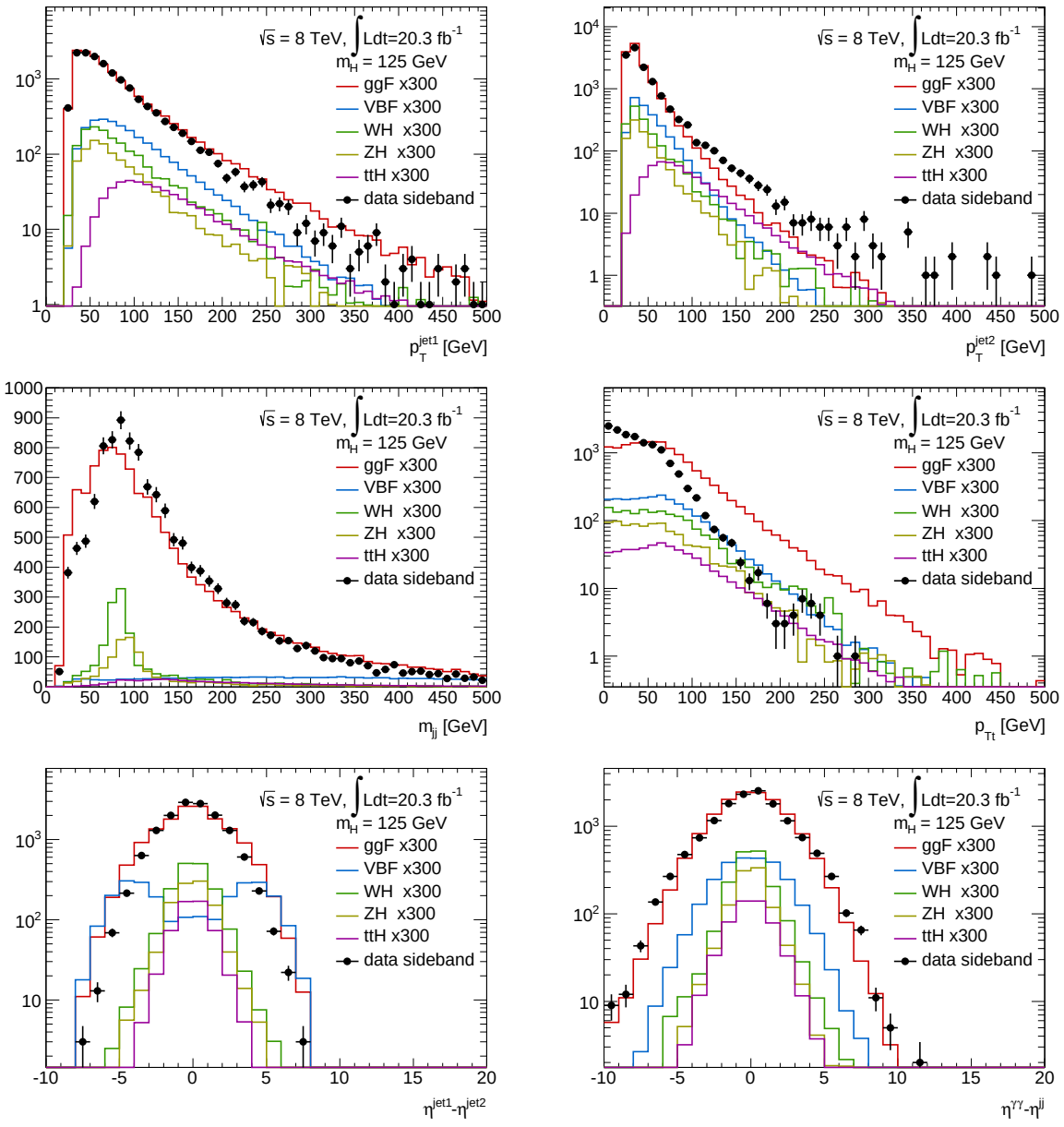

Figure 6.2.8: Distributions of variables used for low mass di-jet category when di-jet is required after event selection. The signal distributions are separately for different production process. The backgrounds are emulated by data sideband (excluding $m_{\gamma\gamma} \in [120, 130]$ GeV).

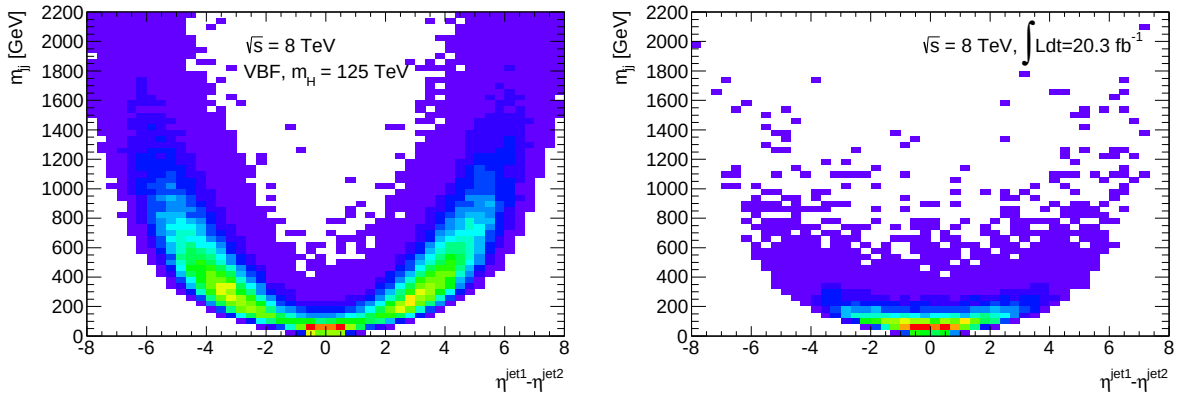

Figure 6.2.9: Correlation between $\eta^{\text{jet1}} - \eta^{\text{jet2}}$ and m_{jj} in VBF events (left) and in data sideband(excluding $m_{\gamma\gamma} \in [120, 130]$ GeV) (right) for $\sqrt{s} = 8$ TeV.

	VBF	data (sideband)
At least 2 jets	56.7 %	12.2 %
$400 < m_{jj}$ GeV	32.0 %	0.92 %
$2.8 < \left\|\eta^{\text{jet1}} - \eta^{\text{jet2}}\right\|$	31.1 %	0.63 %
$2.6 < \left\|\phi^{\gamma\gamma} - \phi^{jj}\right\|$	28.9 %	0.37 %

Table 6.2.5: The categorization efficiency of the high mass di-jet category for VBF events at $m_H = 125$ GeV and data sideband (excluding $m_{\gamma\gamma} \in [120, 130]$ GeV) which emulate backgrounds for $\sqrt{s} = 7$ TeV.

analysis. The distributions of the variables used for the high mass di-jet categorization are shown in Figure 6.2.10.

6.2.3.2 VBF categories for $\sqrt{s} = 8$ TeV analysis

A multivariate analysis is performed to defined two VBF categories. Multivariate analysis is suitable in case that discriminant variables are highly correlated with each other. In VBF events, jets and photons kinetic quantities are correlated (e.g. correlation between $\left|\eta^{\text{jet1}} - \eta^{\text{jet2}}\right|$ and m_{jj} as shown in Figure 6.2.9), hence the multivariate analysis can separate VBF events from backgrounds better than cut-based selection. Input variables are required to have little correlation with $m_{\gamma\gamma}$ in order to avoid bias from the mass of training sample. Eight variables are used to build a boosted decision tree (BDT) [97]: $p_{\text{T}t}$, m_{jj}, $\left|\eta^{\text{jet1}} - \eta^{\text{jet2}}\right|$, $\left|\phi^{\gamma\gamma} - \phi^{jj}\right|$, η^{jet1}, η^{jet2}, $\eta^{\star} \equiv \left|\eta^{\gamma\gamma} - \left(\eta^{\text{jet1}} + \eta^{\text{jet2}}\right)/2\right|$ and the minimum ΔR between one of the photons and one of the two leading jets ($\Delta R^{\gamma j}_{\text{min}}$). Some distributions of the input variables are shown in Figure 6.2.11, while other distributions are already shown in Figure 6.2.8.

The BDT is trained with MC samples. The input signal sample is a VBF sample with $m_{\gamma\gamma} = 125$ GeV. The input background samples are di-photon sample generated with SHERPA, while the photon-jet and the di-jet components are emulated by a control region in data. The control region is defined that one of the two photon candidates fails the isolation criteria. Each component is weighted according to the background composition measured in data. The BDT responses are shown in Figure 6.2.12.

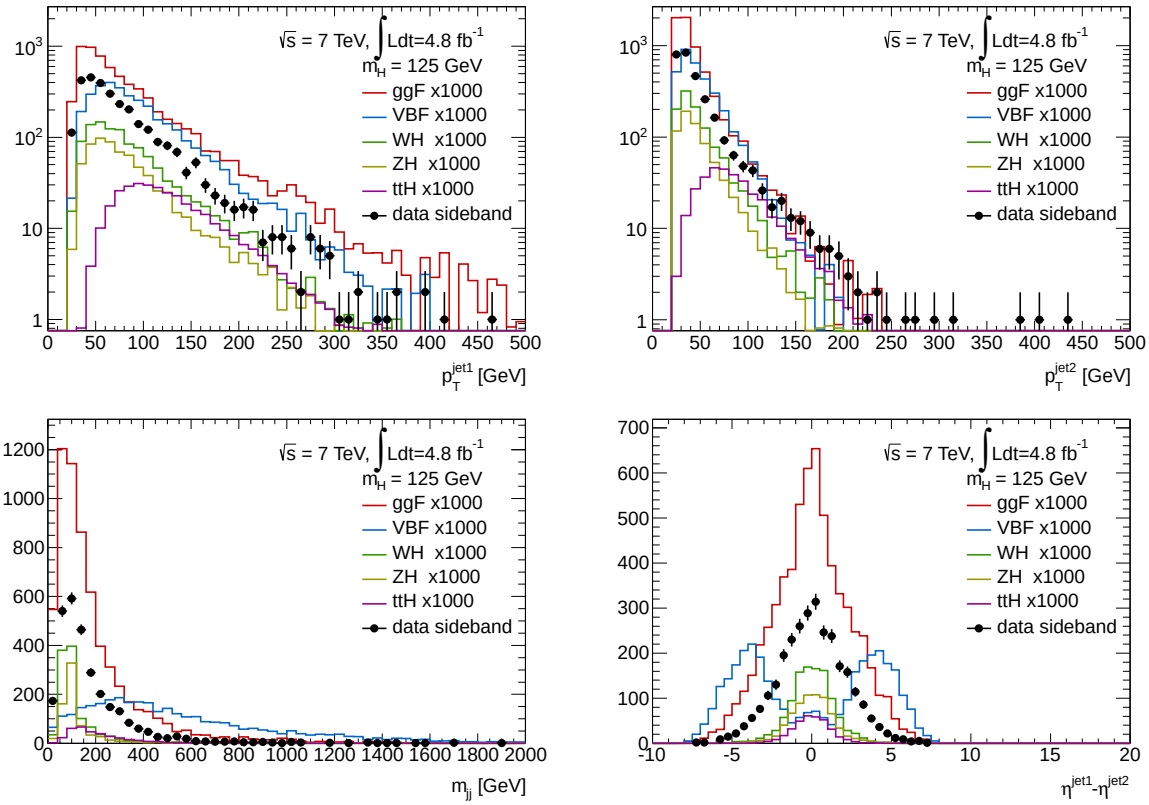

Figure 6.2.10: Distributions of variables used for high mass di-jet category for $\sqrt{s} = 7$ TeV when di-jet is required after event selection. The signal distributions are separately for different production process. The backgrounds are emulated by data sideband (excluding $m_{\gamma\gamma} \in [120, 130]$ GeV).

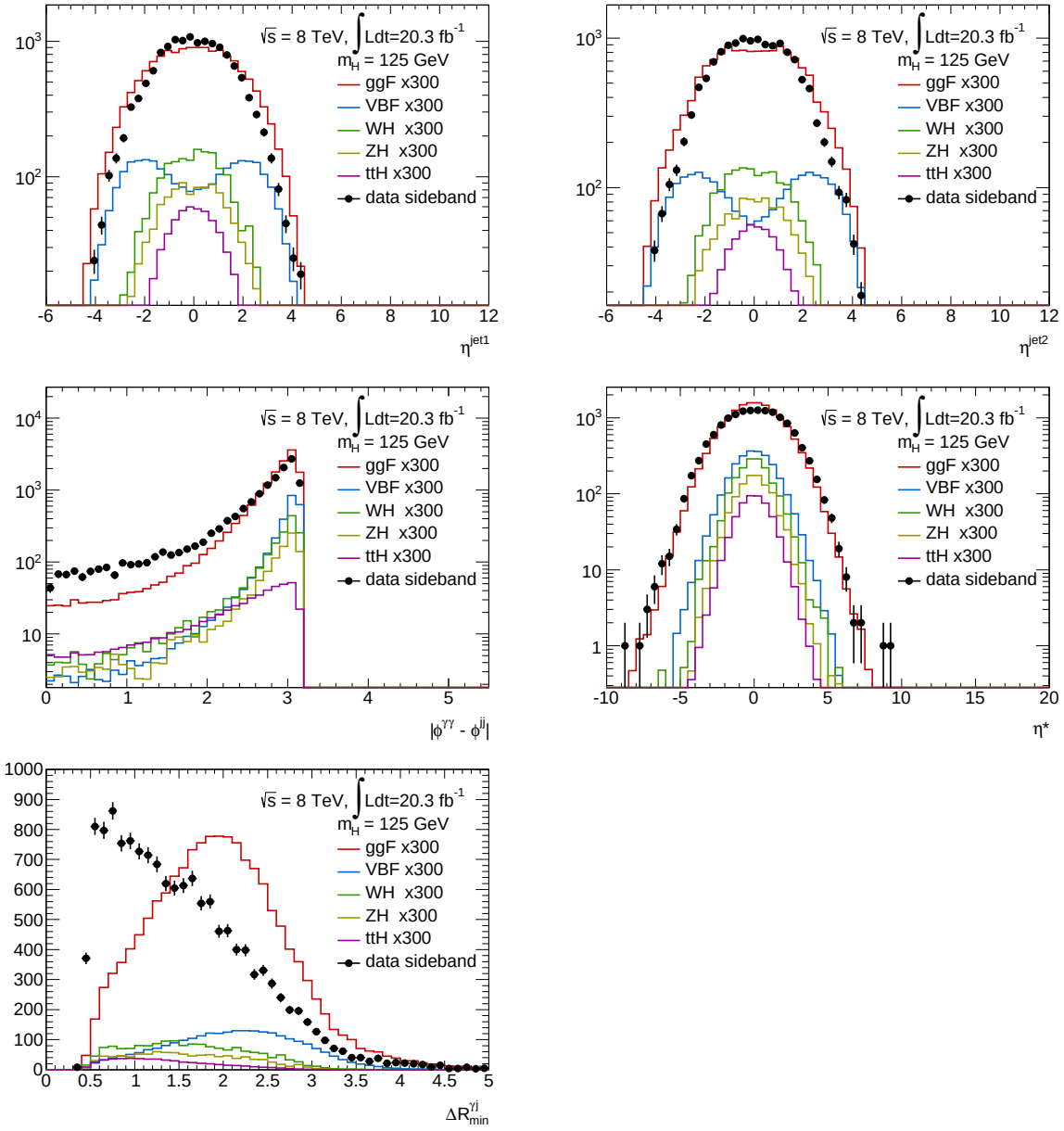

Figure 6.2.11: Distributions of variables used for high mass di-jet category for $\sqrt{s} = 8$ TeV when di-jet is required after event selection. $p_{\mathrm{T}t}$, m_{jj} and $\left|\eta^{\mathrm{jet1}} - \eta^{\mathrm{jet2}}\right|$ distributions are already shown in Figure 6.2.8. The signal distributions are separately for different production process. The backgrounds are emulated by data sideband (excluding $m_{\gamma\gamma} \in [120, 130]$ GeV).

インターネット公表に関する同意がインターネット公表に関する同意が得られなかったため非公表　　得られなかったため非公表

Figure 6.2.12: The output of the BDT for VBF categorization when applied to data sideband (excluding $m_{\gamma\gamma} \in [120, 130]$ GeV) and to the expected background (left). The BDT output when applied to signal samples and the expected background, normalized to unity (right) [91].

	VBF	data (sideband)
Category ordering	99.6 %	99.5 %
At least 2 jets	59.9 %	16.5 %
$0.19 <$ BDT response	31.4 %	0.49 %
$0.77 <$ BDT response	21.5 %	0.17 %

Table 6.2.6: Efficiency of the high mass di-jet category for VBF events at $m_H = 125$ GeV and data sideband (excluding $m_{\gamma\gamma} \in [120, 130]$ GeV) which emulate backgrounds for $\sqrt{s} = 8$ TeV.

The two high mass di-jet categories are defined for $\sqrt{s} = 8$ TeV analysis as:

- *Tight VBF* category: $0.77 <$ BDT response
- *Loose VBF* category: $0.19 <$ BDT response < 0.77

Table 6.2.6 shows the efficiency of the high mass di-jet categories.

6.2.4 Untagged categories

The remaining events are divided into nine categories for ggF events. No additional objects are required but $p_{\mathrm{T}t}$, η and conversion status are used for categorization in these categories. When both photon candidates are unconverted photons, an event is called *unconverted*, otherwise called *converted*. An event is called *central* when both photon candidates are within $|\eta| < 0.75$, otherwise *rest*. The events are classified by whether the events have $p_{\mathrm{T}t} > 60$ GeV (*high* $p_{\mathrm{T}t}$), or not (*low* $p_{\mathrm{T}t}$). The distribution of $p_{\mathrm{T}t}$ is shown in Figure 6.2.13.

When a *converted* event has at least one photon candidate in$1.3 < |\eta| < 1.75$, the event is categorized as *converted transition*. Because the energy resolution for converted photons in this region is degraded due to large amount of material in front of the EM calorimeter, no $p_{\mathrm{T}t}$ cut is applied to the *converted transition* events. Figure 6.2.14 illustrates η regions for the untagged categories.

Table 6.2.7 summarizes the fraction of the untagged categories for ggF events in the nine untagged categories. The mass resolutions of each category are estimated in the following chapter.

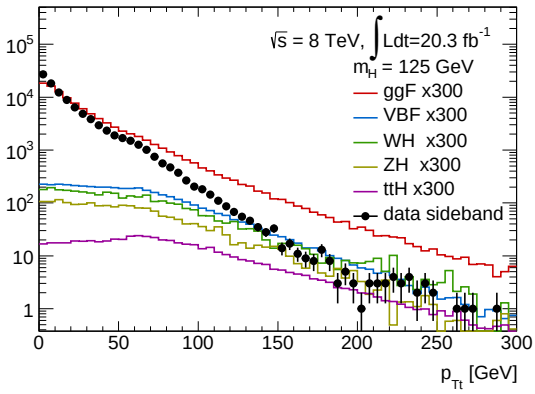

Figure 6.2.13: $p_{\mathrm{T}t}$ distribution after event selection.

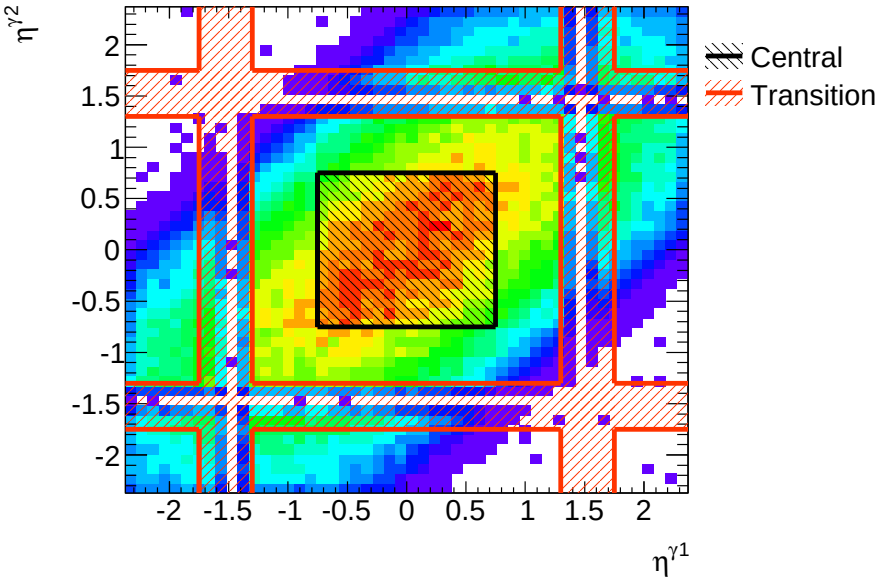

Figure 6.2.14: η regions for the untagged categories.

Category	Fraction of ggF sample	Fraction in data sideband
Unconverted central, low $p_{\mathrm{T}t}$	14.1 %	10.5 %
Unconverted central, high $p_{\mathrm{T}t}$	2.1 %	1.2 %
Unconverted rest, low $p_{\mathrm{T}t}$	29.1 %	29.9 %
Unconverted rest, high $p_{\mathrm{T}t}$	4.0 %	3.5 %
Converted central, low $p_{\mathrm{T}t}$	9.0 %	7.2 %
Converted central, high $p_{\mathrm{T}t}$	1.3 %	0.8 %
Converted rest, low $p_{\mathrm{T}t}$	26.3 %	29.8 %
Converted rest, high $p_{\mathrm{T}t}$	3.5 %	3.4 %
Converted transition	10.6 %	13.6 %

Table 6.2.7: Fraction of the untagged categories for ggF events at $m_H = 125$ GeV.

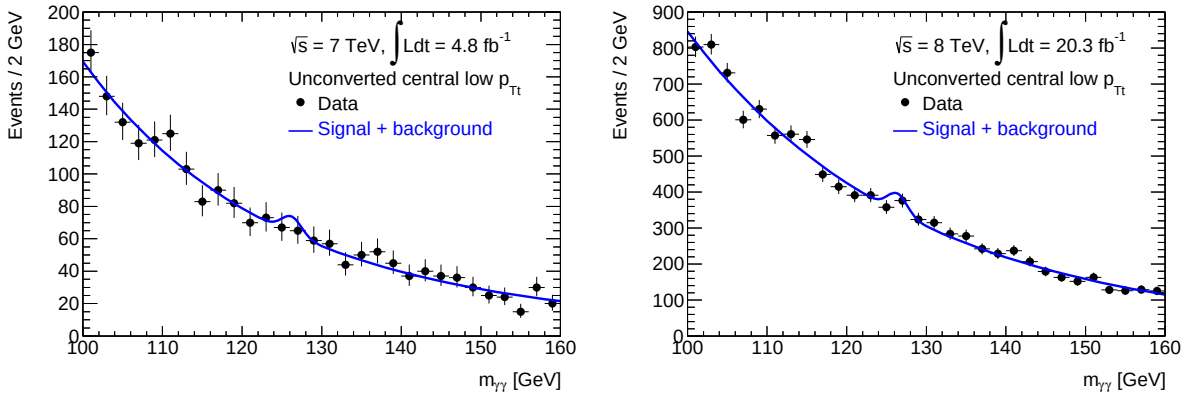

Figure 6.2.15: Di-photon mass distributions in different categories. The parameters of the signal and the background models are best fit values.

6.2.5 Di-photon mass distributions

Figure 6.2.15, 6.2.16, 6.2.17 and 6.2.18 show the observed invariant mass distributions for each category with fit results, which are explained in following chapters.

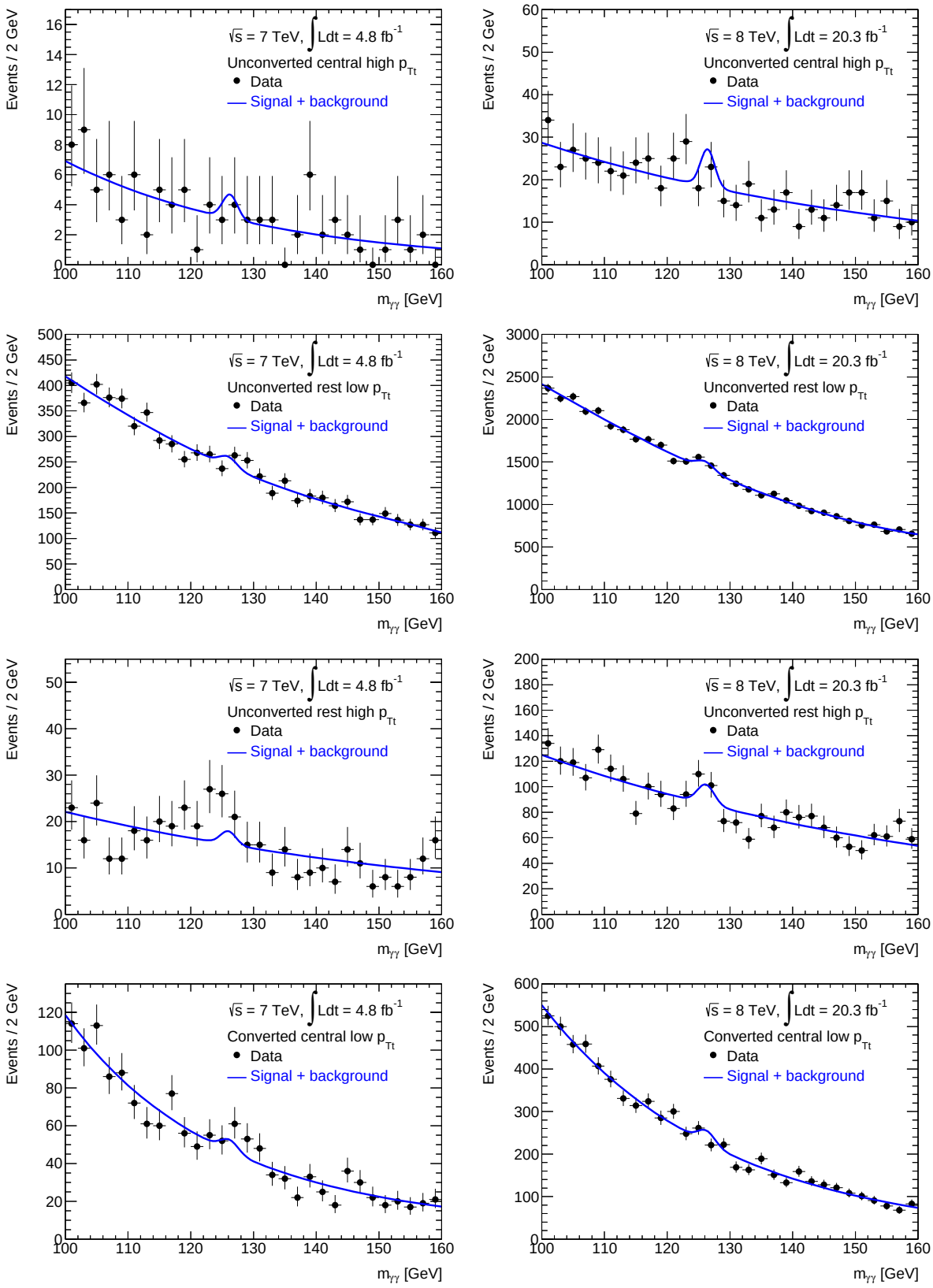

Figure 6.2.16: Di-photon mass distributions in different categories. The parameters of the signal and the background models are best fit values.

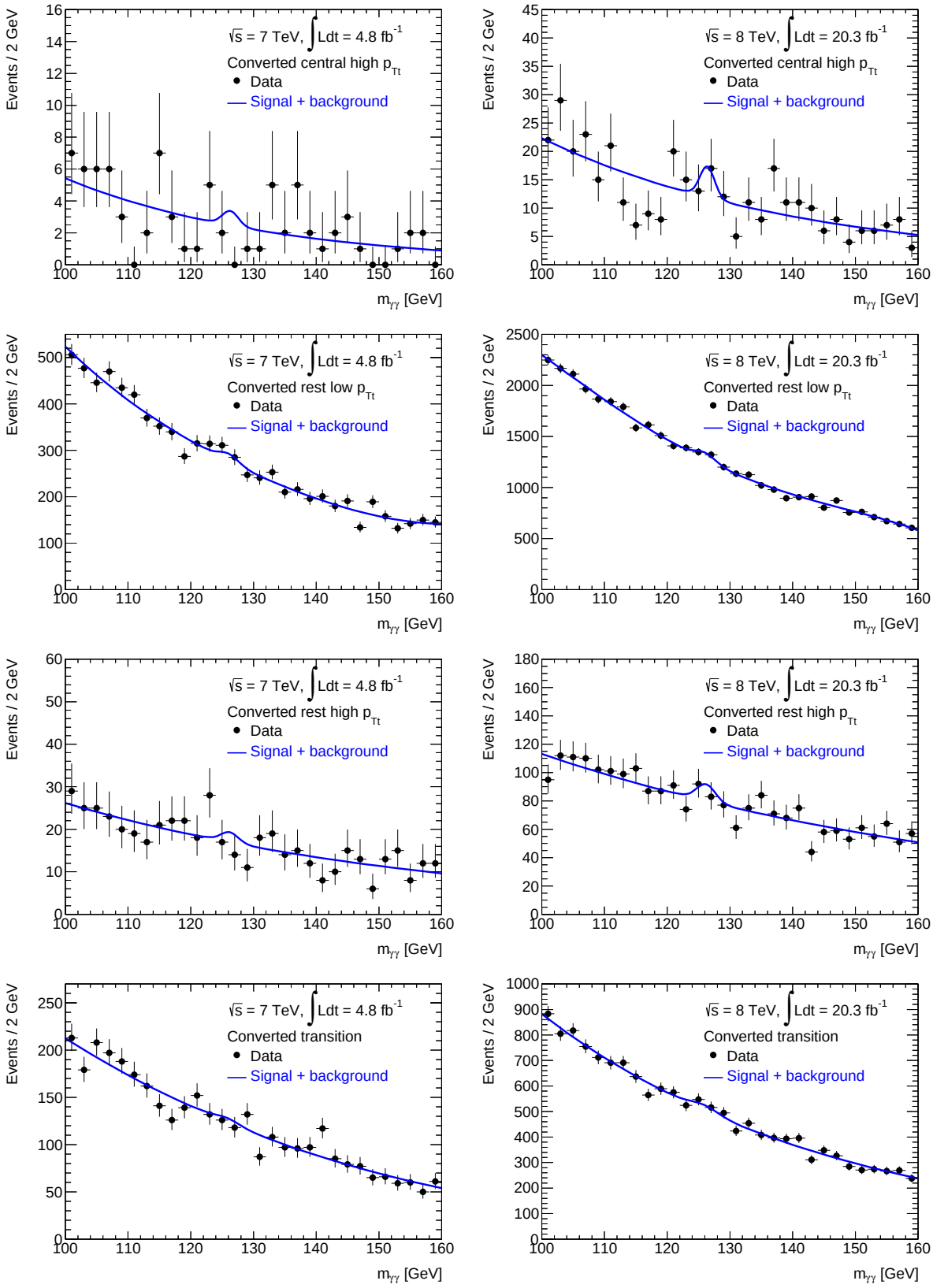

Figure 6.2.17: Di-photon mass distributions in different categories. The parameters of the signal and the background models are best fit values.

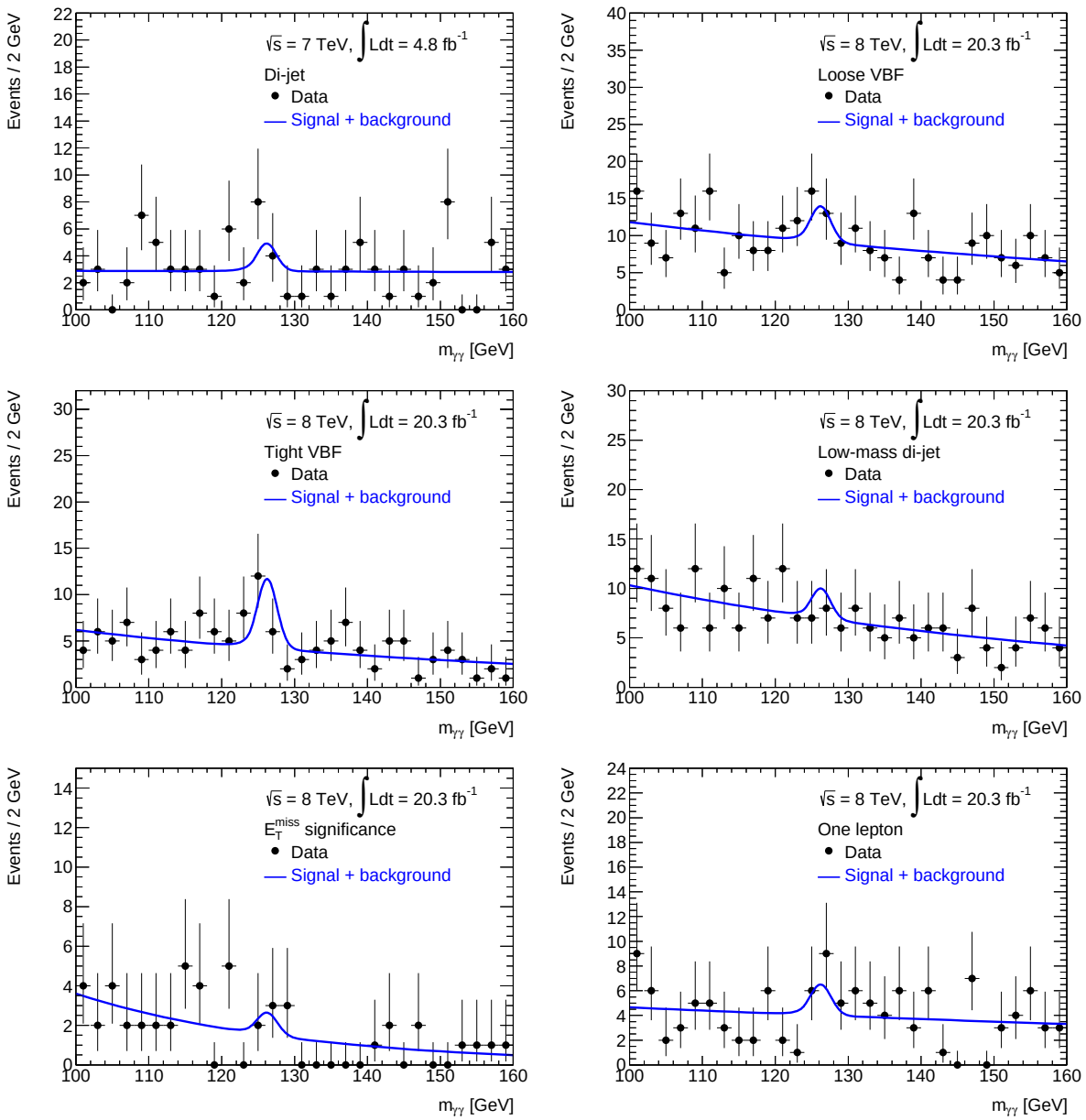

Figure 6.2.18: Di-photon mass distributions in different categories. The parameters of the signal and the background models are best fit values.

Chapter 7

Signal and background modeling

The statistical procedure with a likelihood function is used to test the Standard Model Higgs boson hypothesis and to measure couplings, mass and width. The likelihood function is constructed from probability density functions (PDF) of signal and background components with respect to $m_{\gamma\gamma}$. The modeling of the signal and background is described in this chapter.

7.1 Signal modeling

The signal is modeled with MC-simulated events of the SM Higgs processes as described in Sec 3.2. The yield and shape of the signal events are parametrized as a function of a hypothesized m_H. The detector response is also modeled with GEANT4 program. Thus the yield and the shape of the signal events are parametrized for a hypothesized m_H. The signal model is used for a likelihood which is described in Section 8.1.

7.1.1 Signal probability density function

The function of the PDF is the sum of a *Crystal Ball* function and a wider Gaussian tail component. The parameters of the function are different for each event category. The Crystal Ball function has a Gaussian and a non-Gaussian low mass tail. The tail is described by a power-law function. The Crystal Ball function is defined by:

$$f_{CB}\left(m_{\gamma\gamma}|m_H\right) = N \begin{cases} \exp\left(-\frac{t^2}{2}\right) & t > -\alpha_{CB} \\ \left(\frac{n_{CB}}{|\alpha_{CB}|}\right)^{n_{CB}} \exp\left(-\frac{|\alpha_{CB}|^2}{2}\right) \left(\frac{n_{CB}}{|\alpha_{CB}|} - |\alpha_{CB}| - t\right)^{-n_{CB}} & t \leq -\alpha_{CB} \end{cases} \tag{7.1.1}$$

where $t \equiv \frac{m_{\gamma\gamma}-\mu_{CB}}{\sigma_{CB}}$, σ_{CB} is the sigma of the Gaussian part, μ_{CB} is the peak position of the Gaussian , N is a normalization parameter and α_{CB} and n_{CB} parametrize the non-Gaussian tail. Figure 7.1.1 illustrates the Crystal Ball function. The signal shape function f_s is modeled by:

$$f_s\left(m_{\gamma\gamma}|m_H\right) = c_{CB} f_{CB}\left(m_{\gamma\gamma}|m_H\right) + \left(1 - c_{CB}\right) \frac{1}{\sqrt{2\pi\sigma_{GA}^2}} \exp\left(-\frac{\left(m_{\gamma\gamma} - \mu_{GA}\right)^2}{2\sigma_{GA}^2}\right) \tag{7.1.2}$$

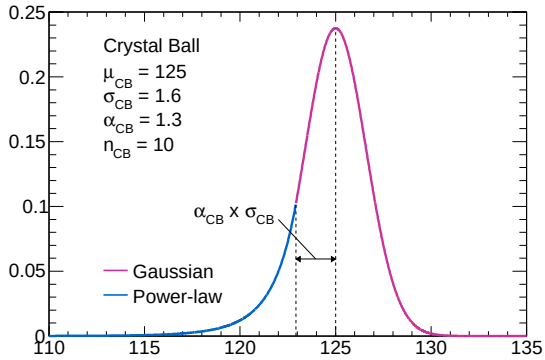

Figure 7.1.1: Illustration of Crystal Ball function.

where c_{CB} is the fraction of the Crystal Ball function. The σ_{CB} and σ_{GA} correspond to the mass resolution of the di-photon events. All event categories use the same signal function form while parameters are determined category-by-category.

For the improvement of the accuracy of parameters, the fit is performed with signal of all the mass points simultaneously under the assumption that the parameters have the following dependence on m_H:

$$\begin{cases} \mu_{CB}(m_H) &= m_H + (\mu_0 + \mu_1 m_H + \mu_2 m_H^2) \\ \sigma_{CB}(m_H) &= \sigma_0 + \sigma_1 m_H + \sigma_2 m_H^2 \\ \alpha_{CB}(m_H) &= \alpha_0 + \alpha_1 m_H \\ n_{CB}(m_H) &= 10 \\ \mu_{GA}(m_H) &= \mu_{CB}(m_H) \\ \sigma_{GA}(m_H) &= (k_0 + k_1 m_H)\,\sigma_{CB}(m_H) \\ c_{CB}(m_H) &= c_0 + c_1 m_H \end{cases} \tag{7.1.3}$$

where μ_i, σ_i, α_i, n, k_i and c_i $(i = 0, 1, ..)$ are fitting parameters. $n_{CB}(m_H)$ is fixed to be 10 from a simulation study. Figure 7.1.2 shows results of the simultaneous fit in Unconverted central, low $p_{\mathrm{T}t}$ category. The errors of the simultaneous fit is so small compared with other systematic uncertainties that the fitting errors are not taken into account as a systematic uncertainty.

Figure 7.1.3 compares the signal histograms between Unconverted central, high $p_{\mathrm{T}t}$ category and Converted transition category in $\sqrt{s} = 8$ TeV analysis at $m_H = 125$ GeV. The former category has the best mass resolution ($\sigma_{CB} = 1.35$ GeV), while the latter has the widest shape ($\sigma_{CB} = 2.25$ GeV). Table 7.1.1 gives the parameters of the signal functions for $m_H = 125$ GeV. Their uncertainties are discussed in Section 7.3.3 and 7.3.4.

7.1.2 Signal yield

The differential cross section and branching ratio of the signal events are calculated in signal MC as described in Section 3.2. The signal efficiency is also computed in the MC events based on GEANT4 program. The total efficiency depends on the efficiency of photon reconstruction described in Chapter 4 and estimated to be 37.5 % at $m_H = 125$ GeV. For this mass, the expected total signal yield is 80.8 in $\sqrt{s} = 7$ TeV data and 355.5

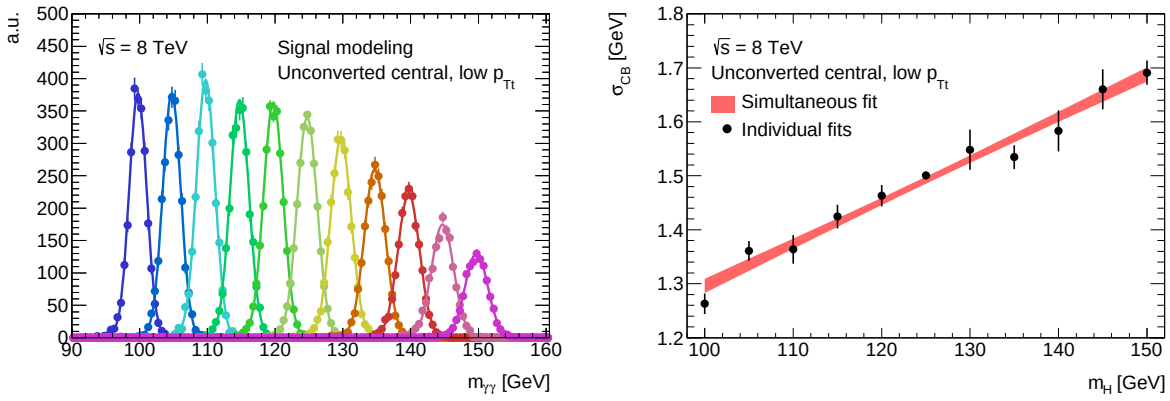

(a) (b)

Figure 7.1.2: Simultaneous fit to 11 signal MC samples with m_H between 100 and 150 GeV in Unconverted central, low $p_{\mathrm{T}t}$ category (a). Resulting σ_{CB} of simultaneous fit and individual fits in Unconverted central, low $p_{\mathrm{T}t}$ category. Band of σ_{CB} from simultaneous fit shows the error from the fit (b).

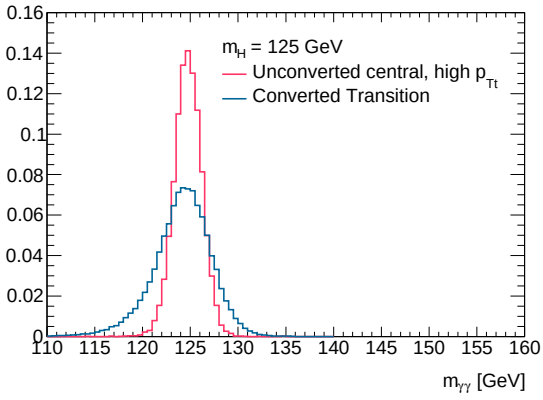

Figure 7.1.3: $m_{\gamma\gamma}$ histograms in Unconverted central, high $p_{\mathrm{T}t}$ category and Converted transition category in $\sqrt{s} = 8$ TeV analysis at $m_H = 125$ GeV.

		μ_{CB}	σ_{CB}	α_{CB}	n_{CB}	σ_{GA}	c_{CB}
$\sqrt{s} = 7$ TeV	Inclusive	124.6	1.61	1.3	10	5.6	0.96
	Unconverted central, low $p_{\mathrm{T}t}$	124.7	1.43	2.3	10	5.1	1.00
	Unconverted central, high $p_{\mathrm{T}t}$	124.7	1.35	2.5	10	7.2	1.00
	Unconverted rest, low $p_{\mathrm{T}t}$	124.6	1.56	1.7	10	5.1	0.96
	Unconverted rest, high $p_{\mathrm{T}t}$	124.7	1.41	1.8	10	5.3	0.96
	Converted central, low $p_{\mathrm{T}t}$	124.5	1.62	1.6	10	7.4	1.00
	Converted central, high $p_{\mathrm{T}t}$	124.6	1.46	1.7	10	8.2	1.00
	Converted rest, low $p_{\mathrm{T}t}$	124.5	1.78	1.3	10	4.7	0.98
	Converted rest, high $p_{\mathrm{T}t}$	124.6	1.60	1.4	10	5.8	0.99
	Converted transition	124.4	2.25	0.9	10	5.2	0.88
	Di-jet	124.6	1.50	1.3	10	6.1	0.97
$\sqrt{s} = 8$ TeV	Inclusive	124.6	1.76	1.5	10	3.8	0.96
	Unconverted central, low $p_{\mathrm{T}t}$	124.7	1.49	2.1	10	5.7	1.00
	Unconverted central, high $p_{\mathrm{T}t}$	124.8	1.39	1.9	10	6.2	1.00
	Unconverted rest, low $p_{\mathrm{T}t}$	124.6	1.72	1.9	10	3.0	0.93
	Unconverted rest, high $p_{\mathrm{T}t}$	124.7	1.67	2.2	10	4.4	0.98
	Converted central, low $p_{\mathrm{T}t}$	124.5	1.67	1.5	10	7.2	1.00
	Converted central, high $p_{\mathrm{T}t}$	124.7	1.53	1.8	10	6.5	1.00
	Converted rest, low $p_{\mathrm{T}t}$	124.4	2.00	1.5	10	4.2	0.97
	Converted rest, high $p_{\mathrm{T}t}$	124.6	1.85	1.6	10	6.3	0.99
	Converted transition	124.5	2.50	1.3	10	4.6	0.94
	Loose VBF	124.7	1.69	1.6	10	3.7	0.96
	Tight VBF	124.7	1.62	1.6	10	3.9	0.96
	Low mass di-jet	124.7	1.60	1.6	10	4.6	0.97
	$E_{\mathrm{T}}^{\mathrm{miss}}$significance	124.7	1.72	1.6	10	8.5	0.99
	One-lepton	124.6	1.73	1.5	10	8.0	0.98

Table 7.1.1: The parameters of signal functions in the different categories for $m_H = 125$ GeV. The unit of μ_{CB}, σ_{CB} and σ_{GA} is GeV.

	Observed	Expected	
		Signal	Spurious signal
Inclusive	23788	80.8	7.3
Unconverted central, low $p_{\mathrm{T}t}$	2054	10.7	2.0
Unconverted central, high $p_{\mathrm{T}t}$	97	1.5	0.2
Unconverted rest, low $p_{\mathrm{T}t}$	7129	22.0	2.2
Unconverted rest, high $p_{\mathrm{T}t}$	444	2.8	0.5
Converted central, low $p_{\mathrm{T}t}$	1493	6.8	1.6
Converted central, high $p_{\mathrm{T}t}$	77	1.0	2.7
Converted rest, low $p_{\mathrm{T}t}$	8313	21.4	4.6
Converted rest, high $p_{\mathrm{T}t}$	501	2.8	0.5
Converted transition	3591	9.1	3.2
Di-jet	89	2.2	0.4

Table 7.1.2: The number of events in data and the expected number of signal events for $m_H = 126.5$ GeV for $\sqrt{s} = 7$ TeV analysis. *Spurious signal* represents the uncertainty of the signal yield due to background mismodeling, which Section 7.3.1.7 describes in detail.

in $\sqrt{s} = 8$ TeV data. The expected signal yield for each category depends not only on the photon reconstruction efficiency but also on the probabilities of photon conversion and reconstruction of additional objects used for event categorization. Table 7.1.2 and 7.1.3 summarize the number of events observed in data and the expected number of signal events for different categories. The uncertainties are discussed in Section 7.3.1 and 7.3.2. Figure 7.1.4 and 7.1.5 shows the expected signal composition for $\sqrt{s} = 7$ and 8 TeV.

7.2 Background modeling

The invariant mass distributions of the background for each category are parametrized with an analytic function. Different functions are chosen for different categories based on studies with MC samples. The shape of the background are completely different from the signal; the signal events have a sharp resonance at the Higgs mass, while the background events have monotonous shapes in the di-photon invariant mass distribution. This is one of the largest advantages of the $H \to \gamma\gamma$ analysis. Considered backgrounds are γ-γ, γ-jet, jet-jet, Drell-Yan and other electroweak background processes ($Z + \gamma$ and $W + \gamma\gamma$).

The main contribution to the γ-γ background is the $q\bar{q}, qg \to \gamma\gamma X$ processes, namely the Born and Bremsstrahlung. Another main γ-γ background is due to the $gg \to \gamma\gamma$, referred to as the box contribution. Figure 7.2.1 shows their diagrams. The γ-jet and jet-jet background events have fake photons due to the presence of a leading π^0 resulting from the fragmentation of a quark or a gluon. The diagrams of the γ-jet and jet-jet backgrounds are shown in Figure 7.2.2 and 7.2.3. The ratio of cross sections of the γ-γ, γ-jet and jet-jet is about $1 : 10^4 : 10^7$, where the photons and the jets are required to have $E_{\mathrm{T}} > 25$ GeV and $|\eta| < 2.5$ and $80 < m_{\gamma\gamma} < 150$ GeV [98].

Drell-Yan events contaminate the signal region when two electrons are misidentified as photons due to failure in the track-to-cluster matching described in Section 4.3. The

	Observed	Expected	
		Signal	Spurious signal
Inclusive	118893	355.5	12.0
Unconverted central, low $p_{\mathrm{T}t}$	10900	46.6	4.6
Unconverted central, high $p_{\mathrm{T}t}$	553	7.1	0.8
Unconverted rest, low $p_{\mathrm{T}t}$	41236	97.1	11.4
Unconverted rest, high $p_{\mathrm{T}t}$	2558	14.4	2.0
Converted central, low $p_{\mathrm{T}t}$	7109	29.8	2.4
Converted central, high $p_{\mathrm{T}t}$	363	4.6	0.8
Converted rest, low $p_{\mathrm{T}t}$	38156	88.0	8.0
Converted rest, high $p_{\mathrm{T}t}$	2360	12.9	1.1
Converted transition	14864	36.1	9.1
Loose VBF	276	4.8	1.1
Tight VBF	136	7.3	0.3
Low mass di-jet	210	3.0	0.6
$E_{\mathrm{T}}^{\mathrm{miss}}$significance	49	1.1	0.1
One-lepton	123	2.6	0.3

Table 7.1.3: The number of events in data and the expected number of signal events for $m_H = 126.5$ GeV for $\sqrt{s} = 8$ TeV analysis. *Spurious signal* represents the uncertainty of the signal yield due to background mismodeling, which Section 7.3.1.7 describes in detail.

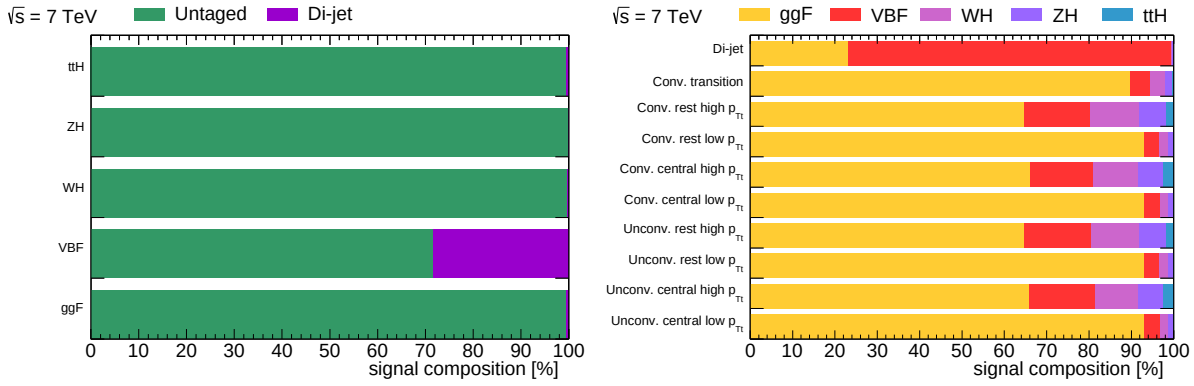

Figure 7.1.4: The signal composition for each production process as a function of the event category (left) The signal composition for each event category as a function of the signal process (right) for $\sqrt{s} = 7$ TeV analysis at $m_H = 125$ GeV.

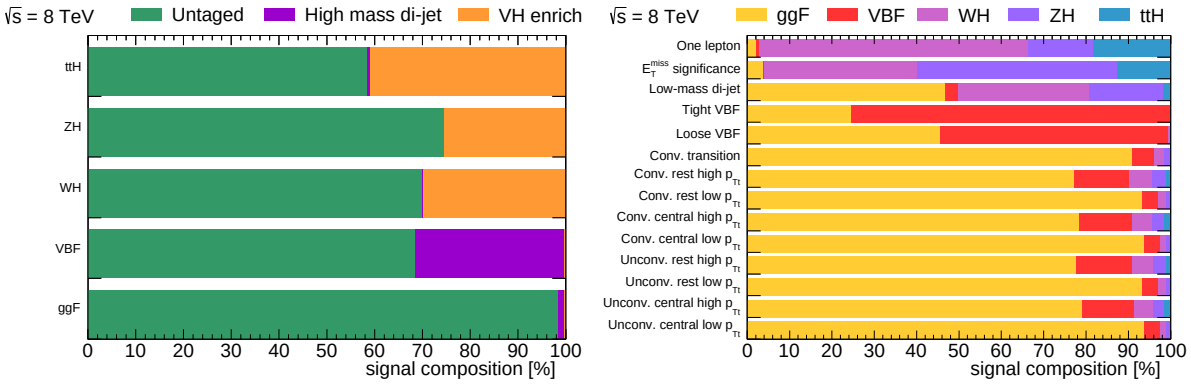

Figure 7.1.5: The signal composition for each production process as a function of the event category (left) The signal composition for each event category as a function of the signal process (right) for $\sqrt{s} = 8$ TeV analysis at $m_H = 125$ GeV.

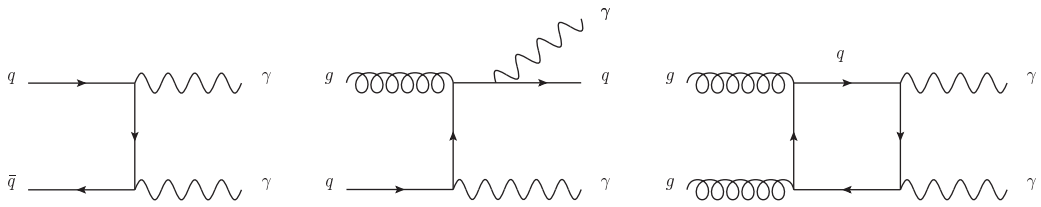

Figure 7.2.1: Diagrams of the main γ-γ backgrounds: Born (left), Bremsstrahlung (middle) and Box (right)

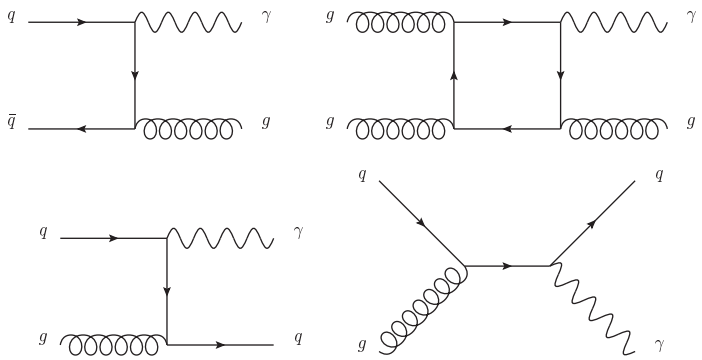

Figure 7.2.2: Diagrams of γ-jet background (Leading-order)

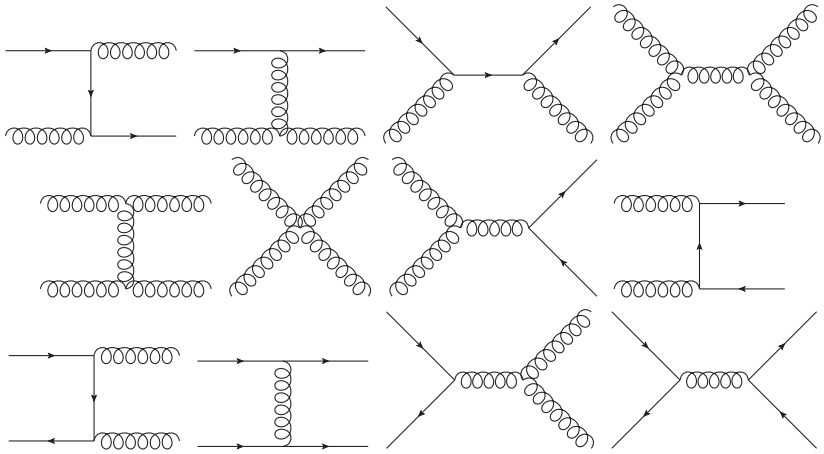

Figure 7.2.3: Diagrams of jet-jet backgrounds (Leading-order)

high mass tail of the Drell-Yan peak in the mass window ([100, 160] GeV) is the source of background. Because electrons have similar isolation distributions to photons as well as shower shape, they have much higher fake rate to photons than jets. However since the cross section of Drell-Yan within the mass window is much smaller than γ-γ, γ-jet and jet-jet, the expected fraction of Drell-Yan events is small. Other electroweak backgrounds, such as $Z + \gamma$ and $W + \gamma\gamma$ events, also have fake photons due to electrons and have non-negligible contribution to the VH categories.

7.2.1 Background composition

In order to choose fitting functions, the fraction of each background component is need to be estimated. For Drell-Yan events, the misidentification rate is extracted in data with using $Z \to ee$ events reconstructed as di-electron and $e-\gamma$ pairs. The fraction of Drell-Yan events is estimated to be ~ 1 % [93]. The $Z + \gamma$ and the $W + \gamma\gamma$ samples are normalized according to the cross section of the process. They have very small contributions except in VH categories.

The fractions of γ-γ, γ-jet and jet-jet events are measured using several data-driven techniques [99]. One of them is template fit method [100]. In this method, templates of isolation distributions of genuine photons and fake photons are formed for both leading and sub-leading photons in data. The template of fake photons is obtained from photons which fail the photon identification criteria but pass certain relaxed identification criteria. The template of genuine photons is obtained by subtracting the fake photon template from the isolation distribution of photon candidates which pass the identification criteria. For subtracting, the fake photon template is normalized such that the integrals of the two distributions are equal for bad isolation (high $E_{\mathrm{T}cone40}$) region. The template fit is performed to the leading photon and sub-leading photon simultaneously in each bin of the di-photon invariant mass distribution relaxed isolation criteria. From the fit result, the fractions of each background are estimated to be 80 ± 4 %, 19 ± 3 % and 1.8 ± 0.5 % for the γ-γ, the γ-jet and jet-jet events in $\sqrt{s} = 7$ TeV data, while $75\ ^{+3}_{-2}$ %, 22 ± 2 % and 2.6 ± 0.5 % in $\sqrt{s} = 8$ TeV data. In this estimation, the signal events and the Drell-Yan

インターネット公表に関する同意が
得られなかったため非公表

Figure 7.2.4: Composition of the inclusive data sample as a function of $m_{\gamma\gamma}$, extracted from the double two dimensional sideband method after the inclusive event selection. The various components are stacked on top of each other. The error bars correspond to the statistical uncertainties on each component separately. The gray bands show the overall uncertainty on each component [99].

are included in the γ-γ fraction. However their contributions are so small. Figure 7.2.4 shows the di-photon sample composition as a function of the invariant mass at $\sqrt{s} = 7$ TeV. The fractions are estimated in the inclusive category, and the results are applied to all categories.

The results of background decomposition is used for fit function choice, but not used for likelihood fit. Therefore the estimation of background decomposition does not affect final physics results directly.

7.2.2 Fitting function for each event category

Fitting functions for each category are chosen to achieve a good compromise between the bias for signal yield due to the chosen parametrization and retaining the significance of observation and measurement. Depending on the category, an exponential function, a 4th-order Bernstein polynomial or an exponential function of a 2nd-order polynomial is used as shown in Table 7.2.1. The 4th-order Bernstein polynomial and the exponential function of a 2nd-order polynomial are defined as:

$$\begin{aligned} \mathrm{Bern4}\left(m_{\gamma\gamma}\right) =& \sum_{i=0}^{4} a_i \frac{4!}{i!\,(4-i)!} m_{\gamma\gamma}^{i} \left(m_{\gamma\gamma\mathrm{max}} - m_{\gamma\gamma}\right)^{4-i} \\ \mathrm{Exp2nd}\left(m_{\gamma\gamma}\right) =& N \exp\left(c_1 m_{\gamma\gamma} + c_2 m_{\gamma\gamma}^2\right) \end{aligned} \tag{7.2.1}$$

where Bern4 is a 4th-order Bernstein polynomial, Exp2nd is an exponential function of 2nd-order polynomial and coefficients a_i, c_1, c_2, N are fitting parameters as well as $m_{\gamma\gamma\mathrm{max}}$ is the maximum of $m_{\gamma\gamma}$ (160 GeV). The coefficient a_i is constrained to be $a_i \geq 0$, hence Bern4 a has non-negative value. If the background modeling is not perfect, when the $m_{\gamma\gamma}$ histogram of background processes are fitted with signal + background model, the non-zero signal is obtained from the fit. This signal biases, called *spurious signal*, for each category from the choice of background parametrization are estimated using MC samples normalized according to the studies in Section 7.2.1. The *spurious signal* is discussed in Section 7.3.1.7.

Category		Function
$\sqrt{s} = 7$ TeV	$\sqrt{s} = 8$ TeV	
Inclusive		4th-order Bernstein polynomial
Unconverted central, low $p_{\mathrm{T}t}$		Exponential of 2nd-order pol.
Unconverted central, high $p_{\mathrm{T}t}$		Exponential
Unconverted rest, low $p_{\mathrm{T}t}$		4th-order Bernstein polynomial
Unconverted rest, high $p_{\mathrm{T}t}$		Exponential
Converted central, low $p_{\mathrm{T}t}$		Exponential of 2nd-order pol.
Converted central, high $p_{\mathrm{T}t}$		Exponential
Converted rest, low $p_{\mathrm{T}t}$		4th-order Bernstein polynomial
Converted rest, high $p_{\mathrm{T}t}$		Exponential
Converted transition		Exponential of 2nd-order pol.
Di-jet	Loose VBF	Exponential
	Tight VBF	Exponential
—	Low mass di-jet	Exponential
—	$E_{\mathrm{T}}^{\mathrm{miss}}$significance	Exponential
—	One-lepton	Exponential

Table 7.2.1: Functions for background events in the each event category.

Uncertainty	$\sqrt{s} = 7$ TeV	$\sqrt{s} = 8$ TeV
Luminosity	± 1.8 %	± 3.6 %
Trigger	± 1.0 %	± 0.5 %
Identification	± 8.4 %	± 2.4 %
Isolation	± 0.4 %	± 1.0 %
Kinematics	± 0.3 %	± 0.3 %
Theory: cross section	Table 7.3.2	Table 7.3.3
Theory: branching fraction	$^{+5.0}_{-4.9}$ %	
Background modeling	Table 7.1.2	Table 7.1.3

Table 7.3.1: Systematic uncertainties on signal yield at $m_H = 125$ GeV.

7.3 Systematic uncertainties

Four different groups of the systematic uncertainties are considered: signal yield, event migration, mass scale and mass resolution. The "signal yield" is the estimation of uncertainties on the amount of signal events observed. The "event migration" is the uncertainty on categorization, that is, uncertainties on the fraction of events being classified in different event categories. The "mass scale" and "mass resolution" are uncertainties on the Higgs mass position and resolution, respectively.

7.3.1 Signal yield

Seven different sources of the systematic uncertainty on signal yield are considered as summarized in Table 7.3.1. Each uncertainty is described below.

Uncertainty				
QCD scale	ggF: $^{+7.1}_{-7.8}$ %	VBF: ±0.3 %	*WH*: ±0.9 %	
	ZH: ±2.9 %	*ttH*: $^{+3.2}_{-9.3}$ %		
PDF $+\alpha_S$	ggF: $^{+7.6}_{-7.1}$ %	VBF: $^{+2.5}_{-2.1}$ %	*WH*: ±2.6 %	
	ZH: ±2.7 %	*ttH*: ±8.4 %		
QCD scale for ggF + multi-jet		2 jet in di-jet category: ±20 %		
		3 jet in di-jet category: ±15 %		

Table 7.3.2: Systematic uncertainties on Higgs boson cross section for $\sqrt{s} = 7$ TeV analysis at $m_H = 125$ GeV.

Uncertainty				
QCD scale	ggF: $^{+7.2}_{-7.8}$ %	VBF: ±0.2 %	*WH*: ±1.0 %	
	ZH: ±3.1 %	*ttH*: $^{+3.8}_{-9.3}$ %		
PDF $+\alpha_S$	ggF: $^{+7.5}_{-6.9}$ %	VBF: $^{+2.6}_{-2.8}$ %	*WH*: ±2.3 %	
	ZH: ±2.5 %	*ttH*: ±8.1 %		
QCD scale for ggF + multi-jet		2 jet in tight VBF category: ±20 %		
		3 jet in tight VBF category: ±44 %		
		2 jet in loose VBF category: ± 20 %		
		3 jet in loose VBF category: ± 20 %		
		2 jet in low mass di-jet category: ± 30 %		

Table 7.3.3: Systematic uncertainties on Higgs boson cross section for $\sqrt{s} = 8$ TeV analysis at $m_H = 125$ GeV.

7.3.1.1 Luminosity

The uncertainty of luminosity is evaluated with the luminosity detector. The measurement method is described in Appendix A. The estimated uncertainty on the integrated luminosity is ±1.8 % for $\sqrt{s} = 7$ TeV data and ±3.6 % for $\sqrt{s} = 8$ TeV data.

7.3.1.2 Trigger efficiency

As described in Section 4.2, the di-photon trigger efficiency is measured by the Bootstrap method. In order to estimate the bias of the method, the efficiency is also evaluated using other measurements: data-driven study with high purity photons in $Z \to ll\gamma$ events, as well as MC simulation analysis with using $H \to \gamma\gamma$ events and fake photon contaminating events. The difference of the results with respect to the results from the Bootstrap method is ±1.0 (±0.5) % for $\sqrt{s} = 7$ (8) TeV, and is considered as the systematic uncertainty of the di-photon trigger efficiency.

7.3.1.3 Photon identification efficiency

The uncertainty of identification efficiency per photon candidate is estimated in Section 5.3. For the $H \to \gamma\gamma$ analysis, the multi-photon correlation are taken into account. Because some identification uncertainties are correlated between two photons, the correlation coefficients are calculated as a function of η, E_{T} and conversion status of two photons. From the correlation coefficients and the uncertainty per photon, the uncertainties of photon identification efficiency is calculated event by event in the $H \to \gamma\gamma$ signal samples. Then the uncertainties are combined, and the total uncertainty is measured to be ±2.4 % for $\sqrt{s} = 8$ TeV analysis.

For $\sqrt{s} = 7$ TeV analysis, photons are assumed to be fully correlated. This is more conservative model. The uncertainty is estimated to be ±8.4 %.

7.3.1.4 Isolation criteria efficiency

In Section 5.5, the efficiency uncertainty of isolation criteria for di-photon is measured to be ±0.4 % for $\sqrt{s} = 7$ TeV, and ±1.0 % for $\sqrt{s} = 8$ TeV analysis.

7.3.1.5 Kinematic threshold efficiency

The energy scale uncertainty of photons causes signal yield uncertainty because the leading (sub-leading) photon candidates are required to pass 40 (30) GeV E_{T} threshold. The uncertainty is estimated to be ±0.3 %. This uncertainty is correlated with the mass scale uncertainties which are described in Section 7.3.3.

7.3.1.6 Theoretical uncertainties for Higgs cross section and branching ratio

The theoretical uncertainties on the Higgs boson cross section for each production process, as well as branching ratio are taken from [17, 18] as summarized in Table 7.3.2 and 7.3.3. The uncertainties on the cross section include PDF and missing higher order perturbative QCD corrections. The α_S uncertainty is added in quadrature to the PDF variation. Hence PDF uncertainty is called *PDF*+α_S. On the other hand, the uncertainty of QCD

renormalization and factorization is called *QCD scale*. These theoretical uncertainties have the m_H dependence. The typical value of the theoretical uncertainty is ± 11 %.

For the ggF+2 jet as well as 3 jet cross section, the QCD perturbative uncertainties are calculated separately.

7.3.1.7 Background modeling

The uncertainties on background modeling are sources of the signal yield uncertainty. The bias on the signal yield is estimated for each event category by a likelihood fit with signal and background models to a simulated background only data set. The obtained signal yield from the fit is assumed as the signal yield bias. The signal bias due to background modeling is called *spurious signal*, and is estimated to be between ± 4 and ± 23 % depending on event category.

7.3.2 Event migration

Some systematic uncertainties do not lead to the total signal yield uncertainty but lead to the event migration uncertainties. Ten different migration sources are taken into account as described below. Appendix E summarizes the uncertainties.

7.3.2.1 Material mismodeling

The material mapping mismodeling causes bias on the fraction of converted photons. The impact of the mismodeling is estimated with using signal MC samples with a special material configuration, where the material amount is shifted by the geometry uncertainties. The potential migration is -4 % for unconverted photon categories and $+3.5$ % for converted photon categories. The sign of the uncertainty is plus (minus) if the fraction of the category is increased (decreased) when the material amount is increased.

7.3.2.2 Jet energy scale

The jet energy scale (JES) uncertainties lead to the event migration between categories requiring jets and other categories. The potential migration is estimated by varying the JES within their uncertainties [101]. The JES uncertainties are categorized into some non-negligible independent uncertainties (called *OffsetMu, Flavor Composition, Flavor Response, Model 1, EtaCalib, Pileup and Close-By*). They are described in Appendix D.3. The estimated uncertainties are up to 12 % (11 %) for the tight (loose) VBF category, 6.7 % for the low mass di-jet category and up to 0.7 % for the other categories in $\sqrt{s} = 8$ TeV data, while in $\sqrt{s} = 7$ TeV data, up to 15 % for di-jet category and up to 0.4 % for the other categories.

7.3.2.3 Jet energy resolution

The jet energy resolution (JER) uncertainty affects the event migration. The impact is found to be up to 3.8 % (3.4 %) on the tight (loose) VBF category, 3.4 % on the low-mass di-jet category, and up to 0.9 % on the other categories in $\sqrt{s} = 8$ TeV data.

7.3.2.4 Jet vertex fraction

The differences of jet vertex fraction (JVF) efficiency between data and MC is estimated for pileup jets and jets from a hard process separately (see Appendix D). The uncertainties are 0.3 (1.2) % in the loose VBF category for ggF (VBF), ans 2.3 (2.4) % in the low mass di-jet category for ggF (VBF). The uncertainties are only applied to $\sqrt{s} = 8$ TeV data because of high pileup condition.

7.3.2.5 Higgs p_{T} of gluon-gluon process

The Higgs p_{T} uncertainty due to the modeling of the Higgs boson kinematic properties is estimated from the HqT2.0 [86] as a function of the Higgs p_{T}. The potential event migration is evaluated from the Higgs p_{T} uncertainty. For $\sqrt{s} = 8$ TeV analysis, the potential migration is 10.2 % on the high $p_{\mathrm{T}t}$ categories, 10.4 % (8.5 %) on the tight (loose) VBF categories, 12.5 % on the low mass di-jet category and up to 4.0 % on the other categories. For $\sqrt{s} = 7$ TeV analysis, the uncertainties are 12.5 % on the high $p_{\mathrm{T}t}$ categories, 9 % on the di-jet categories and 1.1 % on the other categories.

7.3.2.6 Underlying event

Underlying event is everything in single parton collisions except the hard process of interest [102]. The mismodeling of the underlying event in MC events leads to the migration between di-jet events. For the systematic studies, special samples without multi-parton interaction are used. From the comparison of the predicted fractions of the categories between the default and the special sample events, up to 30 (13) % uncertainty for the di-jet categories are assigned to ggF for $\sqrt{s} = 7$ (8) TeV analysis. To the other production process, the assigned uncertainties are up to 6 (4) % for $\sqrt{s} = 7$ (8) TeV analysis.

7.3.2.7 Lepton efficiency

The lepton efficiency uncertainties affects the number of signal events of the one-lepton category. The uncertainties of lepton reconstruction, identification, energy scale and energy resolution are taken into account. The uncertainties of the event migration are estimated to be up to 1 %.

7.3.2.8 $E_{\mathrm{T}}^{\mathrm{miss}}$

The uncertainties of $E_{\mathrm{T}}^{\mathrm{miss}}$ are estimated by propagating the E_{T} uncertainties of input objects (photons, electron, jets and cell out). The largest contribution comes from the cell-out term. The jet energy scale has the second largest contribution, and the uncertainty of other objects are negligible. The potential event migration is estimated by varying the $E_{\mathrm{T}}^{\mathrm{miss}}$ up and down by the uncertainty. In the $E_{\mathrm{T}}^{\mathrm{miss}}$ significance category, the assigned uncertainty is 66.4 % to ggF, 30.7 % to VBF and 1.2 % to *VH*.

7.3.2.9 $\eta^{\star} = \left|\eta^{\gamma\gamma} - \left(\eta^{\mathrm{jet1}} + \eta^{\mathrm{jet2}}\right)/2\right|$

The uncertainty of $\eta^{\star}$ modeling affects the efficiency of the di-jet categories. The uncertainty due to $\eta^{\star}$ modeling is estimated by reweighting the jet distribution at MC generator

Category	Z line shape	Material $\|\eta\| < 1.8$	Material $\|\eta\| > 1.8$
Unconverted central, low $p_{\mathrm{T}t}$	0.30 %	0.30 %	-
Unconverted central, high $p_{\mathrm{T}t}$	0.30 %	0.30 %	-
Unconverted rest, low $p_{\mathrm{T}t}$	0.30 %	0.50 %	0.10 %
Unconverted rest, high $p_{\mathrm{T}t}$	0.30 %	0.50 %	0.10 %
Converted central, low $p_{\mathrm{T}t}$	0.30 %	0.10 %	-
Converted central, high $p_{\mathrm{T}t}$	0.30 %	0.10 %	-
Converted rest, low $p_{\mathrm{T}t}$	0.30 %	0.20 %	0.10 %
Converted rest, high $p_{\mathrm{T}t}$	0.30 %	0.20 %	0.10 %
Converted transition	0.40 %	0.60 %	-
Di-jet	0.30 %	0.30 %	-

Table 7.3.4: Uncertainties on mass scale for $\sqrt{s} = 7$ TeV.

Category	Presampler barrel	Presampler endcap
Unconverted central, low $p_{\mathrm{T}t}$	0.10 %	-
Unconverted central, high $p_{\mathrm{T}t}$	0.10 %	-
Unconverted rest, low $p_{\mathrm{T}t}$	0.20 %	-
Unconverted rest, high $p_{\mathrm{T}t}$	0.30 %	-
Converted central, low $p_{\mathrm{T}t}$	-	-
Converted central, high $p_{\mathrm{T}t}$	-	-
Converted rest, low $p_{\mathrm{T}t}$	0.10 %	-
Converted rest, high $p_{\mathrm{T}t}$	0.10 %	-
Converted transition	-	0.10 %
Di-jet	0.10 %	-

Table 7.3.5: Uncertainties on mass scale for $\sqrt{s} = 7$ TeV.

level to another generator distribution. The uncertainty of the event migration for the tight (loose) VBF category is 7.6 (6.2) %.

7.3.2.10 $|\phi^{\gamma\gamma} - \phi^{jj}|$

In the same way as $\eta^{\star}$, the uncertainty is estimated by reweighting the jet distribution. The resulting uncertainty is 12.1 (8.5) % for the tight (loose) VBF categories.

7.3.3 Mass scale

Nine mass scale uncertainties affect μ_{CB} of the signal PDF. The uncertainties are summarized in Table 7.3.4, 7.3.5, 7.3.6, 7.3.7 and 7.3.8.

7.3.3.1 Energy correction using Z line shape

As described in 4.5.2, the correction of photon energy in data is obtained from the $Z \to ee$ line shape. The uncertainty of the correction has one of the largest impacts on the mass scale uncertainty, which is the range between 0.3% and 0.4% (see Table 7.3.4 and 7.3.6).

Category	Z line shape	Material $\|\eta\| < 1.8$	Material $\|\eta\| > 1.8$
Unconverted central, low $p_{\mathrm{T}t}$	0.30 %	0.26 %	-
Unconverted central, high $p_{\mathrm{T}t}$	0.31 %	0.26 %	-
Unconverted rest, low $p_{\mathrm{T}t}$	0.35 %	0.47 %	0.10 %
Unconverted rest, high $p_{\mathrm{T}t}$	0.35 %	0.49 %	0.08 %
Converted central, low $p_{\mathrm{T}t}$	0.31 %	0.19 %	-
Converted central, high $p_{\mathrm{T}t}$	0.31 %	0.20 %	-
Converted rest, low $p_{\mathrm{T}t}$	0.35 %	0.31 %	0.09 %
Converted rest, high $p_{\mathrm{T}t}$	0.35 %	0.39 %	0.11 %
Converted transition	0.38 %	0.71 %	0.07 %
Loose VBF	0.33 %	0.41 %	0.07 %
Tight VBF	0.33 %	0.38 %	0.03 %
Low mass di-jet	0.33 %	0.43 %	0.06 %
$E_{\mathrm{T}}^{\mathrm{miss}}$significance	0.34 %	0.39 %	0.05 %
One-lepton	0.34 %	0.40 %	0.07 %

Table 7.3.6: Uncertainties on mass scale for $\sqrt{s} = 8$ TeV.

Category	Presampler barrel	Presampler endcap
Unconverted central, low $p_{\mathrm{T}t}$	0.10 %	-
Unconverted central, high $p_{\mathrm{T}t}$	0.11 %	-
Unconverted rest, low $p_{\mathrm{T}t}$	0.16 %	0.02 %
Unconverted rest, high $p_{\mathrm{T}t}$	0.18 %	0.01 %
Converted central, low $p_{\mathrm{T}t}$	0.03 %	-
Converted central, high $p_{\mathrm{T}t}$	0.07 %	-
Converted rest, low $p_{\mathrm{T}t}$	0.05 %	-
Converted rest, high $p_{\mathrm{T}t}$	0.08 %	-
Converted transition	0.05 %	0.06 %
Loose VBF	0.10 %	-
Tight VBF	0.13 %	-
Low mass di-jet	0.12 %	-
$E_{\mathrm{T}}^{\mathrm{miss}}$significance	0.12 %	-
One-lepton	0.10 %	-

Table 7.3.7: Uncertainties on mass scale for $\sqrt{s} = 8$ TeV.

Uncertainty	Value
Conversion fraction	0.13 %
Lateral leakage, e/γ difference	0.10 %
Lateral leakage, energy dependence	0.02 %
High/medium gain	0.15 %
Layer intercalibration	0.20 %
Primary vertex	0.03 %
Background model	0.10 %

Table 7.3.8: Uncertainties on mass scale for $\sqrt{s} = 8$ TeV. Listed uncertainties have the same values in all categories.

7.3.3.2 Material mapping

If mismodeling of the ATLAS detector material mapping exists in the MC samples, the energies lost in front of the EM calorimeter are different between data and MC. The impact of material mapping on mass scale uncertainty is estimated with special MC samples, named *distorted sample*, where the amount of material is shifted by the uncertainty. Because the amount of material strongly depends on η, mass scale uncertainty due to the material mapping is divided into impacts from high η ($|\eta| > 1.8$) and low η ($|\eta| < 1.8$). The estimated uncertainties are up to 0.7 %.

7.3.3.3 Presampler energy scale

The relative energy scale between the presampler and the accordion, which consists of the 1st, 2nd and 3rd layers in the EM calorimeter, affects the energy scale because the presampler is used for the energy correction based on the Calibration hit method (Eq.(4.5.2)). The energy scale in data is corrected with using Z line shape. Therefore the energies of electrons used for the correction are not affected by the relative energy scale. However the relative energy scale has an impact on photon energy scale. The impact is divided into the barrel and endcap regions, and estimated to be up to 0.3 %.

7.3.3.4 Conversion fraction

The energy calibration for photons depends on photon conversion status. Consequently, misreconstruction of photon conversion leads to the energy miscalibration. Because the conversion fraction relies on the material mapping in front of the EM calorimeter, the uncertainty of the fraction is estimated with using the distorted samples. From the results, the mass scale uncertainty due to conversion fraction is estimated to be 0.13 %.

7.3.3.5 Energy leakage

The energy leakage is corrected in the MC based calibration. However, the shower width is underestimated in the MC samples as shown in Section 4.4. Consequently, the lateral leakage correction has uncertainty. The difference of leakage between data and MC is studied with $Z \to ee$ or $Z \to \ell\ell\gamma$ events. The isolation variables are measured with various cone sizes, and from the results, the leakage is parametrized as a function of radius from the cluster center. Then the uncertainty of leakage correction is estimated from comparison between data and MC. The mass scale uncertainties due to the energy leakage are estimated to be 0.1 % from the difference between the results from $Z \to ee$ and $Z \to \ell\ell\gamma$, and to be 0.02 % from energy dependence.

7.3.3.6 Energy scale difference between calorimeter gains

As described in Section 2.2.5.1, the shaper on the EM calorimeter front-end board has three different gains. The energy deposits of electrons for the energy calibration using Z line shapes are amplified with the highest gain, while sometimes in $H \to \gamma\gamma$ events, energy deposits of photons are amplified with the medium gain because of their higher energy deposits. Hence the miscalibration of the two gains causes the mass scale uncertainty. The uncertainty is estimated to be 0.15 %.

	$\sqrt{s} = 7$ TeV		$\sqrt{s} = 8$ TeV	
	Smearing	Pileup	Smearing	Pileup
Unconverted central, low $p_{\mathrm{T}t}$	13.4 %	3.0 %	18.9 %	1.5 %
Unconverted central, high $p_{\mathrm{T}t}$			21.6 %	
Unconverted rest, low $p_{\mathrm{T}t}$			23.2 %	
Unconverted rest, high $p_{\mathrm{T}t}$			23.3 %	
Converted central, low $p_{\mathrm{T}t}$			19.3 %	
Converted central, high $p_{\mathrm{T}t}$			27.2 %	
Converted rest, low $p_{\mathrm{T}t}$			19.6 %	
Converted rest, high $p_{\mathrm{T}t}$			21.8 %	
Converted transition			14.4 %	
Others			21.0 %	

Table 7.3.9: Uncertainties on mass resolution.

7.3.3.7 Layer inter-calibration

The relative energy scales in each layer of the EM calorimeter have an impact on the shower depth X, which is used for the MC based energy correction as described in Section 4.5.1. Therefore difference of the energy scales between data and MC lead bias for mass scale. The ratio E_1/E_2 is estimated with electrons in $Z \to ee$ and $W \to e\nu$ events, where E_1 and E_2 are energy deposits in the 1st and 2nd layers, respectively. From the measured difference of the relative scales between data and MC, the mass scale uncertainty is estimated to be 0.20 %.

7.3.3.8 Primary vertex

The invariant mass is calculated with the energies, η and ϕ of the two photons, and photon η is determined from the position of the primary vertex and the energy cluster position in the EM calorimeter. Hence the systematic uncertainty of primary vertex determination is taken into account for the mass scale uncertainty. Several algorithms to select the primary vertex are checked with $Z \to ee$ events in data and MC, and the impact of the primary vertex determination on the mass scale uncertainty is estimated to be 0.03 %.

7.3.3.9 Background modeling

The choice of background function have an impact on the fitted signal through the signal + background likelihood fit. Therefore the several functions are tested for background model, and the differences of estimated m_H are assumed as the systematic uncertainty. The estimated mass scale systematic uncertainty is 0.1 %.

7.3.4 Mass resolution

The mass resolution is estimated as σ_{CB} or σ_{GA} in the signal PDF. The uncertainties of mass resolution are summarized in Table 7.3.9.

7.3.4.1 Energy smearing

The MC energies are smeared such that the width of Z line shape in MC agrees with that in data as described in Section 4.5.2. The uncertainty of the smearing is a main source of the mass resolution uncertainty. In addition, because the smearing factors are determined with using not photons but electrons, mismodeling of electron $\rightarrow$ photon extrapolation has impact on the mass resolution uncertainty. They are merged and estimated between 14.4 and 27.2 % depending on the category for $\sqrt{s} = 8$ TeV analysis, while 13.4 % for $\sqrt{s} = 7$ TeV analysis.

7.3.4.2 Pileup mismodeling

Since pileup events affect the energy resolution of the EM calorimeter, the pileup mismodeling leads to mass resolution uncertainty. A 3.0 (1.5) % uncertainty is assigned for $\sqrt{s} = 7$ (8) TeV analysis by comparing high and low pileup condition simulation samples.

Chapter 8

Observation of a Higgs boson and measurement of its properties

8.1 Observation of a Higgs boson

A likelihood is defined by using the signal and background model. Then a maximum likelihood fit is performed. From the fit results, the p-value for the background-only hypothesis is calculated for discovery of the Higgs boson.

8.1.1 Statistical method

The statistical analysis in this thesis is based on an unbinned maximum likelihood using $m_{\gamma\gamma}$ distribution. A signal strength μ, which represents the observed scale of signal event rate compared with the Standard Model prediction, is used as the hypothesized value for discovery of the Higgs boson. The μ is defined as:

$$\mu \equiv \frac{\sigma \cdot Br}{\sigma_{\rm SM} \cdot Br_{\rm SM}} \tag{8.1.1}$$

where $\sigma \cdot Br$ is the observed Higgs boson production cross section times decay branching fraction to $\gamma\gamma$ final state, and the subscript SM means the values are predicted by the Standard Model. The Higgs mass m_H is the other hypothesized value and scanned from 110 GeV to 150 GeV.

8.1.1.1 Likelihood

The likelihood L includes the information of the numbers and $m_{\gamma\gamma}$ shapes of signal and background events. It involves nuisance parameters which are not parameters of interest but must be determined from the fit. The nuisance parameters are associated to the systematic uncertainties of the numbers and shapes. The L is constructed from Poisson and constraint factors; $L = L_P \times L_\theta$, where L_P and L_θ are the Poisson and constraint factors, respectively. The Poisson factor is defined by:

$$L_P(\mu, m_H) = \prod_c^{N_{\rm cat}} \frac{1}{N_{{\rm evt},c}!} \exp\left(-\mu s_c - b_c\right) \prod_{i_c}^{N_{{\rm evt},c}} \left(\mu s_c f_{s,c}\left(m_{\gamma\gamma,i_c}|m_H\right) + b_c f_{b,c}\left(m_{\gamma\gamma,i_c}\right)\right) \tag{8.1.2}$$

where $N_{\rm evt}$ is the number of events in the data set, $N_{\rm cat}$ is the number of the event categories, s and b are the number of signal and background events, f_s and f_b are PDFs of signal and background for hypothesized m_H, the subscript c means the label of the event category and the subscript i is the label of the event number. The constraint factors are described as the product of Gaussian or asymmetric Gaussian functions which constrain nuisance parameters.

$$\begin{aligned} L_\theta =& \prod_j f_{\rm Gaus}\left(\theta_j\right) \prod_k f_{\rm asymGaus}\left(\theta_k\right) \\ f_{\rm Gaus}\left(\theta_j\right) \equiv& \frac{1}{\sqrt{2\pi}} \exp\left(-\frac{\theta_j^2}{2}\right) \\ f_{\rm asymGaus}\left(\theta_k\right) \equiv& \sqrt{\frac{2}{\pi}} \frac{\sigma_{L,k}}{\left(\sigma_{L,k} + \sigma_{R,k}\right)} \begin{cases} \exp\left(-\frac{\theta_k^2}{2}\right) & \theta_k < 0 \\ \exp\left(-\frac{\sigma_{L,k}^2 \theta_k^2}{2\sigma_{R,k}^2}\right) & \theta_k > 0 \end{cases} \end{aligned} \tag{8.1.3}$$

where θ is a nuisance parameter and $\sigma_{R(L)}$ is the corresponding upper(lower) error. The asymmetric Gaussian functions are used for the asymmetric uncertainties. The likelihood L can be written as the product of L_P and L_θ.

8.1.1.2 Nuisance parameter

The likelihood L has many nuisance parameters. The number of background events b is treated as a nuisance parameter which does not have any constraint. The parameters of the background functions are also nuisance parameters which are not constrained. On the other hand, nuisance parameters of s and f_s are constrained by Gaussian or asymmetric Gaussian functions. The uncertainties of signal yield and event migration between event categories affect s, while the uncertainties of mass scale and resolution affect f_s. All constrained nuisance parameters and corresponding systematic uncertainties are listed in Appendix F.

Signal yield The uncertainties of signal yield ($\sigma_{{\rm yield}1,c}$, $\sigma_{{\rm yield}2,c}$, ...) are estimated in Section 7.3.1. They are taken into account as scale factors, which are applied to the number of signal events. The scale factors are defined with four different ways:

$$\begin{aligned} s_c^a\left(\theta_{{\rm yield}l}\right) &= \exp\left(\sqrt{\ln\left(1+\sigma_{{\rm yield}l,c}^2\right)}\theta_{{\rm yield}l}\right) \\ s_c^b\left(\theta_{{\rm yield}l}\right) &= \exp\left(\sqrt{\ln\left(1+\sigma_{L,{\rm yield}l,c}^2\right)}\theta_{{\rm yield}l}\right) \\ s_c^c\left(\theta_{{\rm yield}l}\right) &= \left(1+\sigma_{L(R){\rm yield}l,c}\right)^{\theta_{{\rm yield}l}} \\ s_c^d\left(\theta_{{\rm yield}l}\right) &= \left(1+\sigma_{{\rm yield}l,c}\theta_{{\rm yield}l}\right) \end{aligned} \tag{8.1.4}$$

where $\theta_{\text{yield}l}$ is a nuisance parameter for the corresponding systematic uncertainty $\sigma_{\text{yield}l,c}$. These four formulas are different but have similar mean and variance values. A nuisance parameter θ_l does not have the label c because all categories have a common nuisance parameter except *spurious signal*. Since the uncertainties due to the *spurious signal* are not correlated among the event categories, different nuisance parameters are used for different categories.

The choice of the formula depends on the type of uncertainties. For *spurious signal*, $s_c^d\left(\theta_{\text{yield}l}\right)$ is used. For the other yield uncertainties, the $s_c\left(\theta_{\text{yield}l}\right)$ is restricted to positive value. Therefore $s_c^a\left(\theta_{\text{yield}l}\right)$, $s_c^b\left(\theta_{\text{yield}l}\right)$ or $s_c^c\left(\theta_{\text{yield}l}\right)$ is used. Particularly when the uncertainty is symmetric, $s_c^a\left(\theta_{\text{yield}l}\right)$ is used. On the other hand, because the uncertainties of branching ratio and cross section due to QCD scale have asymmetric values, $s_c^b\left(\theta_{\text{yield}l}\right)$ is used. By contrast, $s_c^c\left(\theta_{\text{yield}l}\right)$ is used for the cross section uncertainty due to PDF+α_S which also has asymmetric values. The QCD scale uncertainties have different nuisance parameters for different production processes except *WH* and *ZH*. The PDF+α_S uncertainties have two nuisance parameters. One is for ggF and *ttH* processes, while the other is for VBF, *WH* and *ZH* processes.

Event migration The event migration ($\sigma_{\text{mig1},c}$, $\sigma_{\text{mig2},c}$, ...) are estimated in Section 7.3.2. Scale factors are defined like the signal yield case:

$$s_c\left(\theta_{\text{mig}l}\right) = \left(1 + \sigma_{\text{mig}l,c}\theta_{\text{mig}l}\right) \tag{8.1.5}$$

where $\theta_{\text{mig}l}$ is a nuisance parameter for the corresponding systematic uncertainty $\sigma_{\text{mig}l,c}$. The$\theta_{\text{mig}l}$ is constrained by a Gaussian. The number of signal in category c is written as the product of $s_c\left(\theta_{\text{yield}l}\right)$ and $s_c\left(\theta_{\text{mig}l'}\right)$:

$$s_c = s_{c\,\text{nominal}} \prod_l s_c\left(\theta_{\text{yield}l}\right) \prod_{l'} s_c\left(\theta_{\text{mig}l'}\right) \tag{8.1.6}$$

where $s_{c\,\text{nominal}}$ is the expected nominal signal yield. The total signal yield $s_{\text{tot}} = \sum_c^{N_{\text{cat}}} s_c$ is independent of $\sigma_{\text{mig}l.c}$ because the total number of selected events cannot be changed by event migration.

Mass scale The uncertainties in the mass resolutions ($\sigma_{\text{res1},c}$, $\sigma_{\text{res2},c}$, ...) are estimated in Section 7.3.4. The peak position of the signal PDF is scaled by the following factor:

$$m_{\text{peak},c}\left(\theta_{\text{peak}l}\right) = \left(1 + \sigma_{\text{peak}l,c}\theta_{\text{peak}l}\right) \tag{8.1.7}$$

where $\theta_{\text{peak}l}$ corresponds to a nuisance parameter.

Mass resolution The mass resolution uncertainties ($\sigma_{\text{resol1},c}$, $\sigma_{\text{resol2},c}$, ...) are estimated in Section 7.3.4. The corresponding nuisance parameter $\theta_{\text{resol}l}$ shifts the sigma of the crystal ball and Gaussian function (σ_{CB}, σ_{GA}) by following factors:

$$\sigma_{\text{CB(GA)},c}\left(\theta_{\text{resol}l}\right) = \exp\left(\sqrt{\ln\left(1 + \sigma^2_{\text{resol}l,c}\right)}\theta_{\text{resol}l}\right) \tag{8.1.8}$$

The parameters of s, m_{peak} and $\sigma_{\text{CB(GA)}}$ for each category are written by:

$$
\begin{aligned}
s_c &= s_{c0} \prod_l s_c\left(\theta_{\text{yield}l}\right) \prod_{l'} s_c\left(\theta_{\text{mig}l'}\right) \\
m_{\text{peak},c} &= m_{\text{peak},c0} \prod_l m_{\text{peak},c}\left(\theta_{\text{peak}l}\right) \\
\sigma_{\text{CB(GA)},c} &= \sigma_{\text{CB(GA)}c0} \prod_l \sigma_{\text{CB(GA)}}\left(\theta_{\text{resol}l}\right)
\end{aligned}
\tag{8.1.9}
$$

where s_{c0}, $m_{\text{peak},c0}$ and $\sigma_{\text{CB(GA)}c0}$ are the nominal values.

8.1.1.3 Test statistic for $\mu \geq 0$

The discovery of Higgs boson is established by a frequentist significance test using a likelihood ratio as a test statistic. The test statistic is defined by:

$$
q_{\mu,m_H} \equiv \begin{cases} -2\ln\lambda\left(\mu, m_H\right) \equiv -2\ln\frac{L\left(\mu, m_H, \hat{\hat{\boldsymbol{\theta}}}\right)}{L\left(\hat{\mu}, m_H, \hat{\boldsymbol{\theta}}\right)} & \hat{\mu} \geq \mu \\ 0 & \hat{\mu} < \mu \end{cases}
\tag{8.1.10}
$$

where $\boldsymbol{\theta}$ is set of nuisance parameters, $\hat{\hat{\boldsymbol{\theta}}}$ are the values of $\boldsymbol{\theta}$ that maximize L for the specified μ and m_H, $\hat{\mu}$ and $\hat{\boldsymbol{\theta}}$ are the maximum likelihood estimators (MLEs) that maximize L with a given m_H. Higher values of q_{μ,m_H} thus correspond to increasing incompatibility between the data set and hypothesized μ and m_H. Therefore $q_{\mu,m_H} = 0$ for $\hat{\mu} < \mu$ means that we only test if $\hat{\mu}$ is larger than μ, in other words, this is one-sided test for lower limit.

Nuisance parameters broaden the distribution of the test statistic as a function of μ compared with a test statistic that has no nuisance parameter, or a test statistic that has fixed parameters. This reflects the systematic uncertainties decrease the sensitivity of discovery. The level of incompatibility can be shown by p-value as shown Eq.(8.1.11).

$$
p_{\mu,m_H} = \int_{q_{\mu,m_H}}^{\infty} f\left(q'_{\mu,m_H}|\mu, m_H\right) dq'_{\mu,m_H}
\tag{8.1.11}
$$

where $f\left(q'_{\mu,m_H}|\mu, m_H\right)$ is the PDF of q'_{μ,m_H} under the assumption of μ and m_H.

8.1.1.4 Asymptotic estimation

In order to find the p-value which is defined in Eq.(8.1.11), the PDF of q_{μ,m_H} is needed. One method is to generate many toy data sets from the information of the target data set then get the distribution $f\left(q'_{\mu,m_H}|\mu, m_H\right)$. Another method is asymptotic approximation that can be used for the case of the following equation is established:

$$
-2\ln\lambda\left(\mu\right) = \frac{\left(\mu - \hat{\mu}\left(m_H\right)\right)^2}{\sigma^2\left(m_H\right)} + \mathcal{O}\left(\frac{1}{\sqrt{N}}\right)
\tag{8.1.12}
$$

where $\hat{\mu}\left(m_H\right)$ follows a Gaussian function with a mean $\mu'\left(m_H\right)$ and standard deviation $\sigma\left(m_H\right)$ and N denotes the size of data set. In case of the $\mu'\left(m_H\right) = \mu$ and if we neglect the $\mathcal{O}\left((N)^{-\frac{1}{2}}\right)$ term in Eq.(8.1.12), the PDF is calculated by Wald [103] and Wilks [104].

$$
f\left(q'_{\mu,m_H}|\mu, m_H\right) = \frac{1}{2}\delta\left(q'_{\mu,m_H}\right) + \frac{1}{2\sqrt{2\pi}} \frac{1}{\sqrt{q'_{\mu,m_H}}} \exp\left(-\frac{q'_{\mu,m_H}}{2}\right)
\tag{8.1.13}
$$

then the p-value can be calculated as:

$$p_{\mu,m_H} = 1 - \Phi\left(\sqrt{q_{\mu,m_H}}\right) \tag{8.1.14}$$

where Φ is the cumulative distribution of the standard Gaussian.

For the discovery of the Higgs boson, a hypothesis $\mu = 0$ is tested. This means we test background-only hypothesis. If this hypothesis is rejected, we discover a new particle. Therefore $p_0\left(m_H\right) = p_{0,m_H}$ is used.

$$p_0\left(m_H\right) = 1 - \Phi\left(\sqrt{q_0\left(m_H\right)}\right) \tag{8.1.15}$$

where $q_0\left(m_H\right) = q_{0,m_H}$. Thus the significance $Z\left(m_H\right)$ for discovery can be written as:

$$Z\left(m_H\right) = 1 - \Phi^{-1}\left(1 - p_0\right) = \sqrt{q_0\left(m_H\right)} \tag{8.1.16}$$

where Φ^{-1} is the inverse of the Φ.

m_H is scanned to seek significantly small $p_0\left(m_H\right)$, hence large $Z\left(m_H\right)$ for the discovery of the Higgs boson. If a standard Higgs boson has a mass m'_H, the distribution of the observed p_0-value has a narrow peak at m'_H, and at the mass point, $p_{0,\,\mathrm{obs}} = p_{0,\,\mathrm{exp}}$ is expected, where $p_{0,\,\mathrm{exp(obs)}}$ is an expected (observed) p_0-value. In addition, $p_{0,\,\mathrm{obs}} = 1$ is expected except the surrounding the peak.

8.1.1.5 Asimov data set

The expected results are estimated with an Asimov data set which is generated from a signal and a background model for each m_H. The signal model has the nominal signal yield and shape for the specified m_H. The parameters of the background functions are given by fitting to the observed data set with background-only model. Consequently, an Asimov data set has the most probable $m_{\gamma\gamma}$ distribution under the hypothesis of certain m_H and μ.

Even though the observed data set is unbinned, Asimov data set is binned. Accordingly, the binning of the Asimov data set have to be enough fine. 1000 bins are used for the mass window from 100 to 160 GeV. For generation of an Asimov data set for the Standard Model Higgs hypothesis, the observed data set is fitted with signal + background model with fixing $\mu = 1$.

8.1.2 Results

Figure 6.2.15, 6.2.16, 6.2.17 and 6.2.18 show the signal + background model after the likelihood fit. The best fit value of the observed signal strength is $\hat{\mu} = 1.65$ at $m_H = 125$ GeV. The detail of coupling measurement is discussed in Section 8.2. Besides, the best fit value of Higgs mass is $\hat{m}_H = 126.8$ GeV. The mass measurement is described in Section 8.3. The MLEs of the signal and the background models are also obtained. Figure 8.1.1 and 8.1.2 show the best fit values and their uncertainties of constrained nuisance parameters in the observed data set.

When the estimation of a systematic uncertainty is proper, an observed value of a corresponding constrained nuisance parameter is consistent with 0, as well as the uncertainty is nominal value, that is 1. When an observed value is not consistent with the nominal

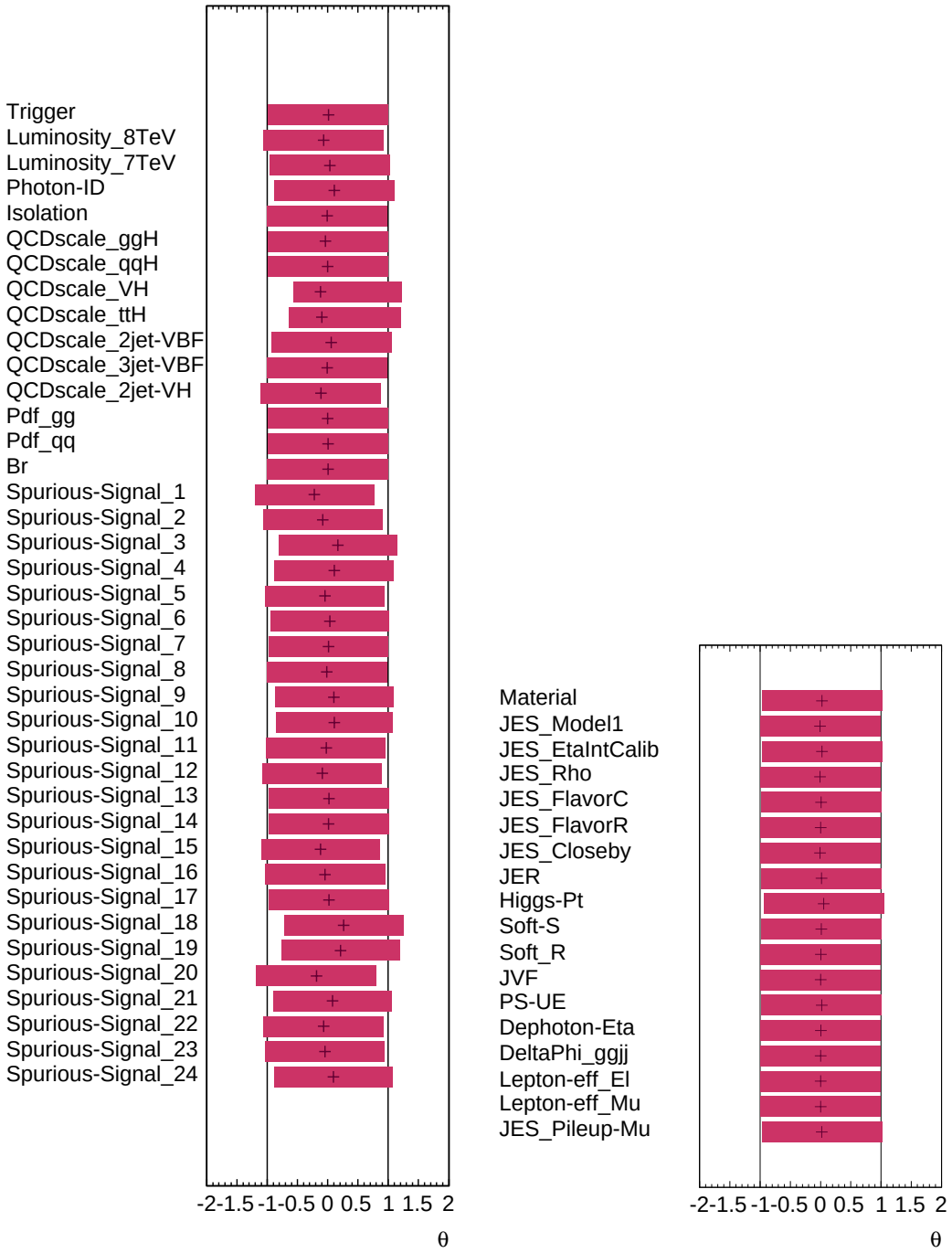

Figure 8.1.1: The maximum likelihood estimators corresponding to the signal yield uncertainties (a) and the event migration uncertainties (b). Markers show the best fit values, while the bands show their errors. (See Appendix F)

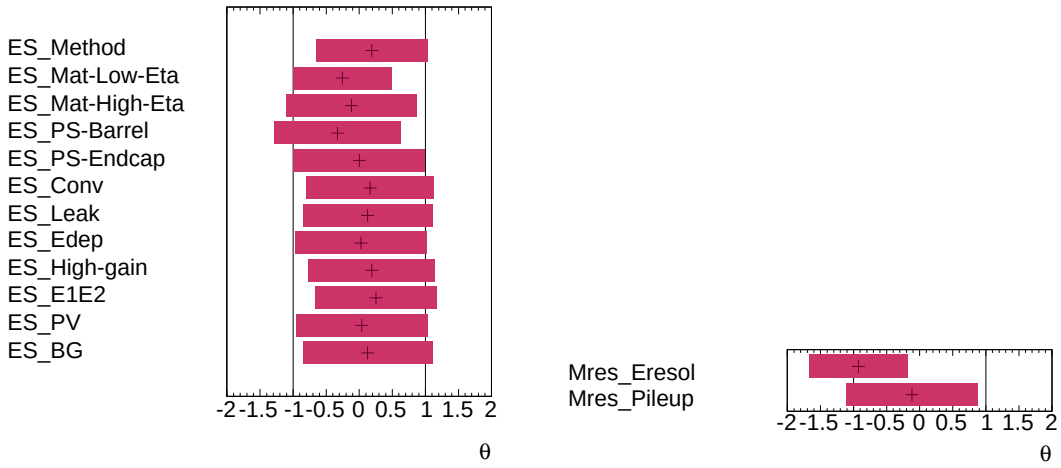

Figure 8.1.2: The maximum likelihood estimators corresponding to the mass scale uncertainties (a) and the mass resolution uncertainties (b). Markers show the best fit values, while the bands show their errors. (See Appendix F)

value, the estimation of a corresponding systematic uncertainty has to be checked. In addition, when the error of the observed value is significantly smaller than the nominal value, the corresponding observable is measured with better resolution than input uncertainty. In principle, a systematic uncertainty that has a constrained nuisance parameter is estimated from some control regions, and the estimation should have better sensitivity to the uncertainty. Hence the significantly small error suggests a mismeasurement. In the Figure 8.1.2, the observed value corresponding to the energy resolution is -0.93 ± 0.74. Therefore, the best fit value of mass resolution is smaller than expected because the observed resonance is narrower than the expected. However the difference from the nominal value is less than 1σ and not significant.

Figure 8.1.3 shows the distributions of the likelihood ratio $(-2\ln\lambda(\mu, m_H))$ for the observed and the expected data set. They are asymmetric distributions because $\hat{\mu}(m_H)$ follows not a Gaussian function but a Poisson function when assuming only statistical fluctuation. The difference of shapes between Gaussian and Poisson functions causes the asymmetric distribution. Some systematic uncertainties with asymmetric errors contribute the asymmetry of the distribution of the likelihood ratio as well. Although the distributions are asymmetric, Eq.(8.1.12) is established in both data sets[1]. Therefore the asymptotic approximation can be used for both data sets. Thus p_0-value is calculated by Eq.(8.1.15).

Figure 8.1.4 shows p_0-values for the observed and expected data sets. The energy scale of photons is fixed in this graph. The expected p_0-value is estimated for different hypothesized Higgs mass values with corresponding Asimov data sets. In the figure for the expected p_0-value at a hypothesized Higgs mass m'_H, an Asimov data set which is generated from a signal model when m'_H is hypothesized is used. Very large excess can be seen at ~ 125 GeV. The minimum observed p_0-value in combination of $\sqrt{s} = 7$ TeV

[1]When a distribution of a likelihood ratio is asymmetric, the uncertainty of $\hat{\mu}$ has an asymmetric uncertainty.

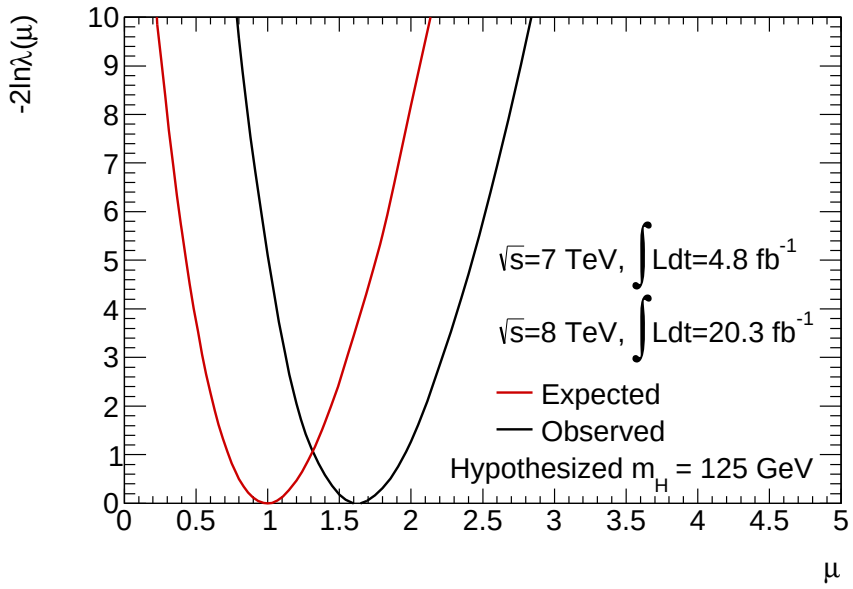

Figure 8.1.3: The likelihood ratio ($-2\ln\lambda(\mu, m_H)$) distributions when $m_H = 125$ GeV is hypothesized.

and $\sqrt{s} = 8$ TeV data sets is:

$$p_0\,(126.5\,\text{GeV}) = 3.5 \times 10^{-14} \tag{8.1.17}$$

(the significance $Z\,(126.5\,\text{GeV}) = 7.4\sigma$), with the expected p_0-value at the mass is:

$$p_0^{\text{exp}}\,(126.5\,\text{GeV}) = 1.3 \times 10^{-5} \tag{8.1.18}$$

($Z^{\text{exp}}\,(126.5\,\text{GeV}) = 4.1\sigma$). The observed excess is larger than the expected by the Standard Model. The observed μ is larger than the expected, and the observed mass peak is narrower. These two lead higher signal-to-background ratio, and then the larger excess. The p_0-values is also calculated for the inclusive analysis as shown in Figure 8.1.4. The expected and observed significance at $m_H = 126.5$ GeV is 2.9σ and 6.1σ, respectively.

These results give strong evidence of the discovery of a new particle. As discussed in Chapter 1, the observed particle is a boson but is not spin-1 particle. By combining the results from $H \to \gamma\gamma$, $H \to ZZ^* \to 4\ell$ and $H \to WW^* \to \ell\nu\ell\nu$ channels, the ATLAS collaboration published a paper on evidence for the spin-0 nature of the observed boson in July 2013 [105]. The spin-0 hypothesis was compared with spin-1 and spin-2 hypotheses. The observed data was compatible with the spin-0 hypothesis. The hypotheses of spin-1 and spin-2 were excluded at confidence levels above 97.8 %. Considering together with the boson having couplings with W and Z boson [9], the results from the ATLAS experiment indicate that the boson is a Higgs boson. Hence a Higgs boson is observed with di-photon events alone. The following sections describe the measurements of the Higgs boson properties.

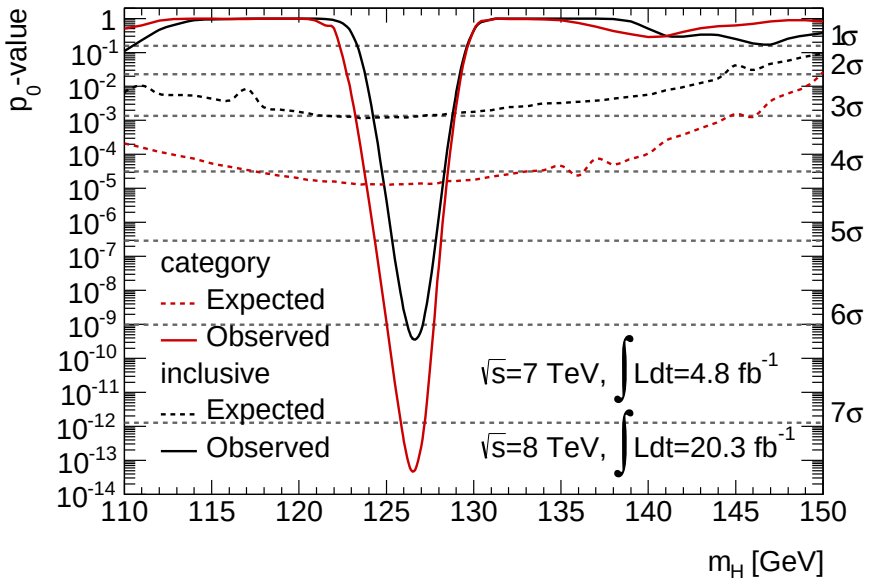

Figure 8.1.4: p_0-values of the observed and expected data set as a function of hypothesized m_H.

8.2 Coupling measurement

The Higgs coupling measurement is a crucial test for the Standard Model as described in Section 1.2.2. Besides, since many BSM theories predict sizable deviation in the Higgs coupling, precise measurement of each Higgs coupling is a probe of new physics. Because the sensitivity to the direct coupling measurements is still limited by the data statistics, the signal strength for total $H \to \gamma\gamma$ process, or signal strengths for each production process are measured in this chapter.

8.2.1 Statistical method

For Higgs coupling measurement, the same likelihood for observation is used. m_H is treated as a free parameter. When assuming each Higgs production process has a common signal strength, a signal strength μ is used as a parameter of interest. In this case, the following test statistic is used:

$$q_\mu \equiv -2\ln\lambda(\mu) = -2\ln\frac{L\left(\mu,\,\hat{\hat{m}}_H,\,\hat{\hat{\boldsymbol{\theta}}}\right)}{L\left(\hat{\mu},\,\hat{\hat{m}}_H,\,\hat{\hat{\boldsymbol{\theta}}}\right)} \tag{8.2.1}$$

This is two-sided test unlike the test statistic for observation because both upper and lower errors are estimated in the coupling measurement. As Figure 8.1.3 shows, q_μ is described by:

$$q_\mu = -2\ln\lambda(\mu) = \frac{(\mu-\hat{\mu})^2}{\sigma^2_{L(R)}} \tag{8.2.2}$$

Hence the asymptotic approximation is established. The best fit value $\hat{\mu}$ is given by the minimum point of q_μ, and the upper and lower errors ($\sigma_{L(R)}$) are given by the points

$q_\mu = 1$. When a constrained nuisance parameter is fixed to the MLE, the estimated error (σ') is reduced by a corresponding systematic error (σ'_{syst}): $\sigma' = \sqrt{\sigma^2 - \sigma'^2_{\text{syst}}}$. When all constrained nuisance parameters are fixed, the statistical error σ_{stat} is estimated. The total systematic error σ_{syst} is calculated by:

$$\sigma_{\text{syst}} = \sqrt{\sigma^2_{\text{total}} - \sigma^2_{\text{stat}}} \tag{8.2.3}$$

Because this is two-sided test, the p-value of μ is expressed with rewriting Eq.(8.1.4):

$$p_\mu = 2\left(1 - \Phi\left(\sqrt{q_\mu}\right)\right) \tag{8.2.4}$$

When assuming each process has each signal strength separately, three test statistics for each signal strength ($\mu_{\text{ggF}+ttH}$, μ_{VBF} and μ_{VH}) are defined. In a test statistic for a coupling, other couplings are treated as free parameters.

$$\begin{aligned}
q_{\mu_{\text{ggF}+ttH}} \equiv -2\ln\lambda\left(\mu_{\text{ggF+ttH}}\right) &= -2\ln\frac{L\left(\mu_{\text{ggF}+ttH},\, \hat{\mu}_{\text{VBF}},\, \hat{\mu}_{VH},\, \hat{m}_H,\, \hat{\boldsymbol{\theta}}\right)}{L\left(\hat{\mu}_{\text{ggF}+ttH},\, \hat{\hat{\mu}}_{\text{VBF}},\, \hat{\hat{\mu}}_{VH},\, \hat{\hat{m}}_{HH},\, \hat{\hat{\boldsymbol{\theta}}}\right)} \\
q_{\mu_{\text{VBF}}} \equiv -2\ln\lambda\left(\mu_{\text{VBF}}\right) &= -2\ln\frac{L\left(\mu_{\text{VBF}},\, \hat{\mu}_{\text{ggF}+ttH},\, \hat{\mu}_{VH},\, \hat{m}_H,\, \hat{\boldsymbol{\theta}}\right)}{L\left(\hat{\mu}_{\text{VBF}},\, \hat{\hat{\mu}}_{\text{ggF}+ttH},\, \hat{\hat{\mu}}_{VH},\, \hat{\hat{m}}_H,\, \hat{\hat{\boldsymbol{\theta}}}\right)} \\
q_{\mu_{\text{VH}}} \equiv -2\ln\lambda\left(\mu_{VH}\right) &= -2\ln\frac{L\left(\mu_{VH},\, \hat{\mu}_{\text{ggF}+ttH},\, \hat{\mu}_{\text{VBF}},\, \hat{m}_H,\, \hat{\boldsymbol{\theta}}\right)}{L\left(\hat{\mu}_{VH},\, \hat{\hat{\mu}}_{\text{ggF}+ttH},\, \hat{\hat{\mu}}_{\text{VBF}},\, \hat{\hat{m}}_H,\, \hat{\hat{\boldsymbol{\theta}}}\right)}
\end{aligned} \tag{8.2.5}$$

For the study of correlation between $\mu_{\text{VBF}+VH}$ and $\mu_{\text{ggF}+ttH}$, another test statistic with the fraction of $\mu_{\text{VBF}+VH}$ and $\mu_{\text{ggF}+ttH}$ is defined:

$$\begin{aligned}
q_{\mu_{\text{VBF}+VH}/\mu_{\text{ggF}+ttH}} &\equiv -2\ln\lambda\left(\mu_{\text{VBF}+VH}/\mu_{\text{ggF}+ttH}\right) \\
&= -2\ln\frac{L\left(\mu_{\text{VBF}+VH}/\mu_{\text{ggF}+ttH},\, \hat{\mu}_{\text{ggF}+ttH},\, \hat{m}_H,\, \hat{\boldsymbol{\theta}}\right)}{L\left(\mu_{\text{VBF}+VH}/\mu_{\text{ggF}+ttH},\, \hat{\hat{\mu}}_{\text{ggF}+ttH},\, \hat{\hat{m}}_H,\, \hat{\hat{\boldsymbol{\theta}}}\right)}
\end{aligned} \tag{8.2.6}$$

where $\mu_{\text{VBF}} = \mu_{VH} = \mu_{\text{VBF}+VH}$ is assumed.

8.2.2 Results

Figure 8.2.1a shows the distributions o f q_μ for the observed data set. The $\hat{\mu}$ is measured to be:

$$\hat{\mu} = 1.65 \pm 0.24(\text{stat.}) \,{}^{+0.25}_{-0.18}\, (\text{syst.}) \tag{8.2.7}$$

From comparison of q_μ with fixing some nuisance parameters, the impacts of each systematic uncertainty are estimated. The dominant systematic uncertainties are summarized in Table 8.2.1. The QCD scale uncertainty for the cross section of the Higgs production and the mass resolution uncertainty have the largest contributions to the systematic uncertainty on the μ measurement. The total systematic and statistical uncertainties are

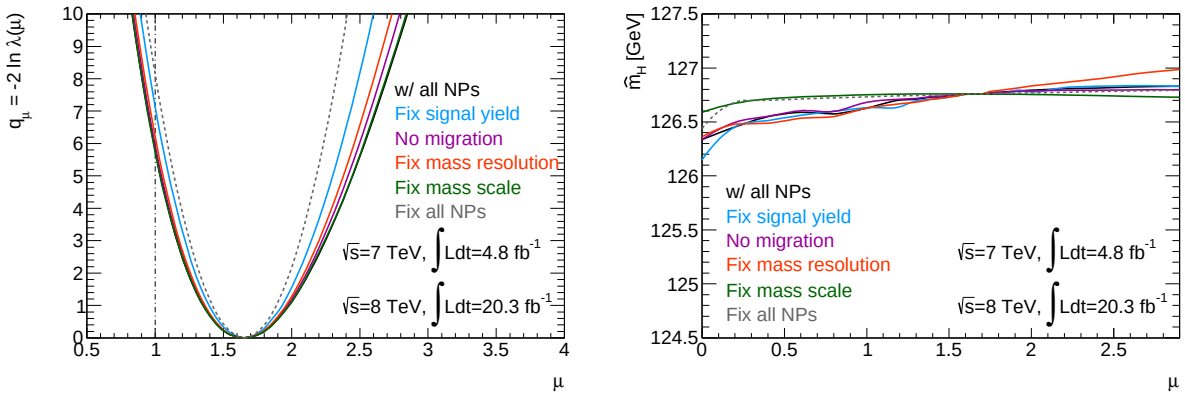

(a) (b)

Figure 8.2.1: Distribution of q_μ for the observed data set with several configurations (a). The best fit value of m_H for each hypothesized μ (b). "w/ all NPs" means fit using all constrained nuisance parameters, that is nominal results. "Fix signal yield", "No migration", "Fix mass resolution" and "Fix mass scale" show distributions with fixing some constrained nuisance parameters at the best fit values. Dashed line shows distribution when all constrained nuisance parameters are fixed.

approximately equal. Because m_H is a free parameter to fit, $\hat{m}_H$ can be different for different μ. Figure 8.2.1b shows the best fit value of m_H for each hypothesized μ. The μ dependence on $\hat{m}_H$ is 0.2 GeV per $\Delta\mu = 1$ due to the mass scale uncertainties. The consistency with the Standard Model prediction is tested with p-value at $\mu = 1$: p_1. From Figure 8.2.1a, $p_1 = 1.1$ % is obtained, which corresponds to 2.3σ. The measured signal strength is consistent with the Standard Model with in 2.3σ.

Figure 8.2.2 shows the test statistics of $\mu_{\mathrm{ggF}+t\bar{t}H}$, μ_{VBF}, μ_{VH} and $\mu_{\mathrm{VBF}+VH}/\mu_{\mathrm{ggF}+t\bar{t}H}$.

Systematic Uncertainty	$\Delta\mu$
QCD scale	$^{+0.15}_{-0.07}$
Mass resolution	$^{+0.11}_{-0.10}$
Branching ratio	$^{+0.08}_{-0.08}$
Luminosity	$^{+0.06}_{-0.04}$
Identification	$^{+0.05}_{-0.06}$

Table 8.2.1: Dominant systematic uncertainties on measurement of μ.

The best fit values for each production process are:

$$\begin{aligned}
\hat{\mu}_{\mathrm{ggF}+ttH} &= 1.6 \pm 0.3(\mathrm{stat.}) \, ^{+0.3}_{-0.2} \, (\mathrm{syst.}) \\
\hat{\mu}_{\mathrm{VBF}} &= 1.7 \pm 0.8(\mathrm{stat.}) \, ^{+0.5}_{-0.4} \, (\mathrm{syst.}) \\
\hat{\mu}_{VH} &= 1.8 \, ^{+1.5}_{-1.3} \, (\mathrm{stat.}) \pm 0.3(\mathrm{syst.})
\end{aligned} \tag{8.2.8}$$

The statistic uncertainties on μ_{VBF} and μ_{VH} are still large. The signal yield systematic uncertainty dominates in $\mu_{\mathrm{ggF}+ttH}$, while the event migration for μ_{VBF} and μ_{VH}. The signal strength is larger than 1 for 3 different production processes.

The signal strengths checks consistencies with the Standard Model on the products of the production process (ggF, VBF, *VH*, *ttH*) and the Higgs decay ($H \to \gamma\gamma$). Their ratios cancel the Higgs decay part and compare only production processes. The ratio $\mu_{\mathrm{VBF}+VH}/\mu_{\mathrm{ggF}+ttH}$ is measured to be :

$$\mu_{\mathrm{VBF}+VH}/\mu_{\mathrm{ggF}+ttH} = 1.1 \, ^{+0.7}_{-0.5} \, (\mathrm{stat.}) \, ^{+0.3}_{-0.2} \, (\mathrm{syst.}) \tag{8.2.9}$$

as shown in Figure 8.2.2. This is consistent with the Standard Model prediction ($\mu_{\mathrm{VBF}+VH}/\mu_{\mathrm{ggF}+ttH} = 1$). It indicates that the observed large μ values for each process could be larger due to the Higgs decay loop unless the cross section of all the production processes. In this case, as described in Section 1.2.2, the candidates of new particles may have no color charge but electromagnetic charge. Many models are proposed to enhance the $H \to \gamma\gamma$ rate: for example, charged scalar [106, 107], heavy fermion [108, 109] and heavy charged gauge boson [107]. In order to test these models, a combined analysis of many decay modes is critical. The increase of statistics is crucially important to improve the significance of the combined analysis. For example, the $H \to Z\gamma$ mode has similar signature of the $H \to \gamma\gamma$ mode. Therefore the signal strength in the the $H \to Z\gamma$ mode has a similar dependence on new particles as the $H \to \gamma\gamma$ mode. However some BSM theories predict the different deviations of signal strengths from the Standard Model prediction between the two modes. Hence the comparison of the two modes is a test for some BSM theories. The property measurement of the Higgs boson in the $H \to Z\gamma$ analysis needs more statistics because the branching fraction is small as shown in Figure 1.2.5.

8.3 Mass measurement

The precise measurement of the Higgs mass is remarkably important to complete the Standard Model and to search BSM as described in Section 1.2.2. The $H \to \gamma\gamma$ channel has one of the highest precision of mass measurement.

8.3.1 Statistical method

A test statistic has a m_H as the parameter of interest. μ is treated as a free parameter for a likelihood fit.

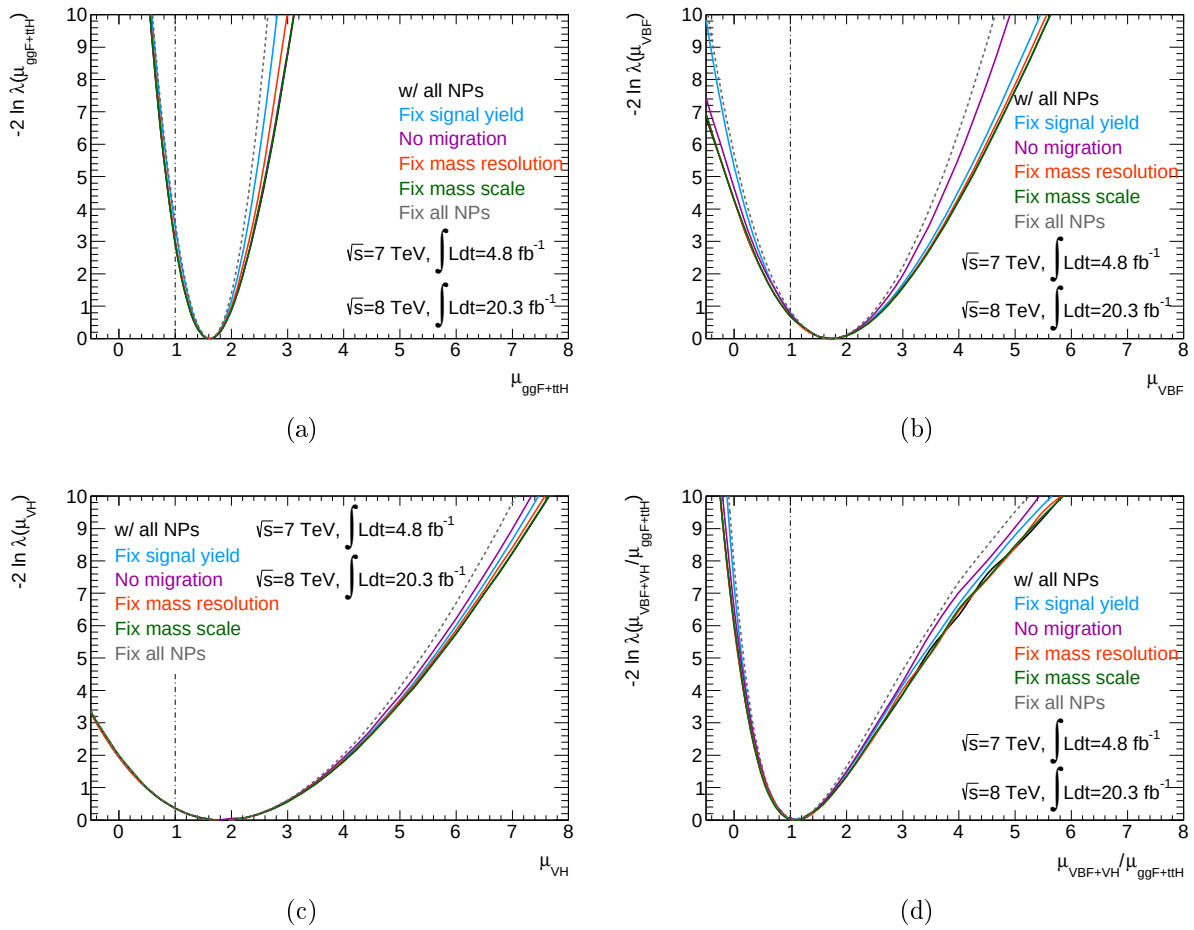

Figure 8.2.2: Distributions of test statistics for $\mu_{\mathrm{ggF}+ttH}$ (a), μ_{VBF} (b), μ_{VH} (c) and $\mu_{\mathrm{VBF}+VH}/\mu_{\mathrm{ggF}+ttH}$ (d) for the observed data set with several configurations. The meanings of each line are the same as Figure 8.2.1.

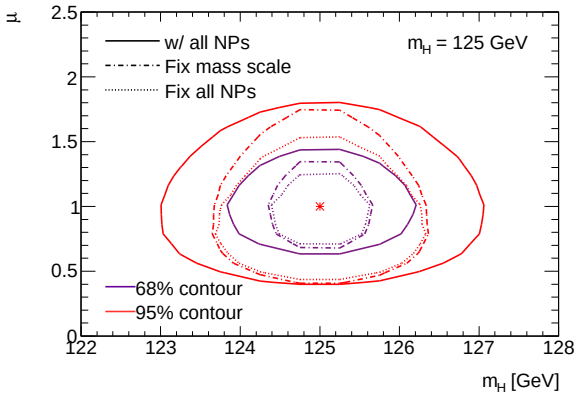

Figure 8.3.1: $-2\ln\lambda(\mu, m_H)$ distribution in μ-m_H plane for Asimov data set under the hypothesized $m_H = 125$ GeV. "w/ all NPs" means fit using all constrained nuisance parameters, that is nominal results. "Fix mass scale" shows distribution with fixing constrained nuisance parameters corresponding to mass scale uncertainties at the best fit values. "Fix all NPs" shows distribution when all constrained nuisance parameters are fixed.

$$q_{m_H} \equiv -2\ln\lambda(m_H) = -2\ln\frac{L\left(m_H,\,\hat{\hat{\mu}},\,\hat{\hat{\boldsymbol{\theta}}}\right)}{L\left(\hat{m}_H,\,\hat{\mu},\,\hat{\boldsymbol{\theta}}\right)} \tag{8.3.1}$$

This is two-sided test. The best fit value of m_H ($\hat{m}_H$) is given by $q_{\hat{m}_H} = 0$. The error of m_H is obtained from the point $q_{m_H} = 1$.

8.3.2 Results

Figure 8.3.1 shows the distribution of $-2\ln\lambda(\mu, m_H)$ in μ-m_H plane for an Asimov data set when the Higgs mass is hypothesized $m_H = 125$ GeV as well as the signal strength is $\mu = 1$. The best fit values of m_H and μ agree with their hypothesized values. One of the merits of the $H \to \gamma\gamma$ channel for the mass measurement is the low correlation between the signal strength and the measured mass as this figure shows. The Higgs mass can be measured almost independently of the signal strength.

Figure 8.3.2 shows the distributions of q_{m_H} for the observed data set. The $\hat{m}_H$ is measured to be:

$$\hat{m}_H = 126.8 \pm 0.2(\text{stat.}) \pm 0.7(\text{syst.})\,\text{GeV} \tag{8.3.2}$$

The statistical uncertainty is estimated in the same way as the measurement of μ. The systematical uncertainty is calculated by comparing the total end the statistical error.

Substituting $\hat{m}_H$ into Eq.(1.1.21), the Higgs potential parameters λ and μ_ϕ^2 are estimated:

$$\begin{aligned} \lambda &\simeq 0.133 \\ \mu_\phi^2 &\simeq -(90\,\text{GeV})^2 \end{aligned} \tag{8.3.3}$$

where $v \simeq 246.22$ GeV [15] is used. From the results, the stability of the vacuum is estimated to be metastability as shown in Figure 1.2.9. Therefore, the vacuum can fall negative infinity at the Planck scale, but the probability of the falling to wrong vacuum

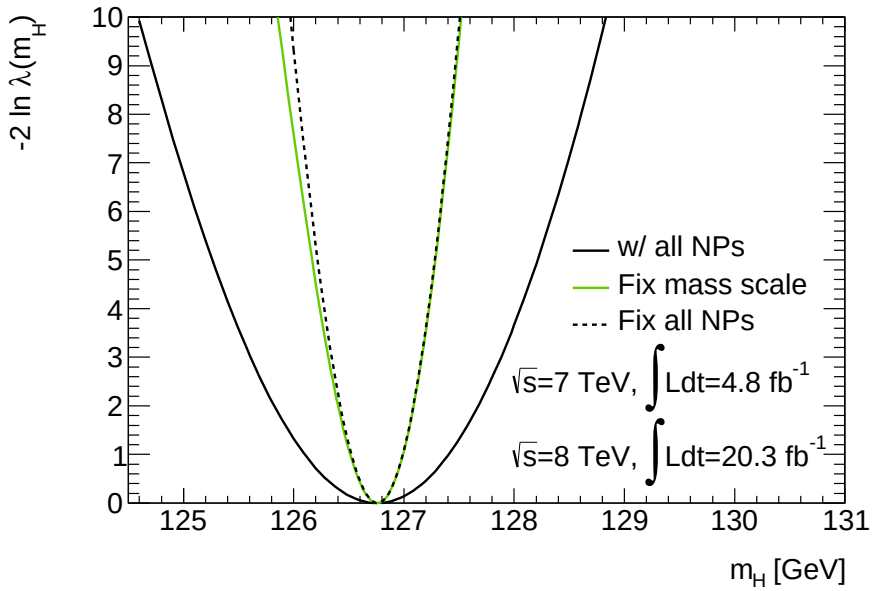

Figure 8.3.2: Distributions of $q_{m_H} = -2\ln\lambda(m_H)$. "w/ all NPs" means fit using all constrained nuisance parameters, that is nominal results. "Fix mass scale" shows distributions with fixing nuisance parameters corresponding to mass scale uncertainties at the best fit values. Dashed line shows distribution when all constrained nuisance parameters are fixed.

is too low. The vacuum is not instable up to the Planck scale under the Standard Model, and then the vacuum stability does not need a new physics.

8.4 Direct measurement of natural width

The natural width of Higgs boson is one of the most important properties especially for studies of invisible decay and BSM. This section describes a direct measurement of the natural width using the shape of $m_{\gamma\gamma}$ peak. The natural width is predicted ~ 4 MeV in FWHM for $m_H \sim 125$ GeV by the Standard Model as described in Section 1.2.1. On the other hand, the uncertainty of mass resolution is ~ 100 MeV, thus the accuracy of this study does not reach the expected width. Consequently, this is a search for a large deviation from the Standard Model. Some theories of BSM predict wider natural width, hence this study can give a constraint on BSM without any hypothesis.

8.4.1 Statistical method

A measurement of the natural width of Higgs uses a likelihood that has the natural width (w) as a parameter of interest. μ and m_H are used as free parameters. The signal shape is changed by w. In the likelihood, the signal shape is changed to have the natural width w by convoluting the nominal shape (Crystal Ball + Gaussian) with the Breit-Wigner function which has the width w. The Breit-Wigner function is defined as:

$$f_{BW} = N\frac{1}{m_{\gamma\gamma}^2 + w^2/4} \tag{8.4.1}$$

where N is a normalization factor. The signal function is convoluted after the event selection. The signal MC samples have the Standard Model natural width (4 MeV for $m_H \sim 125$ GeV) when they are generated. However the impact of the Standard Model natural width is negligible because of the uncertainty of the mass resolution of about 100 MeV.

8.4.1.1 Test statistic

In order to give an upper limit on the natural width, one-sided test is used. The test statistic for one-sided test is therefore defined as:

$$q_w \equiv \begin{cases} -2\ln\lambda(w) = -2\ln\frac{L\left(w,\hat{\mu},\hat{m}_H,\hat{\hat{\boldsymbol{\theta}}}\right)}{L\left(\hat{w},\hat{\mu},\hat{m}_H,\hat{\hat{\boldsymbol{\theta}}}\right)} & (w > \hat{w}) \\ 0 & (w < \hat{w}) \end{cases} \tag{8.4.2}$$

Because Breit-Wigner function which is used for the convolution cannot have negative width, we have a physical boundary at $w = 0$. Due to the boundary, the asymptotic approximation cannot be used. Therefore the p-value is measured by a toy MC study.

8.4.1.2 Toy MC study

In toy MC study, a number of pseudo-data sets are generated with signal and background models.

1. The parameters in the likelihood are given from fitting to the observed or expected data sets for a fixed tested value $w = w_{\text{test}}$. As a result, the maximum likelihood estimators for each nuisance parameters ($\hat{\hat{\boldsymbol{\theta}}}$) are obtained.

2. In order to take errors of MLEs into account, the nuisance parameters that have constraints (e.g. luminosity and $p_{\text{T}t}$ uncertainty) are randomized as their constraints. For example, a nuisance parameter θ that has a Gaussian constraint is given the best fit value $\hat{\theta}$ and the error σ_θ at the first step. Then the parameter is randomized with a Gaussian which mean is $\hat{\theta}$ and sigma is σ_θ.

3. Pseudo-data sets are generated with given parameters.

4. The generated pseudo-data sets are fitted with a free width w and a fixed test width w_{test}, and then $q_{w_{\text{test}}}$ is obtained.

5. The second, third and fourth steps are repeated 1000 times.

6. The confidence levels are estimated from the histogram of $q_{w_{\text{test}}}$, i.e. p-value for w_{test} is calculated as
$$p(w_{\text{oe}}) = \int_{q_{w_{\text{oe}}}}^{\infty} F\left(q_{w_{\text{test}}}|w_{\text{test}}\right) dq_{w_{\text{test}}} \tag{8.4.3}$$
where $q_{w_{\text{oe}}}$ represents the observed or expected test statistic.

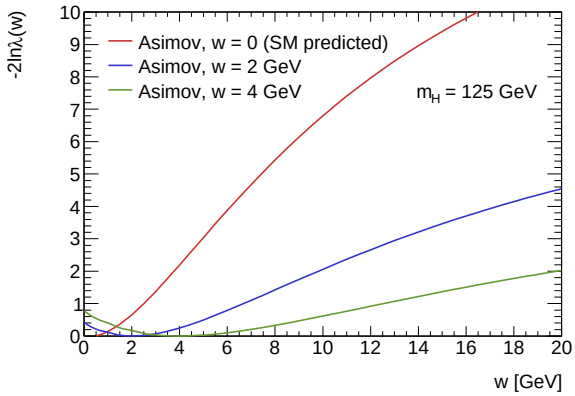

Figure 8.4.1: Distributions of $-2\ln\lambda(w)$ for Asimov data sets with several hypothesized natural width.

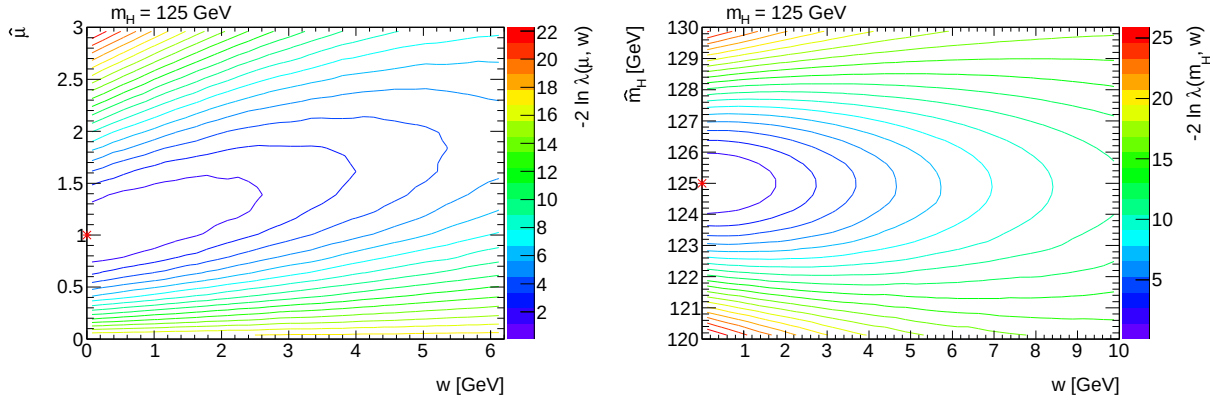

(a) (b)

Figure 8.4.2: Correlation between w and $\hat{\mu}$ for expected data set (a). Correlation between w and $\hat{m}_H$ for expected data set (b). The expected data set is generated with $w = 0$ and $m_H = 125$ GeV.

8.4.2 Results

Figure 8.4.1 shows the distributions of $-2\ln\lambda(w)$ for several Asimov data sets that have hypothesized natural width $w = 0$, 2, 4 GeV. The Asimov data set with $w = 0$ corresponds the standard expected data set. As expected, $-2\ln\lambda(w)$ is minimum at the generated width. The correlations between w and the best fit values of the signal strength and the Higgs mass of the standard expected data set are shown in Figure 8.4.2. The slope of $\hat{\mu}$ against w at $w = 0$ is 0.2 GeV^{-1}. This is because the likelihood is larger when the height of signal shape is matched to the data. In contrast, the correlation between $\hat{m}_H$ and w is negligibly small.

Figure 8.4.3a compares $-2\ln\lambda(w)$ between the observed and the standard expected data sets. The maximum likelihood is given by $w = 0$ in both data sets. This is consistent with the Standard Model prediction. Thus a large deviation from the Standard Model is not observed. The observed data set has very sharp $-2\ln\lambda(w)$ shape compared with the expected data set. In order to investigate the cause, a special Asimov data set that has

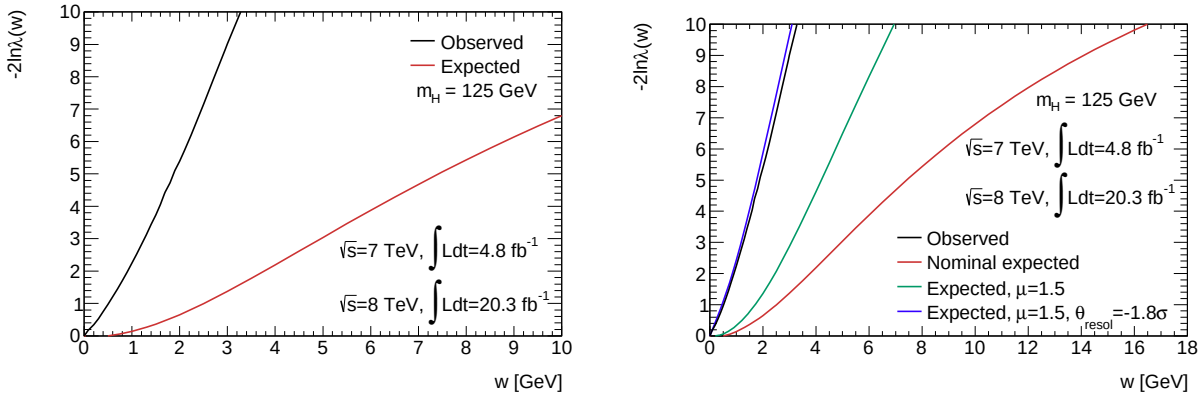

(a) (b)

Figure 8.4.3: Distributions of $-2\ln\lambda(w)$ for the observed and expected data set (a). Distributions of $-2\ln\lambda(w)$ for special Asimov data sets that have the large signal strength and the narrow mass resolution (b).

$\mu = \hat{\mu}_{\rm obs}$ and a nuisance parameter of mass resolution $\theta^{\rm resol} = \hat{\theta}^{\rm resol}_{\rm obs}$ is generated, where $\hat{\mu}_{\rm obs}$ and $\hat{\theta}^{\rm resol}_{\rm obs}$ are the best fit values in the observed data set. Figure 8.4.3b shows that the special Asimov data set has very similar $-2\ln\lambda(w)$ shape as the observed data set. Hence the observed difference on the $-2\ln\lambda(w)$ curves is due to the observation of the narrow mass resonance with the large μ.

The upper limit on natural width in FWHM with 95 % CL is estimated to be:

$$w < 1.8\,{\rm GeV}\ ({\rm observed}) \tag{8.4.4}$$

$$w < 5.8\,{\rm GeV}\ ({\rm expected}) \tag{8.4.5}$$

Figure 8.4.5 shows the PDF of q_w obtained from pseudo-data sets for $w_{\rm test} = 1.8$ GeV. The p-value is then calculated from Eq.(8.4.3). The $1-p$-value corresponds to the confidence level. As described above, the observed large μ and the narrow $m_{\gamma\gamma}$ peak make the upper limit for the observed data set small. The contribution of statistical uncertainty is estimated by fitting the pseudo-data sets with fixing all constrained nuisance parameters as shown in Figure 8.4.4. The resulting upper limit without systematic uncertainty is $w < 1.6$ GeV (95 % CL) for observed data set. The contribution of the systematic uncertainty is estimated by subtracting the contribution of the statistical uncertainty from the total upper limit: $w = 0.8$ GeV.

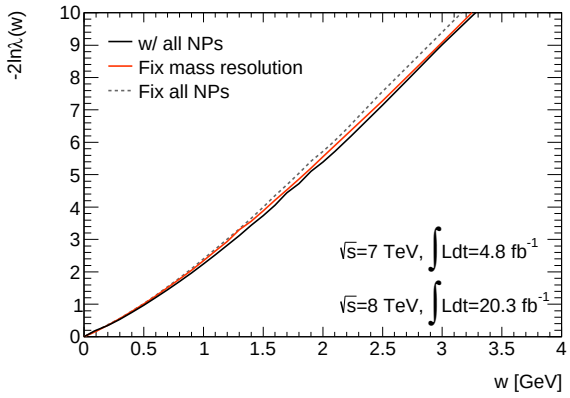

Figure 8.4.4: Distributions of $-2\ln\lambda(w)$ for the observed data set. "w/ all NPs" means fit using all constrained nuisance parameters, that is nominal results. "Fix mass resolution" shows distributions with fixing nuisance parameters corresponding to mass resolution uncertainties at the best fit values. Dashed line shows distribution when all constrained nuisance parameters are fixed.

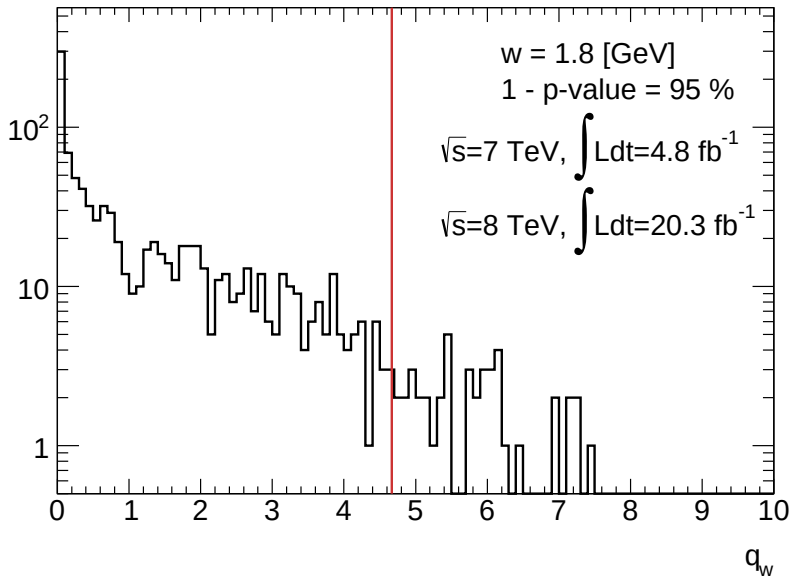

Figure 8.4.5: PDF of q_w obtained from pseudo-data sets for $w_{\rm test} = 1.8$ GeV. Red line shows the observed $q_{w_{\rm test}}$. $1-p$-value is estimated to be 95 %.

Chapter 9

Conclusion

A search for the Standard Model Higgs boson in di-photon final states is performed using data collected with the ATLAS detector in proton-proton collisions at $\sqrt{s} = 7$ TeV with an integrated luminosity of 4.8 fb^{-1} and $\sqrt{s} = 8$ TeV with 20.3 fb^{-1}.

The Higgs field gives mass to elementary particles through the gauge symmetry breaking of $SU(2)_L \times U(1)_Y$ into $U(1)_{EM}$. The Higgs boson is the visible manifestation of the Higgs field, and couples with massive particles. The dominant production processes in proton-proton collisions are gluon-gluon fusion, vector boson fusion, associated production with a W or Z boson, or associated production with a pair of top quarks. The Higgs boson decays into di-photon via a t/W loop. Although the branching fraction of di-photon final state is smaller than many other decay modes, the $H \to \gamma\gamma$ mode has a large significance for the discovery of the Higgs boson because of the high efficiency of event reconstruction, a sharp peak at the Higgs mass in the di-photon invariant mass distribution.

The set of selection criteria of signal region for the $H \to \gamma\gamma$ analysis removes fake photons due to the presence of a leading π^0 resulting from the fragmentation of a quark or a gluon. The selected events are divided into 10 categories for $\sqrt{s} = 7$ TeV analysis and 14 categories for $\sqrt{s} = 8$ TeV analysis in order to improve the sensitivities for the discovery and for the property measurement. The event categorization is performed such that different categories have different significances and have large fractions of different production processes.

Clear evidence for a Higgs boson resonance is discovered with the significance of 7.4σ in the two photon invariant mass spectrum above background expectations. Then the measurement of the Higgs boson properties is carried out. From all the measurement results, this particle is consistent with the Standard Model Higgs boson.

The mass of the Higgs boson, which is an input parameter of the Standard Model, is measured with the signal peak shape. The mass is determined with 0.6 % accuracy:

$$m_H = 126.8 \pm 0.2(\text{stat.}) \pm 0.7(\text{syst.})\,\text{GeV}.$$

Under the Standard Model, the Higgs potential is determined by the Higgs mass:

$$\lambda \simeq 0.133$$
$$\mu_\phi^2 \simeq -(90\,\text{GeV})^2$$

From the numbers of observed events in each category, the overall signal strength μ,

which denotes a cross section times branching fraction normalized to the Standard Model prediction, is estimated to be:

$$\mu = 1.65 \pm 0.24(\text{stat.}) \begin{smallmatrix} +0.25 \\ -0.18 \end{smallmatrix} (\text{syst.}).$$

The total cross section times branching fraction are predicted to be 38.4 fb and 49.0 fb for $\sqrt{s} = 7$ and 8 TeV, respectively, in the Standard Model. The signal strength for each production process is:

$$\begin{aligned} \mu_{\text{ggF}+ttH} =& 1.6 \pm 0.3(\text{stat.}) \begin{smallmatrix} +0.3 \\ -0.2 \end{smallmatrix} (\text{syst.}) \\ \mu_{\text{VBF}} =& 1.7 \pm 0.8(\text{stat.}) \begin{smallmatrix} +0.5 \\ -0.4 \end{smallmatrix} (\text{syst.}) \\ \mu_{VH} =& 1.8 \begin{smallmatrix} +1.5 \\ -1.3 \end{smallmatrix} (\text{stat.}) \pm 0.3(\text{syst.}), \end{aligned}$$

where $\mu_{\text{ggF}+ttH}$ is signal strength for gluon-gluon fusion and associated production with a pair of top quarks, μ_{VBF} is for vector boson fusion and μ_{VH} is for associated production with a W or Z boson. The fraction of $\mu_{\text{VBF}+VH}$ and $\mu_{\text{ggF}+ttH}$ is estimated to be:

$$\mu_{\text{VBF}+VH}/\mu_{\text{ggF}+ttH} = 1.1 \begin{smallmatrix} +0.7 \\ -0.5 \end{smallmatrix} (\text{stat.}) \begin{smallmatrix} +0.3 \\ -0.2 \end{smallmatrix} (\text{syst.}).$$

The results of signal strength measurement are summarized in Figure 9.0.1. The most probable values of the signal strengths are larger than 1, and are consistent in different production processes. The measured signal strength is estimated to be consistent with the Standard Model with in 2.3σ. However, if new particles make the signal strength larger, they may have impacts on the decay loop. Many candidates are proposed to enhance the $H \to \gamma\gamma$ rate: charged scalar, heavy fermion and heavy charged gauge boson. The significance to test these models is increased by a combined analysis of many decay modes and increase of statistics.

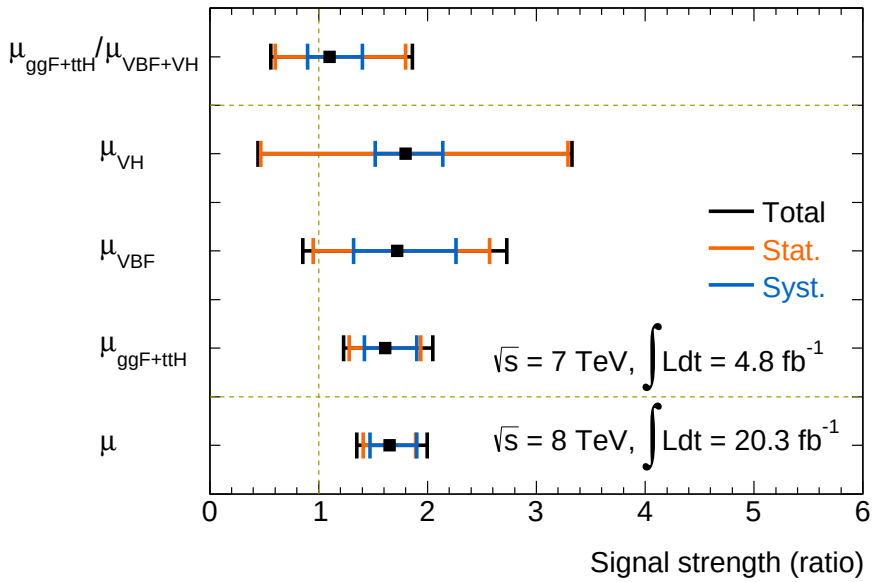

Figure 9.0.1: Measured signal strengths for the different production processes, overall strength μ and the ratio of strength for the Yukawa coupling production and the gauge coupling production $\mu_{\mathrm{VBF}+VH}/\mu_{\mathrm{ggF}+ttH}$.

A search for deviation of the natural width of the Higgs boson from the Standard Model prediction with the width of signal peak is presented. No significant deviation is observed, thus the upper limit on natural width of the Higgs boson is estimated. The observed upper limit is estimated to be:

$$w < 1.8\,\mathrm{GeV}\,(95\,\%\,\mathrm{CL})$$

The discovery of the Higgs boson was a great achievement to complete the Standard Model. The measurement of Higgs boson properties is a probe of new physics beyond the Standard Model. Further data will reveal the nature of the Higgs boson more precisely in order to see whether the Standard Model is still valid or the physics beyond the Standard Model can be found in a TeV energy scale. A new era of particle physics has started with this discovery.

Acknowledgments

I would like to express my deepest appreciation to my supervisor, Prof. Sachio Komamiya. I thank him for introducing me to wonders of scientific research. I thank him for encouraging me during this work.

I am really grateful to Prof. Junichi Tanaka. He has been teaching me all about research at the ATLAS. I think I could not accomplish this study without his instruction, help and encouragement.

I would like to warmly thanks Dr. Taiki Yamamura for his guidance and assistance, and for giving me valuable insights into the Higgs search.

Staff members of International Center for Elementary Particle Physics (ICEPP) in the university of Tokyo, Prof. Tatsuo Kawamoto, Prof. Asai Shoji, Prof. Naoko Kanaya, Prof. Yuji Enari, Prof. Koji Terashi , Prof. Shimpei Yamamoto, Prof. Yousuke Kataoka, Dr. Tatsuya Masubuchi, Dr. Koji Nakamura, Dr. Takashi Yamanaka and Dr. Keita Hanawa, they have been helping and teaching me very kindly and professionally. I would like to express my gratitude to them. Prof. Enari gave me a lot helpful suggestions to my thesis.

I deeply appreciate the conveners and collaborators of the $H \to \gamma\gamma$ sub-working group. The conveners of the group, Prof. Tanaka, Prof. Krisztian Peters, Dr. Kerstin Tackmann, Dr. Nicolas Berger have been always taking care of my research. I also appreciate members of the e/gamma working group. Dr. Maarten Boonekamp has been helping and teaching me greatly.

I am very grateful to my friends in the same period in the University of Tokyo. I thank Mr. Yutaro Iiyama, Mr. Akira Miyazaki, Mr. Yuichi Sasaki, Mr. Shingo Kazama, Mr. Keisuke Yoshihara for numerous advices and inspiring discussions.

I am very grateful to Mr. Jean-Jacques Bauswein, Prof. Kanaya, Mr. Iiyama for supporting my life at CERN.

I want to express my sincere gratitude to past and present members of ICEPP and Komamiya laboratory, Mr. Takashi Goto, Mr. Kaoru Tanaka, Ms. Aine Kobayashi, Ms. Maya Okawa, Mr. Shingo Terao, Mr. Shingo Hisajima, Mr. Yuji Minegishi, Prof. Yoshio Kamiya, Dr. Shinsuke Kawasaki, Dr. Shinya Sonoda, Dr. Masahiro Oroku, Dr. Go Ichikawa, Ms. Jacqueline Yan, Mr. Yuto Minami, Ms. Misato Tani.

I would like to express my eternal gratitude to my family for their support.

Appendix A

Luminosity determination

The luminosity $\mathcal{L}$ delivered to the ATLAS detector is measured with the luminosity detectors described in Section 2.2.8 [38]. The luminosity can be converted to the average number of inelastic interactions per bunch crossing μ_{av}.

For a storage ring, the luminosity can be expressed as

$$\mathcal{L} = \frac{\mu_{\text{av}} n_b f_r}{\sigma_{\text{inel}}} \tag{A.0.1}$$

where n_b is the number of bunch pairs colliding per revolution, f_r is the revolution frequency and σ_{inel} is the pp inelastic cross-section. The observed interaction rate per crossing μ_{vis} is used for the luminosity measurement instead of μ_{av} because μ_{av} cannot be measured directly with the luminosity monitor. The luminosity can be written as

$$\mathcal{L} = \frac{\mu_{\text{vis}} n_b f_r}{\sigma_{\text{vis}}} \tag{A.0.2}$$

where $\sigma_{\text{vis}} = \epsilon\sigma_{\text{inel}}$ is the visible cross-section for a particular detector, and similarly $\mu_{\text{vis}} = \epsilon\mu_{\text{av}}$. n_b and f_r are determined by the LHC operating condition and μ_{vis} is an experimentally observable quantity.

A.1 μ_{vis} measurement

For μ_{vis} measurement, several algorithms are used. Especially for $\sqrt{s} = 7$ and 8 TeV data, an *EventOR* algorithm is used. In the algorithm, the luminosity monitor counts a bunch crossing when at least one hit is detected on either side of the detector. Since the visible number of interactions per bunch can be described by a Poisson distribution with the mean is μ_{vis}, the probability of observing at least one hit can be written as

$$1 - P\left(0|\lambda = \mu_{\text{vis}}\right) = 1 - \exp\left(-\mu_{\text{vis}}\right)$$

Then when N_{OR} events are counted during a number of bunch crossing N_{BC}, μ_{vis} is estimated as

$$\mu_{\text{vis}} = -\ln\left(1 - \frac{N_{\text{OR}}}{N_{\text{BC}}}\right) \tag{A.1.1}$$

For the estimation of μ_{vis}, the vertical pairs of BCM detectors are used. The basic time unit for storing luminosity information is the Luminosity Block (LB). Then μ_{vis} is averaged in every LB. The typical duration of each LB is one minute.

A.2 van der Meer scan

$\sigma_{\rm vis}$ in Eq.(A.0.2) can be measured with van der Meer (vdM) scans.

In term of the colliding-beam parameters, $\mathcal{L}$ is defined as

$$\mathcal{L} = n_b f_r n_1 n_2 \int \rho_1(x,y)\,\rho_2(x,y)\,dxdy \tag{A.2.1}$$

where n_1 and n_2 are bunch populations and $\rho_1(x,y)$ and $\rho_2(x,y)$ are the normalized densities in the transverse plane of beam 1 and 2 at the interaction point. $n_{1(2)}$ is measured with current monitors at the LHC.

Under the assumption that $\rho_{1(2)}(x,y)$ is a 2-dimensional Gaussian and both beams have the same sigma $\Sigma_{x(y)}/\sqrt{2}$, Eq.(A.2.1) can be rewritten as

$$\mathcal{L} = n_b f_r n_1 n_2 \int \frac{1}{(\pi\Sigma_x\Sigma_y)^2} \exp\left(-\frac{x^2}{\Sigma_x^2} - \frac{y^2}{\Sigma_y^2} - \frac{(x-\delta_x)^2}{\Sigma_x^2} - \frac{(y-\delta_y)^2}{\Sigma_y^2}\right) dxdy \tag{A.2.2}$$

where $\delta_{x(y)}$ is the horizontal (vertical) distance between 2 beams. In a vdM scan, the beam are separated by steps of a known distance[1]. Therefore $\delta_{x(y)}$ in Eq.(A.2.2) is scanned. Thus $\Sigma_{x(y)}$ is measured from the shape of $\mathcal{L}$ as a function of $\delta_{x(y)}$.

In case of $\delta_x = \delta_y = 0$, Eq.(A.2.2) is described as

$$\mathcal{L} = \frac{n_b f_r n_1 n_2}{2\pi\Sigma_x\Sigma_y} \tag{A.2.3}$$

$\sigma_{\rm vis}$ is computed using Eq.(A.0.2) and (A.2.3):

$$\sigma_{\rm vis} = \mu_{\rm vis}^{\rm MAX} \frac{2\pi\Sigma_x\Sigma_y}{n_1 n_2} \tag{A.2.4}$$

where $\mu_{\rm vis}^{\rm MAX}$ is $\mu_{\rm vis}$ in case of $\delta_x = \delta_y = 0$, in other words the visible cross-section at the peak of the vdM scan. This is the calibration of $\sigma_{\rm vis}$. Because vdM scans cannot be performed during nominal physics runs, the measured $\sigma_{\rm vis}$ is used for physics runs after the scan.

$\mathcal{L}$ for physics runs are determined by substituting Eq.(A.2.4) and (A.1.1) to Eq.(A.0.2) for each LB. Based on the assumption $\sigma_{\rm inel} = 71.5$ mb [38], $\mu_{\rm av}$ is also computed using Eq.(A.0.1):

$$\mu_{\rm av} = \frac{\mathcal{L}\sigma_{\rm inel}}{n_b f_r}$$

[1] The scale of the step is calibrated by the vertex reconstruction with the inner detector.

Appendix B

Electron reconstruction

B.1 Reconstruction procedure

Energy clusters in the EM calorimeter and tracks in the inner detector are used for electron reconstruction. The tracks are extrapolated to the calorimeter, and then the extrapolated tracks are required to match the clusters. Direction of electrons is determined by using tracks. In contrast, energy of electrons is measured with the EM calorimeter. The energy of electrons is corrected with the MVA calibration and $Z \to ee$ line shape correction.

B.2 Identification criteria

In the same way as photons, shower shape is used for separation from jets. The criteria are similar to but somewhat looser than those for photons. In addition, track parameters are also used for the identification: number of hits in the inner detector and transverse impact parameter (< 5mm).

B.2.1 Electron selection

Track and calorimeter isolation variables are computed with the inner detector and the EM calorimeter, respectively. The isolation criteria use the ratio of the isolation variables to p_{T} for relaxing the selection to high p_{T} electron candidates which have originally high purity. The longitudinal and transverse impact parameters with respect to the primary vertex z_0 and d_0 are used as well as σ_{d0}, which is the resolution of d_0 for separation from pileup jets. The impact parameters are not used for the $H \to \gamma\gamma$ analysis because of low primary vertex reconstruction efficiency. The selection criteria are summarized in Table B.2.1 and B.2.2.

Pass the identification criteria	
Transverse energy	$p_{\mathrm{T}} > 10$ GeV
Pseudo-rapidity	$\lvert\eta\rvert < 2.47$
Longitudinal impact parameter	$\lvert z_0\rvert < 1.5$ mm
Transverse impact parameter	$\lvert d_0\rvert / \sigma_{d0} < 10$
Calorimeter isolation	$E_{\mathrm{T}cone30}/p_{\mathrm{T}} < 0.18$
Track isolation	$p_{\mathrm{T}cone20}/p_{\mathrm{T}} < 0.1$

Table B.2.1: Electron Selection for $Z \to ll\gamma$ analysis.

Pass the identification criteria	
Transverse energy	$p_{\mathrm{T}} > 15$ GeV
Pseudo-rapidity	$\lvert\eta\rvert < 2.47$
Calorimeter isolation	$E_{\mathrm{T}cone40}/p_{\mathrm{T}} < 0.2$
Track isolation	$p_{\mathrm{T}cone20}/p_{\mathrm{T}} < 0.15$

Table B.2.2: Electron Selection for $H \to \gamma\gamma$ analysis.

Appendix C

Muon reconstruction

C.1 Reconstruction procedure

Tracks are reconstructed with the ID and the Muon spectrometer individually. Then muons are reconstructed from combined tracks between ID and the Muon spectrometer. Direction of muons is determined by the tracks. In MC simulation, the momentum is smeared such that they have the same momentum resolution as observed data in $Z \to \mu\mu$ peak.

C.2 Muon selection

The impact parameters and isolation variables are used for separation from jets. Table C.2.1 and C.2.2 summarize the muon selection.

Pass the identification criteria	
Transverse energy	$p_{\mathrm{T}} > 10$ GeV
Pseudo-rapidity	$\lvert\eta\rvert < 2.5$
Longitudinal impact parameter	$\lvert z_0\rvert < 5$ mm
Transverse impact parameter	$\lvert d_0\rvert < 1.5$ mm
Calorimeter isolation	$E_{Tcone40}/p_{\mathrm{T}} < 0.25$
Track isolation	$p_{\mathrm{T}cone20}/p_{\mathrm{T}} < 0.15$

Table C.2.1: Muon Selection for $Z \to ll\gamma$ analysis.

Pass the identification criteria	
Transverse energy	$p_{\mathrm{T}} > 10$ GeV
Pseudo-rapidity	$\lvert\eta\rvert < 2.7$
Longitudinal impact parameter	$\lvert z_0\rvert < 10$ mm
Transverse impact parameter	$\lvert d_0\rvert < 1$ mm
Calorimeter isolation	$E_{Tcone40}/p_{\mathrm{T}} < 0.2$
Track isolation	$p_{\mathrm{T}cone20}/p_{\mathrm{T}} < 0.15$

Table C.2.2: Muon Selection for $H \to \gamma\gamma$ analysis.

Appendix D

Jet reconstruction

D.1 Reconstruction procedure

Jets are reconstructed from the energy clusters in the hadronic and hadronic calorimeter as well as the EM calorimeter. The hadronic clusters are obtained by topological clustering: group of calorimeter cells topologically connected (η, ϕ and R direction). Then clusters are merged with "anti-k_{T}" algorithm [95] if the distances are nearer than a certain threshold. The distance d_{ij} between the i-th and j-th hadronic cluster is defined as:

$$d_{ij} = \min\left(\frac{1}{p_{\mathrm{T}\,i}^2}, \frac{1}{p_{\mathrm{T}\,j}^2}\right)\frac{(\mathrm{y}_i - \mathrm{y}_j)^2 + (\phi_i - \phi_j)^2}{R^2}$$

where $p_{\mathrm{T}\,i}$ is transverse momentum, y_i is rapidity, ϕ_i is azimuthal angle of i-th cluster, and R is cone size. The threshold d_{min} is defined as:

$$d_{min} = \min\left(d_{ij}, \frac{1}{p_{\mathrm{T}\,i}^2}\right)$$

If $d_{ij} < d_{min}$, the i-th cluster is merged with the j-th cluster by calculating vector sum of four-momenta of clusters. Then d_{min} of the new cluster object is evaluate for all the remaining clusters. This procedure is repeated until the all of the jet candidates are not remained. Then the merged cluster is assumed as a jet candidate.

After jet reconstruction, the energy is rescaled from EM scale to hadronic scale [110]. The calibration factor is obtained from MC simulation. The energy loss in the dead material is also corrected. The correction restores the calorimeter response of the reconstructed jet to the true jet response

D.2 Jet vertex fraction

Event categorization in the $H \to \gamma\gamma$ analysis requires jets from a primary vertex (Section 6.2). For effective categorization, jets from a hard process are separated from pileup jets. Jet Vertex Fraction (JVF), which is the sum of p_{T} of all matched-tracks from a given primary vertex candidate by total jet-matched track, measures the probability that a jet

originated from a primary vertex. When $track_1$, $track_2$, ..., $track_n$ in the jet are associated to the primary vertex, while $track_{n+1}$, $track_{n+2}$, .., $track_m$ are not, JVF is defined as:

$$\mathrm{JVF} \equiv \frac{\sum_i^n p_{\mathrm{T}}^{track_i}}{\sum_j^m p_{\mathrm{T}}^{track_j}} \tag{D.2.1}$$

If a jet is a pileup jet like, JVF is close to 0, whereas a jet coming from a primary vertex has JVF close to 1. The separation of a hard process jet and a pileup jet by JVF depends on the efficiency of the primary vertex selection.

The uncertainty of the JVF is estimated with Z+jet events, where Z boson decays di-lepton. When the p_{T} of Z boson and jet are well balanced and they are back-to-back, the jet is produced at the ISR. The jet is used for estimation of the JVF efficiency for hard process jets. On the other hand when the Z boson is at rest and the Z boson and jet are unbalanced, the jet is a pileup jet. Then the jet is used for estimation of JVF performance for pileup jets.

D.3 Uncertainty of jet energy scale

Flavor response uncertainty The jet energy scale is derived for a particular admixture of light-quark and gluon jets. For a different admixture, the jet energy scale uncertainty could be different. This uncertainty is estimated using MC with studying the difference between the gluon and light-quark jet response under various assumptions.

Flavor composition uncertainty The fraction of light-quark and gluon jets in samples for jet energy calibration in data could differ from the fraction predicted by the simulations, thus leading to a systematic shift in the jet energy scale.

OffsetMu uncertainty The pileup correction is applied based on MC-based studies. The amount of transverse momentum generated by pileup in a jet is estimated in MC simulation. The pileup offset is subtracted from the reconstructed jet p_{T} as a function of the average number of inelastic interactions. The uncertainty of pileup correction is derived from the difference between data/MC using di-jet and γ+jet events.

Pileup uncertainty After the pileup correction as a function of the average number of inelastic interactions, the remaining pileup influence is suppressed based on energy depositions outside hard jets. The uncertainty is estimated from a potential mis-modeling of the sample dependence. The difference of the energy depositions outside hard jets between data and MC is evaluated in di-jet, γ+jet and Z+jet events.

Model 1 uncertainty The energy calibration uncertainty is estimated from comparison between MC generators (HERWIG and PYTHIA).

EtaCalib uncertainty The MC-based calibration is validated by a jet eta intercalibration. The validation is performed with physics processes in which the transverse momenta of a Z boson or a photon are balancing to the transverse momentum of a jet. The uncertainty on the jet energy scale correction is estimated with the intercalibration.

Close-By uncertainty The jet energy scale is determined with isolated jets that have no other jet within a certain distance. Presence of any jets near-by could cause difference in jet response, and hence result in a JES systematic uncertainty.

Appendix E

Event migration summary

	Material	Higgs p_{T}	Underlying
Unconverted central, low $p_{\mathrm{T}t}$	−4.0 %	1.1 %	
Unconverted central, high $p_{\mathrm{T}t}$	−4.0 %	−12.5 %	
Unconverted rest, low $p_{\mathrm{T}t}$	−4.0 %	1.1 %	
Unconverted rest, high $p_{\mathrm{T}t}$	−4.0 %	−12.5 %	
Converted central, low $p_{\mathrm{T}t}$	+3.5 %	1.1 %	
Converted central, high $p_{\mathrm{T}t}$	+3.5 %	−12.5 %	
Converted rest, low $p_{\mathrm{T}t}$	+3.5 %	1.1 %	
Converted rest, high $p_{\mathrm{T}t}$	+3.5 %	−12.5 %	
Converted transition	+3.5 %	1.1 %	
Di-jet		−9.0 %	VBF: 6.0 %
			the others: 30 %

Table E.0.1: Migration uncertainties due to material mapping, Higgs p_{T} and underlying event for $\sqrt{s} = 7$ TeV analysis.

	Material	JVF	Higgs p_{T}	Underlying
Unconverted central, low $p_{\mathrm{T}t}$	−4.0 %		1.3 %	
Unconverted central, high $p_{\mathrm{T}t}$	−4.0 %		−10.2 %	
Unconverted rest, low $p_{\mathrm{T}t}$	−4.0 %		1.3 %	
Unconverted rest, high $p_{\mathrm{T}t}$	−4.0 %		−10.2 %	
Converted central, low $p_{\mathrm{T}t}$	+3.5 %		1.3 %	
Converted central, high $p_{\mathrm{T}t}$	+3.5 %		−10.2 %	
Converted rest, low $p_{\mathrm{T}t}$	+3.5 %		1.3 %	
Converted rest, high $p_{\mathrm{T}t}$	+3.5 %		−10.2 %	
Converted transition	+3.5 %		1.3 %	
Loose VBF		ggF: −1.2 % VBF: -0.3 %	−8.5 %	VBF: 3.9 % the others: 12.0 %
Tight VBF			−10.4 %	VBF: 2.0 % the others: 8.8 %
Low mass di-jet		ggF: −2.3 % VBF: −2.4 %	1.3 %	VBF: 3.3 % the others: 12.8 %
$E_{\mathrm{T}}^{\mathrm{miss}}$significance			−2.0 %	
One-lepton			−4.0 %	

Table E.0.2: Migration uncertainties due to the material mapping, JVF, Higgs p_{T} and underlying event for $\sqrt{s} = 8$ TeV analysis.

	$\eta^{\star}$	$\lvert\phi^{\gamma\gamma} - \phi^{jj}\rvert$	Lepton (electron)	Lepton (muon)
Untagged				
Loose VBF	ggF: 6.2 %	ggF: 8.5 %		
Tight VBF	ggF: 7.6 %	ggF: 12.1 %		
Low mass di-jet				
$E_{\mathrm{T}}^{\mathrm{miss}}$significance				
One-lepton			WH: 0.7 % ZH: 0.9 % ttH: 0.7 %	WH 0.2 %: ZH: 0.3 % ttH: 0.2 %

Table E.0.3: Migration uncertainties due to $\eta^{\star}$, $\lvert\phi^{\gamma\gamma} - \phi^{jj}\rvert$ and lepton efficiencies for $\sqrt{s} = 8$ TeV analysis.

		JES Close-By	JES Model 1	JES EtaCalib
ggF	Low $p_{\mathrm{T}t}$	-0.0 %	-0.0 %	-0.0 %
	High $p_{\mathrm{T}t}$	0.0 %	0.0 %	0.0 %
	$E_{\mathrm{T}}^{\mathrm{miss}}$	7.2 %	4.5 %	5.8 %
VBF	Low $p_{\mathrm{T}t}$	-0.0 %	0.0 %	-0.0 %
	High $p_{\mathrm{T}t}$	0.0 %	-0.0 %	-0.0 %
	$E_{\mathrm{T}}^{\mathrm{miss}}$	10.5 %	6.2 %	8.6 %
VH/*ttH*	Low $p_{\mathrm{T}t}$	-0.1 %	-0.0 %	-0.0 %
	High $p_{\mathrm{T}t}$	0.1 %	0.0 %	-0.0 %
	$E_{\mathrm{T}}^{\mathrm{miss}}$	0.5 %	-0.2 %	0.3 %

Table E.0.4: Migration uncertainties due to $E_{\mathrm{T}}^{\mathrm{miss}}$ uncertainties coming from JES uncertainties in the $E_{\mathrm{T}}^{\mathrm{miss}}$ significance category for $\sqrt{s} = 8$ TeV analysis.

		JER	Soft Scale	Soft Resolution
ggF	Low $p_{\mathrm{T}t}$	-0.0 %	-0.0 %	-0.0 %
	High $p_{\mathrm{T}t}$	0.0 %	-0.0 %	-0.0 %
	$E_{\mathrm{T}}^{\mathrm{miss}}$	16.3 %	60.0 %	21.1 %
VBF	Low $p_{\mathrm{T}t}$	-0.0 %	-0.0 %	-0.0 %
	High $p_{\mathrm{T}t}$	-0.0 %	0.0 %	0.0 %
	$E_{\mathrm{T}}^{\mathrm{miss}}$	11.0 %	22.4 %	10.0 %
VH/*ttH*	Low $p_{\mathrm{T}t}$	-0.0 %	-0.1 %	0.0 %
	High $p_{\mathrm{T}t}$	0.0 %	0.1 %	-0.1 %
	$E_{\mathrm{T}}^{\mathrm{miss}}$	-0.1 %	1.0 %	0.2 %

Table E.0.5: Migration uncertainties due to $E_{\mathrm{T}}^{\mathrm{miss}}$ uncertainties coming from JER and CellOut uncertainties in the $E_{\mathrm{T}}^{\mathrm{miss}}$ significance category for $\sqrt{s} = 8$ TeV analysis.

	ggF	VBF	the others
Low $p_{\mathrm{T}t}$	-0.0 %	-0.7 %	-0.0 %
High $p_{\mathrm{T}t}$	-0.1 %	-1.1 %	-0.0 %
Di-jet	5.4 %	2.1 %	4.9 %

Table E.0.6: Migration uncertainties due to JES OffsetMu uncertainty for $\sqrt{s} = 7$TeV analysis.

	ggF	VBF	the others
Low $p_{\mathrm{T}t}$	-0.0 %	-1.2 %	-0.0 %
High $p_{\mathrm{T}t}$	-0.2 %	-2.0 %	-0.0 %
Di-jet	7.9 %	3.7 %	5.1 %

Table E.0.7: Migration uncertainties due to JES Flavor Composition uncertainty for $\sqrt{s} = 7$ TeV analysis.

	ggF	VBF	the others
Low $p_{\mathrm{T}t}$	-0.0 %	-0.6 %	-0.0 %
High $p_{\mathrm{T}t}$	-0.1 %	-1.0 %	-0.0 %
Di-jet	3.5 %	1.9 %	2.0 %

Table E.0.8: Migration uncertainties due to JES Flavor Response uncertainty for $\sqrt{s} = 7$ TeV analysis.

	ggF	VBF	the others
Low $p_{\mathrm{T}t}$	-0.0 %	-0.3 %	0.0 %
High $p_{\mathrm{T}t}$	-0.2 %	-0.4 %	0.2 %
Loose VBF	3.3 %	1.3 %	-1.1 %
Tight VBF	3.1 %	1.9 %	7.4 %
Low mass di-jet	1.4 %	0.9 %	-0.4 %
$E_{\mathrm{T}}^{\mathrm{miss}}$significance	0.0 %	0.0 %	0.0 %
One-lepton	0.0 %	0.0 %	-0.1 %

Table E.0.9: Migration uncertainties due to JES Model 1 uncertainty for $\sqrt{s} = 8$ TeV analysis.

	ggF	VBF	the others
Low $p_{\mathrm{T}t}$	-0.1 %	-0.7 %	-0.0 %
High $p_{\mathrm{T}t}$	-0.4 %	-0.9 %	0.1 %
Loose VBF	6.8 %	2.6 %	2.8 %
Tight VBF	8.5 %	4.8 %	11.4 %
Low mass di-jet	0.4 %	-1.3 %	-0.4 %
$E_{\mathrm{T}}^{\mathrm{miss}}$significance	0.0 %	0.0 %	0.0 %
One-lepton	0.0 %	0.0 %	0.0 %

Table E.0.10: Migration uncertainties due to JES EtaCalib uncertainty for $\sqrt{s} = 8$ TeV analysis.

	ggF	VBF	the others
Low $p_{\mathrm{T}t}$	-0.0 %	-0.2 %	0.0 %
High $p_{\mathrm{T}t}$	-0.1 %	-0.2 %	-0.1 %
Loose VBF	1.6 %	0.8 %	-2.0 %
Tight VBF	1.5 %	1.0 %	7.3 %
Low mass di-jet	1.2 %	0.3 %	0.3 %
$E_{\mathrm{T}}^{\mathrm{miss}}$significance	0.0 %	0.0 %	0.0 %
One-lepton	0.0 %	0.0 %	-0.0 %

Table E.0.11: Migration uncertainties due to JES Pileup uncertainty for $\sqrt{s} = 8$ TeV analysis.

	ggF	VBF	the others
Low $p_{\mathrm{T}t}$	-0.1 %	-0.5 %	-0.1 %
High $p_{\mathrm{T}t}$	-0.0 %	-0.7 %	0.3 %
Loose VBF	6.5 %	2.3 %	2.0 %
Tight VBF	6.5 %	3.6 %	9.1 %
Low mass di-jet	2.9 %	1.1 %	0.8 %
$E_{\mathrm{T}}^{\mathrm{miss}}$significance	0.0 %	0.0 %	0.0 %
One-lepton	0.0 %	0.0 %	-0.1 %

Table E.0.12: Migration uncertainties due to JES Flavor Composition uncertainty for $\sqrt{s} = 8$ TeV analysis.

	ggF	VBF	the others
Low $p_{\mathrm{T}t}$	-0.0 %	-0.3 %	-0.0 %
High $p_{\mathrm{T}t}$	-0.2 %	-0.4 %	-0.2 %
Loose VBF	3.4 %	1.2 %	-1.2 %
Tight VBF	3.0 %	1.8 %	8.7 %
Low mass di-jet	1.8 %	0.8 %	0.6 %
$E_{\mathrm{T}}^{\mathrm{miss}}$significance	0.0 %	0.0 %	0.0 %
One-lepton	0.0 %	0.0 %	-0.1 %

Table E.0.13: Migration uncertainties due to JES Flavor Response uncertainty for $\sqrt{s} = 8$ TeV analysis.

	ggF	VBF	the others
Low $p_{\mathrm{T}t}$	-0.0 %	-0.2 %	0.1 %
High $p_{\mathrm{T}t}$	-0.2 %	-0.2 %	-0.2 %
Loose VBF	1.4 %	0.8 %	3.8 %
Tight VBF	2.1 %	0.9 %	-3.5 %
Low mass di-jet	2.6 %	1.4 %	-0.7 %
$E_{\mathrm{T}}^{\mathrm{miss}}$significance	0.0 %	0.0 %	0.0 %
One-lepton	0.0 %	0.0 %	-0.0 %

Table E.0.14: Migration uncertainties due to JES Close-By uncertainty for $\sqrt{s} = 8$ TeV analysis.

	ggF	VBF	the others
Low $p_{\mathrm{T}t}$	-0.0 %	0.2 %	0.0 %
High $p_{\mathrm{T}t}$	-0.3 %	0.2 %	0.6 %
Loose VBF	3.4 %	-0.7 %	1.2 %
Tight VBF	3.8 %	-1.3 %	7.0 %
Low mass di-jet	0.5 %	3.4 %	-1.3 %
$E_{\mathrm{T}}^{\mathrm{miss}}$significance	0.0 %	0.0 %	-0.0 %
One-lepton	-0.9 %	-0.5 %	-0.1 %

Table E.0.15: Migration uncertainties due to JER uncertainty for $\sqrt{s} = 8$ TeV analysis.

Appendix F

Tables of nuisance parameters

Nuisance parameter	Systematic uncertainty
ES_Method	Z line shape
ES_Mat-Low-Eta	Material $\|\eta\| < 1.8$
ES_Mat-High-Eta	Material $\|\eta\| > 1.8$
ES_PS-Barrel	Presampler barrel
ES_PS-Emdcap	Presampler endcap
ES_Conv	Conversion fraction
ES_Leak	Lateral leakage, e/γ difference
ES_Edep	Lateral leakage, energy dependence
ES_High-gain	High/medium gain
ES_E1E2	Layer intercalibration
ES_PV	Primary vertex
ES_BG	Background model

Table F.0.1: Nuisance parameters for mass scale and corresponding systematic uncertainties.

Nuisance parameter	Systematic uncertainty
Mres_Eresol	Energy smearing
Mres_Pileup	Pileup mismodeling

Table F.0.2: Nuisance parameters for mass resolution and corresponding systematic uncertainties.

Nuisance parameter	Systematic uncertainty
Trigger	trigger efficiency
Luminosity_8TeV	luminosity for $\sqrt{s} = 8$ TeV
Luminosity_7TeV	luminosity for $\sqrt{s} = 7$ TeV
Photon-ID	identification efficiency
Isolation	isolation efficiency
QCDscale_ggH	QCD scale for ggF cross section
QCDscale_VBF	QCD scale for VBF cross section
QCDscale_VH	QCD scale for WH and ZH cross sections
QCDscale_ttH	QCD scale for ttH cross section
QCDscale_2jet_VBF	QCD scale for ggF+2jet cross section in VBF enriched categories
QCDscale_3jet_VBF	QCD scale for ggF+3jet cross section in VBF enriched categories
QCDscale_2jet_VH	QCD scale for ggF+2jet cross section in VH enriched categories
Pdf_gg	PDF+α_S for ggF and ttH cross sections
Pdf_qq	PDF+α_S for VBF and VH cross sections
Br	branching fraction of Higgs to di-photon
Spurious_Signal_1	*spurious signal* in Unconverted central, low $p_{\mathrm{T}t}$ category for $\sqrt{s} = 8$ TeV
Spurious_Signal_2	*spurious signal* in Unconverted central, high $p_{\mathrm{T}t}$ category for $\sqrt{s} = 8$ TeV
Spurious_Signal_3	*spurious signal* in Unconverted rest, low $p_{\mathrm{T}t}$ category for $\sqrt{s} = 8$ TeV
Spurious_Signal_4	*spurious signal* in Unconverted rest, high $p_{\mathrm{T}t}$ category for $\sqrt{s} = 8$ TeV
Spurious_Signal_5	*spurious signal* in Converted central, low $p_{\mathrm{T}t}$ category for $\sqrt{s} = 8$ TeV
Spurious_Signal_6	*spurious signal* in Converted central, high $p_{\mathrm{T}t}$ category for $\sqrt{s} = 8$ TeV
Spurious_Signal_7	*spurious signal* in Converted rest, low $p_{\mathrm{T}t}$ category for $\sqrt{s} = 8$ TeV
Spurious_Signal_8	*spurious signal* in Converted rest, high $p_{\mathrm{T}t}$ category for $\sqrt{s} = 8$ TeV
Spurious_Signal_9	*spurious signal* in Converted transition category for $\sqrt{s} = 8$ TeV
Spurious_Signal_10	*spurious signal* in loose VBF category for $\sqrt{s} = 8$ TeV
Spurious_Signal_11	*spurious signal* in tight VBF category for $\sqrt{s} = 8$ TeV
Spurious_Signal_12	*spurious signal* in low mass di-jet category for $\sqrt{s} = 8$ TeV
Spurious_Signal_13	*spurious signal* in $E_{\mathrm{T}}^{\mathrm{miss}}$ significance category for $\sqrt{s} = 8$ TeV
Spurious_Signal_14	*spurious signal* in one-lepton category for $\sqrt{s} = 8$ TeV

Table F.0.3: Nuisance parameters for signal yield and corresponding systematic uncertainties.

Nuisance parameter	Systematic uncertainty
Spurious_Signal_15	*spurious signal* in Unconverted central, low $p_{\mathrm{T}t}$ category for $\sqrt{s} = 7$ TeV
Spurious_Signal_16	*spurious signal* in Unconverted central, high $p_{\mathrm{T}t}$ category for $\sqrt{s} = 7$ TeV
Spurious_Signal_17	*spurious signal* in Unconverted rest, low $p_{\mathrm{T}t}$ category for $\sqrt{s} = 7$ TeV
Spurious_Signal_18	*spurious signal* in Unconverted rest, high $p_{\mathrm{T}t}$ category for $\sqrt{s} = 7$ TeV
Spurious_Signal_19	*spurious signal* in Converted central, low $p_{\mathrm{T}t}$ category for $\sqrt{s} = 7$ TeV
Spurious_Signal_20	*spurious signal* in Converted central, high $p_{\mathrm{T}t}$ category for $\sqrt{s} = 7$ TeV
Spurious_Signal_21	*spurious signal* in Converted rest, low $p_{\mathrm{T}t}$ category for $\sqrt{s} = 7$ TeV
Spurious_Signal_22	*spurious signal* in Converted rest, high $p_{\mathrm{T}t}$ category for $\sqrt{s} = 7$ TeV
Spurious_Signal_23	*spurious signal* in Converted transition category for $\sqrt{s} = 7$ TeV
Spurious_Signal_24	*spurious signal* in di-jet category for $\sqrt{s} = 8$ TeV

Table F.0.4: Nuisance parameters for signal yield and corresponding systematic uncertainties.

Nuisance parameter	Systematic uncertainty
Material	Material mismodeling in front of the EM calorimeter
JES_Pileup-Mu	Jet energy scale (OffsetMu)
JES_FlavorC	Jet energy scale (Flavor Composition)
JES_FlavorR	Jet energy scale (Flavor Response)
JES_Model1	Jet energy scale (Model 1)
JES_EtaIntCalib	Jet energy scale (EtaCalib)
JES_Rho	Jet energy scale (Pileup)
JES_Closeby	Jet energy scale (Close-By)
JER	Jet energy resolution
JVF	Jet vertex fraction efficiency
Higgs-Pt	Higgs p_{T}
PS-UE	Underlying event
Lepton-eff_El	Electron efficiency
Lepton-eff_Mu	Muon efficiency
Soft-S	$E_{\mathrm{T}}^{\mathrm{miss}}$ uncertainty due to energy scale of cell out term
Soft_R	$E_{\mathrm{T}}^{\mathrm{miss}}$ uncertainty due to energy resolution of cell out term
Dephoton-Eta	$\eta^{\star}$
DeltaPhi_ggjj	$\lvert\phi^{\gamma\gamma} - \phi^{jj}\rvert$

Table F.0.5: Nuisance parameters for event migration and corresponding systematic uncertainties.

Bibliography

[1] F. Englert and R. Brout, *Broken symmetry and the mass of gauge vector mesons*, Phys. Rev. Lett. 13 (1964) 321.

[2] P. W. Higgs, *Broken symmetries, massless particles and gauge fields*, Phys. Lett. 12 (1964) 132.

[3] P. W. Higgs, *Broken symmetries and the masses of gauge bosons*, Phys. Rev. Lett. 13 (1964) 508.

[4] G. S. Guralnik, C. R. Hagen, and T. W. B. Kibble, *Global conservation laws and massless particles*, Phys. Rev. Lett. 13 (1964) 585.

[5] P. W. Higgs, *Spontaneous symmetry breakdown without massless bosons*, Phys. Rev. 145 (1966) 1156.

[6] T. W. B. Kibble, *Symmetry breaking in non-Abelian gauge theories*, Phys. Rev. 155 (1967) 1554.

[7] LEP Working Group for Higgs boson searches, ALEPH, DELPHI, L3, OPAL Collaboration, R. Barate et al., *Search for the standard model Higgs boson at LEP*, Phys.Lett. B565 (2003) 61–75, arXiv:hep-ex/0306033 [hep-ex].

[8] Tevatron New Physics, Higgs Working Group, CDF and D0 Collaboration, *Updated Combination of CDF and D0 Searches for Standard Model Higgs Boson Production with up to 10.0 fb−1 of Data*, arXiv:1207.0449 [hep-ex].

[9] ATLAS Collaboration, *Observation of a new particle in the search for the Standard Model Higgs boson with the ATLAS detector at the LHC*, Phys. Lett. B 716 (2012) 1, arXiv:1207.7214 [hep-ex].

[10] CMS Collaboration, *Observation of a new boson at a mass of 125 GeV with the CMS experiment at the LHC*, Phys. Lett. B 716 (2012) 30, arXiv:1207.7235 [hep-ex].

[11] S. L. Glashow, *Partial-symmetries of weak interactions*, Nucl. Phys. 22 no. 4, (1961) 579.

[12] S. Weinberg, *A Model of Leptons*, Phys. Rev. Lett. 19 (1967) 1264.

[13] A. Salam, *Weak and electromagnetic interactions*, in Elementary particle theory: relativistic groups and analyticity, N. Svartholm, ed., p. 367. Almqvist & Wiksell, 1968. Proceedings of the eighth Nobel symposium.

[14] G. 't Hooft and M. Veltman, *Regularization and Renormalization of Gauge Fields*, Nucl. Phys. B44 (1972) 189.

[15] J. Beringer et al.(PDG), PR D86, 010001 (2012) and 2013 update for the 2014 edition (http://pdg.lbl.gov).

[16] John F. Gunion, Howard E. Haber, Gordon L. Kane, and Sally Dawson. *The Higgs Hunter's. Guide*. Front.Phys., 80:1–448, 2000.

[17] LHC Higgs Cross Section Working Group, *Handbook of LHC Higgs Cross Sections: 1. Inclusive Observables*, CERN-2011-002 (2011), arXiv:1101.0593 [hep-ph].

[18] LHC Higgs Cross Section Working Group, *Handbook of LHC Higgs Cross Sections: 2. Differential Distributions*, CERN-2012-002 (2012), arXiv:1201.3084 [hep-ph].

[19] LHC Higgs Cross Section Working Group, *Handbook of LHC Higgs Cross Sections: 3. Higgs Properties*, CERN-2013-004 (2013), arXiv:1307.1347 [hep-ph].

[20] C. N. Yang, *Selection Rules for the Dematerialization of a Particle Into Two Photons*, Phys. Rev. 77 (1950) 242.

[21] M. E. Cabrera, J. A. Casas and R. R. de Austri, *The health of SUSY after the Higgs discovery and the XENON100 data*, arXiv:1212.4821 [hep-ph].

[22] G. Degrassi, S. Vita, J. Elias-Mir, J. Espinosa, G. Giudice, G. Isidori, and A. Strumia, *Higgs mass and vacuum stability in the Standard Model at NNLO*, Journal of High Energy Physics 2012 481 (2012) 1–33.

[23] CERN Document Server, http://cds.cern.ch/collection/Photos

[24] The LHCStudy Group, LHC – The Large HadronCollider – Conceptual Design, CERN/AC/95-05 (LHC) (1995).

[25] J. Wenninger et al., *Operation of the LHC at high luminosity and high stored energy*, Proceedings of IPAC2012, New Orleans, Louisiana, USA.

[26] G. Arduini, *Performance reach in the LHC for 2012*, Proceedings of Chamonix 2012 workshop on LHC Performance, Geneva, Switzerland.

[27] M. Kuhn et al., *LHC emittance preservation during the 2012 run*, Proceedings of the 2012 Evian workshop on LHC beam operation, Geneva, Switzerland.

[28] ATLAS Experiment Public Results: Luminosity Public Results, https://twiki.cern.ch/twiki/bin/view/AtlasPublic/LuminosityPublicResults

[29] *ATLAS inner detector: Technical Design Report, 1.* Technical Design Report ATLAS. CERN, Geneva, 1997.

[30] *ATLAS inner detector: Technical Design Report, 2.* Technical Design Report ATLAS. CERN, Geneva, 1997.

[31] ATLAS Magnet System: Illustrations, http://atlas-magnet.web.cern.ch/atlas-magnet/gallery/images/

[32] The ATLAS Collaboration, *The ATLAS Experiment at the CERN Large Hadron Collider*, JINST 3 (2008) S08003.

[33] *ATLAS calorimeter performance: Technical Design Report.* Technical Design Report ATLAS. CERN, Geneva, 1996.

[34] *ATLAS liquid argon calorimeter: Technical design report.* Technical Design Report ATLAS. CERN, Geneva, 1996.

[35] ATLAS Electromagnetic Barrel Calorimeter Collaboration, M. Aharrouche et al., *Energy linearity and resolution of the ATLAS electromagnetic barrel calorimeter in an electron test-beam*, Nucl.Instrum.Meth. A568 (2006) 601–623.

[36] *ATLAS level-1 trigger: Technical Design Report.* Technical Design Report ATLAS. CERN, Geneva, 1998.

[37] P. Jenni, M. Nessi, M. Nordberg, and K. Smith, *ATLAS high-level trigger, data-acquisition and controls: Technical Design Report.* Technical Design Report ATLAS. CERN, Geneva, 2003.

[38] The ATLAS Collaboration, *Improved luminosity determination in pp collisions at* $\sqrt{s}$ *= 7 TeV using the ATLAS detector at the LHC*, arXiv:1302.4393 [hep-ex].

[39] GEANT4 Collaboration, S. Agostinelli et al., *GEANT4: A simulation toolkit* , Nucl. Inst. Meth. A506 (2003) 250–303.

[40] ATLAS Collaboration, *The ATLAS simulation infrastructure*, Eur. Phys. J. C 70 (2010) 823, arXiv:1005.4568 [physics.ins-det].

[41] S. Alioli, P. Nason, C. Oleari, and E. Re, *NLO Higgs boson production via gluon fusion matched with shower in POWHEG*, JHEP 0904 (2009) 002.

[42] P. Nason and C. Oleari, *NLO Higgs boson production via vector-boson fusion matched with shower in POWHEG*, JHEP 1002 (2010) 037.

[43] T. Gleisberg et al., *Event generation with SHERPA 1.1*, JHEP 0902 (2009) 007.

[44] T. Binoth, J. Guillet, E. Pilon, and M. Werlen, *A full next-to-leading order study of direct photon pair production in hadronic collisions*, Eur. Phys. J C16 (2000) 311.

[45] J. Alwall, M. Herquet, F. Maltoni, O. Mattelaer, and T. Stelzer, *MadGraph 5 : Going Beyond*, JHEP 1106 (2011) 128, arXiv:1106.0522 [hep-ph].

[46] PT. Sjostrand, S. Mrenna, and P. Z. Skands, *PYTHIA 6.4 Physics and Manual*, JHEP 0605 (2006) 026.

[47] T. Sjostrand, S. Mrenna, and P. Z. Skands, *A Brief Introduction to PYTHIA 8.1*, Comput. Phys. Commun. 178 (2008) 852.

[48] H. Georgi, S. Glashow, M. Machacek, and D. V. Nanopoulos, *Higgs bosons from two gluon annihilation in proton proton collisions*, Phys. Rev. Lett. 40 (1978) 692.

[49] A. Djouadi, M. Spira, and P. M. Zerwas, *Production of Higgs bosons in proton colliders: QCD corrections*, Phys. Lett. B 264 (1991) 440.

[50] S. Dawson, *Radiative corrections to Higgs boson production*, Nucl. Phys. B359 (1991) 283.

[51] M. Spira, A. Djouadi, D. Graudenz, and P. M. Zerwas, *Higgs boson production at the LHC*, Nucl. Phys. B453 (1995) 17.

[52] R. Harlander and W. B. Kilgore, *Next-to-next-to-leading order Higgs production at hadron colliders*, Phys. Rev. Lett. 88 (2002) 201801.

[53] C. Anastasiou and K. Melnikov, *Higgs boson production at hadron colliders in NNLO QCD*, Nucl. Phys. B646 (2002) 220.

[54] V. Ravindran, J. Smith, and W. L. van Neerven, *NNLO corrections to the total cross section for Higgs boson production in hadron hadron collisions*, Nucl. Phys. B665 (2003) 325.

[55] U. Aglietti, R. Bonciani, G. Degrassi, and A. Vicini, *Two-loop light fermion contribution to Higgs production and decays*, Phys. Lett. B 595 (2004) 432.

[56] S. Actis, G. Passarino, C. Sturm, and S. Uccirati, *NLO electroweak corrections to Higgs boson production at hadron colliders*, Phys. Lett. B 670 (2008) 12.

[57] S. Catani, D. de Florian, M. Grazzini, and P. Nason, *Soft-gluon re-summation for Higgs boson production at hadron colliders*, JHEP 0307 (2003) 028.

[58] D. de Florian and M. Grazzini, *Higgs production at the LHC: updated cross sections at* $\sqrt{s} = 8$ *TeV*, arXiv:1206.4133 [hep-ph].

[59] C. Anastasiou, S. Buehler, F. Herzog, and A. Lazopoulos, *Inclusive Higgs boson cross-section for the LHC at 8 TeV*, JHEP 1204 (2012) 004.

[60] J. Baglio and A. Djouadi, *Higgs production at the lHC*, JHEP 1103 (2011) 055.

[61] D. de Florian, G. Ferrera, M. Grazzini, and D. Tommasini, *Transverse-momentum resummation: Higgs boson production at the Tevatron and the LHC*, JHEP 1111 (2011) 064.

[62] E. Bagnaschi, G. Degrassi, P. Slavich, and A. Vicini, *Higgs production via gluon fusion in the POWHEG approach in the SM and in the MSSM*, JHEP 1202 (2012) 88.

[63] R. Cahn and S. Dawson, *Production of very massive Higgs bosons*, Phys. Lett. B 136 (1984) 196, Erratum–ibid. B 138 (1984) 464.

[64] M. Ciccolini, A. Denner, and S. Dittmaier, *Strong and electroweak corrections to the production of Higgs+2jets via weak interactions at the LHC*, Phys. Rev. Lett. 99 (2007) 161803.

[65] M. Ciccolini, A. Denner, and S. Dittmaier, *Electroweak and QCD corrections to Higgs production via vector-boson fusion at the LHC*, Phys. Rev. D 77 (2008) 013002.

[66] K. Arnold, M. Bahr, G. Bozzi, F. Campanario, C. Englert, et al., *VBFNLO: A parton level Monte Carlo for processes with electroweak bosons*, Comput. Phys. Commun. 180 (2009) 1661.

[67] P. Bolzoni, F. Maltoni, S.-O. Moch, and M. Zaro, *Higgs production via vector-boson fusion at NNLO in QCD*, Phys. Rev. Lett. 105 (2010) 011801.

[68] S. Glashow, D. V. Nanopoulos, and A. Yildiz, *Associated production of Higgs bosons and Z particles*, Phys. Rev. D 18 (1978) 1724.

[69] T. Han and S. Willenbrock, *QCD correction to the pp →WH and ZH total cross sections*, Phys. Lett. B 273 (1991) 167.

[70] O. Brein, A. Djouadi, and R. Harlander, *NNLO QCD corrections to the Higgs-strahlung processes at hadron colliders*, Phys. Lett. B 579 (2004) 149.

[71] M. L. Ciccolini, S. Dittmaier, and M. Kramer, *Electroweak radiative corrections to associated WH and ZH production at hadron colliders,* Phys. Rev. D 68 (2003) 073003.

[72] Z. Kunszt, *Associated production of heavy Higgs boson with top quarks*, Nucl. Phys. B 247 (1984) 339.

[73] W. Beenakker et al., *Higgs Radiation Off Top Quarks at the Tevatron and the LHC*, Phys. Rev. Lett. 87 (2001) 201805.

[74] W. Beenakker et al., *NLO QCD corrections to t¯tH production in hadron collisions*, Nucl. Phys. B 653 (2003) 151.

[75] S. Dawson, L. H. Orr, L. Reina, and D. Wackeroth, *Next-to-leading order QCD corrections to pp → tt̄h at the CERN Large Hadron Collider*, Phys. Rev. D 67 (2003) 071503.

[76] S. Dawson, C. Jackson, L. H. Orr, L. Reina, and D. Wackeroth, *Associated Higgs production with top quarks at the Large Hadron Collider: NLO QCD corrections*, Phys. Rev. D 68 (2003) 034022.

[77] G. Corcella, I. Knowles, G. Marchesini, S. Moretti, K. Odagiri, et al., *HERWIG 6: An Event generator for hadron emission reactions with interfering gluons (including supersymmetric processes)*, JHEP 0101 (2001) 010.

[78] J. M. Butterworth, J. R. Forshaw, and M. H. Seymour, *Multiparton interactions in photoproduction at HERA*, Z. Phys. C 72 (1996) 637.

[79] P. Golonka and Z.Was, *PHOTOS Monte Carlo: A Precision tool for QED corrections in Z and W decays*, Eur. Phys. J. C 45 (2006) 97.

[80] N. Davidson, T. Przedzinski, and Z. Was, *PHOTOS interface in C++: technical and physics documentation*, arXiv:1011.0937 [hep-ph].

[81] H.-L. Lai et al., *New parton distributions for collider physics*, Phys. Rev. D 82 (2010) 074024.

[82] P. M. Nadolsky et al., *Implications of CTEQ global analysis for collider observables*, Phys. Rev. D 78 (2008) 013004.

[83] A. Sherstnev and R. S. Thorne, *Parton distributions for the LHC*, Eur. Phys. J C 55 (2009) 553, arXiv:0711.2473 [hep-ph].

[84] The ATLAS Collaboration, *Measurements of the photon identification efficiency with the ATLAS detector using 4.9 fb^{-1} of pp collision data collected in 2011.* ATLAS-CONF-2012-123 (2012).

[85] Lance Dixon, M. Stewart Siu, *Resonance-continuum interference in the di-photon Higgs signal at the LHC*, Phys. Rev. Lett. 90 (2003) 252001.

[86] D. de Florian, G. Ferrera, M. Grazzini, and D. Tommasini, *Transverse-momentum resummation: Higgs boson production at the Tevatron and the LHC*, JHEP 1111 (2011) 064, arXiv:1109.2109 [hep-ph].

[87] ATLAS Collaboration, *Expected photon performance in the ATLAS experiment*, ATLAS-PHYS-PUB-2011-007 (2011).

[88] ATLAS Stand-Alone Event Displays, https://twiki.cern.ch/twiki/bin/view/AtlasPublic/EventDisplayStandAlone

[89] ATLAS Collaboration, *Performance of primary vertex reconstruction in proton-proton collisions at $\sqrt{s}$ =7 TeV in the ATLAS experiment*, ATLAS-CONF-2010-069 (2010).

[90] ATLAS Collaboration, *Performance of the ATLAS Inner Detector Track and Vertex Reconstruction in the High Pile-Up LHC Environment*, ATLAS-CONF-2012-042 (2012).

[91] ATLAS collaboration, *Measurements of the properties of the Higgs-like boson in the two photon decay channel with the ATLAS detector using 25 fb^{-1} of proton-proton collision data*, ATLAS-CONF-2013-012 (2013).

[92] The ATLAS Collaboration, *Performance of the ATLAS Trigger System in 2010*, Eur. Phys. J. C72 938 (2012).

[93] ATLAS Collaboration, *Observation of an excess of events in the search for the Standard Model Higgs boson in the gamma-gamma channel with the ATLAS detector*, ATLAS-CONF-2012-091 (2012).

[94] The ATLAS Collaboration, *Improved electron reconstruction in ATLAS using the Gaussian Sum Filter-based model for bremsstrahlung*, ATLAS-CONF-2012-047 (2012).

[95] M. Cacciari, G. P. Salam, and G. Soyez, *The anti-kt jet clustering algorithm*, JHEP 0804 (2008) 063.

[96] ATLAS collaboration, *Performance of missing transverse momentum reconstruction in ATLAS with 2011 proton-proton collisions at* $\sqrt{s} = 7$ *TeV*, ATLAS-CONF-2012-101 (2012).

[97] A. Hoecker, P. Speckmayer, J. Stelzer, J. Therhaag, E. von Toerne, and H. Voss, *TMVA 4 (Toolkit for multivariate data analysis with ROOT) Users Guide*. 2009.

[98] ATLAS Collaboration, *Expected performance of the ATLAS experiment : detector, trigger and physics*, CERN Document Server.

[99] The ATLAS Collaboration, *Search for the Standard Model Higgs boson in the diphoton decay channel with 4.9* fb^{-1} *of ATLAS data at* $\sqrt{s} = 7$ *TeV*, ATLAS-CONF-2011-161 (2011) .

[100] The ATLAS Collaboration, *Measurement of the isolated di-photon cross-section in pp collisions at* $\sqrt{s} = 7$ *TeV with the ATLAS detector*, Phys. Rev. D85 (2012) 012003.

[101] The ATLAS Collaboration, *Jet energy measurement with the ATLAS detector in proton-proton collisions at* $\sqrt{s} =$*7 TeV*, arXiv:1112.6426 [hep-ex].

[102] ATLAS Collaboration, *Summary of ATLAS Pythia 8 tunes*, ATL-PHYS-PUB-2012-003 (2012).

[103] A. Wald, *Tests of Statistical Hypotheses Concerning Several Parameters When the Number of Observations is Large*, Transactions of the American Mathematical Society, Vol. 54, No. 3 (Nov., 1943), pp. 426-482.

[104] S.S. Wilks, *The large-sample distribution of the likelihood ratio for testing composite hypotheses*, Ann. Math. Statist. 9 (1938) 60-2.

[105] ATLAS Collaboration, *Evidence for the spin-0 nature of the Higgs boson using ATLAS data*, Phys.Lett. B726 (2013) 120-144.

[106] M. Carena, S. Gori, N. R. Shah, and C. E. M. Wagner, *A 125 GeV SM-like Higgs in the MSSM and the* $\gamma\gamma$ *rate*, Journal of High Energy Physics, vol. 2012, no. 3, article 014, 2012.

[107] M. Carena, I. Low and C.E.M Wagner, *Implications of a modified Higgs to diphoton decay width*, JHEP 1208 (2012) 060.

[108] A. Joglekar, P. Schwaller and C.E.M. Wagner, *Dark matter and enhanced Higgs to di-photon rate from vector-like leptons*, JHEP 12 (2012) 064.

[109] H. Davoudiasl, H.-S. Lee, and W. J. Marciano, *Dark Side of Higgs Diphoton Decays and Muon g-2*, Phys.Rev. D86 (2012) 095009.

[110] ATLAS Collaboration, *Jet energy scale and its sytematic uncertainty in proton-proton collisions at $\sqrt{s} = 7$ TeV with ATLAS 2010 data*, tech. rep., CERN, 2011. ATLAS-CONF-2011-032.

[111] The ATLAS Collaboration, *Measurements of Higgs boson production and couplings in diboson final states with the ATLAS detector at the LHC*, Phys. Lett. B 726 (2013) 88.